



Université de Liège

Faculté des Sciences Appliquées



# Array recordings of ambient vibrations: surface-wave inversion

A thesis submitted for the degree of  
Doctor of Applied Sciences  
presented by Marc Wathelet

February, 2005



# Contents

<b>List of figures</b>	<b>iv</b>
<b>List of tables</b>	<b>ix</b>
<b>Résumé</b>	<b>xi</b>
<b>Abstract</b>	<b>xiii</b>
<b>Introduction</b>	<b>1</b>
Objectives . . . . .	2
Thesis outline . . . . .	3
<b>1 Measuring wave velocity</b>	<b>5</b>
1.1 Ambient vibrations . . . . .	5
1.1.1 Frequency-wavenumber method . . . . .	6
1.1.2 High resolution method . . . . .	12
1.1.3 Spatial auto-correlation method . . . . .	13
1.2 Artificial sources . . . . .	14
1.2.1 $P - S_V$ refracted waves . . . . .	15
1.2.2 $S_H$ refracted waves . . . . .	17
1.2.3 Surface wave inversion . . . . .	17
1.3 Conclusions . . . . .	18
<b>2 The inversion algorithm</b>	<b>19</b>
2.1 Definition . . . . .	19
2.2 Available methods . . . . .	20
2.2.1 Gridding method . . . . .	21
2.2.2 Iterative methods . . . . .	21
2.2.3 Neural Networks . . . . .	22
2.2.4 Monte Carlo methods . . . . .	22
2.3 The neighbourhood algorithm . . . . .	23
2.4 Conditional parameter spaces . . . . .	25
2.5 Conclusions . . . . .	28

<b>3</b>	<b>Forward computation</b>	<b>29</b>
3.1	Dispersion Curves . . . . .	29
3.1.1	Propagator-matrix method . . . . .	30
3.1.2	Displacements, Stresses, and strains . . . . .	31
3.1.3	Eigenvalue problem for Love waves . . . . .	31
3.1.4	Eigenvalue problem for Rayleigh waves . . . . .	35
3.1.5	A quick root search . . . . .	40
3.1.6	Mode jumping control . . . . .	44
3.1.7	Misfit . . . . .	46
3.1.8	Sensitivity of the dispersion against layer parameters . . . . .	46
3.1.9	Conclusion . . . . .	56
3.2	Ellipticity . . . . .	56
3.2.1	Computation . . . . .	57
3.2.2	Sensitivity . . . . .	58
3.2.3	Misfit . . . . .	60
3.3	Spatial auto-correlation . . . . .	61
3.3.1	Computation . . . . .	61
3.3.2	Misfit . . . . .	62
3.3.3	Sensitivity . . . . .	63
3.4	Conclusion . . . . .	64
<b>4</b>	<b>Parameterization of a ground model</b>	<b>65</b>
4.1	Theoretical model used in parameterization tests . . . . .	65
4.2	Thickness, $V_p$ , and $V_s$ . . . . .	67
4.2.1	Two layers . . . . .	69
4.2.2	Three layers . . . . .	72
4.3	Stack of N layers . . . . .	79
4.3.1	Arbitrary profile . . . . .	79
4.3.2	$V_s$ inversion without LVZ . . . . .	81
4.4	Non-uniform layers . . . . .	83
4.4.1	Linear variation . . . . .	83
4.4.2	Power law variation . . . . .	83
4.5	Conclusions . . . . .	86
<b>5</b>	<b>Enhanced inversions</b>	<b>89</b>
5.1	Multimodal curves . . . . .	89
5.1.1	Rayleigh higher modes . . . . .	90
5.1.2	Love and Rayleigh . . . . .	95
5.1.3	Higher mode identification . . . . .	95
5.2	Spatial auto-correlation . . . . .	100
5.2.1	Uniqueness of auto-correlation curves . . . . .	101

5.2.2	Synthetic model . . . . .	101
5.2.3	Validation of auto-correlations . . . . .	101
5.2.4	Inversion . . . . .	104
5.3	Ellipticity inversion . . . . .	106
<b>6</b>	<b>Test cases</b>	<b>109</b>
6.1	Synthetic ambient vibrations . . . . .	109
6.1.1	Model description . . . . .	109
6.1.2	Single source wavefield . . . . .	112
6.1.3	Frequency-wavenumber method . . . . .	114
6.1.4	High resolution method . . . . .	117
6.1.5	Spatial auto-correlation method . . . . .	119
6.1.6	Discussion and Conclusions . . . . .	120
6.2	Liège site . . . . .	124
6.2.1	The test site . . . . .	124
6.2.2	Ambient vibrations recording . . . . .	130
6.2.3	Frequency-wavenumber method . . . . .	131
6.2.4	High resolution method . . . . .	136
6.2.5	Spatial auto-correlation method . . . . .	137
6.2.6	Conclusions . . . . .	140
	<b>Conclusion</b>	<b>141</b>
<b>A</b>	<b>Sub-determinants of <math>R^{(i)}</math></b>	<b>145</b>
<b>B</b>	<b>Generating increasing velocity profiles</b>	<b>149</b>
B.1	Selection method . . . . .	150
B.2	Sorting method . . . . .	150
B.3	Velocity-jump method . . . . .	150
B.4	Interpolation method . . . . .	151
B.5	Interpolation method with random start . . . . .	151
B.6	Bisection method . . . . .	152
B.7	Diagonal method . . . . .	152
B.8	Including Poisson's ratio . . . . .	153
B.9	Conclusions . . . . .	153
	<b>References</b>	<b>155</b>



# List of Figures

1.1	Theoretical array responses for 25 sensors . . . . .	8
1.2	Theoretical array responses for 10 sensors . . . . .	9
1.3	Reference model for refraction synthetic travelttime-distance plot . . . . .	15
1.4	Inversion of synthetic travelttime-distance plot . . . . .	16
1.5	Theoretical array responses for a line of sensors . . . . .	18
1.6	Example of a f-k analysis for triggered surface waves . . . . .	18
2.1	Definition of an inversion problem . . . . .	19
2.2	Voronoi cells for a two-dimensional parameter space . . . . .	24
2.3	Comparison of variable transformation and selection methods . . . . .	26
2.4	High level condition intersection with Voronoi cells . . . . .	27
3.1	Schematic one-dimensional model . . . . .	30
3.2	Values taken by $l_{21}(z_0)$ . . . . .	35
3.3	Values taken by $R_{1212}(z_0)$ . . . . .	39
3.4	Velocity limits of Love and Rayleigh dispersion curves . . . . .	40
3.5	Method for bracketing roots. . . . .	42
3.6	Method for refining roots . . . . .	43
3.7	Dispersion curve of a model with a LVZ. . . . .	45
3.8	Two layers: influence of $V_{s0}$ with a constant $V_p$ profile . . . . .	47
3.9	Two layers: influence of $V_{s0}$ with a constant Poisson's ratio . . . . .	48
3.10	Two layers: influence of $V_{p0}$ . . . . .	49
3.11	Two layers: influence of $z_1$ . . . . .	49
3.12	Two layers: influence of $z_1$ for $V_s$ profile . . . . .	50
3.13	Two layers: influence of $z_1$ for $V_p$ profile . . . . .	51
3.14	Two layers: influence of $\rho_0$ . . . . .	52
3.15	Two layers: influence of $V_{s1}$ with a constant $V_p$ profile . . . . .	52
3.16	Two layers: influence of $V_{p1}$ . . . . .	53
3.17	Two layers: influence of $\rho_1$ . . . . .	53
3.18	Three layers: influence of $V_{s1}$ with a constant Poisson's ratio . . . . .	54
3.19	Three layers: equivalent two-layer model at high frequency . . . . .	55
3.20	Three layers: influence of $V_{p1}$ . . . . .	55
3.21	Ellipticity 2 layers: influence of $V_{s0}$ with a constant $V_p$ profile . . . . .	59

3.22	Ellipticity 2 layers: influence of $V_{s0}$ with a constant Poisson's ratio . . . . .	59
3.23	Ellipticity 3 layers: influence of $V_{s1}$ with a constant Poisson's ratio . . . . .	60
3.24	Auto-correlation, azimuth-inter-distance plot example . . . . .	62
3.25	Auto-correlation: influence of $V_{s0}$ with a constant Poisson's ratio . . . . .	63
4.1	Theoretical case for testing parameterizations . . . . .	66
4.2	Inversion of the full dispersion curve with a two-layer model . . . . .	69
4.3	Inversion with a two-layer model: variation of the minimum misfit . . . . .	70
4.4	Inversion with a two-layer model: parameter space . . . . .	70
4.5	Inversion with a two-layer model: velocity profiles . . . . .	71
4.6	Inversion with a three-layer model over a broad frequency range . . . . .	73
4.7	Inversion with a three-layer model over a restricted frequency range . . . . .	74
4.8	Inversion with a three-layer model over a low frequency range . . . . .	74
4.9	Inversion with a three-layer model with prior depth . . . . .	76
4.10	Inversion with a three-layer model at high frequency with prior depth . . . . .	76
4.11	Inversion with a three-layer model with prior $V_p$ . . . . .	78
4.12	Inversion with a three-layer $V$ model at high frequency with prior $V_p$ . . . . .	78
4.13	Inversion with a N-layer model accepting LVZ ( $V_s$ only) . . . . .	80
4.14	Inversion with a N-layer model accepting LVZ ( $V_p$ and $V_s$ ) . . . . .	81
4.15	Inversion with a N-layer model rejecting LVZ by the diagonal method . . . . .	82
4.16	Comparison of a three-layer and N-layer inversions . . . . .	82
4.17	Inversion with a three-layer model with heterogeneous layers . . . . .	85
4.18	Inversion with a three-layer model with heterogeneous layers . . . . .	85
4.19	Comparison of three type of parameterizations . . . . .	86
5.1	Inversion of first higher mode alone: no prior information . . . . .	90
5.2	Inversion of first higher mode alone: depth between 1 and 20 m/s . . . . .	91
5.3	Inversion of the fundamental mode alone . . . . .	92
5.4	Inversion of the fundamental and the first higher mode . . . . .	93
5.5	Inversion of the fundamental and the first higher mode: narrow band . . . . .	94
5.6	Joint inversion of the Love and Rayleigh fundamental modes . . . . .	96
5.7	Composite dispersion curve . . . . .	97
5.8	Inversion of the composite curve assuming fundamental mode . . . . .	98
5.9	Inversion of the composite curve with mode identification(a) . . . . .	98
5.10	Inversion of the composite curve with mode identification(b) . . . . .	99
5.11	Reference model for auto-correlation inversion . . . . .	102
5.12	Grids in frequency-slowness for auto-correlation pre-processing . . . . .	103
5.13	Inversion of the auto-correlation curves . . . . .	105
5.14	Inversion of the ellipticity alone . . . . .	106
5.15	Join inversion of the dispersion curve and the ellipticity peak . . . . .	107
6.1	Theoretical model for synthetic ambient vibrations . . . . .	110

6.2	Spectral curves of the central station of array A to C . . . . .	110
6.3	Array geometries and their f-k responses . . . . .	111
6.4	Single source wavefield: signals . . . . .	112
6.5	Single source wavefield: influence of window length . . . . .	113
6.6	Single source wavefield: f-k for arrays A and C . . . . .	114
6.7	Single source wavefield: array responses at 6.5 Hz . . . . .	114
6.8	f-k analysis for array C: influence of window length . . . . .	115
6.9	f-k analysis for array A and B . . . . .	116
6.10	Average dispersion from f-k analysis . . . . .	116
6.11	Inversion of average dispersion from f-k analysis . . . . .	117
6.12	High resolution analysis for arrays A, B and C . . . . .	118
6.13	Inversion of dispersion curves from high resolution analysis . . . . .	118
6.14	Influence of time window lengths on auto-correlation curves . . . . .	120
6.15	Azimuth-inter-distance plot . . . . .	121
6.16	Calculated and selected auto-correlation samples . . . . .	121
6.17	Grids in frequency-slowness for auto-correlation pre-processing . . . . .	121
6.18	Inversion of auto-correlation curves . . . . .	122
6.19	Inversion of Love and Rayleigh fundamental modes . . . . .	123
6.20	Local map of the test site . . . . .	125
6.21	Recorded signals for East-West $P - S_V$ refraction line . . . . .	126
6.22	Refraction results for profile East-West . . . . .	127
6.23	Refraction results for profile North-South . . . . .	127
6.24	Triggered surface waves along $P - S_V$ profiles: spectra . . . . .	128
6.25	Triggered surface waves along $P - S_V$ profiles: f-k analysis . . . . .	129
6.26	Refraction results for $S_H$ profile . . . . .	130
6.27	Array geometries . . . . .	131
6.28	Spectral curves of the central station . . . . .	131
6.29	Theoretical array response . . . . .	132
6.30	Results of the frequency-wavenumber method . . . . .	133
6.31	Average of apparent dispersion curves . . . . .	133
6.32	Inversion of the average dispersion curve . . . . .	134
6.33	Inversion of the average dispersion curve and ellipticity peak . . . . .	135
6.34	Results of the high resolution frequency-wavenumber method . . . . .	136
6.35	Calculated and selected auto-correlation samples . . . . .	138
6.36	Azimuth-inter-distance plot . . . . .	138
6.37	Grids in frequency-slowness for auto-correlation pre-processing . . . . .	138
6.38	Inversion of auto-correlation curves . . . . .	139
B.1	Prior information carried by parameterization: LVZ . . . . .	149
B.2	Prior information carried by parameterization: velocity jump . . . . .	150
B.3	Prior information carried by parameterization: interpolation . . . . .	151

B.4	Prior information carried by parameterization: random interpolation . . . . .	152
B.5	Prior information carried by parameterization: bisection . . . . .	153
B.6	Prior information carried by parameterization: diagonal . . . . .	153
B.7	Prior information carried by parameterization: scaled diagonal . . . . .	154
B.8	Prior information carried by parameterization: scaled interpolate . . . . .	154

# List of Tables

1.1	Properties of the array geometries . . . . .	10
4.1	Properties of the reference model . . . . .	66
4.2	Parameterized model for two-layer inversions . . . . .	69
4.3	Parameterized model for three-layer inversions . . . . .	72
4.4	Parameterized model for three-layer inversions with prior depth . . . . .	75
4.5	Parameterized model for three-layer inversions with prior $V_p$ . . . . .	77
4.6	Parameterized model for N-layer inversions . . . . .	79
5.1	Parameterized model with a basement between 30 and 120 m . . . . .	93
5.2	Parameterized model with a basement between 15 and 30 m . . . . .	93
5.3	Inversion runs for Love-Rayleigh dispersion curves . . . . .	95
5.4	Parameters for auto-correlation inversion . . . . .	104
5.5	Parameters for ellipticity alone inversion . . . . .	106
6.1	Properties of the reference model . . . . .	109
6.2	Properties of the array geometries . . . . .	112
6.3	Wavenumber limits deduced from high resolution analysis . . . . .	117
6.4	Minima and maxima radii of rings . . . . .	119
6.5	Apparent limits for auto-correlation methods . . . . .	120
6.6	Borehole descriptions around the site . . . . .	126
6.7	Wavenumber limits from theoretical array responses . . . . .	132
6.8	Parameters and their prior interval for inversions . . . . .	134



# Résumé

Le bruit de fond sismique est une technique de plus en plus utilisée en génie parasismique pour estimer le profil de vitesse des ondes de cisaillement pour un site donné. Admettant l'hypothèse qu'elles sont majoritairement composées d'ondes de surface, les vibrations ambiantes enregistrées par un réseau de capteurs peuvent être utilisées pour déterminer la courbe de dispersion. En général, cela fournit une courbe sur une large gamme de fréquences et cela comporte l'avantage de ne pas nécessiter l'usage de source artificielle. A cause de l'incertitude sur les données et des non-linéarités du problème, la solution de l'inversion des courbes de dispersion n'est pas unique. Les méthodes de recherche directe comme l'algorithme de voisinage permettent l'investigation de tout l'espace des paramètres et l'introduction d'informations a priori de manière rationnelle. Suite au nombre limité de paramètres pour l'inversion des ondes de surface, elles constituent une alternative intéressante aux méthodes linéarisées. Au cours de cette thèse, des outils efficaces basés sur l'algorithme de voisinage sont développés pour obtenir les profils uni-dimensionnel de  $V_s$  à partir d'enregistrements avec des sources actives ou passives. Comme le nombre de modèles générés est habituellement grand avec ces méthodes stochastiques, une attention particulière a été attachée à l'optimisation et à la qualité de la résolution du problème direct.

Le code développé a été testé sur plusieurs modèles synthétiques, dont un est présenté ici. Les effets de la gamme de fréquence disponible et l'influence de l'information a priori sont particulièrement mis en évidence. Les modes supérieurs peuvent apporter des contraintes supplémentaires lors de l'inversion mais ils posent également de nombreux problèmes quant à leur identification correcte, pour laquelle un algorithme est proposé. Nous montrons aussi que l'inversion des modes de Love et de Rayleigh est une technique prometteuse pour augmenter la profondeur de pénétration de la méthode. De plus, nous avons développé un outil spécifique pour l'inversion des courbes d'auto-corrélation qui prend en compte les incertitudes observées sur les courbes expérimentales et les propage aux profils de vitesse inversés.

L'interprétation complète depuis l'acquisition jusqu'à obtention des profils de vitesse est illustrée par deux exemples avec un champ d'onde synthétique et réel (Liège, Belgique). Les informations déduites de forages, de tests de réfraction classiques, d'enregistrements avec des sources actives, et de la fréquence du pic H/V sont analysées pour valider les résultats des réseaux.



# Abstract

Microtremors are increasingly used in earthquake engineering to infer the shear-wave velocity profile at a given site. Assuming they are mainly composed of surface waves, ambient vibrations recorded by an array of sensors can be used to determine the dispersion curve. Generally, it provides a large frequency band dispersion curve and it has the advantage of not requiring artificial sources, making it particularly suitable for urban applications. Due to the data uncertainties and the non-linearity of the problem, the solution of the dispersion curve inversion is not unique. Direct search methods like the neighbourhood algorithm allow the investigation of the whole parameter space and the introduction of prior information in a rational way. Due to the limited number of parameters in surface-wave inversion, they constitute an attractive alternative to linearized methods. During this thesis, efficient tools based on the neighbourhood algorithm are developed to obtain the one-dimensional  $V_s$  profile from passive or active source experiments. As the number of generated models is usually high with stochastic techniques, special attention is paid to the optimization and to the reliability of the forward computations.

The developed code has been tested on several synthetic models, among them one is presented here. The effects of the available frequency range and the influence of the prior information are particularly emphasized. Higher modes might bring additional constraints during the inversion but they also raise the crucial problem of their correct identification, for which an algorithm is proposed. We also show that the inversion of Love and Rayleigh modes is a promising technique to increase the penetration depth of the method. Moreover, we developed a specific tool for the inversion of auto-correlation curves which takes into account the uncertainties observed on experimental curves and propagates it to the inverted velocity profiles.

The whole interpretation chain from field acquisitions to the achievement of velocity profiles is illustrated by two examples with synthetic and real wavefields (Liège, Belgium). Information from boreholes, classical refraction tests, active surface wave experiments, and from the H/V peak frequency are analysed to check the validity of the array results.



# Introduction

During the last twenty years, several major earthquakes (Mexico 1985, Loma Prieta 1989, Kobe 1995, Izmit 1999, El Salvador 2001, Bam 2003, ...) were directly responsible of tens of thousands of persons killed and injured. The damage to human infrastructures and the disturbances of the local life represent an inestimable cost for national and local authorities, usually requiring international cooperation. Most of the cities and high populated areas are located on soft sediments (valleys, estuaries, recent deposits, ...) the soil structure of which are prone to amplify seismic waves (Murphy and Shah 1988, Bard 1994). This phenomenon is usually called site effect or site amplification since the amplitude of the motion highly depends upon the local properties of the soil. Consequently, the risk mitigation requires fine investigations of each geological setting. The investments necessary with conventional techniques, i.e. boreholes, are prohibitive for developing countries and for regions with a moderate seismic activity (e.g. Western Europe). In this context, the European project SESAME (Site EffectS assessment using AMbient Excitation, Project EVG1-CT-2000-00026) was initiated in 2001 to study the reliability of low cost methods based on the measurement of ambient vibrations<sup>1</sup>. The focus was put on two methods: the so-called H/V (Horizontal to vertical ratio) which became widely used after the work of Nakamura (1989), and the more complex array measurements based on the simultaneous recordings of the ambient vibrations at various locations. This thesis, which has been partly financed by the SESAME project, focuses on the array methods, which aim at inferring the one-dimensional shear-wave velocity profile at a given site.

Seismic wave propagation in a geological structure depends on its characteristics: the geometry of the layers, the shear and compressional-wave velocities, the density, and the attenuation factor inside each of them. For one-dimensional geological environments (property variations limited to the vertical axis), it can be theoretically shown that the shear-wave velocity ( $V_s$ ) has the greatest influence. Conventional methods to access this parameter usually require the drilling of invasive and expensive boreholes which might be very disturbant for the inhabitants of dense cities. The determination of  $V_s$  in the layers close to the surface (down to few tens of metres) is now possible without destructive methods thanks to the development of the surface wave methods during the last fifteen years, i.e spectral analysis of surface waves (SASW, Stokoe et al. 1989, Tokimatsu 1995, Foti et al. 2003, Socco and Strobbia 2004). Surface waves travel

---

<sup>1</sup>Also called ambient noise, microtremor, ... However, the word "noise" is ambiguous because it generally designates all apparently random variations not explained by the current scientific model. For ambient vibration methods the noise is separated in coherent and incoherent noise. The first category contains valuable information.

along the ground surface (at the soil-air interface). In vertically heterogeneous media, surface waves are dispersive: their velocity varies as a function of frequency, which in turn controls their penetration depth (Aki and Richards 2002). This dispersion property can be used to derive  $V_s$  versus depth through an inversion process (Herrmann 1994, Wathelet et al. 2004).

Though attractive on many aspects, the surface wave methods using artificial sources generally offer a restricted investigation depth (a few tens of metres usually) due to the limited frequency range of the signals (Jongmans and Demanet 1993, Tokimatsu 1995). Moreover, in various geological environment with thick soft sediments (e.g. 500 m for Grenoble in France), the site effects depend also upon the properties of the deep structure. The improvement of the penetration is possible through the use of higher energy sources rich of low frequency. In an urban context, the use of explosive loads or mechanical generators is limited to avoid disturbance to the neighbouring houses and buildings. For regions with high seismicity and a dense observation network, the experience of past events is intensively used for inferring the site dynamic response. However, for regions with a moderate seismicity, the observation networks are less dense and there are fewer significant events. Consequently, it is necessary to develop other techniques to calculate the site transfer function, for which  $V_s$  is a key parameter.

On the other hand, the frequency content of microtremor record is distributed over a wider range and the measurement of ambient vibrations through an array of sensors has appeared as a promising option to complement active sources (Asten and Henstridge 1984, Tokimatsu 1995, Satoh et al. 2001, Bettig et al. 2001, Nguyen et al. 2004, Wathelet et al. 2004). Noise energy depends upon the source locations and upon the impedance contrast between the rocky basement and the overlying soft sediments (Chouet et al. 1998, Milana et al. 1996). The main hypothesis for using ambient vibrations is that they are dominantly composed of surface waves, which allows the dispersion property to be used (Tokimatsu 1995, Chouet et al. 1998).

The properties of the sources that generate the measured ground excitation are generally unknown. Consequently, the interpretation is generally a two-step process. First, the velocity of the travelling waves at a given frequency is derived from the processing of simultaneous ground-motion recordings at various stations. The common approaches used to derive the dispersion curve from the raw signals can be classified into two main families: frequency-wavenumber methods (Capon 1969, Lacoss et al. 1969, Kvaerna and Ringdahl 1986, Ohrnberger 2001) and spatial auto-correlation methods (Aki 1957, Roberts and Asten 2004). At the second stage, the dispersion curve is inverted to obtain the  $V_s$  (and eventually the  $V_p$ ) vertical profile, as in the classical active-source methods (Stokoe et al. 1989, Malagnini et al. 1995). Like all surface wave methods, the obtained geometry is purely one-dimensional and is averaged across the array, implying that the technique is not suitable when strong lateral variations are present.

## Objectives

The objective of this work is the improvement of existing inversion techniques in the context of ambient vibration methods in order to obtain  $V_s(z)$ . A special attention has been paid to

the reliability of the inverted profiles and to the possibility of including information from other types of experiments in the inversion process.

The derivation of one-dimensional shear-wave velocity profiles from surface wave dispersion curves is a classical inversion problem in geophysics, generally solved using linearized methods (Nolet 1981, Tarantola 1987). The inversion of dispersion curves is known to be strongly non-linear and is affected by non-uniqueness, i.e. various models may explain the same data set with an equal misfit. Linearized methods behave poorly in such contexts and a Monte Carlo like approach has been chosen here. During this thesis, we have developed a new code using the neighbourhood algorithm (Sambridge 1999a) for inverting dispersion curves. The software allows the inclusion of prior information on the different parameters and a major effort has been made to optimize the computation time at the different stages of inversion. In particular, we have re-implemented the dispersion curve computation in C++ language using Dunkin's formalism (1965). The code is tested on synthetic cases as well as on real data sets, combining ambient vibrations and active-source data. In both cases, the role of a prior information for constraining the solution is emphasized. Moreover, specific methods are proposed to invert the auto-correlation curves to obtain directly the ground structure, to identify and to invert higher modes, and to include frequency information measured with the H/V technique.

Aside, a software package has been developed for preparing array campaigns, storing, visualizing and analysing the recorded signals (open source project, GEOPSY). The techniques for processing raw signals were revisited and the corresponding algorithms were implemented in this unified platform dedicated to seismic prospecting.

## Thesis outline

This document is organized in six chapters.

Chapter 1 recalls the available methods for processing the recordings of ambient vibrations. An extension to active-source experiments is also detailed. The output of all these techniques is the dispersion curve of surface waves (or a parent curve).

Chapter 2 summarizes all the general options that can be considered to infer the soil properties from an observed dispersion curve. The chosen algorithm (neighbourhood algorithm) is presented with more details. A personal improvement of this technique is discussed at the end.

Chapter 3 presents the algorithm used for computing the dispersion curves for one-dimensional models. A number of improvements are proposed to speed up the calculations and to ensure a correct answer. The sensitivity of the dispersion curve to input parameters is tested as well.

Between the inversion algorithm and the forward computation, a crucial step is the parameterization of the ground model. The parameter value ranges are chosen and the prior information is included at this stage. Chapter 4 explains all the strategies for choosing parameter based on synthetic dispersion curve examples.

Chapter 5 details various uncommon inversions, that include higher modes, Love and Ray-

leigh modes, the frequency information from H/V techniques, and the direct inversion of auto-correlation curves.

Chapter 6, the array technique is tested on synthetic ambient vibrations with various signal processing methods. The parallel interpretation of arrays of distinct apertures is a key aspect to obtain unbiased dispersion curves, and hence correct  $V_s$  profiles. The processing techniques are applied to array vibration measurements in the city of Liège, Belgium and the results are compared to other prospecting methods (boreholes, seismic refraction, Cone Penetration Tests, H/V).

# Chapter 1

## Measuring wave velocity

During this thesis, we mainly focus on the inversion of the dispersion curves. This first chapter presents the experimental techniques that are commonly used to measure them. After the development of the inversion tool in chapters 2 to 5, chapter 6 describes the whole interpretation chain from the experimental measurements of the dispersion curves (by the means of the methods described in this chapter) to the inversion of the velocity profiles of test sites. The discussion of chapter 6 is based on a synthetic and a real case.

Surface wave methods are divided in two main categories based on the kind of sources that generate the observed signals, i.e. active and passive methods. The first ones record vibrations generated by an artificial source the frequency band of which is generally above 2 Hz (Tokimatsu 1995). Their penetration depths are usually limited to a few tens of metres (Jongmans and Demanet 1993, Tokimatsu 1995, Socco and Strobbia 2004). On the contrary, ambient vibrations or microtremors are produced with sources of much larger spectra, making both methods complementary for investigating deep geological structures (Nguyen et al. 2004, Wathelet et al. 2004).

The determination of the dispersion characteristics (dispersion or auto-correlation curves) from passive recordings is first reviewed. Frequency wavenumber (f-k, Lacoss et al. 1969, Kvaerna and Ringdahl 1986), high resolution frequency wavenumber (Capon 1969, Horike 1985) and spatial auto-correlation methods (Aki 1957, Roberts and Asten 2004) are the most popular ones. The processing technique used in this thesis for active experiment is a particular case of the general frequency wavenumber method. Additionally, the sensor layout deployed for the active surface wave method is the same as for refraction surveys and allows the measurement of  $V_p$  and  $V_s$  profiles on the first tens of metres, which brings valuable information for the inversion of the dispersion curve (chapter 3).

### 1.1 Ambient vibrations

The main objective when processing ambient vibration recordings is to measure the velocity of surface waves which varies with frequency. The first assumption is hence that the wavefield mainly consists of surface waves. For a horizontally stratified soil structure, the measured

velocities might be the body wave velocities ( $V_p$  and  $V_s$ ) or the dispersion curve of surface waves including the fundamental and the higher modes (Aki and Richards 2002). If the direction of propagation is known and if one single wave dominates, the velocity can be calculated by picking the arrival time at two sensors separated by a fixed distance. However, the ambient wavefield is made of the superposition of many waves travelling in any direction. Picking is no longer possible because the individual propagating waves cannot be identified, and more sensors are necessary to scan all potential azimuths. Signal processing techniques are essential to retrieve the apparent velocities. We restrict our work to the vertical component of the wavefield which does not contain Love contributions.

Theoretically, better velocity measurements are achieved when numerous sensors are available to sample the wavefield at the ground surface. Ideally, the number of stations should be greater than the number of waves present at one time (Asten and Henstridge 1984). Practically, the ambient wavefield is recorded by a limited number of sensors for cost and logistical reasons (ten to a few tens of elements per array, Chouet et al. 1997, Saccorotti et al. 2003, Scherbaum et al. 2003). The three components are generally recorded simultaneously at each station. The optimum of the array geometry is still a matter of debates. However, the array output must be identical for all incident azimuths because there is generally no prior knowledge about the characteristics of the ambient wavefield (Asten and Henstridge 1984). Hence, a roughly circular shape is probably the best option. All sensors must not necessarily lay on the same circle, but there must be a certain kind of rotational symmetry in the sensor positions. In section 1.1.1 on page 7, a quantitative method is proposed to analyse the efficiency of arrays.

Once the signals are recorded for a sufficient duration (at least half an hour, or longer for deep soil structures that require low frequency information), they are processed with the three techniques described hereafter, which extract the same velocity information from the raw signals in three different ways. Agreement between the three methods is usually expected for good quality results. Tests of the three processing methods on a synthetic and a real case are given in chapter 6. Other methods, like multiple signal classification (MUSIC, Schmidt 1981, Cornou et al. 2003) are not considered here.

### 1.1.1 Frequency-wavenumber method

#### Principles

The horizontal velocity is calculated for various frequency bands. The raw signals are first divided in short time windows the length of which may depend upon the considered frequency band. The optimum window length is discussed in sections 6.1.2 and 6.1.3 from synthetic signal analysis. Eventually, a pre-processing method may be used to reject certain parts of the measured signals (transient or saturated signals, Bard 1998). A Fourier transform is calculated for the signal of each sensor after a proper cutting of the current time window (a 10% cosine taper is applied). The frequency-wavenumber transformation itself is calculated in the frequency domain on the cut signals.

Frequency-wavenumber (f-k, Lacoss et al. 1969, Kvaerna and Ringdahl 1986) analysis assumes horizontal plane waves to travel across the array of sensors laid out at the surface. Considering a wave with frequency  $f$ , a direction of propagation and a velocity (or equivalently  $k_x$  and  $k_y$ , wavenumbers along X and Y horizontal axis, respectively) the relative arrival times are calculated at all sensor locations and the phases are shifted according to the time delays. The array output is calculated by the summation of shifted signals in the frequency domain. If the waves effectively travel with the given direction and velocity, all contributions will stack constructively, resulting in a high array output. The array output divided by the spectral power is called the semblance (Lacoss et al. 1969, Asten and Henstridge 1984). The location of the maximum of semblance in the plane  $(k_x, k_y)$  provides an estimate of the velocity and of the azimuth of the travelling waves across the array.

The velocity corresponding to the maximum of semblance is searched between limits which depend upon each particular software implementation. This part is detailed on page 11. For each time window, a velocity value is calculated, and an histogram is generally constructed for each frequency band. Examples of such results are found in chapter 6.

In the case of waves travelling simultaneously in various directions (usual situation for ambient vibrations), the assumption of uncorrelated signals may not be satisfied, leading to incorrect velocity estimates (Goldstein and Archuleta 1987). With a limited number of sensors, stacking during a long enough period of time (a few tens of minutes) is then necessary to obtain correct velocity values. This issue will also be detailed in chapter 6.

### Theoretical array response

The theoretical frequency-wavenumber response of an array is a semblance map that would have been obtained for a single vertically incident plane wave  $((k_x^{(1)}, k_y^{(1)})$  equal to  $(0, 0)$  in equation 1.2). It is also called the array transfer function because the array output is the convolution of the wavefield and of the theoretical frequency-wavenumber response. The normalized theoretical array response in the  $(k_x, k_y)$  plane is given by

$$R_{th}(k_x, k_y) = \frac{1}{n^2} \left| \sum_{i=1}^n e^{-j(k_x x_i + k_y y_i)} \right|^2 \quad (1.1)$$

where  $n$  is the number of sensors in the array, and  $(x_i, y_i)$  are their coordinates. For one single plane wave  $S_i(f) = A(f)e^{j(x_i k_x^{(1)} + y_i k_y^{(1)} - 2\pi f t + \phi)}$  crossing the array at wavenumber  $(k_x^{(1)}, k_y^{(1)})$  at frequency  $f$ , recorded at sensor  $i$ , at time  $t$  and with a phase  $\phi$ , the array output is

$$R(k_x, k_y, f) = \left| \sum_{i=1}^n S_i(f) e^{-j(k_x x_i + k_y y_i)} \right|^2 = n^2 A^2(f) R_{th}(k_x - k_x^{(1)}, k_y - k_y^{(1)}) \quad (1.2)$$

where  $A(f)$  is the amplitude spectrum. The array output is equal to the theoretical response translated by vector  $(k_x^{(1)}, k_y^{(1)})$  and multiplied by the square of the amplitude. For multiple

plane waves travelling across the array,  $S^{(1)}$  to  $S^{(m)}$ , the array output is

$$R(k_x, k_y, f) = \left| \sum_{i=1}^n \left( \sum_{l=1}^m S_i^{(l)}(f) \right) e^{-j(k_x x_i + k_y y_i)} \right|^2 \leq n^2 \sum_{l=1}^m R^{(l)}(k_x, k_y, f) \quad (1.3)$$

where  $R^{(l)}$  are the array outputs for single plane waves defined by equation (1.2), and  $S_i^{(l)}$  the wave  $l$  recorded at station  $i$ . In this case, the array output is always lower than the sum of translated theoretical responses, the maximum being reached when all waves are in phase.

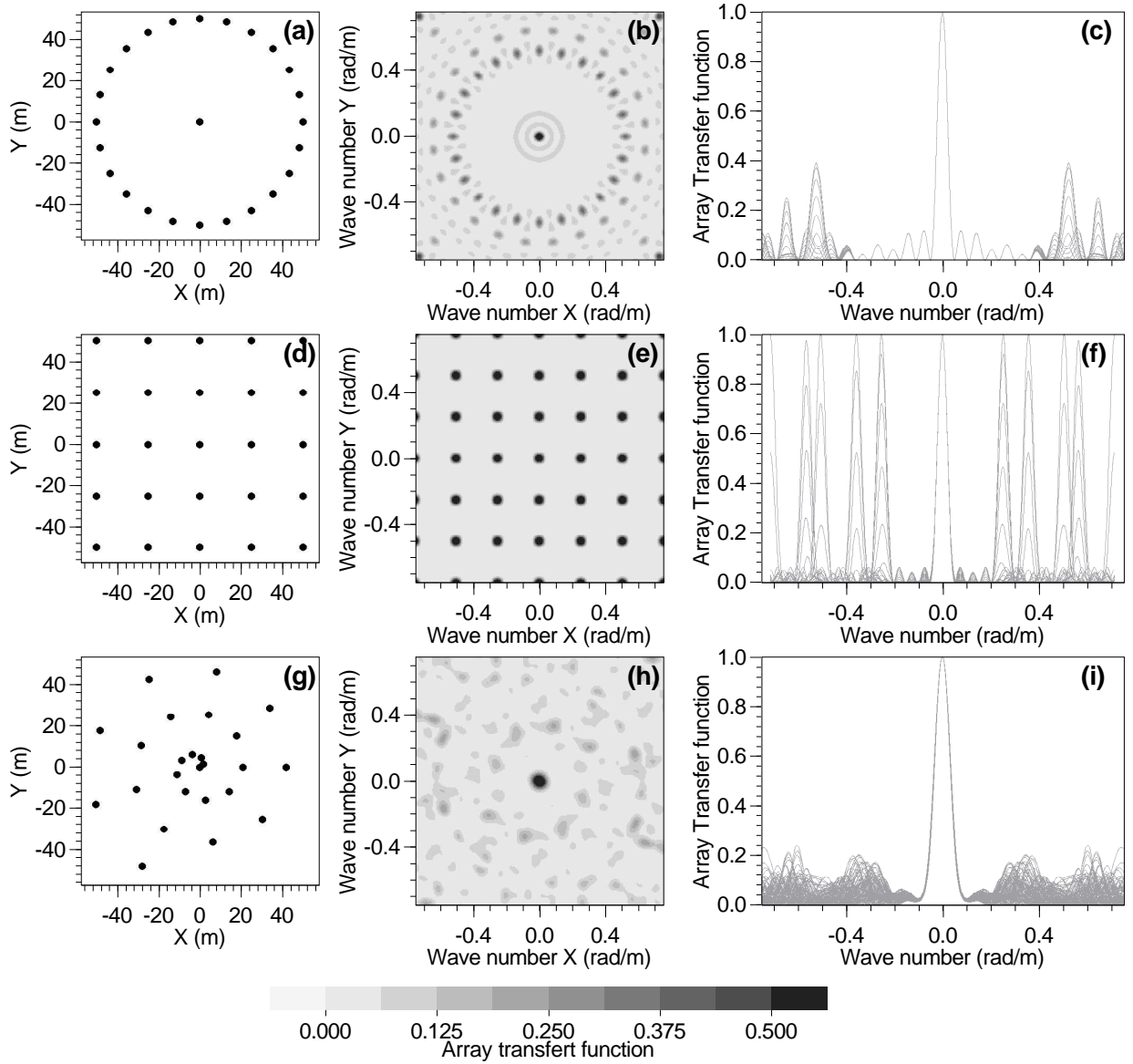


**Figure 1.1:** Theoretical array responses for 25 sensors. Array geometries: (a) circle, (d) Cartesian grid, and (g) spiral. (b), (e), and (h) Theoretical array responses in the plane  $(k_x, k_y)$ . (c), (f), and (i) Sections across theoretical array responses for various propagation azimuths (628 values between 0 and  $2\pi$ ).

From equation (1.1),  $R_{th}$  always exhibits a central peak the value of which is one ( $k_x$  and  $k_y = 0$ ) and lateral aliasing peaks the amplitude of which is less than one. Beyond a certain limit which is called the theoretical aliasing wavenumber, this pattern is repeated due to the periodic nature of  $e^{jx}$ . Below this theoretical limit, equation (1.2) shows that the position of the highest peak of the array output is directly linked to the apparent velocity and the

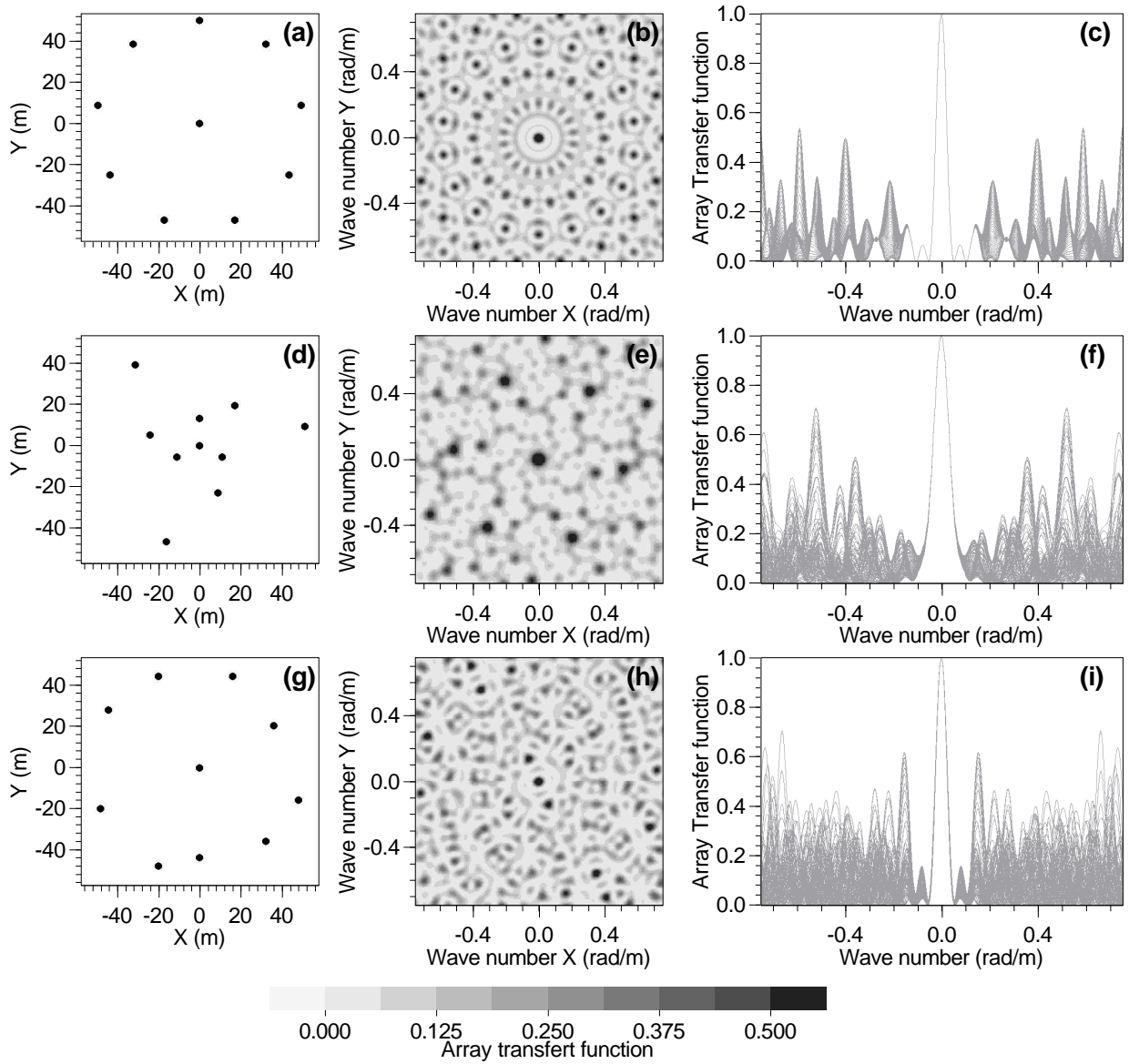


**Figure 1.2:** Theoretical array responses for 10 sensors. (a), (d), and (g) Array geometries. (b), (e), and (h) Theoretical array responses in the plane  $(k_x, k_y)$ . (c), (f), and (i) Sections across theoretical array responses for various propagation azimuths (628 values between 0 and  $2\pi$ ).

azimuth of the propagating wave. For a complex wavefield described by equation (1.3), and assuming that all contributing waves are in phase to get equality, aliasing is likely to occur for lower wavenumbers due to the summation of the lateral peaks of  $R_{th}$ . Hence,  $R_{th}$  is of prime importance to define the potential aliasing limits ( $k_{max}$ ) of the chosen array geometry. On the other hand, it is obvious that the thinner the central peak is, the more capable is the array to distinguish two waves travelling at close wavenumbers. The resolution limit ( $k_{min}$ ) is controlled by the width of the central peak. For simple array geometries, for instance a cartesian grid,  $k_{min}$  and  $k_{max}$  are linked to the minimum and maximum distance between sensors. For usual irregular array geometries,  $R_{th}$  is necessary for the definition of objective wavenumber limits.

We define practical rules for the aliasing and resolution limits from  $R_{th}$ , setting  $k_{max}$  at the first peak exceeding 0.5 (or -3 dB) and  $k_{min}$  being measured at the mid-height of the central peak (Woods and Lintz 1973, Asten and Henstridge 1984, Gaffet 1998). If the aliasing peaks are less than the central peak, and if a single source is acting,  $k_{max}$  does not effectively limit the power of the array. However for multiple sources, even if the aliasing peaks are less than the central peak, the superposition may create artefacts leading to the confusion of aliasing peaks with the main one. If the aliasing peaks are of the same order of magnitude as the main peak, the wavenumber limit is always  $k_{max}/2$ . In a safe approach, it is better to limit the valid array output to  $k_{max}/2$  in all cases. These rules are compared to frequency-wavenumber output in chapter 6.

Array geometry	Number of sensors	$k_{min}$	$k_{max}$
Perfect circle	25	0.024	1.00
Cartesian grid	25	0.022	0.25
Spiral	25	0.036	2.75
Perfect circle	10	0.024	0.40
Three triangles	10	0.038	0.36
Irregular circle	10	0.026	0.15

**Table 1.1:** Properties of the array geometries. For each array, the minimum and maximum wavenumbers (rad/m) deduced from the theoretical frequency-wavenumber responses in figures 1.1 and 1.2.

The theoretical array response is calculated for various array geometries containing 25 and 10 sensors in figures 1.1 and 1.2, respectively: a perfect circle (figures 1.1(a) to 1.1(c), and 1.2(a) to 1.2(c)), a Cartesian grid (figures 1.1(d) to 1.1(f)), a perfect spiral (figures 1.1(g) to 1.1(i)), an ensemble of three triangles rotated by 40° (figures 1.2(d) to 1.2(f)), and an irregular circle (figures 1.2(g) to 1.2(i)). The aperture<sup>1</sup> is always around 100 m. The grey curve of plots (c), (f) and (i) are sections across the theoretical array response for various propagating azimuths. The  $k_{min}$  and the  $k_{max}$  are estimated in table 1.1. The width of the central peak at its mid height presents small variations versus the geometries. For instance, the perfect circle in figure 1.1(a) has an aperture of exactly 100 m and a  $k_{min}$  around 0.024 rad/s. On the other hand, the spiral array in figure 1.1(g) has an aperture of 98.5 m and a  $k_{min}$  around 0.036 rad/s. Hence,  $k_{min}$  cannot be deduced from the aperture by a simple linear relationship. On another hand,  $k_{max}$  is

<sup>1</sup>Maximum distance between any pair of sensors

strongly dependent upon the number of sensors and their geometries. When multiple waves are travelling across the array at the same time, the performances of an array depend also upon the "ground" level of its theoretical array response. For example, the rectangular array is almost flat between 0.05 and 0.2 compared to the circular array, which means that two semblance peaks separated by  $k_{min}$  are not affected by each other in the summation of equation (1.3).

The arrays of figure 1.2 with 10 sensors are more common than arrays with 25 sensors, but their available wavenumber range between  $k_{min}$  and  $k_{max}$  is usually not large enough to obtain a complete dispersion curve. Hence, various array apertures and geometries with overlapping wavenumber ranges must be planned before any experiment. It can be based on a first guess of the dispersion curve calculated with common properties for the expected geology. The wavenumber ranges must cover the whole dispersion curve down to the expected resonance frequency. This limit only applies to arrays for which the vertical components are processed. Extension towards lower frequencies might be necessary if horizontal components are planned to be processed (chapter 6).

## Implementation

The f-k algorithm has been implemented in C++ as a plug-in module of the seismic signal database GEOPSY<sup>2</sup>. The Fourier transform is calculated with the FFTW package (Frigo and Steven 2005, [www.fftw.org](http://www.fftw.org)) which allows any arbitrary number of samples, not restricted to powers of two.

In this work and for the f-k method, we consider the semblance as the ratio of the array output over the spectral power. The search of the maximum of semblance is performed with a rough gridding of the plane  $(k_x, k_y)$ . The exact maximum is then refined within the eight cells that surround the cell with the highest value. A secondary grid is constructed with 16 cells inside the area delineated by the preceding 9 cells (8+1). The cell with the maximum semblance and its 8 surrounding cells delineate an area that it is 9/16 smaller than the original area. The process is repeated until reaching a sufficient precision. The search is performed in the wavenumber domain contrary to other implementations (`cap`, Ohrnberger 2001) which work in the slowness domain. The advantage of the wavenumber domain is that the size of the peaks are not varying with the frequency. Effectively, equations (1.2) and (1.3) show that the array output is the sum of the translated theoretical array responses of the most energetic waves, which do not decrease the size of the main peak. Consequently, in wavenumber domain, the maximum of semblance can be searched for all frequency bands with the same grid step. To not miss the true semblance maximum, the grid cell must be less than a half of  $k_{min}$ .

From the considerations of the preceding section, it is useless to search for peaks above  $k_{max}$ . Moreover, the velocity of the semblance peak must be consistent with physical limits of the Rayleigh or Love dispersion curves (section 3.1.5 on page 40). Consequently when calculating the array output for a pair  $(k_x, k_y)$ , if the velocity corresponding to the wavenumber  $(\sqrt{k_x^2 + k_y^2})$

---

<sup>2</sup>Database with a graphical user interface (Qt libraries, [www.trolltech.com](http://www.trolltech.com)) dedicated to seismic prospecting and developed during this thesis. Its dynamic signal loader is able to work on very long recordings (hours) with an efficient memory and time consumption. It works on any desktop PC (Linux or Windows) or Mac.

and the current frequency is not between common limits (e.g. [150, 3500] m/s), a zero value is returned.

### 1.1.2 High resolution method

With the aim of improving the f-k method, Capon (1969) added weighting factors to each sensor contribution in the computation of the array output. They are calculated in order to minimize the energy carried by wavenumbers differing from the considered one. The high resolution frequency-wavenumber technique is theoretically able to distinguish two waves travelling at close wavenumbers in a better way than the f-k method.

#### Principles

If the ambient wavefield is recorded with  $n$  sensors located at  $\vec{r}_i$ , let  $X(\vec{r}_i, \omega)$  being the spectra calculated for station  $i$

$$X(\vec{r}_i, \omega) = \sum_{m=1}^q S_m(\omega) e^{j(\vec{k}_m \cdot \vec{r}_i)} + \eta(\vec{r}_i, \omega) \quad (1.4)$$

where  $\omega = 2\pi f$  is the angular frequency,  $S_m(\omega)$  is the complex spectrum and  $\vec{k}_m$  is the wavenumber vector of the plane wave triggered by source  $m$ , and  $\eta$  is the uncorrelated part of the signal ("the noise of the ambient vibrations"). The array output is

$$R(\vec{k}, \omega) = \sum_{i=1}^n W_i(\omega) X(\vec{r}_i, \omega) e^{-j\vec{k} \cdot \vec{r}_i} \quad (1.5)$$

where  $W_i(\omega)$  are arbitrary weighting functions. The f-k method presented in section 1.1.1 uses constant weighting functions equal to 1. In this case, equations 1.3 and 1.5 are equivalent.

Estimates of the wave velocity at frequency  $\omega$  ( $\vec{k}(\omega)$ ) are hence obtained by maximizing the complex modulus of  $R(\vec{k}, \omega)$  in the wavenumber plane. At the maximum,  $\vec{k}$  equals to  $\vec{k}_m$ , the wavenumber of the dominant plane wave. Using matrix notations,

$$R = AWX \quad (1.6)$$

where,

$$\begin{aligned} A &= [e^{-j\vec{k} \cdot \vec{r}_1}, \dots, e^{-j\vec{k} \cdot \vec{r}_n}] \\ W &= \begin{bmatrix} W_1(\omega) & 0 & \dots & 0 \\ 0 & & & \dots \\ \dots & & & 0 \\ 0 & \dots & 0 & W_n(\omega) \end{bmatrix} \\ X &= [X_1(\omega), \dots, X_n(\omega)] \end{aligned} \quad (1.7)$$

The frequency-wavenumber cross-spectrum is hence

$$P = AWCW^H A^H \quad (1.8)$$

where  $C = E[XX^H]$  is the cross spectral matrix evaluated using frequency or spatial smoothing, and  $^H$  denotes hermitian conjugate operator.

Capon (1969) introduced particular weighting functions optimized by minimizing the signal power of  $WCW^H$  for all wavenumbers differing from the considered  $\vec{k}$ , which leads to

$$W = \frac{C^{-1}A}{A^H C^{-1}A} \quad (1.9)$$

Theoretically, this high-resolution method allows higher resolution. This assertion is checked for a simulated and a real case in chapter 6.

## Implementation

No particular code has been developed for the high resolution method during this thesis. We used the software `cap` (Ohrnberger 2001, Kind 2002, Ohrnberger et al. 2004a, Ohrnberger 2004b). `cap` can access a GEOPSY database to obtain the input signals. It was available within the SESAME European project (Site EffectS assessment using AMbient Excitation, Project EVG1-CT-2000-00026).

### 1.1.3 Spatial auto-correlation method

The spatial auto-correlation techniques take advantage of the random distribution of sources in time and space to link auto-correlation ratios to phase velocities. In the case of a single-valued phase velocity per frequency band, Aki (1957) demonstrated that these ratios have the shape of Bessel functions of order 0, the argument of which is dependent upon the dispersion curve values and the array aperture. Bettig et al. (2001) brought some slight modifications to the original formula to extend the method for irregular arrays. Those concepts are briefly recall in the next section. An original inversion strategy has been developed for auto-correlation ratios during this thesis (section 3.3). Examples for synthetic and real cases are discussed in sections 5.2, 6.1.5, and 6.2.5.

## Principles

The spatial auto-correlation function between two sensors is defined by (Aki 1957)

$$\phi(\xi) = \frac{1}{T} \int_0^T v_0(t)v_\xi(t)dt \quad (1.10)$$

where  $v_0$  and  $v_\xi$  are the signals recorded during  $T$  seconds at two stations separated by a distance  $\xi$ . If the signals are filtered with a narrow frequency band around  $\omega_0$ , the auto-correlation ratios

defined by

$$\rho(\xi, \omega_0) = \frac{\phi(\xi, \omega_0)}{\phi(0, \omega_0)} \quad (1.11)$$

are calculated for all pairs of receivers. For a given inter-distance  $\xi$ , Aki (1957) demonstrated that the azimuthal average of  $\rho(\xi, \omega_0)$  has the shape of Bessel functions (same as equation (3.47)).

$$\overline{\rho(\xi, \omega_0)} = J_0 \left( \frac{\omega_0 \xi}{c(\omega_0)} \right) \quad (1.12)$$

where  $J_0$  is the Bessel function of the first order and  $c(\omega_0)$  is the dispersion curve. Equation (1.11) is computed in the time domain on filtered signals (a taper in the frequency domain is used to ensure a zero phase filter). Another expression is also available in the frequency domain which avoids one computation of the Fourier transform, but its results are not as precise as equation (1.11) (Metaxian 1994).

Like for the f-k method, the raw signals are cut in smaller time windows (section 1.1.1) on which the auto-correlation ratios are computed. Consequently, for each frequency band, for each range of inter-distance, and for each individual time windows, an azimuthally averaged auto-correlation ratio is calculated. The results are generally presented under the form of auto-correlation curves with error bars plotted against frequency or inter-distance (e.g. figure 6.14).

## Implementation

The computation of auto-correlation ratio from recorded signals has been implemented as a plug-in module in GEOPSY. The FFTW algorithm is used for all Fourier transforms.

## 1.2 Artificial sources

The case of one single and instantaneous point source is considered here. The sensors and the source points are usually distributed along a line. Contrary to ambient vibrations, there is a total control over the source parameters (location, type of source, frequency content, time of occurrence, ...). On the recorded signals, the body waves (P and/or S) and the surface waves are generally visible. The last ones appear at the end of the signal with high amplitudes and a triangular dispersion pattern. During the last 20 years, surface wave properties have been intensively exploited by various authors. The first applications consist of inverting the measured dispersion curve as the fundamental Rayleigh mode including eventual on or more clearly identified higher modes (McMechan and Yedlin 1981, Gabriels et al. 1987, Stokoe et al. 1989, Herrmann 1994, Malagnini et al. 1995, Foti 2000, Socco and Strobbia 2004). Inversions of the measured curve taking into account the mode contributions or inversions of the full waveforms were recently proposed (Yoshizawa and Kennett 2002, Forbriger 2003b).

Here, we are only considering the inversion of the theoretical dispersion curve to adopt an approach consistent with the ambient vibration method for which no other type of inversion is currently feasible. The body and the surface wave are hence analysed separately.

### 1.2.1 $P - S_V$ refracted waves

Classical refraction (Mota 1954) is achieved with sources placed at the two ends and at the middle of the line. Sources are located at sensor positions in order to control the time reference. The first P-wave arrival times are picked on the signals. If the ground structure is made of inclined homogeneous layers with increasing velocity with depth, the travelttime-distance plot allows the geometry and the seismic velocity of the layers to be retrieved (Mota 1954). With a limited set of data (24 values maximum) and considering the experimental uncertainties which can be high in noisy conditions, the solution is rarely unique and several  $V_p$  profiles may fit the data in a similar way.

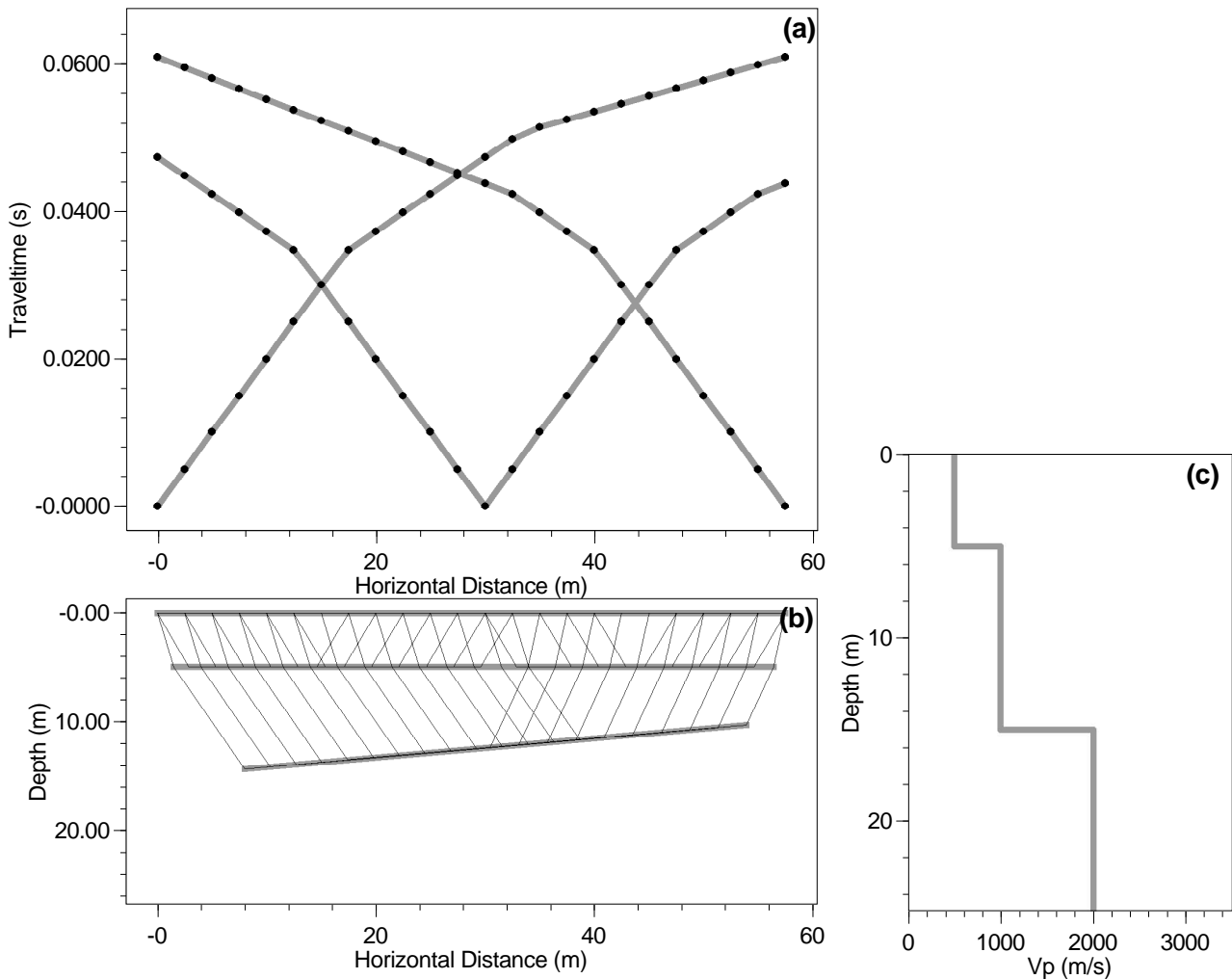


**Figure 1.3:** Reference model for refraction synthetic travelttime-distance plot. (a) Travelttime-distance plot for three sources. (b) Interfaces of the reference model and the ray paths with the minimum travelttimes. (c) Velocity profile at horizontal distance 0.

With the aim of extracting the different solutions explaining the experimental travelttimes in an objective way we developed a simple method based on the neighbourhood algorithm (Sambridge 1999a, chapter 2). The method, the principles of which are identical to the inversion of dispersion curves (Wathelet et al. 2004), generates two random one-dimensional  $V_p$  profiles with a fixed number of layers, which define a model with inclined layers. The  $V_p$  value within each layer is randomly chosen inside an interval defined from a prior knowledge of the geological

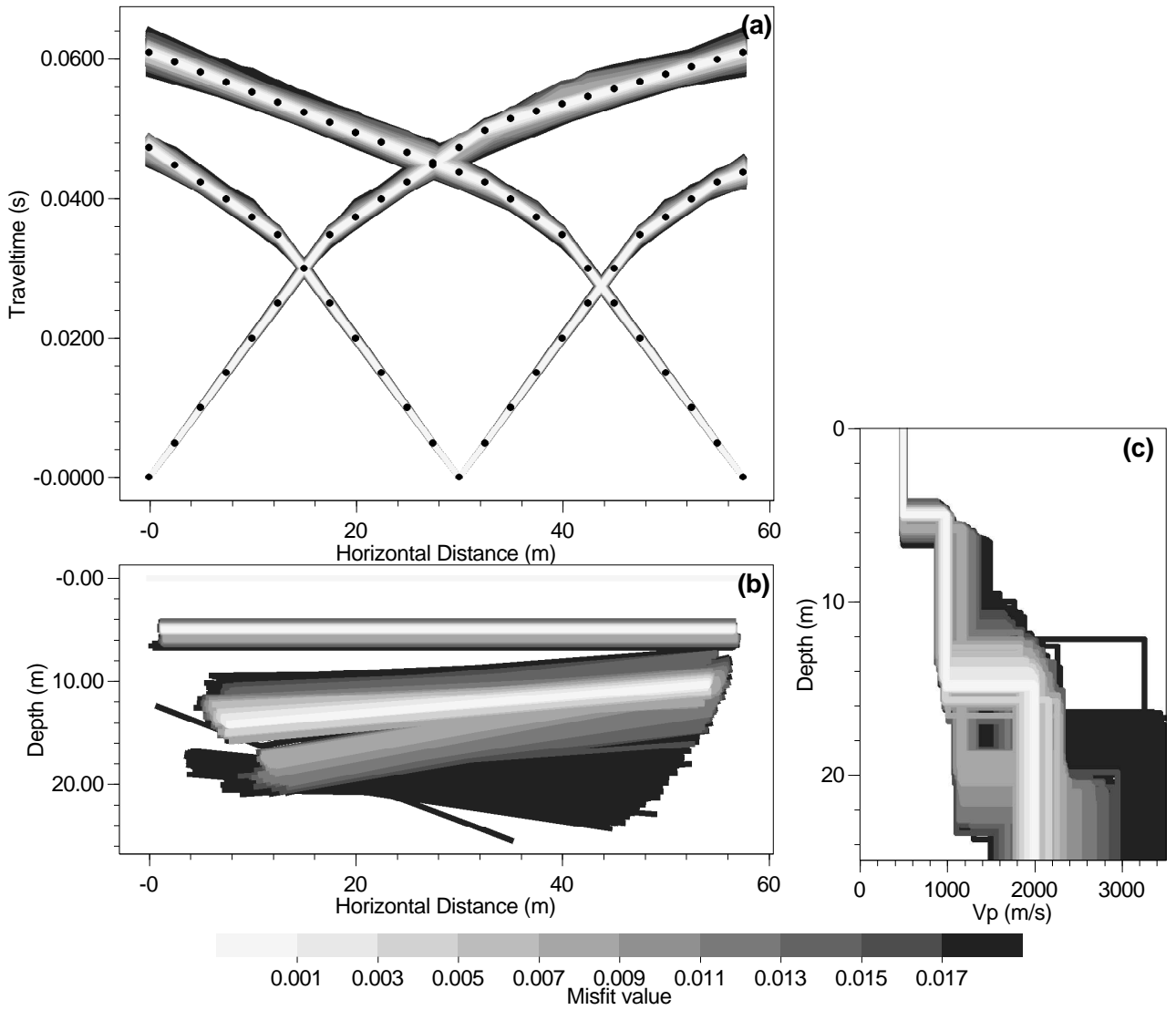


**Figure 1.4:** Inversion of synthetic traveltime-distance plot. (a) Traveltime-distance plot for three sources calculated for the generated models. (b) Interfaces of the generated models. (c) Generated velocity profiles at horizontal distance 0.

structure. For each generated model, the ray paths are analytically calculated using the Snell-Descartes refraction law for inclined interfaces and the traveltimes are computed for all source-receiver distances. The experimental time-distance values are compared to the calculated ones using the following misfit function:

$$misfit = \sqrt{\frac{1}{n} \sum_{i=0}^n \left( \frac{t_{exp} - t_{calc}}{t_{err}} \right)^2} \quad (1.13)$$

where,  $t_{exp}$  is the experimental arrival time corrected by the initial time delay,  $t_{calc}$  is the calculated arrival time for the current model,  $t_{err}$  is the phase picking error or equal to  $t_{exp}$  if no error estimation is available, and  $n$  is the number of receivers. The experimental error, which depends upon the sharpness of the P-wave arrival and the signal to noise ratio, is manually estimated. This method was tested with success on synthetic models with constant velocity layers and dipping interfaces, using two shots made in opposite directions. This technique is

used for our real test case in section 6.2.1 on page 6.2.1.

The method is illustrated for a reference model with three layers (figure 1.3(b)). The constant velocity inside each layer is represented in figure 1.3(c) by the  $V_p$  profile measured on the left side of the model (distance=0). The thin black lines in figure 1.3(b) are the ray paths with the minimum traveltimes corresponding to the plot of figure 1.3(a). Figure 1.3(a) is the traveltime-distance plot obtained with three sources placed at the two extremities and in the middle of the section. Two inversion processes are launched generating 30,000 models among which 18,000 have a misfit lower than 0.02. The lowest misfit found is 0.00063. The generated models are shown in figure 1.4(b) and 1.4(c). The corresponding traveltime-distance plots are visible in figure 1.4(a). Considering 0.02 as an acceptable misfit, the depth of the first interface is correctly retrieved but the depth of the second one is poorly constrained by the refraction experiment, unless a very high precision can be achieved while picking the arrival phase of the distant receivers. From figure 1.4(c), the velocity is correctly inverted down to 16 m. Below 16 m, if all models with a misfit lower than 0.02 are equally acceptable, any velocity between 1000 and 4000 m/s is equally valid to explain the experiment results.

### 1.2.2 $S_H$ refracted waves

The practical requirements and data processing for  $S_H$  waves are very similar to the  $P - S_V$  case. Shear waves polarized in the transversal direction are generated by beating on both sides of a loaded wood timber oriented perpendicular to the recording line (Jongmans 1992). Both sides are used to remove the P-wave contribution by the means of negative stacking. The signals are recorded on horizontal sensors the main axis of which is oriented perpendicular to the receiver line. The processing of the traveltime-distance curves is exactly the same as for  $P - S_V$  refraction.

### 1.2.3 Surface wave inversion

The sensors along the line are considered in the same way as for ambient vibration arrays. However, linear arrays have particular theoretical responses that prevent from using exactly the same algorithms. An example is calculated for 24 receivers placed every 2 m in figure 1.5. The vertical aliasing lines are visible at every multiple of  $\pi$  ( $= k_{max}$ ). Hence,  $k_{max}/2$  corresponds to  $\lambda=4$  m= $2\lambda_{sampling}$  (one-dimensional sampling theorem) where  $\lambda$  is the wave length. The maxima of the semblance are searched only in the known direction of propagation (supplementary parameter). Also, the signals are always transient which means that sliding windows cannot be calculated to evaluate the uncertainties. A single time window of fixed duration is thus taken for all frequencies. This unique time window is processed in the same way as in section 1.1.1 on page 1.1.1. No histogram is constructed (section 1.1.1 on page 6) but the semblance is plotted with a colour grid in the frequency-velocity plane. The maxima of semblance delineate the dispersion curve with eventually higher modes as sketched in figure 1.6 for an explosive load shot at 20 m of a line of 24 receivers. The details of this experiment are given

in section 6.2.1, on page 128.

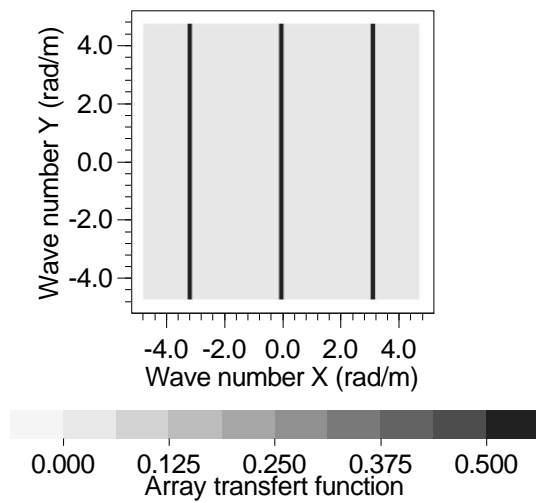


**Figure 1.5:** Theoretical array responses for a line of 24 sensors placed every 2 m along X axis.

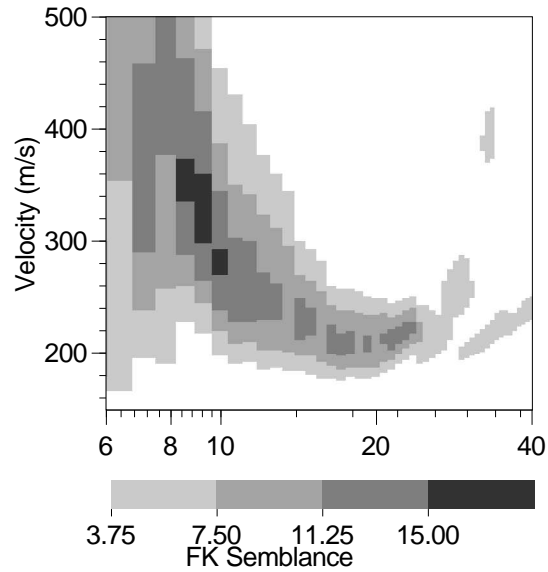


**Figure 1.6:** Example of a f-k analysis for surface waves triggered by an explosive shot.

## Implementation

Like the general f-k algorithm, this linear f-k has been implemented as a plug-in module in GEOPSY. The results were compared with the slantstack method available in the surface wave package distributed by Herrmann (1994).

## 1.3 Conclusions

In this chapter, we presented several methods to extract the dispersion (or the auto-correlation) curves from ambient vibration wavefields and from triggered waves. In the next chapters, we develop an inversion technique to infer sub-surface properties from the dispersion curve. In chapter 6, the signal processing methods briefly introduced in this chapter (f-k, high-resolution, auto-correlation, refraction tests and surface wave inversion of active experiments) are illustrated by synthetic and real field experiments.

# Chapter 2

## The inversion algorithm

After the estimation of the dispersion or the auto-correlation curves, an inversion tool is developed to infer the ground structure, especially the seismic velocities  $V_p$  and  $V_s$ . Chapters 2 and 3 are dedicated to the inversion principles and to the forward algorithm, respectively.

This chapter recalls the basic concepts involved in the inversion theory. Several inversion methods of common use in geophysics are briefly reviewed. The principles of the neighbourhood algorithm (Sambridge 1999a) are detailed because it has been chosen as the core of our dispersion curve inversion tool. Finally, an improvement to the standard neighbourhood algorithm is proposed when the external limits of the parameter space are not fixed (conditional neighbourhood algorithm).

### 2.1 Definition

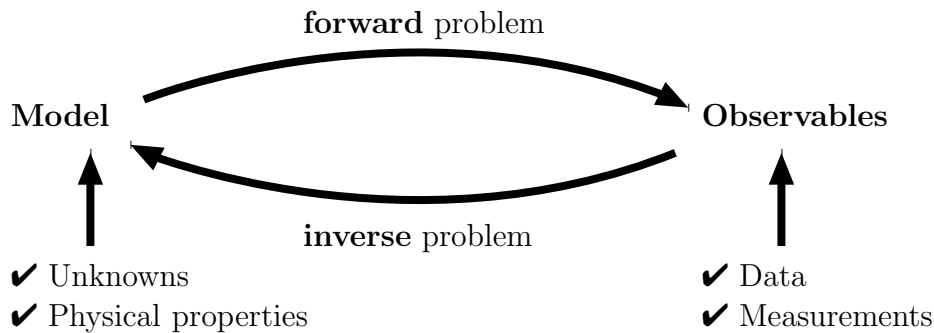


**Figure 2.1:** Definition of an inversion problem

Physical properties are usually measured through a scientific experiment. For instance, Torricelli invented the mercury barometer to measure the atmospheric pressure  $P_{atm}$ .  $P_{atm}$  is estimated by comparing the height of the mercury column ( $h_{merc}$ ) with a graduated scale. If  $P_{atm}$  is known,  $h_{merc}$  can be calculated with a simple linear relationship involving the density of mercury.

$$h_{merc} = \frac{P_{atm}}{13.5} \quad (2.1)$$

This is the **forward problem**. However, during the scientific experiment, the observable is

not the pressure but the height of mercury. Hence equation (2.1) must be inverted to calculate the **model parameter**  $P_{atm}$  from the **observable** quantity  $h_{merc}$ . The **inverse problem** is solved with the following equation

$$P_{atm} = 13.5 h_{merc} \quad (2.2)$$

This is an example of the inversion of a linear problem which is pretty simple and always solved analytically. In this case, the number of unknowns is one as well as the number of observable (or data). Scientific models are generally completely described by the means of more than one parameter. With these models, it is also possible to calculate various theoretical characteristics. For instance, a characteristic of the model may be a curve which is numerically represented by a vector of  $n_{obs}$  components. Hence the forward problem is a function that transforms a parameter space of dimension  $n_{param}$  (number of involved parameters) into the observable space of dimension  $n_{obs}$ .

If the function is linear, the linear algebra is used to solve the inversion problem. In this case, there is no absolute limit for the number of observables and the number of parameters. If  $n_{obs}$  is less than  $n_{param}$ , there is an infinite number of solutions for the parameter vector. On the contrary, if  $n_{obs}$  is greater than  $n_{param}$ , a least-square method is generally used to find the best set of parameters.

However, in most situations, the relationship is not linear and even more, the forward problem cannot be solved analytically. Even if the forward problem has an analytical expression, there are very few special cases where the inversion problem is also analytical. Hence, in most cases, an inversion method is necessary to calculate the set of parameters corresponding to the observables. The number of solutions of the inverse problem is generally a complex issue. For instance, if the forward function is simply  $y = x^2$  between two one-dimensional spaces, the inverse problem may have zero, one or two solutions. The non-uniqueness is hence specific to each problem and has to be studied on a case-by-case basis.

All scientific observables are measured with a certain degree of error, even if it is not explicitly quantified. In Torricelli's experiment, the height of mercury can be measured for instance down to a 0.5 mm precision. In this one-dimensional linear example, the error on  $P_{atm}$  is easily deduced. For multi-dimensional linear problems the error propagation is also possible. But for non linear and multi-dimensional problems, calculating the errors on the model parameters from the errors on the acquired measurements is not straightforward.

## 2.2 Available methods

All forward problems can be summarized by

$$O = [O_1, \dots, O_{n_{obs}}]^T = f([p_1, \dots, p_{n_{param}}]^T) \quad (2.3)$$

where  $O_i$  are the observable values<sup>1</sup> and  $p_i$  are the model parameters<sup>2</sup>. Generally, a new function  $L \in \Re$  is constructed<sup>3</sup> which vanishes when  $f$  is equal to  $O$ . The inverse problem is equivalent to find the set of  $p_1, \dots, p_{n_{param}}$  that verifies

$$L([O_1, \dots, O_{n_{obs}}]^T - f([p_1, \dots, p_{n_{param}}]^T)) = 0 \quad (2.4)$$

Practically, the minimum of  $L$  is searched across the parameter space in different ways briefly explained in the following sections.

### 2.2.1 Gridding method

If the number of parameters is small, less than four<sup>4</sup>, it is conceivable to calculate  $L$  for each combination of parameters. Theoretically, this method offers the best exploration of the parameter space compared to all other techniques. However, considering the number of forward problems to solve, this method is very limited. For example, if the prior range of each parameter is discretized with 50 samples, if the time to calculate one forward problem is one second, and if the dimension of the parameter space is five, the total time required for the inversion is 10 years.

### 2.2.2 Iterative methods

Starting from a first estimation of the model parameters or from whatever appropriate model, the iterative method converges to the minimum of  $L$  by modifying the current model according to the local properties of function  $L$ . In the case of Newton-Raphson, damped least-square or gradient methods, the partial derivatives or the Jacobian matrix at the current model orientates the descent towards the solution (Nolet 1981, Tarantola 1987, Herrmann 1994, . . .). Calculating the partial derivatives allows a linearization of the problem and linear algebra is used to calculate a new estimate of the solution. The process is repeated through several iterations until finding an acceptable minimum. Downhill simplex (Press et al. 1992) is an other iterative method that requires only function evaluations, not derivative. It is based on geometrical principles.

These kinds of methods are the exact opposite of the gridding method. The exploration of the parameter space is limited to the path followed during the successive iterations. They are mostly used for high dimensional parameter spaces for their ability to quickly converge to the solution. The number of function computations is very small compared to all other methods.

If there are more than one minimum or if the function  $L$  has a complex shape with multiple secondary minima, those methods are likely to converge to one of them which is probably not the unique and the absolute minimum. The final solution highly depends upon the starting model. The non-uniqueness, a common phenomenon in inverse problems (Sambridge 2001), can

---

<sup>1</sup>Also called data curve, measurements, or target curve.

<sup>2</sup>Also called unknowns or, simply, parameters.

<sup>3</sup>This function is called the misfit, the cost, the error or the residual function. It is a real number

<sup>4</sup>According to the time needed for one computation.

be apprehended only by a manual selection of "good" starting models. These methods are then inadequate when the nonlinearity becomes severe, and can produce optimistic resolution estimates, usually calculated around a single best data-fit model (Sambridge 2001). Shapiro (1996) showed, that the solutions obtained from classical surface wave inversion schemes (damped least-square) are too restrictive and uncertainties are not correctly estimated.

From the starting model, the iterative process may lead the current model to whatever part of the parameter space, being in this case  $\mathfrak{R}^n$ <sup>5</sup>. It depends upon the unknown shape of function  $L$ . Indeed,  $L$  is known for only a discrete number of points where the forward problem has been solved. In this framework, it is impossible to guarantee that the current model stays within a defined zone of the parameter space for all iterations. The limits of this zone are adjusted so that it encloses all potential solutions, given the prior knowledge we have about the model.

### 2.2.3 Neural Networks

Michaels and Smith (1997) suggested to use neural networks to invert surface waves, inferring the sub-surface properties. Artificial neural networks are computer programs that simulate the biological neural networks. Calderón-Macías et al. (2000) also used them to inverse electrical data. From input stimuli (= observables values), it provides an output set of values (= model parameters). As a human brain, it needs education to react correctly in each situations. Hence, the neural network used for surface wave inversion is trained with series of the synthetic signals for which the model is perfectly known. To summarize, the network is a generic mean of mapping observable to model parameters.

A correct behaviour is obtained only if the network has been trained with synthetic models close to the true model. Hence, this method cannot be used to scan all potential models that correspond to experimental data. Moreover, the error propagation cannot be included in an easy way and the non-uniqueness is never handled.

### 2.2.4 Monte Carlo methods

These methods are based on a uniform pseudo-random sampling of the parameter space. If their principle is not new, they gain success amongst the geophysicists during the last 20 years, due to the increasing power of modern computers. The question addressed by such methods is not only finding the model with the best data fit but also to retrieve information about the resolution power of a particular application. This area of statistical inference is reviewed for example by Edwards (1992), Mosegaard and Tarantola (1995), Sambridge (1999b). The role of prior information is investigated by all these authors but especially by Scales and Tenorio (2001). The parameter space does not generally extend to  $\mathfrak{R}^n$  like in the case of iterative methods but it is restricted to a volume defined by the parameter prior ranges. All generated models are always confined in this volume.

When the dimensionality of the parameter space increases, the basic random generation

---

<sup>5</sup>The number of dimension of the ensemble is  $n = n_{param}$

of models becomes totally inefficient. This is why several refined approaches were developed during the last two decades, for instance the simulated annealing (Rothman 1985, Sen and Stoffa 1991) and the genetic algorithms (Stoffa and Sen 1991, Lomax and Snieder 1995, Boschetti et al. 1996, Yamanaka and Ishida 1996). There are also many variants of these methods, combining them with neural networks or with gradient methods (e.g. Chundururu et al. 1996, Devilee 1999, Boschetti and Moresi 2001). The objective of these techniques is to seek a model with a globally optimal data misfit value. These methods and their variants usually need empirical tuning of several parameters that control the inversion process, ensuring computational efficiency and robustness against entrapment in local minima.

Recently, Sambridge (1999a) proposed an entirely different method based on the partition of the parameter space into Voronoi cells<sup>6</sup>( neighbourhood algorithm). It has only two tuning parameters and it is claimed as self-adaptive in searching a parameter space. The objective, which is different from the previously mentioned methods, is to sample (in an optimal situation) all the regions of the parameter space where models with acceptable data fit are found. This last technique has been chosen for our dispersion curve inversion tool. Its principles are examined with more details in the next section.

## 2.3 The neighbourhood algorithm

The Voronoi decomposition of the parameter space is the base of an approximation of the misfit function  $L$  which is progressively refined during the inversion process. The approximation is set as constant inside each cell and the misfit value calculated at the central point is affected to the whole cell. A two-dimensional parameter space is given as an example in figure 2.2(a). The black dots are some model points for which a misfit is calculated.

The neighbourhood algorithm needs four tuning parameters:

$\underline{it_{max}}$  is the number of iteration to perform;

$\underline{n_{s0}}$  is the number of models chosen at random inside the parameter space at the beginning of the inversion;

$\underline{n_s}$  is the number of models to generate at each iteration;

$\underline{n_r}$  is the number of best cells (with the lowest misfit) where the  $n_s$  models are generated.

The inversion process is composed of the following phases:

1. a set of  $n_{s0}$  models is randomly generated with a uniform probability in the parameter space;
2. the misfit function is calculated for the most recently generated models;
3. the  $n_r$  models with the lowest misfit of all models generated so far are selected;

---

<sup>6</sup>It is a unique decomposition of the space into  $n$  cells around  $n$  points  $p_i$ . The cell around point  $p_i$  is defined by the ensemble of points that are closer to  $p_i$  than to whatever other point  $p_j$  where  $j \neq i$ .

4. generate an average of  $\frac{n_s}{n_r}$  new samples with a uniform probability in each selected cell;
5. add the  $n_s$  new samples to the previous ensemble of models and go back to (2).

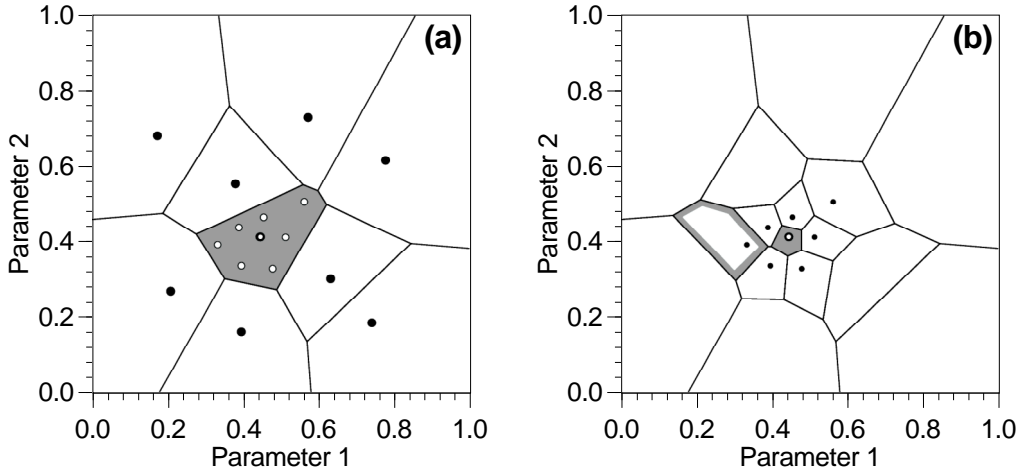


**Figure 2.2:** Voronoi cells for a two-dimensional parameter space (from Sambridge (1999a)).

Figure 2.2(a) is an example of a two-dimensional parameter space showing the models (black dots) and the limits of the Voronoi cells.  $n_{s0}$  (=9, in this case) models are generated and the grey cell has the lowest misfit. In this example, seven new models are generated in one cell ( $n_r = 1$ , and  $n_s = 7$ ). Figure 2.2(b) depicts the Voronoi geometry after the first iteration. The size of the original cell decreases as the sampling rate increases. If the cell with the grey outline has the lowest misfit, the density of sampling will not decrease systematically after each iteration. This is an interesting property of the Voronoi geometry that allows the centre of sampling to jump from place to place, whilst always sampling the most promising  $n_r$  regions simultaneously.

In the neighbourhood algorithm, a random walk (Gibbs sampler) is performed with a uniform probability density function inside the cell and zero outside. A walk is a sequence of perturbations to a model along all axis. The modified model is statistically independent of the original model. Asymptotically, the samples produced by this walk will be uniformly distributed inside the cell regardless of its shape. To confine the random walk inside a particular cell it is mandatory to calculate the multi-dimensional limits of the cell. Calculating the complete Voronoi geometry for high dimensional spaces becomes practically impossible when the number of models increases. Sambridge (1999a) proposed an original algorithm to compute only the limits along lines which are parallel to axis, in a precise and efficient way. These lines support the successive segments of the random walks.

There are only a few number of control parameters:  $n_{s0}$ ,  $n_s$ ,  $n_r$ , and  $it_{max}$  which is the maximum number of iterations. The neighbourhood algorithm is more exploratory if the  $n_s$  new samples are distributed on many cells and it optimizes more if they are restricted to the very few best cells. Typical values for the tuning parameters are 100 for  $n_{s0}$ ,  $n_s$ ,  $n_r$ . To force a better optimization,  $n_r$  may be set to 5, 10 or 50. Tests show that generally better misfits are obtained with fewer iterations if  $n_r$  is low, but the inversion is more trapped in local minima. The exploratory mode (e.g.  $n_r=100$  and  $n_s=100$ ) usually provides better final misfits if the

inversion is conducted with a great number of iterations. The number of iterations ranges from 50 to 200. This makes a total of 5,000 to 20,000 generated models. Compared to linearized methods the number of forward computations is much greater. Consequently, the forward computation has to be correct for each parameter set without a visual check and it must be highly optimized to reduce the total computation time. These aspects are analysed in chapter 3 when designing the dispersion curve algorithm.

The neighbourhood algorithm like all other Monte Carlo techniques relies on a quasi or pseudo-random generator. A basic random generator on a computer is a series of numbers with a uniform probability, which is initialized by a special number called the random seed. The seed may take any integer value. Two inversion processes started with distinct seeds generate different models. However, if the problem is sufficiently constrained, the algorithm converges towards the same zone of the parameter space. For less constrained parameters, the investigated zones may be quite different. An interest of launching several inversion processes for the same case is to test the robustness of the fine result. All sets of models generated by separated processes can be merged to construct a more refined approximation of the misfit function.

The ensemble of models obtained from the neighbourhood algorithm has not the same statistical properties as the posterior probability density. Moreover, the statistical properties of the resulting ensemble strongly depend upon the tuning parameters. If lots of iterations are performed, the number of models near the best model is greater than for an inversion with less iterations. By the means of a resampling of the parameter space and approximating the posterior probability density with the misfit function, Sambridge (1999b) calculated the Bayesian integrals on an ensemble of models having the statistical properties corresponding to the posterior probability density. In our work, the algorithm we tested did not work properly, probably due to internal bugs. By the lack of time, we did not investigate more this approach but this second stage of the inversion is certainly valuable to measure the resolution and trade-off in a quantitative way.

## 2.4 Conditional parameter spaces

In its original form, the neighbourhood algorithm handles a parameter space with orthogonal boundaries. All parameters have a uniform probability within prior fixed limits. They are set at the beginning of the process with constant values. If the limit of one parameter depends upon the value of another parameter, it is necessary to implement a variable transformation. For instance if parameter  $p_1$  belongs to  $[l_1, u_1]$  where  $l_1$  and  $u_1$  are constant numbers, and  $p_2 < \alpha p_1$ , the prior interval of parameter  $p_2$  is  $[l_2, u_2]$  (if  $u_2 < \alpha p_1$ ) or  $[l_2, \alpha p_1]$  (if  $u_2 > \alpha p_1$ ),  $l_2$  being less than  $\alpha l_1$ . The variable transformation is  $p_2 = l_2 + p'_2 (\alpha p_1 - l_2)$  where  $p'_2$  is a random parameter between 0 and 1 that replaces  $p_2$  in the neighbourhood model. The random variable  $p_2$  is the product of two random variables with uniform probabilities. The probability of  $p_2$  cannot be calculated analytically in an easy way, but it is certainly not uniform anymore. In chapter 4, for complex ground structures there are numerous conditions of this type, and the

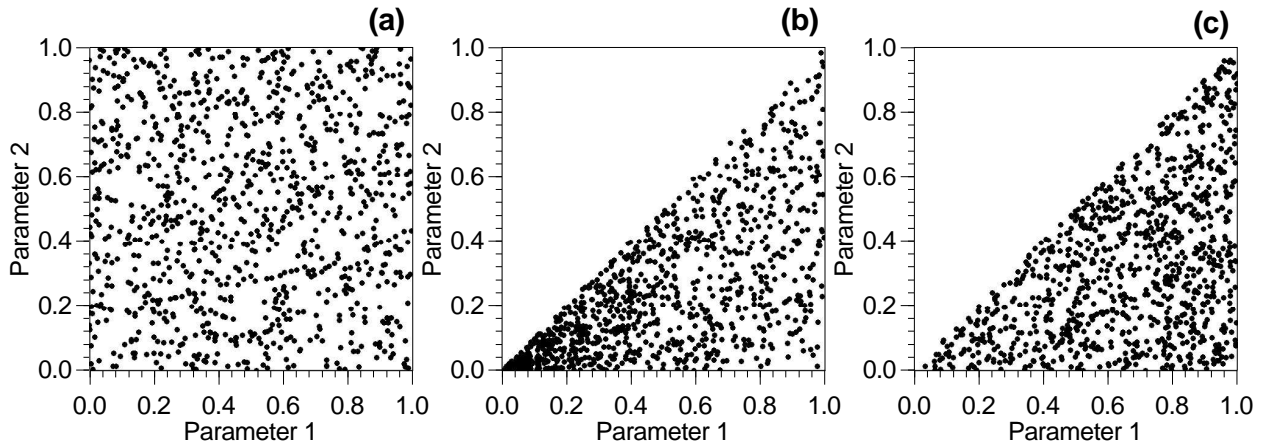


**Figure 2.3:** Comparison of the distributions generated by variable transformation and by selection. 1000 models are generated. (a) Random distribution of two parameters with no condition. (b) The condition  $p_1 < p_2$  is applied with a variable transformation. (c) The condition is  $p_1 < p_2$  is applied by rejecting bad model, but conserving the total number of models.

variable transformation is not an efficient and flexible method. Figure 2.3(b) gives an example of the effects of the variable transformation on the model distribution across the parameter space ( $\alpha = 1$ ). Compared to a uniform distribution (figure 2.3(a)), the region at low  $p_1$  is over-sampled relative to other parts of the space.

The original Fortran code and the steps described in Sambridge (1999a) make a clear distinction between the generation of the random models and the computation of the misfit by a user supplied function. Hence, at the user level, it is not possible to indicate to the neighbourhood algorithm that a particular model is not valid. Modifications of the original code to implement such a feature cannot be done in an easy, elegant and compact way. Moreover, it is written in Fortran77 with static vectors. Consequently, the maximum number of models to be generated is hard coded. All these reasons led us to re-write the algorithm in C++.

A list of parameters and their prior ranges, as well as a list of conditions of the type  $p_i < \alpha p_j$  define the conditional parameter space. The initial ranges are eventually adjusted according to the list of conditions. For instance, if the input ranges are  $p_1 \in [50, 200]$  and  $p_2 \in [100, 250]$ , and if  $p_2 < p_1$ , the intervals are modified as  $p_1 \in [100, 200]$  and  $p_2 \in [100, 200]$ . These conditions are called the **low level conditions**. The above condition is a **forward condition** for parameter  $p_2$ . Its counterpart,  $p_1 > p_2$ , is a **backward condition** for parameter  $p_1$ . Other more complex conditions, eventually involving more than two parameters<sup>7</sup> are called the **high level conditions**. The first type of conditions are checked inside the neighbourhood algorithm itself, whereas the last ones are checked by the user supplied function that calculates the misfit. Contrary to the original Fortran implementation, the misfit function returns also a boolean value that is false if the misfit cannot be calculated (limits of the forward algorithm, physical or prior conditions not met when the final model is constructed).

1. A set of  $n_{s0}$  models is randomly generated with a uniform probability in the parameter

<sup>7</sup>For example, in the case of a one-dimensional ground structure (see chapter 4), the  $V_p$  profile may be fixed from the results of a refraction survey. The thicknesses of the  $V_s$  layers may be set independently, eventually with a more refined discretization. The conditions induced by the natural limits of Poisson's ratio have to take the depth parameters into account, besides usual  $V_p$  and  $V_s$ .

space and with the fulfilment of all conditions..

- (a) random generation of parameter  $p_i$  between  $l_i$  and  $u_i$ ;
  - (b) check of low level forward conditions attached to parameter  $p_i$ , if okay, increment  $i$ ;
  - (c) while all parameters are not generated go back to step (a);
  - (d) As a set of parameter satisfying the low level conditions has been generated, check the high level conditions and calculate the misfit;
  - (e) if the model is not accepted by the high level conditions, restart from the first parameter in step (a);
  - (f) the model is accepted and it is added at the end of the main model vector, a vector of the references to the  $n_r$  best models, sorted by increasing misfits is kept up-to-date;
  - (g) while  $n_{s0}$  models are not generated, restart from the first parameter in step (a) to generate a new model;
2. Save the current  $n_r$  best models
  3. Generate an average of  $\frac{n_s}{n_r}$  new samples with a uniform probability in each selected cell ( $n_r$  cells).
    - (a) generate one model with a Markov chain equivalent to one described by Sambridge (1999a), except that the "triangular" external shape (induced by the low level conditions) of the parameter space is a supplementary limit of the Voronoi cells;
    - (b) if the high level conditions are satisfied, calculate the misfit and store the model in the same way as in step (1)(f);
    - (c) while  $n_s$  new models are not generated, generate a new model in step (a);
  4. While  $it_{max}$  iterations are not completed, go back to (2).

If no conditions are set, this particular implementation of the neighbourhood algorithm gives the same results as the standard code and with approximately the same computation time. Contrary to the standard code implemented in the main dispersion curve inversion tool, this algorithm has not been tested intensively. At least in one situation, when the theoretical or true model is very close to a high level condition, the algorithm fails to generate new models. This is illustrated in figure 2.4 for a 2D case. When generating a new model in the cell with the grey outline, there are about one third of chance to get a good model. For higher dimensions of the parameter space, the situation is even worse. This issue might be

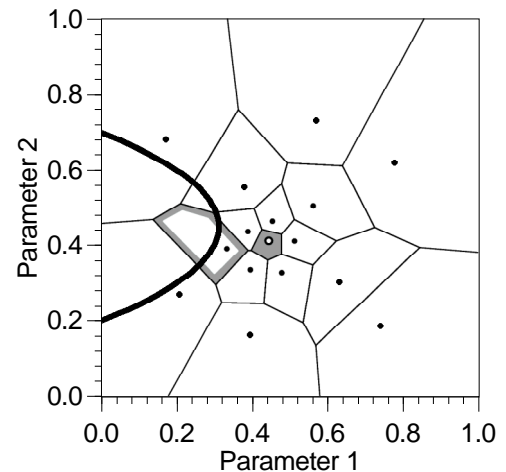


**Figure 2.4:** High level condition intersection with Voronoi cells for a 2D parameter space. The valid models are on the right of the parameter space limit marked by the thick black curve. The black dots

solved by introducing more complex low level conditions, like: “if  $p_1 < p_2$  and  $p_2 < p_3$ , then check is  $p_4 < \alpha p_5$ ”.

Sambridge (2001) proposed a refined definition of the misfit function to sample all regions of the parameter space where the models have an acceptable misfit. Particularly, if the misfit found is less than a threshold, the model is stored with the misfit equal to the threshold. Below this threshold, the differences in the model response are considered as not significant. On this basis, a refined algorithm might be developed with the objective of finding the exact boundaries of all the possible acceptable regions. It may work by trying to find bad fitting models inside the good cells converging to a refined definition of the boundaries region containing the solutions. Recognizing contiguous cells with acceptable misfit cannot be done in a perfect way for high dimensional parameter spaces. But even with an approached computation, it might be sufficient to identify the various modes of the current misfit function. The search may be oriented towards models located between those poles, for instance by creating a new temporary and smaller parameter space focused on the badly sampled region.

This improvement of the standard neighbourhood algorithm is still under testing at the time of writing this thesis. Consequently, no example can be given to illustrate it.

## 2.5 Conclusions

The neighbourhood algorithm is a flexible and powerful inversion method which requires reliable and fast forward calculation codes. Its ability to explore all the possible solutions is a strong advantage over linearized methods for complex and sometimes poorly constrained geophysical problems.

# Chapter 3

## Forward computation

This chapter aims at designing proper algorithms to calculate the dispersion, ellipticity, and auto-correlation curves in the framework of a pseudo-random inversion. A direct search algorithm, such as the neighbourhood algorithm described in section 2.3, generates a great number of models for which the forward calculations are needed to obtain a misfit value. The misfit value summarizes the degree of appropriateness of a generated model to explain the observed data. Because of the amount of computations, the forward algorithm must be fast and secure. Hence, much attention has been paid to the optimizations and to the quality of the final results. Also, the sensitivity of the three curves to the model properties are studied in detail.

### 3.1 Dispersion Curves

This section describes the computation of the theoretical dispersion curve of a ground structure. This curve is calculated for models the properties of which vary with depth only (one-dimensional structure). The profiles are discretized along the depth axis by a stack of layers with uniform properties as sketched by Fig. 3.1. The model parameters are the compressional-wave velocity ( $V_p$ ), the shear-wave velocity ( $V_s$ ), and the density ( $\rho$ ) in the layers.

Though implementations of the dispersion curve for Love and Rayleigh waves already exist for years (e.g. in Fortran, Herrmann 1994), the basic algorithms are studied in detail and optimized to reduce the CPU time consumption. The proposed algorithm is written in C++ and operates only on dynamic memory vectors without any disk access. This considerably decreases the total required time. The specificities of Love and Rayleigh waves are investigated separately from the points of view of the theory and the implementation.

The computation of theoretical dispersion curves is based on the eigenvalue problem described by Thomson (1950) and Haskell (1953), subsequently modified by Knopoff (1964), Dunkin (1965) and Herrmann (1994). We use the Dunkin's notations, here after and inside the source code. The Herrmann's code uses almost the same method as Dunkin. For Love and Rayleigh waves, the equation of motion can be reduced to a system of simple differential equations with a derivative of the first order in  $z$ . In the case of a stack of horizontal layers, this problem can be solved by the propagator-matrix method (Gilbert and Backus 1966, Aki

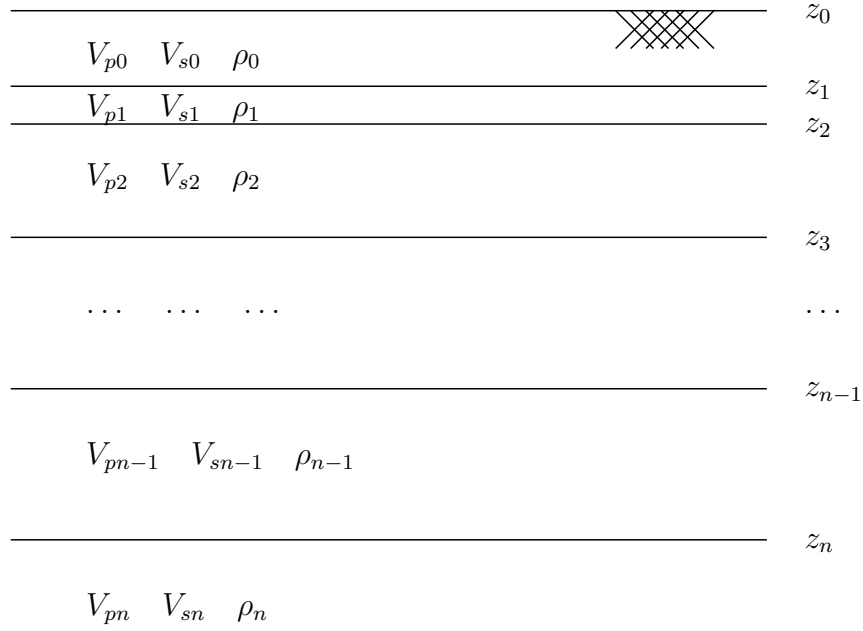


**Figure 3.1:** Schematic one-dimensional model defined by a stack of  $(n + 1)$  layers.  $z_i$  are the depths of the top of each layer.

and Richards 2002), described in the next section.

### 3.1.1 Propagator-matrix method

For a stack of horizontal and uniform layers, Gilbert and Backus (1966) proposed a method to solve the differential equation defined by

$$\frac{df(z)}{dz} = A(z)f(z) \quad (3.1)$$

where  $f$  is a vector of  $n$  components and  $A$  is a  $n \times n$  matrix. If  $A$  is independent of  $z$ , which is valid inside a layer, the solution is given by

$$f(z) = G(z, z_0)f(z_0) \quad (3.2)$$

where,

$$G(z, z_0) = e^{(z-z_0)A(z)} \quad (3.3)$$

Equation (3.3) can be developed to find the elements of matrix  $G$  using an eigenvalue decomposition of matrix  $A$  (Aki and Richards 2002). Because of the continuity of the displacement and the stresses at all interfaces between two layers, the following property is easily deduced from equation (3.2):

$$f(z_2) = G(z_2, z_1)f(z_1) = G(z_2, z_1)G(z_1, z_0)f(z_0) \quad (3.4)$$

Hence, the vector  $f(z)$  at depth  $z$ , inside layer  $n$  is:

$$f(z) = G(z, z_n)G(z_n, z_{n-1}) \dots G(z_1, z_0)f(z_0) \quad (3.5)$$

The propagator matrices  $G$  are functions of the depth at the top and at the bottom of each layer, and of the matrix  $A$  which depends upon layer properties. For Love and Rayleigh, vector  $f(z)$  is called the motion-stress vector defined in sections 3.1.3 and 3.1.4, respectively.

### 3.1.2 Displacements, Stresses, and strains

This section recalls the relationships between the displacement vector, the strain matrix and the stress matrix in the framework of the linear theory of elasticity. If the displacements along axis  $x_i$  are infinitesimal ( $u_i$  where  $i$  may be 1, 2 or 3), the strain matrix is defined by

$$\varepsilon_{ij} = \frac{1}{2} \left( \frac{\partial u_i}{\partial x_j} + \frac{\partial u_j}{\partial x_i} \right) \quad (3.6)$$

The stress matrix is linked to the strain matrix by the means of the Hooke tensor  $c_{ijkl}$  (81 components reducing to 21 due to symmetries). Using the summation rule for replicated indices inside a product, the stress tensor can be written as

$$\sigma_{ij} = c_{ijkl}\varepsilon_{kl} = \sum_{k=1}^3 \sum_{l=1}^3 c_{ijkl}\varepsilon_{kl} \quad (3.7)$$

In the case of isotropic medium, the 21 independent components reduce to the two Lamé moduli,  $\lambda$  and  $\mu$ , and equation (3.7) is now

$$\sigma_{ij} = \lambda\delta_{ij}(\delta_{kl}\varepsilon_{kl}) + \mu(\delta_{ik}\delta_{jl} + \delta_{il}\delta_{jk})\varepsilon_{kl} \quad (3.8)$$

where  $\delta_{ij}$  is the Kronecker symbol ( $\delta_{ij} = 1$  if  $i = j$  or 0 if  $i \neq j$ ).

In the absence of volumetric forces, the equation of motion is a differential equation of displacements and stresses.

$$\rho \frac{d^2 u_i}{dt^2} = \sum_{j=1}^3 \frac{\partial \sigma_{ji}}{\partial x_j} \quad (3.9)$$

where  $\rho$  is the density. For clarity, in the next sections, numerical indices  $i$  are replaced by indices  $x, y$ , and  $z$ , and  $x_i$  are replaced by  $x, y$ , and  $z$ .

### 3.1.3 Eigenvalue problem for Love waves

#### Theory

In a vertically heterogeneous, isotropic and elastic medium occupying a half-space, equation (3.9) for Love waves has a solution of the form:

$$\begin{aligned}
u_x &= 0 \\
u_y &= l(k, z, \omega)e^{i(kx - \omega t)} \\
u_z &= 0
\end{aligned} \tag{3.10}$$

$u_x$ ,  $u_y$  and  $u_z$  are the radial, transversal and vertical components, respectively.  $V_L = \frac{\omega}{k}$  (m/s) is the Love velocity at angular frequency  $\omega$  (rad/s),  $k$  is the wavenumber in the  $x$  direction.  $l(k, z, \omega)$  is the real amplitude, phase shifts are ignored as only one component is considered. The associated non-null stresses are (from equations (3.6) and (3.8)):

$$\begin{aligned}
\sigma_{xy} &= ik\mu(z)le^{i(kx - \omega t)} \\
\sigma_{yz} &= \mu(z)\frac{dl}{dz}e^{i(kx - \omega t)}
\end{aligned} \tag{3.11}$$

$\mu(z) = \rho(z)V_s(z)^2$  is the shear rigidity. Let call  $(\mu(z)\frac{dl}{dz})$  by  $l^\sigma$ . A motion-stress vector for Love waves  $([l, l^\sigma]^T)$  is defined so that equation of motion (3.9) can be transformed into

$$\frac{d}{dz} \begin{pmatrix} l \\ l^\sigma \end{pmatrix} = \begin{pmatrix} 0 & 1/\mu(z) \\ k^2\mu(z) - \omega^2\rho(z) & 0 \end{pmatrix} \begin{pmatrix} l \\ l^\sigma \end{pmatrix} \tag{3.12}$$

which has the form of equation (3.1). For surface waves, the boundary conditions require that:

$$l \rightarrow 0 \quad \text{when} \quad z \rightarrow \infty \tag{3.13}$$

$$l^\sigma = 0 \quad \text{at the free surface} \quad z = z_0 \tag{3.14}$$

Because equation (3.12) has the same form as equation (3.1), the solution for the motion-stress vector is given by equation (3.5). The condition on the motion-stress at infinity (equation (3.13)) cannot be introduced directly. It is transformed into a radiation condition that no up-going waves are found in the bottom half-space. For  $S_H$  plane waves, the amplitudes of downgoing ( $\dot{S}_n$ ) and up going ( $\dot{S}'_n$ ) waves traveling across an homogeneous half space are function of the motion-stress vector at the top of the half space ( $z = z_n$ ) (Aki and Richards 2002)

$$\begin{pmatrix} \dot{S}_n \\ \dot{S}'_n \end{pmatrix} = T_n^{-1} \begin{pmatrix} l(z_n) \\ l^\sigma(z_n) \end{pmatrix} \tag{3.15}$$

where,

$$T_n^{-1} = \frac{1}{2\nu_n\rho_n} \begin{pmatrix} \nu_n\rho_n e^{\nu_n z} & -e^{\nu_n z}/V_{sn}^2 \\ \nu_n\rho_n e^{-\nu_n z} & e^{-\nu_n z}/V_{sn}^2 \end{pmatrix} \tag{3.16}$$

$$\nu_n^2 = k^2 - \frac{\omega^2}{V_{sn}^2} \tag{3.17}$$

$V_{sn}$  is the velocity of S waves (m/s). The subscript  $n$  denotes parameters defined for layer  $n$  as represented in figure 3.1. The motion-stress vector is propagated to  $z_0$  by the means of equation (3.5). Equation (3.15) becomes

$$\begin{pmatrix} \dot{S}_n \\ \dot{S}_n \end{pmatrix} = T_n^{-1} G(z_n, z_{n-1}) \dots G(z_1, z_0) \begin{pmatrix} l(z_0) \\ l^\sigma(z_0) \end{pmatrix} \quad (3.18)$$

where,

$$G(z_n, z_{n-1}) = \begin{pmatrix} \cosh[\nu_{n-1}(z_n - z_{n-1})] & 1/(\nu_{n-1}\mu_{n-1})\sinh[\nu_{n-1}(z_n - z_{n-1})] \\ \nu_{n-1}\mu_{n-1}\sinh[\nu_{n-1}(z_n - z_{n-1})] & \cosh[\nu_{n-1}(z_n - z_{n-1})] \end{pmatrix} \quad (3.19)$$

Introducing the boundary conditions (equations (3.13) and (3.14)) into equation (3.18) gives

$$\begin{aligned} \begin{pmatrix} \dot{S}_n \\ 0 \end{pmatrix} &= T_n^{-1} G_n \dots G_1 \begin{pmatrix} l(z_0) \\ 0 \end{pmatrix} \\ &= \underbrace{\begin{pmatrix} l_{11} & l_{12} \\ l_{21} & l_{22} \end{pmatrix}}_{L(z_0)} \begin{pmatrix} l(z_0) \\ 0 \end{pmatrix} \end{aligned} \quad (3.20)$$

which has only non trivial solutions when  $l_{21}$  vanishes. The problem of finding the dispersion curves for Love waves is hence reduced to a root search along the slowness or the velocity axis for a given frequency. For a given frequency  $(\frac{\omega}{2\pi})$ , only a few discrete values are possible for the velocity of the Love surface wave ( $V_L = \left[ \frac{\omega}{k(\omega)} \right]_i$ ), corresponding to the dispersion curves of various modes.

### Eigenfunctions

The functions  $l$  and  $l^\sigma$  defined in equations (3.10) and (3.11) are the eigenfunctions of Love waves. For each depth and frequency, different values of eigenfunctions exist corresponding to all roots of  $l_{21}(z_0)$  (modes). The motion-stress vector at depth  $z_0$  can be defined numerically by normalizing  $l(z_0)$  to any arbitrary value. The computation of the eigenfunctions at the next layer interface is done by multiplying the motion-stress vector at depth  $z_0$  by  $G_1^{-1}$ . The same task is repeated until reaching the top of the half-space. Inside a particular layer, the values of the eigenfunctions are also calculated from the definition of  $G_n^{-1}$  (equation (3.18)). Examples of eigenfunction variation with depth can be found in Aki and Richards (2002). Among other features, they show that the penetration depth is frequency dependent. For high frequencies, only the most superficial layers are affected by displacements and stresses.

### Implementation

The problem is to find the solutions of the equation  $l_{21}(V_L) = 0$ . The computation of the element  $l_{21}(z_0)$  requires the multiplication of  $n$  2x2 matrices, whereas three of the four elements

of the final matrix  $L(z_0)$  are useless. From the formulae of the product of two 2x2 matrices, only  $l_{21}(z_1)$  and  $l_{22}(z_1)$  are necessary for computing  $l_{21}(z_0)$  which, in turn, requires  $l_{21}(z_2)$  and  $l_{22}(z_2)$  (equation 3.21).

$$\begin{aligned}
\underbrace{\begin{pmatrix} - & - \\ l_{21}(z_0) & - \end{pmatrix}}_{L(z_0)} &= T_n^{-1} G_n \dots G_1 & (3.21) \\
&= \underbrace{\begin{pmatrix} - & - \\ l_{21}(z_n) & l_{22}(z_n) \end{pmatrix}}_{L(z_n)=T_n^{-1}} G_n \dots G_1 \\
&\dots \\
&= \underbrace{\begin{pmatrix} - & - \\ l_{21}(z_2) & l_{22}(z_2) \end{pmatrix}}_{L(z_2)} G_2 G_1 \\
&= \underbrace{\begin{pmatrix} - & - \\ l_{21}(z_1) & l_{22}(z_1) \end{pmatrix}}_{L(z_1)} G_1
\end{aligned}$$

To calculate  $L(z_n) = T_n^{-1}$ , the factors  $e^{-\nu_n z}$  are dropped from elements  $l_{21}(z_n)$  and  $l_{22}(z_n)$  (equation (3.16) because we are looking for the roots of  $l_{21}(V_L)$ .

From equation (3.17),  $\nu_n$  is imaginary if  $k$  is less than the wavenumber of S-waves  $k_{sn} = \frac{\omega^2}{V_{sn}^2}$ . To avoid using complex number libraries, the *sinh* and *cosh* functions of equation (3.19) are replaced by the corresponding trigonometric functions *sin* and *cos*. For real values of  $\nu_n$ , the hyperbolic functions do not tolerate high arguments. They are preferably computed from their analytical formulae:

$$\begin{aligned}
\sinh(ix) &= \frac{e^{ix} - e^{-ix}}{2} = e^x \frac{1 - e^{-2x}}{2} & (3.22) \\
\cosh(ix) &= \frac{e^{ix} + e^{-ix}}{2} = e^x \frac{1 + e^{-2x}}{2}
\end{aligned}$$

Hence, an exponential factor can be dropped from the expression of  $G$  in equation (3.19) because we are seeking for roots. When factor  $e^x$  is dropped, the computation of both hyperbolic functions require the calculation of only one exponential function. As we are working in double precision (floating points of 64 bits), all exponential values  $e^{-2x}$  less than  $10^{-19}$  are equivalent to zeros in equations (3.22). Thus, in equation 3.19, the hyperbolic functions reduce to  $\frac{1}{2}$  if

$$\nu_{n-1}(z_n - z_{n-1}) > \frac{19}{2} * \ln(10) \approx 21.2 \quad (3.23)$$

In each layer, values of  $l_{21}(z_i)$  are scaled to fit in the range between  $-10^5$  to  $10^5$ , to avoid overflow when propagating across a stack with many layers.

In figure 3.2, the values taken by  $l_{21}(z_0)$  for all couples  $(\omega, k)$  are shown in the case of a two-layer model: 200 m/s for  $V_s$  in the first 25 m thick layer, and 1000 m/s in the half-space.

The first 12 modes located at the root of the function are highlighted by black lines. The negative values of the function are not represented (white areas). The normal modes of Love are observed between the minimum and the maximum  $V_s$  of the model. The fundamental mode is present over the whole frequency range, whereas each higher mode has its own threshold frequency under which it does not exist.

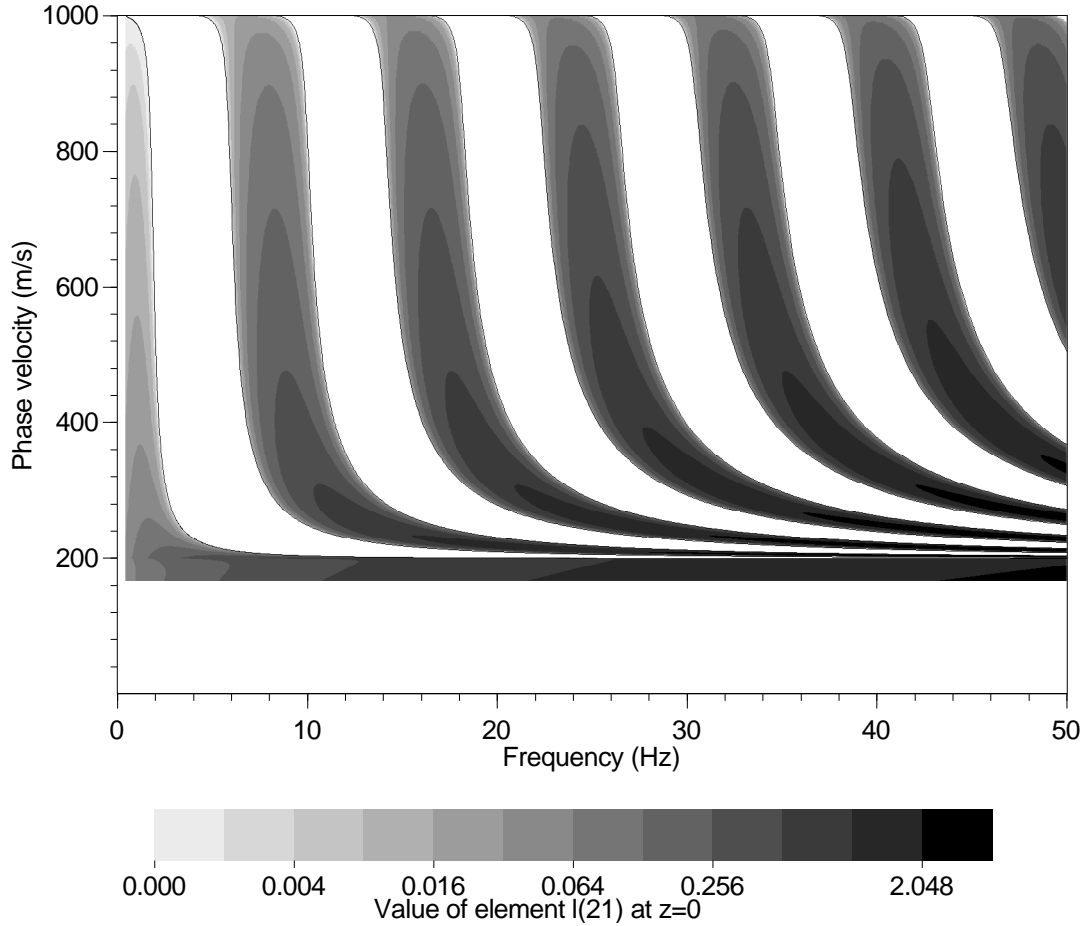


**Figure 3.2:** Values taken by  $l_{21}(z_0)$  at different couples (frequency, velocity) for a two-layer model.

Finding the roots of  $l_{21}(z_0)$  is not straightforward. This issue is treated in section 3.1.5 together with the overall performances of this algorithm.

### 3.1.4 Eigenvalue problem for Rayleigh waves

#### Theory

In a vertically heterogeneous, isotropic and elastic medium occupying a half-space, a  $P - S_V$  wave travelling along X axis generates displacements along X and Z axis of the form

$$\begin{aligned}
 u_x &= r_1(k, z, \omega)e^{i(kx - \omega t)} \\
 u_y &= 0 \\
 u_z &= r_2(k, z, \omega)e^{i(kx - \omega t)}
 \end{aligned}
 \tag{3.24}$$

where  $u_x$ ,  $u_y$  and  $u_z$  are the radial, transversal and vertical components, respectively,  $r_1$  and  $r_2$  are the complex amplitudes (including phase shifts between components),  $\omega$  is the angular frequency, and  $V_R = \frac{\omega}{k}$  is the velocity of Rayleigh waves (m/s). A motion-stress vector for Rayleigh waves is defined in a similar way as for Love case (section 3.1.3).

$$r(k, z, \omega) = \begin{pmatrix} r_1(k, z, \omega) \\ r_2(k, z, \omega) \\ r_1^\sigma(k, z, \omega) \\ r_2^\sigma(k, z, \omega) \end{pmatrix} \quad (3.25)$$

where,

$$\begin{aligned} r_1^\sigma &= i \left( (\lambda + 2\mu) \frac{dr_2}{dz} + k\lambda r_1 \right) \\ r_2^\sigma &= \mu \left( \frac{dr_1}{dz} - kr_2 \right) \end{aligned} \quad (3.26)$$

$r_1^\sigma$  is the amplitude of the vertical compression stress  $\sigma_{zz}$  and  $r_2^\sigma$  is the amplitude of the radial shear stress  $\sigma_{xz}$ . From equation of motion (3.9), the solution must satisfy the following differential equation:

$$\frac{d}{dz} \begin{pmatrix} r_1 \\ r_2 \\ r_1^\sigma \\ r_2^\sigma \end{pmatrix} = \begin{pmatrix} 0 & -ik & 0 & \frac{1}{\mu} \\ \frac{-i\lambda}{\lambda+2\mu} & 0 & \frac{1}{\lambda+2\mu} & 0 \\ 0 & -\omega^2\rho & 0 & -ik \\ \frac{4k^2\mu(\lambda+\mu)}{\lambda+2\mu} & 0 & \frac{-ik\lambda}{\lambda+\mu} & 0 \end{pmatrix} \begin{pmatrix} r_1 \\ r_2 \\ r_1^\sigma \\ r_2^\sigma \end{pmatrix} \quad (3.27)$$

where  $\rho$  is the density,  $\lambda$  and  $\mu$  are Lamé moduli. The  $z$  dependencies of  $\rho$ ,  $\lambda$  and  $\mu$  have been dropped for simplicity. For surface waves, the boundary conditions require that:

$$r_1 \rightarrow 0 \quad \text{and} \quad r_2 \rightarrow 0 \quad \text{when} \quad z \rightarrow \infty \quad (3.28)$$

$$r_1^\sigma = r_2^\sigma = 0 \quad \text{at the free surface} \quad z = z_0 \quad (3.29)$$

Similarly to Love case, the equation of motion is reduced to an equation of the same form as equation (3.1). The solution for the motion-stress vector is given by equation (3.5). The constraint on the motion-stress at infinity is transformed into a radiation condition that no up-going waves are found in the bottom half-space. For  $P - S_V$  plane waves, the amplitudes of downgoing ( $\dot{P}_n$  and  $\dot{S}_n$  for P and S-waves, respectively) and up going ( $\dot{P}_n$  and  $\dot{S}_n$  for P and S-waves, respectively) waves traveling across an homogeneous half space are function of the motion-stress vector at the top of the half space ( $z = z_n$ ) (Dunkin 1965, Aki and Richards 2002). The motion-stress vector is propagated to  $z_0$  by the means of equation (3.5). The

subscript  $n$  is added to all parameters defined for layer  $n$ .

$$\begin{pmatrix} \dot{P}_n \\ \dot{S}_n \\ \dot{P}_n \\ \dot{S}_n \end{pmatrix} = T_n^{-1} \begin{pmatrix} r_1(z_n) \\ r_2(z_n) \\ r_1^\sigma(z_n) \\ r_2^\sigma(z_n) \end{pmatrix} = T_n^{-1} G(z_n, z_{n-1}) \dots G(z_1, z_0) r(z_0) \quad (3.30)$$

where,

$$T_n^{-1} = \frac{-V_{sn}^2}{2\mu_n \hat{h}_n \hat{k}_n \omega^2} \begin{pmatrix} 2i\mu_n k \hat{h}_n \hat{k}_n & \mu_n l_n \hat{k}_n & \hat{h}_n \hat{k}_n & ik \hat{k}_n \\ -\mu_n l_n \hat{k}_n & 2i\mu_n k \hat{h}_n \hat{k}_n & ik \hat{h}_n & -\hat{h}_n \hat{k}_n \\ 2i\mu_n k \hat{h}_n \hat{k}_n & -\mu_n l_n \hat{k}_n & \hat{h}_n \hat{k}_n & -ik \hat{k}_n \\ \mu_n l_n \hat{k}_n & 2i\mu_n k \hat{h}_n \hat{k}_n & -ik \hat{h}_n & -\hat{h}_n \hat{k}_n \end{pmatrix} \quad (3.31)$$

where,  $\hat{h}_n^2 = 2k^2 - \frac{\omega^2}{V_{pn}^2}$ ,  $V_{pn}$  is the velocity of P waves (m/s),  $\hat{k}_n^2 = 2k^2 - \frac{\omega^2}{V_{sn}^2}$ ,  $V_{sn}$  is the velocity of S waves (m/s),  $l_n = k^2 + \hat{k}_n^2$ ,  $\mu_n = \rho_n V_{sn}^2$  is the rigidity, and  $\rho_n$  is the density (t/m<sup>3</sup>).

Merging boundary conditions with equation (3.30),

$$\begin{pmatrix} 0 \\ 0 \\ \dot{P}_n \\ \dot{S}_n \end{pmatrix} = T_n^{-1} G_n \dots G_1 r(z_0) \\ = \underbrace{\begin{pmatrix} r_{11} & r_{12} & r_{13} & r_{14} \\ r_{21} & r_{22} & r_{23} & r_{24} \\ r_{31} & r_{32} & r_{33} & r_{34} \\ r_{41} & r_{42} & r_{43} & r_{44} \end{pmatrix}}_{R(z_0)} \begin{pmatrix} r_1(z_n) \\ r_2(z_n) \\ 0 \\ 0 \end{pmatrix} \quad (3.32)$$

This equation is always true when the sub-determinant ( $r_{11}r_{22} - r_{12}r_{21}$ ) vanishes. Like in the Love case, the problem of finding the dispersion curves is thus reduced to a root search along the slowness or the velocity axis for a given frequency. However as stated by Dunkin (1965), the terms of the sub-determinant can become very large. Subtracting two large numbers results in a loss of significant digits, which implies the use of very high precision computations (e.g. 128 bit numbers or even more whereas computers are classically limited to 32 or 64 bits). Hence, Dunkin proposed an alternative way of propagating motion-stress vector by the means of the following theorem. If  $P = A^{(0)} A^{(1)} \dots A^{(n-1)} A^{(n)}$  then

$$p \begin{vmatrix} i & j \\ k & l \end{vmatrix} = a^{(0)} \begin{vmatrix} i & j \\ m & n \end{vmatrix} a^{(1)} \begin{vmatrix} m & n \\ o & p \end{vmatrix} \dots a^{(n-1)} \begin{vmatrix} s & t \\ u & v \end{vmatrix} a^{(n)} \begin{vmatrix} u & v \\ k & l \end{vmatrix} \quad (3.33)$$

where  $p \begin{vmatrix} i & j \\ k & l \end{vmatrix} = p_{ik}p_{jl} - p_{il}p_{jk}$  is the second order sub-determinant of matrix P. The notation  $P_{ijkl}$  is also used in appendix A.

In equation (3.33), the summation rules<sup>1</sup> apply for indices appearing two times like  $m$  and  $n$ . In this case, the summed pairs of indices are to be only distinct pairs of distinct indices<sup>2</sup> (by convention,  $m < n$ ,  $o < p, \dots$ ,  $s < t$ ,  $u < v$ ). It follows from equation (3.33) that:

$$\begin{aligned} r_{11}(z_0)r_{22}(z_0) - r_{12}(z_0)r_{21}(z_0) &= r(z_0) \begin{vmatrix} 1 & 2 \\ 1 & 2 \end{vmatrix} \\ &= t_n^{-1} \begin{vmatrix} 1 & 2 \\ a & b \end{vmatrix} g_n \begin{vmatrix} a & b \\ c & d \end{vmatrix} \cdots g_1 \begin{vmatrix} e & f \\ 1 & 2 \end{vmatrix} = 0 \end{aligned} \quad (3.34)$$

With the condition on indices, the factor  $t_n^{-1} \begin{vmatrix} 1 & 2 \\ a & b \end{vmatrix}$  has 6 components: 12, 13, 14, 23, 24 and 34 (Dunkin 1965). On the other hand,  $g_n \begin{vmatrix} a & b \\ c & d \end{vmatrix}$  has 6x6 components. Hence, like in the Love case, for a given frequency ( $\frac{\omega}{2\pi}$ ), only a few discrete values are possible for the velocity of the Rayleigh surface wave ( $V_R = \left[ \frac{\omega}{k(\omega)} \right]_i$ ), corresponding to the dispersion curves of various modes.

The dispersion curve is found by seeking the roots of  $r(z_0) \begin{vmatrix} 1 & 2 \\ 1 & 2 \end{vmatrix}$ .

### Eigenfunctions

As for the Love case, the functions  $r_1$  to  $r_2^\sigma$  defined in equation (3.25) are the eigenfunctions for Rayleigh waves. From equation (3.32), it is obvious that

$$\frac{r_1(z_0)}{r_2(z_0)} = -\frac{r_{12}(z_0)}{r_{11}(z_0)} \quad (3.35)$$

The ratio of eigenfunctions  $r_1$  and  $r_2$  is hence fixed to a constant that depends upon the values of the elements of matrix  $R(z_0)$ , itself, a function of the mode and the frequency for which the Rayleigh velocity has been calculated. The motion-stress vector at depth  $z_0$  can be defined numerically, normalizing either  $r_1$  or  $r_2$  to any arbitrary value. The computation of the eigenfunctions at any arbitrary depth is done in the same way as for the Love case. The elements of  $G$  are not given here, but it can be calculated by an eigenvalue decomposition of matrix  $A$  (equations (3.27) and (3.1)).

The eigenfunctions at the surface are useful for computing the ellipticity of Rayleigh waves (section 3.2). It will be shown how to calculate  $\frac{r_{12}(z_0)}{r_{11}(z_0)}$  without the complete knowledge of the elements of matrix  $R(z_0)$ .

### Implementation

The detailed expressions of the determinants of  $R(z_i)$  are given in appendix A. The six-component vector  $R(z_{n-2})$  is obtained by combining the matrix  $G_{n-1}$  and the vector  $R(z_{n-1})$

<sup>1</sup>The summation of indices take place when one or more indices appear two times inside a product. For instance, the formula  $x_{ki}y_{il}$  is in fact equal to  $\sum_{i=\min}^{\max} x_{ki}y_{il}$

<sup>2</sup>In the pair  $(m, n)$   $m$  is always different from  $n$ , and pairs  $(m, n)$  and  $(n, m)$  are strictly equivalent

in the same way as equations (A.12) for  $G_n$  and  $T_n^{-1}$ . The computation is done for each layer for bottom to top up to the first one at the free surface. As  $T_{1214}$  and  $T_{1223}$  (appendix A) are equal (from equation (3.31)), it is obvious that  $R_{1223}(z_{n-1}) = R_{1214}(z_{n-1})$ . From bottom to top, the two components are always equal (equation (3.30)) and we can reduce the number of components to five rather than six. Also,  $R_{1214}(z_{n-1})$  like  $T_{1214}$  is the only imaginary component and this feature is preserved across the layered medium. Thus, the 6 components of  $t_n^{-1}$  reduce to 5 and the matrix  $g_n$  to 5x5 components.

To speed up the computation, we slightly modified the Dunkin's original formulation to reduce the total number of operations, preferring subtractions, additions and multiplications to divisions. The *sinh* and *cosh* functions are calculated in the same way as for Love case, including the real and imaginary cases (equation (3.22), section 3.1.3). A frequency factor of  $\omega^2$  (equation (A.12), appendix A) has been introduced in  $R_{1212}$  to avoid unscaled vector at low frequencies. For each layer, values of sub-determinants are scaled to fit in the range between  $-10^5$  to  $10^5$  to avoid overflow when propagating across a stack with many layers. Compared to Herrmann's formulation (1994) in the same conditions (not in its original Fortran code but already translated in C++), this implementation reduces by 25% the time consumption.

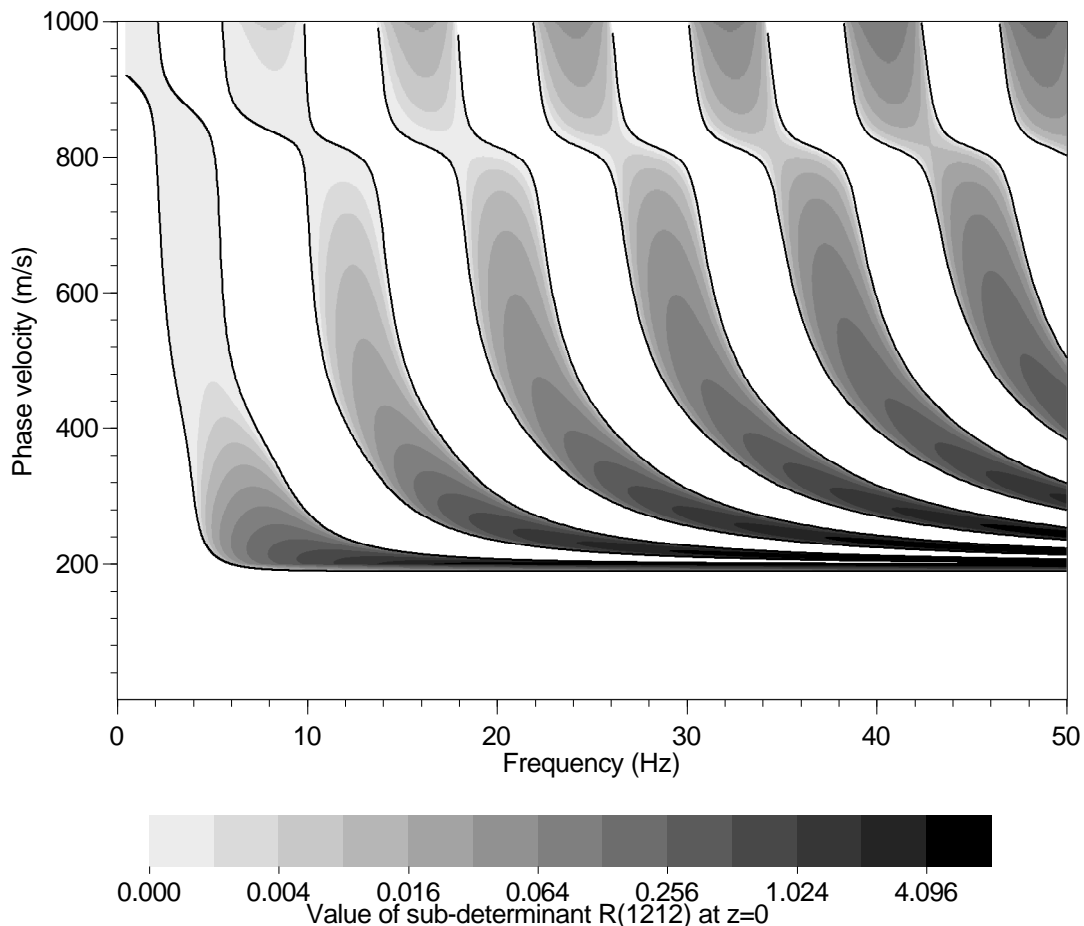


**Figure 3.3:** Values taken by  $R_{1212}(z_0)$  at different couples (frequency, velocity) for a two-layer model.

In figure 3.3, the values taken by  $R_{1212}(z_0)$  for all couples  $(\omega, k)$  are shown in the case of a two-layer model: 1350 and 250 m/s for  $V_p$  and  $V_s$ , respectively in the first 25 m thick layer,

and 2000 and 1000 m/s in the half-space.

### 3.1.5 A quick root search

For a given  $\omega$ , the roots of either  $l_{21}(z_0)$  (Love) or  $R_{1212}(z_0)$  (Rayleigh) are searched along the velocity axis. The problem is not to find some roots of the function but all roots in a correct order to clearly identify the modal curves. Inside the source code, the search is performed on the slowness axis to reduce the number of time consuming divisions and also to take advantage of the better separation of modes at high frequency in the slowness domain compared to the usual velocity domain (figure 3.3). For the sake of clarity, the velocity is used in this section.

#### Physical search interval

Typical dispersion curves are shown on figure 3.4 with their lower and higher velocity limits. All real curves have a velocity less than or equal to the maximum S-wave velocity of the

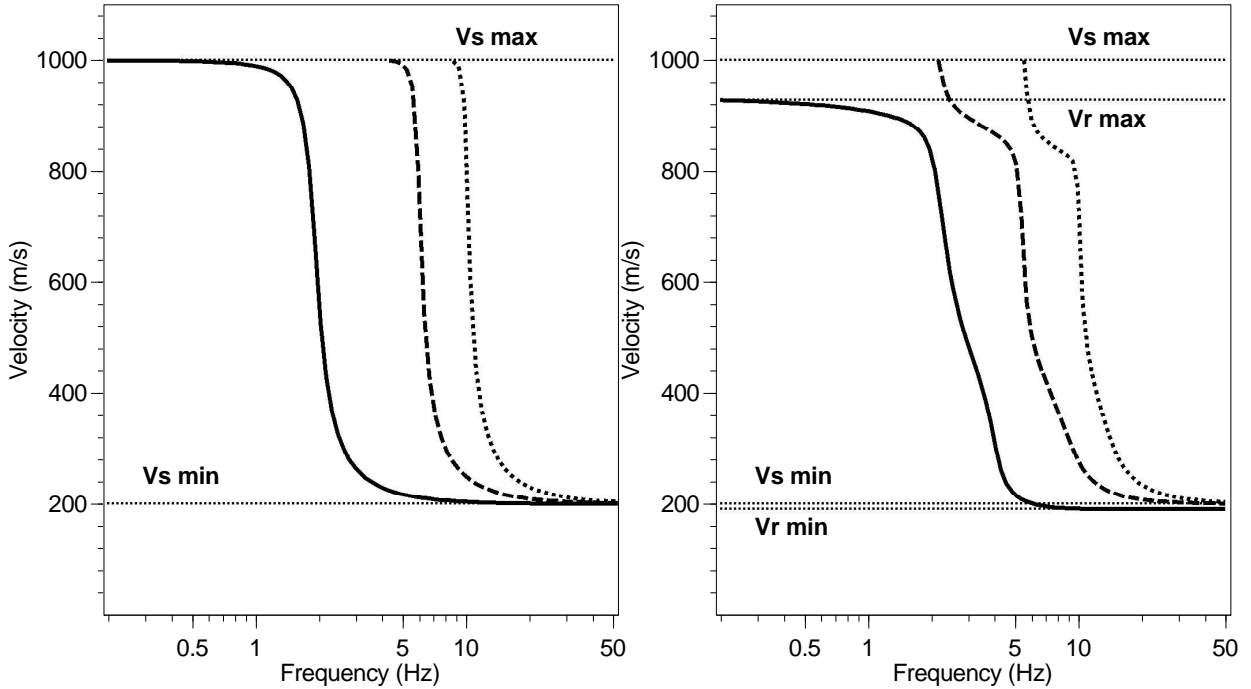


**Figure 3.4:** Velocity limits of Love (a) and Rayleigh (b) dispersion curves. Fundamental mode and the two first higher modes are represented with plain, dashed, dotted lines respectively. The horizontal lines are the physical velocity limits.

model ( $V_{s,max}$ ). The minimum possible velocity is not the same for Love and Rayleigh cases. For Love waves, all modes tend to a common velocity at very high frequencies, equal to the minimum S-wave velocity of the model ( $V_{s,min}$ ). At high frequency, deep layers are ignored by the surface waves behaviour. For Rayleigh waves, all higher modes tend to  $V_{s,min}$  and  $V_{s,max}$  at high and low frequencies respectively. For the fundamental mode, the minimum ( $V_{r,min}$ ) and maximum ( $V_{r,max}$ ) velocities at high and low frequencies are slightly less than  $V_{s,min}$  and  $V_{s,max}$ , respectively.  $V_{r,min}$  and  $V_{r,max}$  are equal to the Rayleigh velocity observed for a homogeneous

half-space with the velocity of the first layer and the bottom half space, respectively. In this latter case, equations (3.31) and (3.32) simplify to

$$\left(\frac{1}{V_s^2} - 2\frac{1}{V_r^2}\right)^2 = 4\frac{1}{V_r} \sqrt{\left(1 - \frac{1}{V_p^2}\right)\left(1 - \frac{1}{V_s^2}\right)} \quad (3.36)$$

where  $V_s$  is the velocity of S-waves,  $V_p$  is the velocity of P-waves, and  $V_r$  is the unknown velocity of Rayleigh waves. Equation (3.36) shows that the velocity of Rayleigh waves is constant for all frequencies, and hence no dispersion takes place.  $V_{r,max}$  for Rayleigh dispersion curves (fundamental mode) is thus calculated by solving equation (3.36) with  $V_s$  and  $V_p$  being the slownesses of the layer with the minimum  $V_s$ . A few Newton-Raphson (Press et al. 1992) iterations are necessary to obtain  $V_{r,min}$  and  $V_{r,max}$ .

### Bracketing the root candidates

The roots are searched starting from the highest to the lowest frequency within the range defined by the user. The method is illustrated in figure 3.5. The grey curves correspond to the same dispersion curves as in figure 3.3. In this section, the Rayleigh case is discussed, but the same method applies to Love's case as well, by replacing  $V_{r,min}$  by  $V_{s,min}$ , and  $R_{1212}(z_0)$  by  $l_{21}(z_0)$ .  $f_1$  is the highest frequency of the user range and  $f_2$  is the second highest frequency. The fundamental and the first two higher modes are represented. The plus and minus signs represent the polarity of function  $R_{1212}(z_0)$ . The polarity below the fundamental curve (initial polarity) is computed for  $\frac{V_{r,max}}{1.05}$  and at low frequency ( $\frac{1}{2\pi}$  Hz). The minimum limit is divided by 1.05 to be sure that the fundamental mode is not missed. The polarity alternates when crossing a modal curve.

The first root with the minimum velocity, that corresponds to the fundamental mode at the highest frequency ( $f_1$ ), is bracketed by increasing the velocity from  $\frac{V_{r,max}}{1.05}$  with an adaptive step until finding a sign change. It always exists as the fundamental mode is present for all frequencies (grey dots and black dots when a root is found). The search step is calculated by multiplying the lower limit of the current interval by a constant step ratio. Either for Love and Rayleigh, half the difference between  $V_{s,min}$  and  $V_{r,min}$  is taken as a reference to adjust the initial velocity step. Hence, the step ratio is defined by

$$\frac{V_{s,min} - V_{r,min}}{2 V_{s,min}} \quad (3.37)$$

This method is particularly justified in this case because the ratio of the minimum and maximum velocities of the admissible range is usually around 4 or 5. The step ratio is eventually reduced and the precision is increased, if mode jumping is detected (section 3.1.6). Once a root has been bracketed, its upper and lower bounds are refined down to the current precision using the algorithm described in the next paragraph. The higher bound of the refined interval is kept as the calculated curve. The modal velocity is then computed for the next frequency sample  $f_2$ .

The starting velocity for the new search is the velocity calculated for the preceding frequency

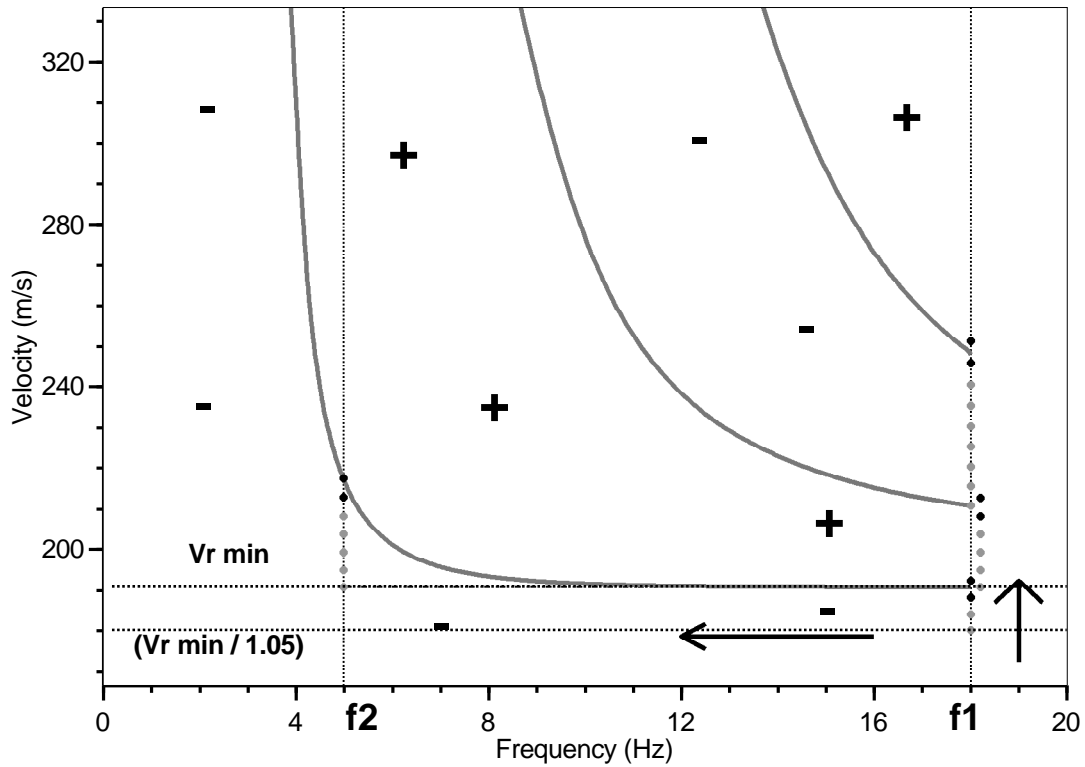


Figure 3.5: Method for bracketing roots.

sample,  $f_1$  in this case (the higher bound is taken). The search direction depends upon the polarity observed at  $f_2$  and at the starting velocity. If it is the same as the initial polarity, the true dispersion is located at a higher velocity (as in figure 3.5) and the root is refined after the same type of search as in  $f_1$ . In the other case, the dispersion has a non-monotonous shape, characteristic of models with low velocity zones (section 3.1.6). No search is made because a polarity change has already been found; the root is directly refined. The same process is applied for all frequency samples until the lowest. A final test described in section 3.1.6 is performed on the obtained modal curve. Afterwards, the curve is definitively accepted.

For higher modes, the minimum of velocity ranges are reduced to the values of the refined higher bounds of the preceding mode. The initial polarity is inverted. The modal curve may not be defined for all frequency samples. If so, the velocity search stops at  $V_{s,max}$ . If the polarity at  $V_{s,max}$  is the same as the initial polarity, no root exists and the computation of this mode is stopped. The same test as for the fundamental mode is performed before definitively accepting the curve.

### Refining the brackets

Once bracketed, there are several classical ways of refining a root of a non-linear or non-analytical function. Among them, the most robust is the bisection (Press et al. 1992). It always gives the correct answer if the root is correctly bracketed and if the function is continuous. However, it is not the quickest way in most of the situations. Like Herrmann (1994), we implemented an algorithm that mixes the bisection method and a Lagrange polynomial fit. The Lagrange polynomial is best constructed using the iterative Neville's algorithm (Press et al.

1992). Corrections have been brought to Herrmann's algorithm to achieve better performances.

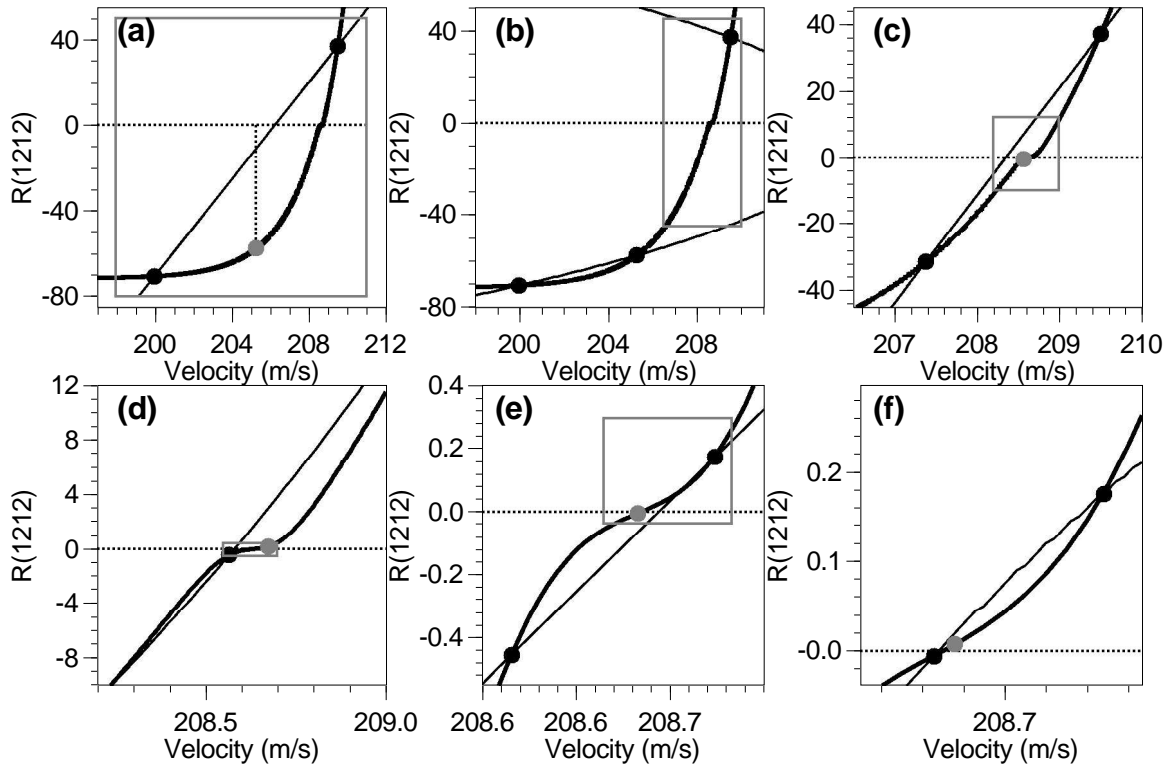


**Figure 3.6:** Method for refining roots. (a) to (f) are successive steps of refinement. The thick plain curve is the unknown theoretical curve. The thin plain line is the polynomial fit from already calculated samples (black dots). The grey dot is the new root computed from polynomial fit. The grey rectangles show the zoom area of the next step.

Practically, from the two initial bracketing values ( $V_1$  and  $V_2$ ), a third point  $V_3$  is calculated by bisection.  $R_1$  to  $R_3$  are the values of  $R_{1212}(z_0)$  for  $V_1$  to  $V_3$ , respectively. According to the sign of  $R_3$ , either  $V_1$  or  $V_2$  is replaced by the value  $V_3$ , swapping them eventually afterwards to keep  $V_1 < V_2$ . It is the state described by figure 3.6(a), where  $V_1$  and  $V_2$  are represented by black dots. A Lagrange polynomial is constructed on those two samples (a line in this case), shown by the thin plain line. From the intersection of the polynomial with axis  $y = 0$ , a new  $V_3$  is deduced, it is shifted by a tenth of  $V_2 - V_1$  towards the limit with the highest  $R_{1212}$  value, and  $R_3$  is re-calculated. If  $R_3$  is located between  $R_1$  and  $R_2$ , the function is bijective inside  $[V_1, V_2]$  and hence invertible between  $V_1$  and  $V_2$ . This is not the case in figure 3.6(b). Consequently, the algorithm returns to bisection to generate a new sample  $V_3$  from the current  $V_1$  and  $V_2$ . As in the first step, either  $V_1$  or  $V_2$  is replaced by the value  $V_3$  (new brackets are shown in figure 3.6(c) by black dots). New samples (grey dots) are generated from the polynomial fit and integrated into it. In figures 3.6(d) to 3.6(f), the degree increases at each step as new samples are added.

To efficiently calculate the root of a Lagrange polynomial  $P(V)$ , the axis X and Y are swapped during its construction. The coordinates of the samples are swapped so that  $P'(R)$  fits  $(R_1, V_1), (R_2, V_2), \dots$ . The current estimate for the root is  $V = P'(0)$ . If  $R_1$  and  $R_2$  differ from a factor 10 or more, the Neville's algorithm may fail and it is better to return to the bisection until reducing the ratio. To avoid a quick return to bisection, the newly generated point has to be on the side of the true root where either  $R_1$  or  $R_2$  is maximum. For doing so,

the calculated value is considered as the true root, and it is shifted by a tenth of the current bracket interval towards the boundary having the highest value for the function. In most cases, when the true function is locally weakly non-linear, the limit with the highest function value is replaced by the new shifted estimate of the root at the next iteration, keeping the order of magnitude of  $R_1$  and  $R_2$  in the same range. This is the minor modification we brought to Herrmann's algorithm (1994), but it has a major influence over the global performances, as the full power of the polynomial fit is used. The maximum degree of the polynomial is set to 19, because its coefficients are stored in a static vector of limited length for efficiency. In a contradictory way, finding the perfect root <sup>3</sup> is a problem because the inferior and superior brackets are lost as no sign can indicate on which side of the true root a new sample is. It may ruin the root search for the next modes. This case is checked, and the computation of the function is redone at a slightly distinct value (minus one tenth of the current bracketed interval).

With this method, only 4 to 6 iterations are generally necessary to obtain a  $10^{-7}$  relative precision. One iteration corresponds to one evaluation of the numerical function  $R_{1212}(z_0)$ . In the original code written by Herrmann (1994), the degree of the polynomial never increases over 2 or 3, quickly returning to bisection. More than 10 iterations are necessary to achieve the same precision. Our code rarely returns to bisection, increasing the degree of the polynomial at each iteration. Together with the removal of all file Input/Output, it has been possible to drop the time consumption by a factor 5 to 6.

### 3.1.6 Mode jumping control

During a direct search inversion, the number of calculated dispersion curves is so huge that it is impossible to manually control the individual results of each model. That is the reason why an automatic quality control has been developed.

Figure 3.2 shows that modal curves might be located very close to each other at certain frequencies: at high frequency for Love case, or at osculation points for Rayleigh case (e.g. Forbriger 2003a). At these points, the distance between two modes might be smaller than the default step calculated above. During the search, crossing two modes in one step results in a constant polarity and hence modes are sought at a higher velocity, ignoring two modes. Another kind of mode jumping may occur for models with low velocity zones (LVZ). For those models only, the dispersion curve may have a non-monotonous shape with a least one maximum (figure 3.7. When moving from frequency  $f_1$  to  $f_2$  in figure 3.5, the horizontal line may cross several modes only if higher modes have also a non-monotonous shape at the considered frequency.

Two kinds of tests (detailed in the next two paragraphs) are performed during the computations of dispersion curve to detect any mode jumping. In case of error, the computation is always restarted for the current modal curve to the highest frequency of the user range. Meanwhile, the search step and the relative precision are both divided by a factor 10. At

---

<sup>3</sup>In the computer sense, the perfect root is obtained when the values of the function are less than the internal precision.

this stage, optimization is not of concern and the step is chosen small enough to avoid mode jumping rather than decreasing slowly until finding the maximum needed size. Four restarts are allowed before stating that the dispersion cannot be calculated for the given model. The default precision and step ratio are reset after each acceptance of a modal curve.

### Non-monotonous shape

If no LVZ is detected in the model, any extrema of the dispersion curve is rejected and computation is restarted. On the other hand, if a LVZ takes place in the model (figure 3.7),

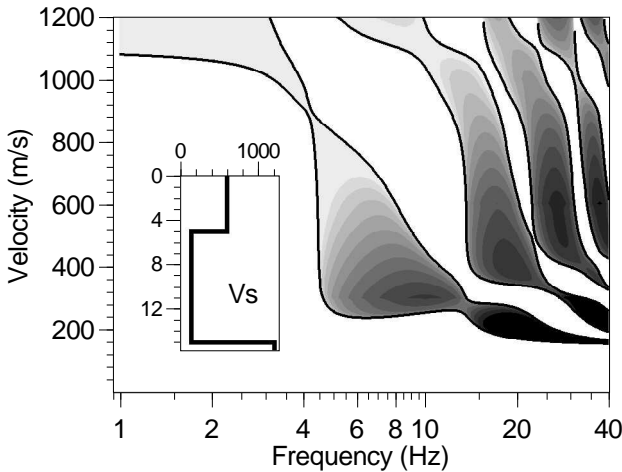


**Figure 3.7:** Dispersion curve of a model with a LVZ.

the dispersion curve may show one or more extrema. The validity of the preceding sample is checked by searching a hypothetical additional mode at a lower velocity (in the reverse direction of the initial search with the same step). If any additional mode is found, it proves that mode jumping occurred and computation is restarted. For those models with LVZ, the computation of dispersion curves may fail for all step sizes, even if the number of admitted restarts were infinite. Hence, some LVZs are tolerated in this implementation but not all of them. For some of them, the correct determination of the modal curve may require a denser frequency sampling

(user input). In this latter case, a more refined technique should try to calculate the root at an intermediate frequency.

### End-point check

For the fundamental mode, the velocity has to be lower than  $V_{s,max}$ , even for Love waves. When it is equal, it generally results from a mode jumping taking place at a higher frequency. For the higher modes, the  $V_{s,max}$  value is obtained when reaching the frequency threshold below which the mode does not exist. For all modes, the last point (at the lowest frequency) is checked by searching a hypothetical additional mode at a lower velocity (in the reverse direction of the initial search with the same step). If any root is encountered between the higher bound of the preceding mode and the lower bound of the last sample of the current mode, it means that at least one mode is missing. Unlike Herrmann's code, the root search and root refinement are always preserving the upper and lower limits of the roots. In this way, there is absolutely no risk to confuse the search result with the previously calculated modes. This check assumes that the distance between modes is changing along the frequency axis. When there are two osculation points with one located at the lowest frequency of the user range, this algorithm may however fail to detect any mode jumping. For the Rayleigh fundamental mode, there is absolutely not risk of such phenomena, if the user frequency range extends to a sufficiently low

frequency, for instance, below the threshold frequency of the first higher mode.

### 3.1.7 Misfit

The misfit is a value that represents the distance between a calculated dispersion curve and an experimental curve. If the data curve is affected by an uncertainty estimate, the misfit is given by:

$$misfit = \sqrt{\sum_{i=1}^{n_F} \frac{(x_{di} - x_{ci})^2}{\sigma_i^2 n_F}} \quad (3.38)$$

where  $x_{di}$  is the velocity of data curve at frequency  $f_i$ ,  $x_{ci}$  is the velocity of calculated curve at frequency  $f_i$ ,  $\sigma_i$  is the uncertainty of the frequency samples considered,  $n_F$  is the number of frequency samples considered. If no uncertainty is provided,  $\sigma_i$  is replaced by  $x_{di}$  in equation (3.38).

When various modes are observed and clearly identified, the inversion of all modes requires a multi-modal misfit. The sum in equation (3.38) is extended to all samples available for all modes. For higher modes, the curves may be defined over a restricted frequency range. Hence, it is not always possible to calculate a theoretical dispersion curve for some experimental samples. If the calculated one-dimensional model is close to the real one, the valid ranges of higher modes are similar and the number of experimental samples is equal to the number of calculated samples. To force both curves to be defined in the same frequency range, the misfit is multiplied by a factor equal to

$$misfit = misfit * (1 + n_{experimental} - n_{calculated}) \quad (3.39)$$

$n_{experimental}$  being the number of available samples for each curve ( $n_{experimental} \geq n_{calculated}$ ).

### 3.1.8 Sensitivity of the dispersion against layer parameters

Four parameters characterize each layer: the thickness,  $V_p$ ,  $V_s$  and the density ( $\rho$ ).  $V_s$  is the most influent parameter (e.g. Xia et al. 2003). It varies from 0 in fluids to 3500 m/s in earth superficial crust (Reynolds 1997).  $V_p$  does not influence Love-dispersion curves and has sometimes a non-negligible influence on Rayleigh-dispersion curve (see below). The natural values are between 100 to 7000 m/s (Reynolds 1997).  $V_s$  and  $V_p$  are linked by Poisson's ratio defined by

$$\nu = \frac{2V_s^2 - V_p^2}{2(V_s^2 - V_p^2)} \quad (3.40)$$

Poisson's ratio is always between 0 and 0.5 (vanishing  $V_s$ ). Common geologic materials have a Poisson's ratio around 0.25. It may be greater for unconsolidated or loose sediments, reaching 0.49 in soft clays. 0.05 can be measured for Very hard rocks (Reynolds 1997). The density ( $\rho$ ) has almost no effect on the dispersion within the usual geologic values from 1 to 3 t/m<sup>3</sup>.

The effects of these parameters on the dispersion curve are detailed in the next sections for a two-layer, a three-layer and n-layer case. The naming convention is the same as in figure 3.1.

### Two-layer model

Figures 3.8 and 3.9 show the influence of  $V_{s0}$  in the case of a fixed  $V_p$  profile and of a constant Poisson's ratio, respectively. Love and Rayleigh dispersion curves ( $V_r(f)$ ) are plotted with plain and dotted lines, respectively. The models and their corresponding dispersion curves are represented by distinct grey levels. In figure 3.8, only  $V_{s0}$  is changing from 100 to 1900 m/s. Poisson's ratio varies as well because  $V_{p0}$  is held constant (written on the right). In figure 3.9, only the variations of  $V_{s0}$  are represented but  $V_{p0}$  is also changing for all models to keep a constant Poisson's ratio being 0, 0.25 and 0.45 in figure (a) to (c), respectively. Love and Rayleigh curves are monotonously decreasing with at least one inflexion point. The first derivative of Love curves has always one minimum. For Rayleigh curves, two minima and a maximum may exist in the first derivative, especially for moderate to high Poisson's ratios.  $V_s$  of the first layer changes the limit of the curves at high frequency. The limit at low frequency is not influenced by the properties of the superficial layer. The lower is Poisson's ratio and the higher is  $V_{s0}$ , bigger is the difference between Love and Rayleigh dispersion curves at high frequency, in accordance with equation (3.36) for a half-space.

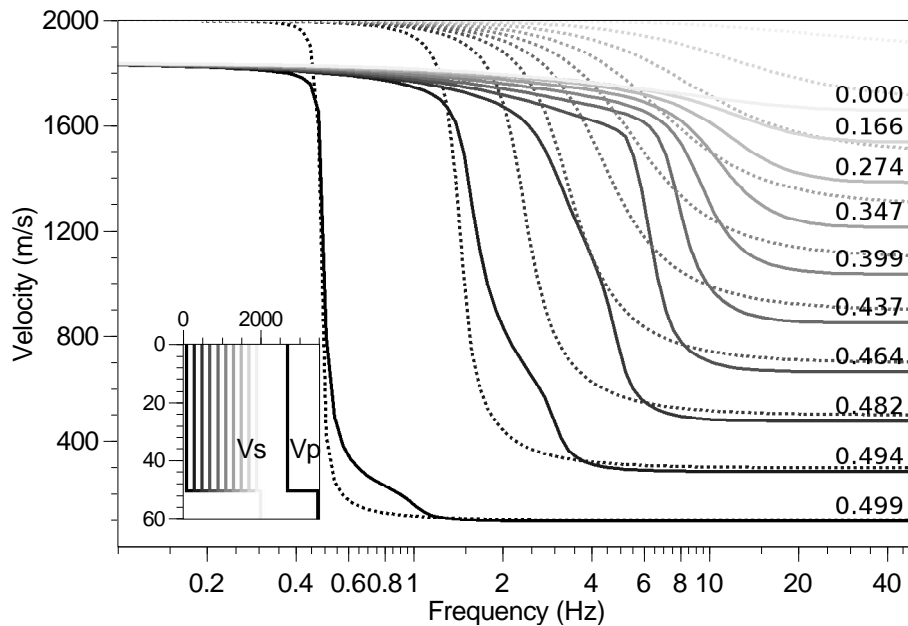


**Figure 3.8:** Influence of  $V_{s0}$  with a constant  $V_p$  profile. Rayleigh and Love fundamental modes are represented by plain and dotted lines, respectively. The values on the right are the Poisson's ratios corresponding to Rayleigh curves.  $V_{s0}$  varies from 100 to 1900 m/s.  $V_{p0}$  is 2687 m/s.  $V_{s1}$  is 2000 m/s. Poisson's ratio is 0.25 below 50 m. The density is  $2 \text{ t/m}^3$  at all depths.

In the Rayleigh case, the influence of  $V_{p0}$  is checked in figure 3.10 for two distinct  $V_{s0}$  values (200 and 1000 m/s). In both cases, Poisson's ratio varies from 0 (dark grey) to 0.45 (light grey).  $V_p$  profiles are shown in the small figure on the left. For case (a), it varies between 280 and 660 m/s, and between 1400 and 3300 m/s for case (b).  $V_p$  has apparently an impact on the dispersion curve when Poisson's ratio is less than a threshold (around 0.27 for case (a) and 0.37

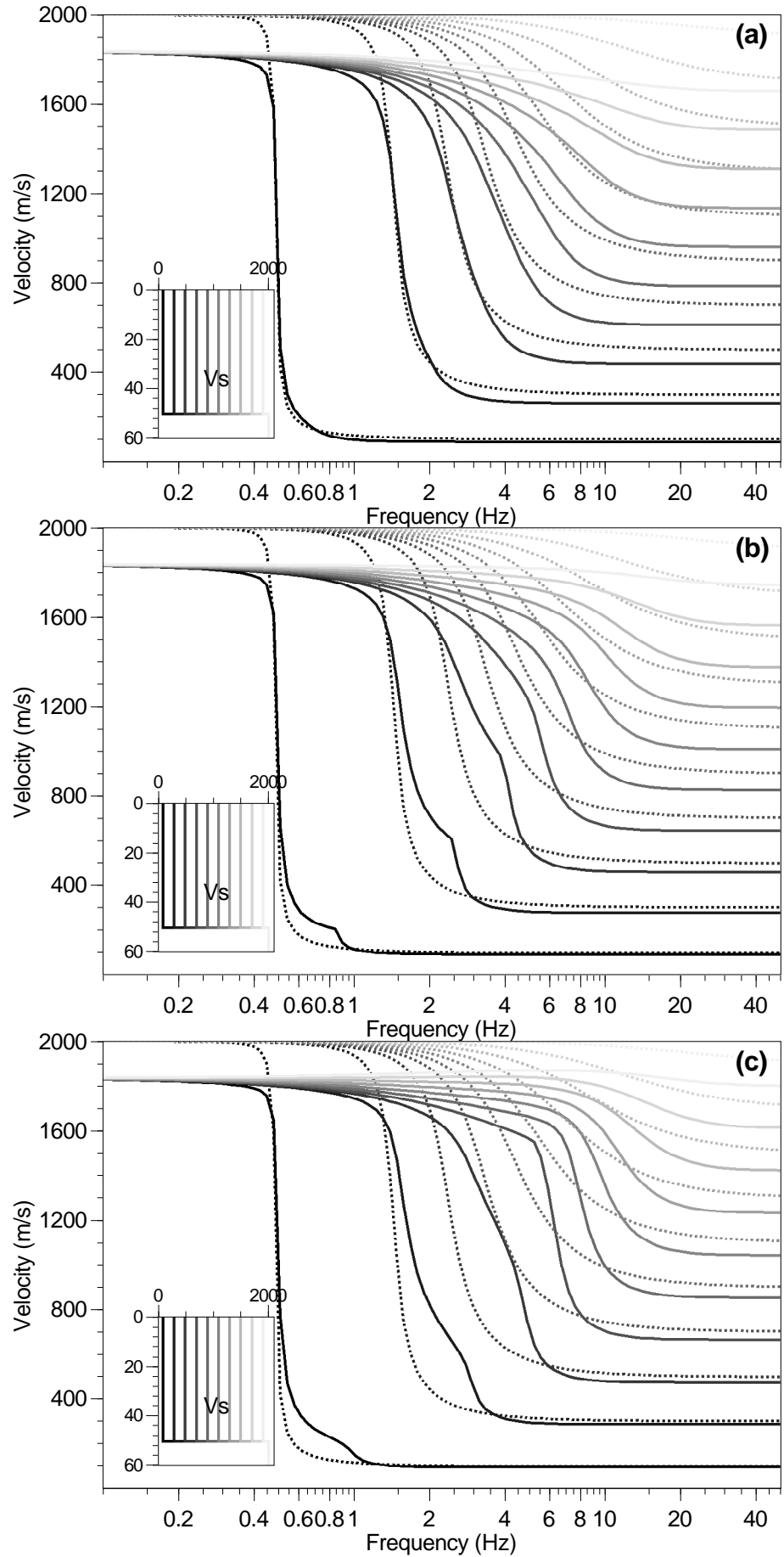


**Figure 3.9:** Influence of  $V_{s0}$  with a constant Poisson's ratio: (a)  $\nu=0$ , (b)  $\nu=0.25$ , and (c)  $\nu=0.45$ . Rayleigh and Love fundamental modes are represented by plain and dotted lines, respectively.  $V_{s0}$  varies from 100 to 1900 m/s.  $V_{s1}$  is 2000 m/s. Poisson's ratio is 0.25 below 50 m. The density is  $2 \text{ t/m}^3$  at all depths.

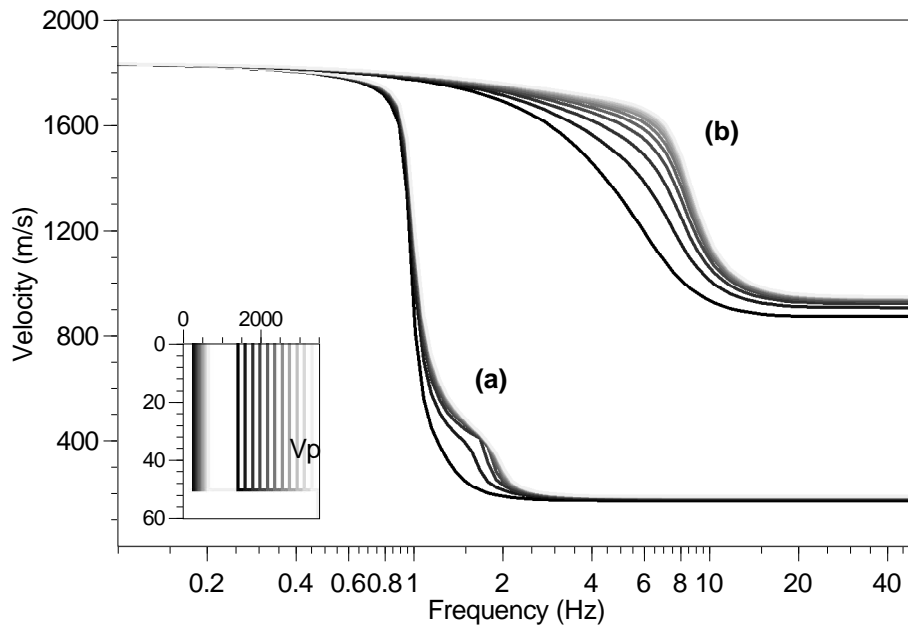


**Figure 3.10:** Influence of  $V_{p0}$  on the Rayleigh dispersion curve for two cases: (a)  $V_{s0} = 200$  m/s, and (b)  $V_{s0} = 1000$  m/s. Poisson's ratio varies from 0 (dark) to 0.45 (light). Hence,  $V_{p0}$  varies from 283 to 663 m/s (case (a)), and from 1414 to 3316 m/s (case (b)).  $V_{s1}$  is 2000 m/s. Poisson's ratio is 0.25 below 50 m. The density is  $2 \text{ t/m}^3$  at all depths.

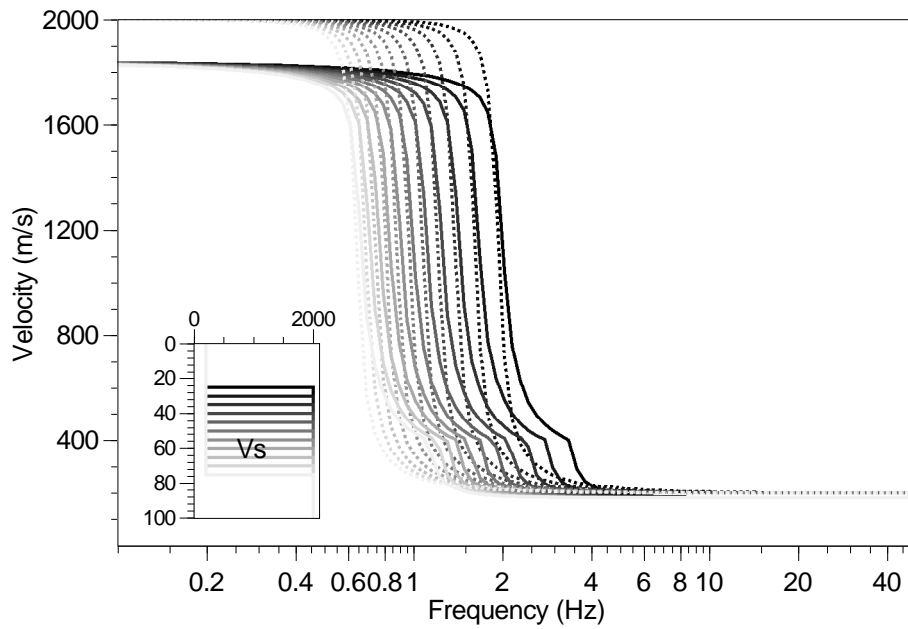


**Figure 3.11:** Influence of  $z_1$ . Rayleigh and Love fundamental modes are represented by plain and dotted lines, respectively.  $V_{s0}$  is 200 m/s.  $V_{s1}$  is 2000 m/s. Poisson's ratio is 0.25 at all depths. The density is  $2 \text{ t/m}^3$  at all depths.

for case (b)) which depends upon  $V_{s0}$ . Above this threshold,  $V_p$  loses its influence. For case (a), only three curves are well individualized, those corresponding to  $V_p$  less than 400 m/s. This conditional dependency explains that, in most cases, only a minimum of  $V_p$  can be retrieved from the inversion of dispersion curves (section 4.2).

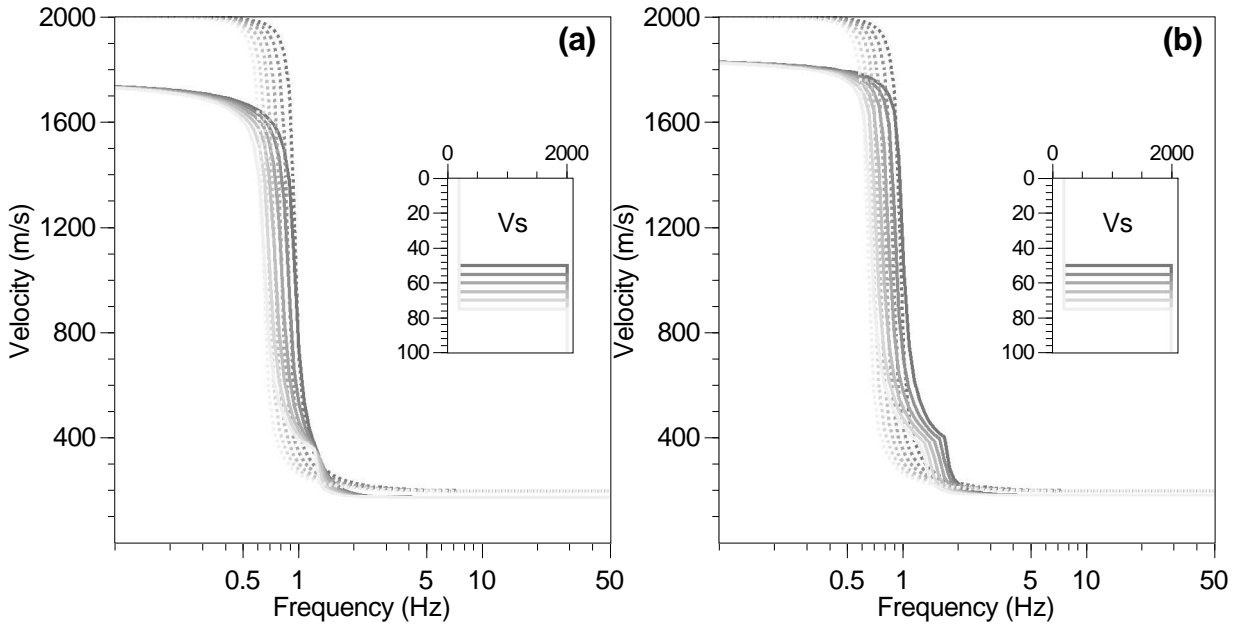


**Figure 3.12:** Influence of  $z_1$  for  $V_s$  profile. Rayleigh and Love fundamental modes are represented by plain and dotted lines, respectively.  $V_{s0}$  is 200 m/s.  $V_{s1}$  is 2000 m/s. Poisson's ratio is (a) 0.00 and (b) 0.25 above 50 m and below 75 m. The density is  $2 \text{ t/m}^3$  at all depths. The results for a Poisson's ratio of 0.45 are quite similar to those of 0.25 (not shown).

In figure 3.11, the influence of the thickness of the first layer is tested.  $V_s$  and  $V_p$  profiles are both modified by this parameter. Love and Rayleigh dispersion curves are translated in the same way when the depth is reduced. As  $V_p$  or Poisson's ratio only changes the shape of Rayleigh curves, it is likely that the effects of the thickness are mainly due to the modification of  $V_s$  profile rather than  $V_p$  profile. This is tested hereafter with figures 3.12 and 3.13.

In figure 3.12,  $V_p$  profile is held constant where  $z_1$  of  $V_s$  profile varies from 50 to 75 m. The same translation as in the general case is observed. For low Poisson's ratios, the velocity at 1.25 Hz is not affected by the changing depth. The third of the wavelength, a common rule of the thumb in surface wave analysis to map frequency scales to depth scales (Tokimatsu 1995), is about 95 m at 1.25 Hz.

In figure 3.13,  $V_s$  profile is held constant. Rayleigh dispersion curve is nearly not influenced except for low Poisson's ratio. For some other cases with higher Poisson's ratios (not shown here), the only affected part of the dispersion is the curvature close to the maximum Rayleigh velocity. Uncoupling depth limits of  $V_s$  and  $V_p$  is one of the perspectives offered by the conditional neighbourhood algorithm (section 2.4).

The density of the first layer has a low influence on the dispersion curves (either Love or Rayleigh) as shown by figure 3.14. The density is changed from 1 to  $3 \text{ t/m}^3$  with  $V_{s0}$  being 200 and 1000 m/s, case (a) and (b), respectively. The effects clearly depend upon  $V_{s0}$ .  $V_{s1}$  is the same for both cases, hence the velocity contrast is also modified between (a) and (b). The

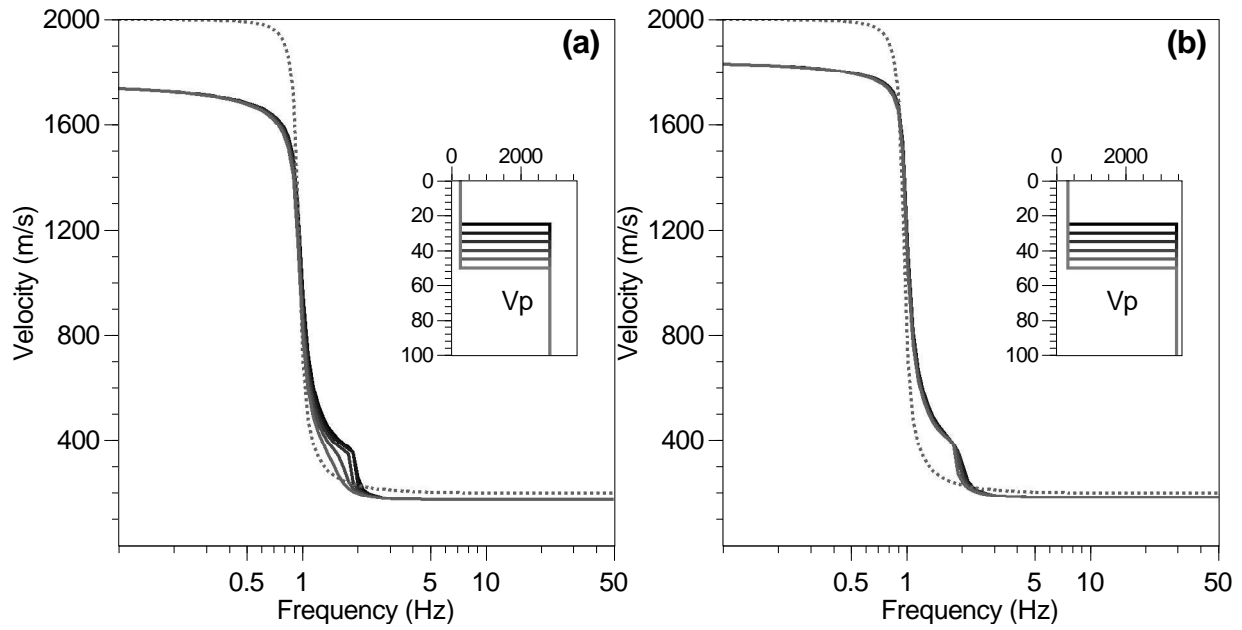


**Figure 3.13:** Influence of  $z_1$  for  $V_p$  profile. Rayleigh and Love fundamental modes are represented by plain and dotted lines, respectively.  $V_{s0}$  is 200 m/s.  $V_{s1}$  is 2000 m/s. Poisson's ratio is (a) 0.00 and (b) 0.25 above 25 m and below 50 m. The density is 2 t/m<sup>3</sup> at all depths. The results for a Poisson's ratio of 0.45 are quite similar to those of 0.25 (not shown).

effect of the density is only visible for case (b). In case (a), the density has almost no influence except around 1 Hz. Only the shape is modified, not the low and high frequency limits. The considered interval (from 1 to 3 t/m<sup>3</sup>) is probably larger than usual prior uncertainty on density. Hence, this parameter is generally fixed to a constant value during inversions of dispersion curve (section 4.2).

The same sensitivity analysis is carried out for the parameters of the bottom half-space. The influence of  $V_{s1}$  is estimated in figure 3.15.  $V_p$  profile is held constant.  $V_{s1}$  and Poisson's ratio in the bottom half space vary from 300 to 2000 m/s, and from 0.5 to 0, respectively. It acts exactly like  $V_{s0}$  replacing high by low frequencies and vice-versa. The difference between Love and Rayleigh curves at low frequency increases like  $V_{s1}$ , and it is maximum for Poisson's ratio equal to 0. Above 2 Hz, no effect can be observed. Poisson's ratio has a little effect on the shape of the dispersion between the low and high frequency limits. The magnitude of the effect is much smaller than the effect of superficial Poisson's ratio.

To corroborate this observation, the effect of  $V_{p1}$  alone is measured in figure 3.16.  $V_{s1}$  is fixed to a constant value equal to 500 m/s and 2000 m/s, for cases (a) and (b), respectively. In a similar way as for  $V_{p0}$ , all curves appear to be merged together for all  $V_{p1}$  greater than a particular threshold (around 4000 m/s for case (b)).

Finally, the influence of the density is shown in figure 3.17. Two cases are chosen with  $V_{s1}$  fixed to 500 and 2000 m/s, noted by (a) and (b), respectively. The density varies from 1 to 3 t/m<sup>3</sup>. Comparing figures 3.14 and 3.17, the densities of the first layer and of the half-space do not affect the dispersion in the same way. The last one reduces the apparent velocity when the density decreases. Like the density of the superficial layer, the interval of variation is probably larger than the prior uncertainties. Hence, the effects of  $\rho$  are generally negligible.

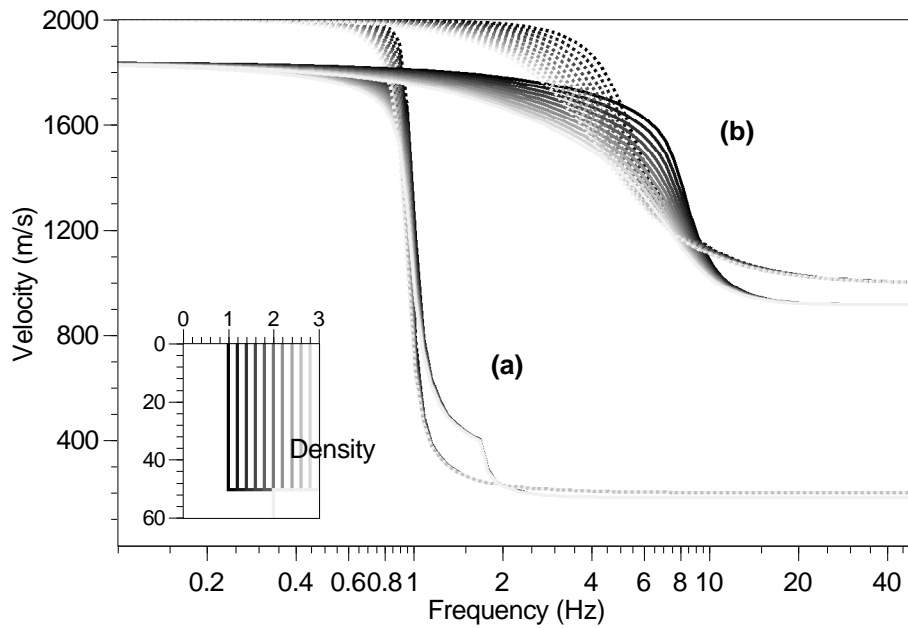


**Figure 3.14:** Influence of  $\rho_0$  for two cases: (a)  $V_{s0}=200$  m/s, and (b)  $V_{s0}=1000$  m/s. Rayleigh and Love fundamental modes are represented by plain and dotted lines, respectively.  $\rho_0$  varies from 1 to 3 t/m<sup>3</sup>.  $V_{s1}$  is 2000 m/s. Poisson's ratio is 0.25 at all depths.

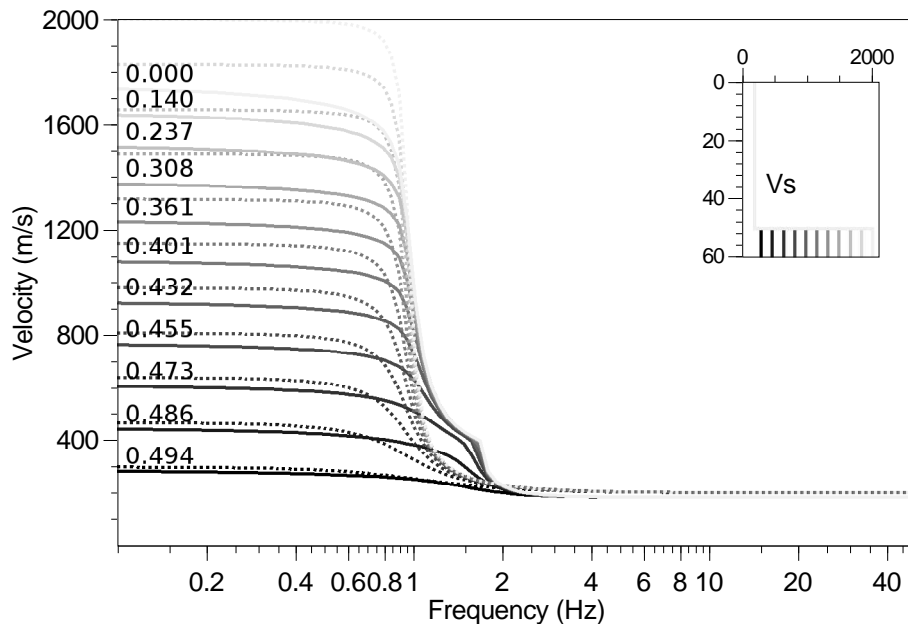


**Figure 3.15:** Influence of  $V_{s1}$  with a constant  $V_p$  profile. Rayleigh and Love fundamental modes are represented by plain and dotted lines, respectively. The values on the left are the Poisson's ratios corresponding to Rayleigh curves.  $V_{s1}$  varies from 300 to 2000 m/s.  $V_{s0}$  is 200 m/s. Poisson's ratio is 0.25 above 50 m. The density is 2 t/m<sup>3</sup> at all depths.

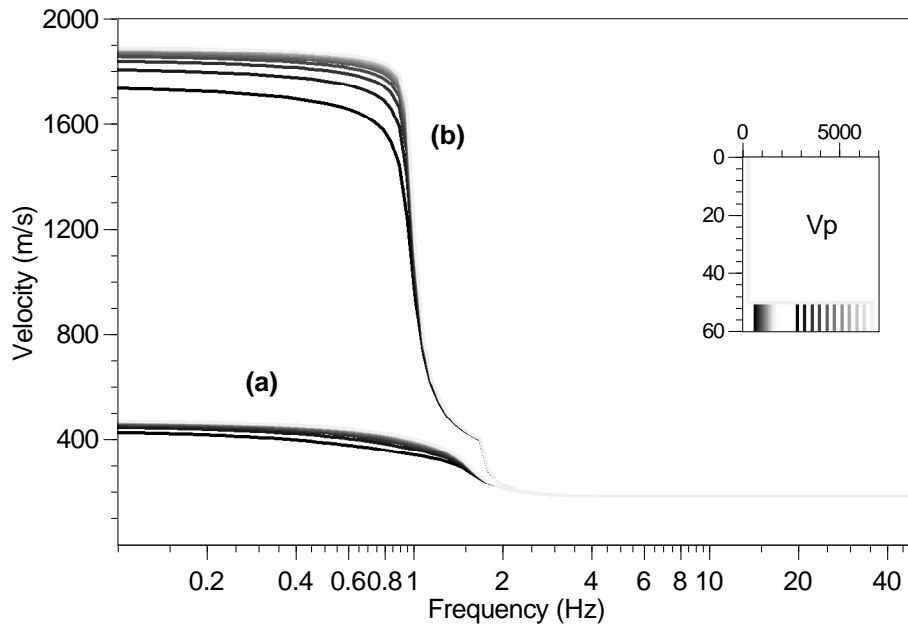


**Figure 3.16:** Influence of  $V_{p1}$  on the Rayleigh dispersion curve for two cases: (a)  $V_{s1}=500$  m/s, and (b)  $V_{s1}=2000$  m/s. Poisson's ratio varies from 0 (dark) to 0.45 (light).  $V_{s0}$  is 200 m/s. Poisson's ratio is 0.25 above 50 m. The density is 2 t/m<sup>3</sup> at all depths.

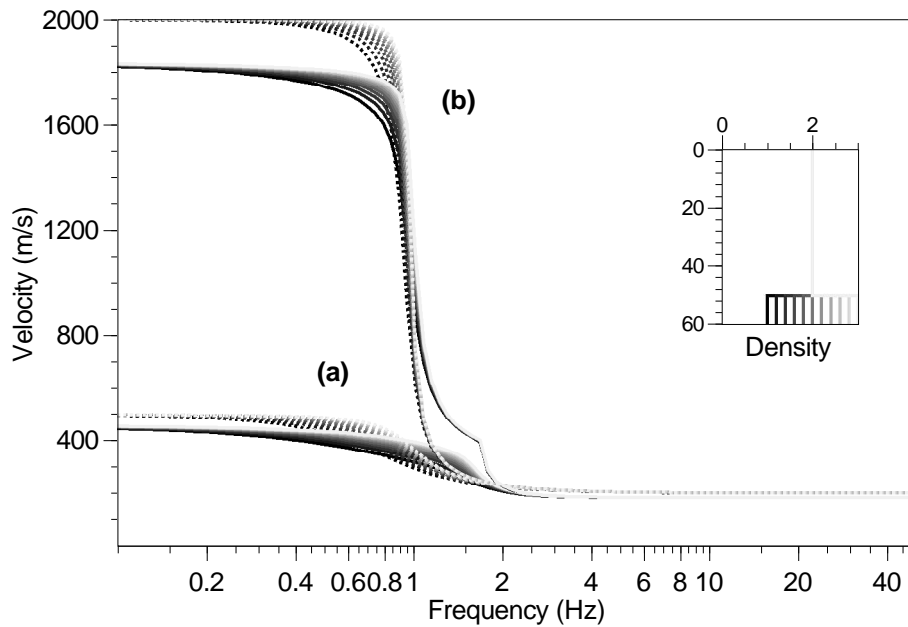


**Figure 3.17:** Influence of  $\rho_1$  for two cases: (a)  $V_{s1}=500$  m/s, and (b)  $V_{s1}=2000$  m/s. Rayleigh and Love fundamental modes are represented by plain and dotted lines, respectively.  $\rho_1$  varies from 1 to 3 t/m<sup>3</sup>.  $V_{s0}$  is 200 m/s. Poisson's ratio is 0.25 at all depths.

### Three-layer model

With this geometry, the properties of the first and the last layer (half-space) have the same effect as for the two-layer case. The influence of the intermediate layer characteristics ( $V_{s1}$ ,  $V_{p1}$ , and  $\rho_1$ ) is investigated here. First, a large variation range is tested for  $V_{s1}$ , between 100 to 2500 m/s (figure 3.18). This variation induces several types of models: a low velocity zone ( $V_{s1} < V_{s0} = 200$  m/s), a normal increase of the velocity ( $V_{s0} < V_{s1} < V_{s2}$ ), and a High Velocity Zone ( $V_{s1} > V_{s2} = 2000$  m/s).  $V_{s0}$  is fixed to 500 m/s.  $V_{s2}$  is set to 2000 m/s.  $V_p$  profiles are calculated with a Poisson's ratio of 0.25.

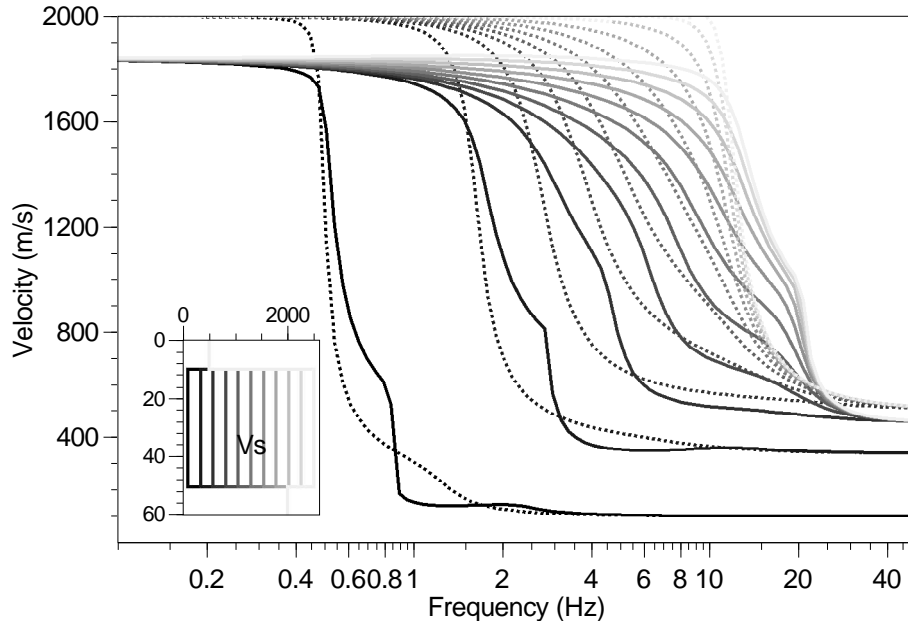


**Figure 3.18:** Influence of  $V_{s1}$  with a constant Poisson's ratio. Rayleigh and Love fundamental modes are represented by plain and dotted lines, respectively.  $V_{s1}$  varies from 100 to 2500 m/s.  $V_{s0}=500$  m/s.  $V_{s2}=2000$  m/s. Poisson's ratio is 0.25 and density is  $2 \text{ t/m}^3$  at all depths. (b) Two-layer model ( $V_s$  profile) and the corresponding dispersion curve.

#### 1. Low velocity zone

At high frequency, Love and Rayleigh waves have approximately the same velocity, which is equal to the minimum  $V_s$  of the model ( $V_{s1}$  in this case). Love curves are monotonously decreasing. On the contrary, Rayleigh curves present a small minimum. At low frequency, the effects of the low velocity zone disappear.

#### 2. Normal increase of the velocity

The general shape of the dispersion curves is very comparable with the ones for a two-layer model (figure 3.9(b), dispersion curves for the model with  $V_{s0}=500$  m/s). The only difference is the higher velocity between 6 and 30 Hz which follows the velocity increase of the second layer  $V_{s1}$ .

#### 3. High velocity zone

At high frequency, the Rayleigh curves are similar to the curves that are obtained with a two-layer model with a contrast at 10 m (figure 3.19). At low frequency, the Rayleigh

curves tend to  $V_{r,max}$  like the other classes of models. For Love, the algorithm ends with an error message. Exceptionally for a fundamental mode, the curve does not exist at all frequencies (available above 10 Hz, or for wavelengths less than 200 m). At low frequency, the first layer (10 m thick) is not "seen" by the propagating waves with a wavelength greater than 200 m. The model is equivalent to a high velocity layer overlying a half space where no real solution exists for the Love surface waves (Aki and Richards 2002, equation 7.6 calculated with complex numbers).

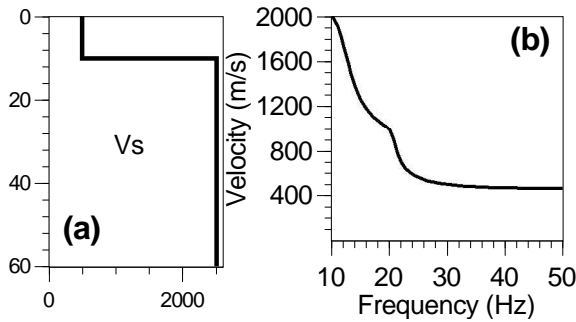


**Figure 3.19:** The light grey model in figure 3.18 is the same as in this figure between 0 and 50 m. (a)  $V_s$  profile. (b) The calculated dispersion for the two-layer model. The dispersion curves are also similar at high frequency.

The influence of  $V_{p1}$  in the intermediate layer is tested with the same model as in figure 3.10. The sediment layer is split in two in the same way as in figure 3.18 (10 and 40 m).  $V_{p1}$  in the intermediate layer of 40 m is changed, keeping other parameters constant. The results are shown in figure 3.20 with two cases for  $V_s$  between 0 and 50 m: (a)  $V_{s0} = V_{s1} = 200$  m/s, and (b)  $V_{s0} = V_{s1} = 1000$  m/s. Figures 3.20 and 3.10 are quite similar, proving that intermediate values  $V_{p1}$  also influence moderately the dispersion curve. At high frequency, in figure 3.20(b), all curves tend to same Rayleigh velocity. On the contrary, in figure 3.10(b), for low  $V_{p0}$  values, a significant influence is observed above

10 Hz. This difference is entirely due to the velocity values between 0 and 10 m, which control the Rayleigh velocity at very high frequency.

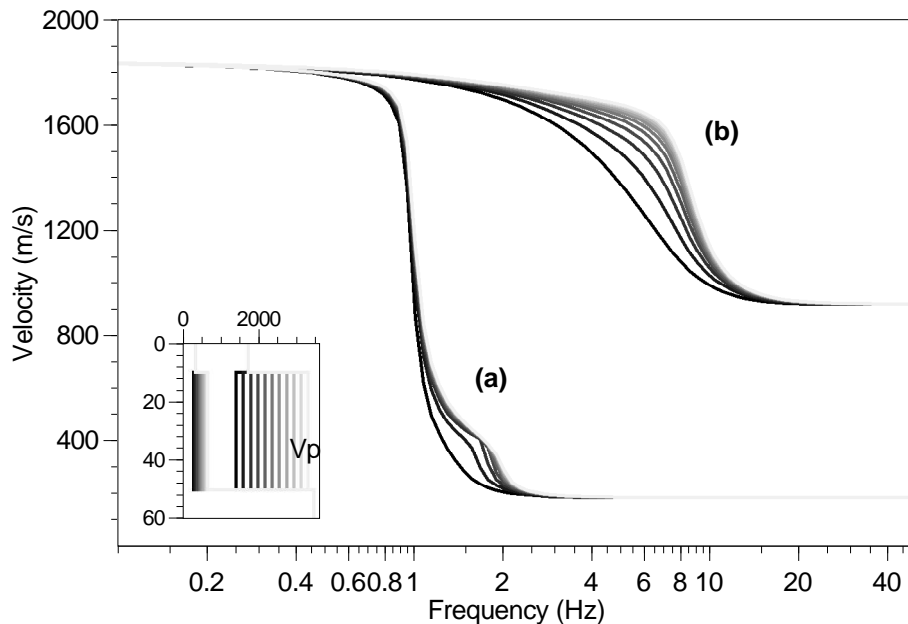


**Figure 3.20:** Influence of  $V_{p1}$  on the Rayleigh dispersion curve for two cases: (a)  $V_{s0} = V_{s1} = 200$  m/s, and (b)  $V_{s0} = V_{s1} = 1000$  m/s. Poisson's ratio varies from 0 (dark) to 0.45 (light).  $V_{s2} = 2000$  m/s. Poisson's ratio is 0.25 in first and bottom half-space. The density is  $2 \text{ t/m}^3$  at all depths.

### 3.1.9 Conclusion

An efficient and safe algorithm for calculating dispersion curves has been developed. On currently available personal computers (e.g. with a processor Athlon 2.2 GHz), the time needed to calculate one sample is about 5 microseconds for a two-layer model. If the dispersion curve of the fundamental mode is sampled with 30 points, more than 6500 models can be calculated in only one second. It has been implemented in a command line program (`os_forward`) and in an inversion tool (`os_na`). This algorithm is also exploited to calculate other spectral properties of the ground model like the ellipticity and the auto-correlation, detailed in the next sections.

## 3.2 Ellipticity

The H/V Method is a common tool used for site-effect investigations (Nogoshi and Igarashi 1970, Nakamura 1989, Bard 1998). The horizontal (H) and vertical (V) components are simultaneously recorded at one single point. The ratio of H over V generally exhibits a peak, that corresponds more or less to the fundamental frequency of the site ( $f_0 = \frac{V_s}{4h}$ , Bonnefoy 2004). However, the ambient wavefield is composed of unknown parts of body and surface waves. In the first case, the ratio is mainly influenced by  $S_H$  resonance in the superficial layers. On the other hand, if Rayleigh surface waves predominate, the theoretical ellipticity dictates the observed curves (Nogoshi and Igarashi 1970, Fäh et al. 2001, Fäh et al. 2003, Scherbaum et al. 2003). Real data peaks usually fit the frequency of the theoretical curves but the amplitude is rarely stable and reliable. Malischewsky and Scherbaum (2004) developed an analytical formulation for two-layer models. They plotted the differences of the peak frequency between the two aforementioned assumptions versus the magnitude of the velocity contrast. At intermediate and low contrasts (below a factor of 4 between  $V_{s0}$  and  $V_{s1}$ ), a drastic gap may exist between the two interpretations. In this case, Bonnefoy (2004) showed that the observed H/V peak better fits with the extrema of the  $S_H$  transfer function.

H/V spectrum contains valuable information about the underlying structure, especially a particular relationship between  $V_s$  of the sediments and their thickness (Boore and Toksöz 1969, Scherbaum et al. 2003). Because the absolute amplitude of the curve cannot be directly compared to the amplitude of the  $S_H$  transfer function or the ellipticity, only the frequency of the peak is considered here. Some preliminary tests showed that using ellipticity amplitude offers a very good constraint even on  $V_p$  profile. However, wrong assumptions on the amplitude also lead to completely biased results. Nevertheless, Fäh et al. (2003) invert the amplitude between the peak and the trough by means of assumptions about the energy partition between Love, Rayleigh and body waves. This alternative has been discarded during our work. The next sections focused on how to calculate the ellipticity of Rayleigh waves and how to calculate the exact frequencies of the peaks.

### 3.2.1 Computation

The ellipticity is defined by the ratio  $\frac{r_1(z_0)}{r_2(z_0)}$  where  $r_1(z_0)$  and  $r_2(z_0)$  are the factors appearing in equation (3.24). This ratio can be calculated from the terms of matrix  $R(z_0)$  as shown by equation (3.35). As detailed in section 3.1.4, the matrix  $R(z)$  is never completely calculated during the dispersion curve computation and values of  $r_{12}(z_0)$  and  $r_{11}(z_0)$  are not available. However, it is possible to calculate the ratio  $\frac{r_{12}(z_0)}{r_{11}(z_0)}$  from sub-determinants  $r(z_0) \begin{vmatrix} 1 & 2 \\ a & b \end{vmatrix}$  as shown here below.

From the computation of the dispersion curve we know that  $r(z_0) \begin{vmatrix} 1 & 2 \\ 1 & 2 \end{vmatrix} \approx 0$ . The approximation comes from the fact that the dispersion curve is solved numerically with a finite precision. Here, the problem is assumed to be perfectly solved, and the approximation is dropped in the following equations. For simplicity, the  $z_0$  dependency is also dropped

$$\begin{aligned} r_{11}r_{22} &= r_{12}r_{21} \\ r \begin{vmatrix} 1 & 2 \\ 1 & 3 \end{vmatrix} &= r_{11}r_{23} - r_{13}r_{21} \\ ir \begin{vmatrix} 1 & 2 \\ 1 & 4 \end{vmatrix} &= r_{12}r_{23} - r_{13}r_{22} \end{aligned} \quad (3.41)$$

It is useful to mention that  $r \begin{vmatrix} 1 & 2 \\ 1 & 4 \end{vmatrix}$  is imaginary as demonstrated by equation (3.35). We multiplied by  $i$  as a real value is internally computed. The solution of the system of equations (3.41) is

$$\frac{r_1(z_0)}{r_2(z_0)} = \frac{r_{12}(z_0)}{r_{11}(z_0)} = i \frac{r \begin{vmatrix} 1 & 2 \\ 1 & 4 \end{vmatrix}}{r \begin{vmatrix} 1 & 2 \\ 1 & 3 \end{vmatrix}} \quad (3.42)$$

Thus, for elastic waves in a layered model, this ratio is an imaginary number either positive (prograde) or negative (retrograde). These terms come from the analogy between a rolling ball and the particle motion

For a half space, using equation (3.31), the classical formula is obtained (Tokimatsu 1995):

$$\frac{r_1(z_0)}{r_2(z_0)} = i \frac{k(l_n - 2k_n h_n)}{h_n(l_n - 2k^2)} = -i \frac{2k_n k}{l_n} = -2i \frac{\sqrt{1 - (V_r/V_s)^2}}{2 - (V_r/V_s)^2} \quad (3.43)$$

It is always a negative imaginary number and  $r_1(z_0)$  and  $r_2(z_0)$  are out of phase by  $90^\circ$  with each other. The particle motion at the surface is then always retrograde elliptical for a half space. In general, only the real absolute amplitude of the ellipticity is shown on a log-log plot.

Equation (3.42) proves that the ellipticity can be calculated at a very low cost once the dispersion has been correctly computed. However, the results are stable and reliable only if

the dispersion problem (equation (3.34)) is sufficiently solved. Taking into account the error, equation (3.42) transforms into

$$\frac{r_1(z_0)}{r_2(z_0)} = i \frac{r \begin{vmatrix} 1 & 2 \\ 1 & 4 \end{vmatrix}}{r \begin{vmatrix} 1 & 2 \\ 1 & 3 \end{vmatrix}} + e \frac{r_{13}(z_0)}{r_{11}(z_0)r \begin{vmatrix} 1 & 2 \\ 1 & 3 \end{vmatrix}} \quad (3.44)$$

where  $e$  is the remainder of equation (3.34). Its magnitude is not constant because the iterations of the root search algorithm are stopped when the Rayleigh slowness (or the velocity) is estimated with a relative precision of  $10^{-7}$ . No test are performed on the absolute value of the remainder. Calculating the error on the ellipticity value is never done because the total error depends upon particular terms of matrix  $R(z_0)$ , not fully computed here. In most cases, experience has proved that the problem is sufficiently solved with a  $10^{-7}$  relative precision on the dispersion curve. An exception to this rule is shown in the next section for a three-layer model where a  $10^{-50}$  relative precision is necessary. Such computations are possible with numbers having more than 50 significant digits handled by the ARPREC library (Bailey 2004).

In contrast to section 3.1.7, the misfit computation is presented after the sensitivity study because a better understanding of the particular shape of the ellipticity curve is necessary to define the misfit.

### 3.2.2 Sensitivity

For a two-layer model the influence of  $V_{s0}$  is shown in figures 3.21 and 3.22, for a constant  $V_p$  profile and a fixed Poisson's ratio, respectively. Hence, the ellipticity of a two-layer model has in most cases a root (at 1 Hz for the darkest curve) and a singular point (the maximum at 0.5 Hz for the darkest curve) but it is not always true as demonstrated in figure 3.22. Even for a two-layer model, a secondary maximum may be encountered (at 0.8 and 2.2 Hz in figure 3.22). There is always one frequency band (narrow or large) where the ellipticity is maximum.

When the number of layers increases, several singularities are sometimes observed but it is not a constant feature. Figure 3.23 illustrates the variation of the ellipticity with  $V_s$  of the intermediate layer for a three-layer case. At high frequency for the darkest model (with  $V_{s1}$  being 100 m/s), usual precision is not sufficient to achieve a correct computation of the ellipticity curve. An experimental algorithm with high precision arithmetics has been developed for this particular case. A striking feature of the ellipticity curve of the two darkest models of figure 3.23, both having a thin hard ground at the surface, is that the ellipticity ratio at high frequency does not tend to the value predicted by equation (3.43). All other models follow equation (3.43) at high frequency. Physically, this could be explained by the trapping of energy within the intermediate layer which alters the classical development of surface waves.

Scherbaum et al. (2003) showed for a two-layer model that an inversion of the frequency of the main peak can bring valuable information. The generalisation to  $n$  layers is not straight-

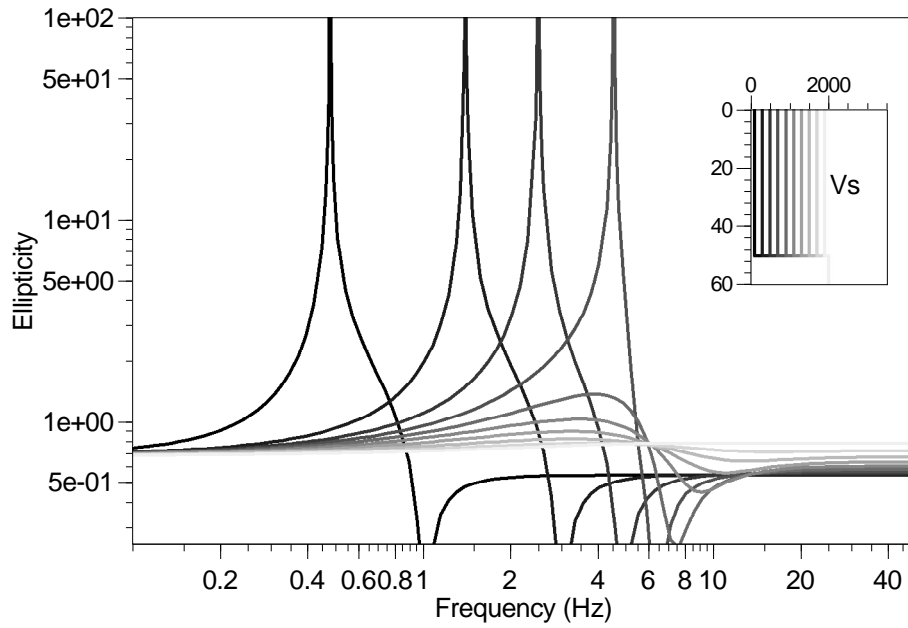


**Figure 3.21:** Influence of  $V_{s0}$  with a constant  $V_p$  profile.  $V_{s0}$  varies from 100 to 1900 m/s.  $V_{p0}$  is 2687 m/s hence, Poisson's ratio varies from 0.499 (dark) to 0 (light) like in figure 3.8.  $V_{s1}$  is 2000 m/s. Poisson's ratio is 0.25 below 50 m. The density is  $2 \text{ t/m}^3$  at all depths.

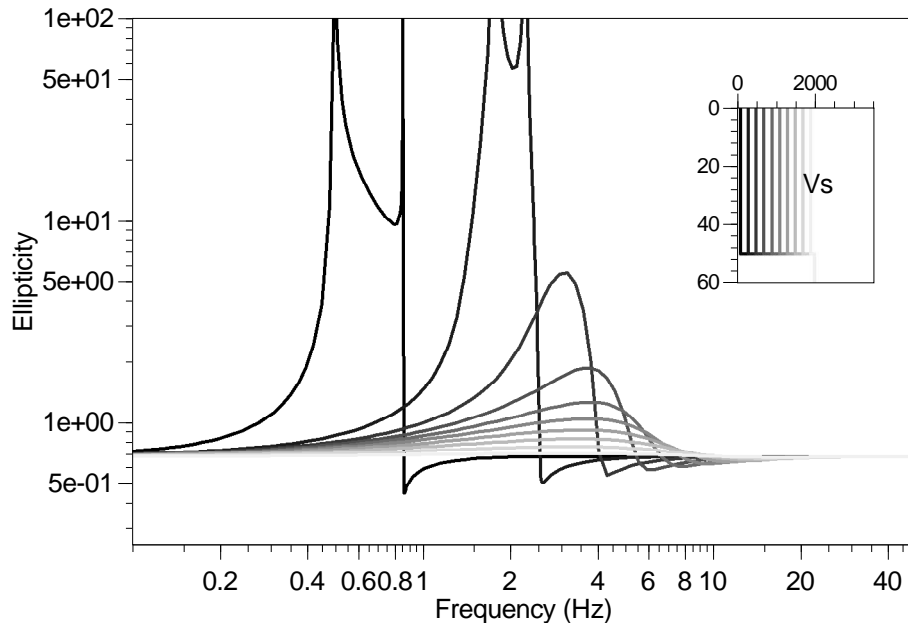


**Figure 3.22:** Influence of  $V_{s0}$  with a constant Poisson's ratio.  $V_{s0}$  varies from 100 to 1900 m/s.  $V_{s1}$  is 2000 m/s. Poisson's ratio is 0.25 and the density is  $2 \text{ t/m}^3$  at all depths.

forward because the shape of the ellipticity curve appears to be very sensitive to the model parameters. In this context, the determination of the frequency of the main peak is not univocal in all cases even for the simplest models. Also, the inversion of the absolute amplitude of the experimental H/V curves with the Rayleigh fundamental ellipticity in the general case of  $n$  layers may not be reliable. If experimental H/V curves may present several peaks, there is no strong evidence of a relationship between those real peaks and the various peaks of the fundamental Rayleigh curve. The ellipticity of the higher modes or body wave resonance may be also suspected. Without a clear agreement on the physical model to explain multiple peaks of the experimental H/V curves, a conservative option, detailed in the next section, is kept to avoid the introduction biased prior information.

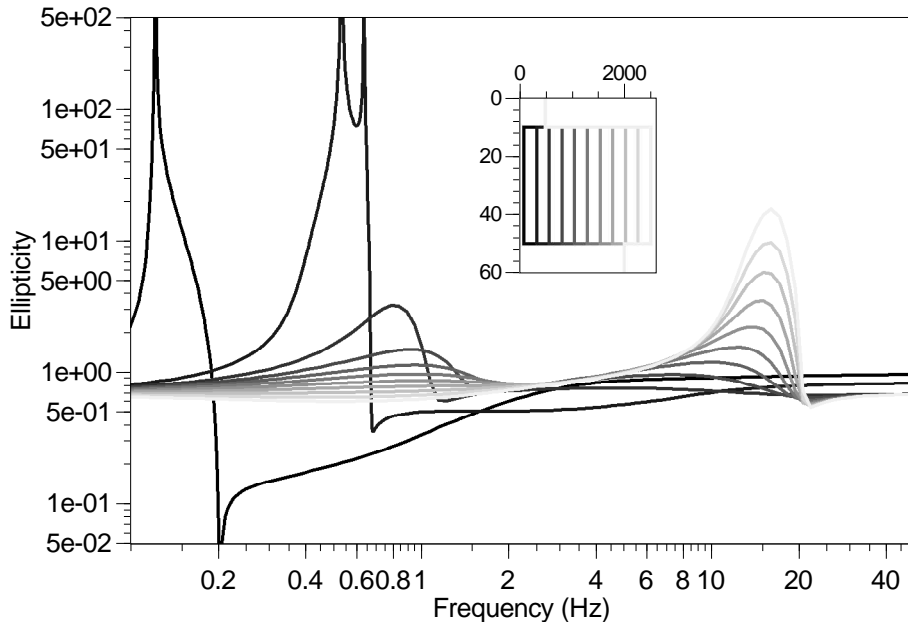


**Figure 3.23:** Influence of  $V_{s1}$  with a constant Poisson's ratio.  $V_{s1}$  varies from 100 to 2500 m/s.  $V_{s0}=200$  m/s.  $V_{s2}=2000$  m/s. Poisson's ratio is 0.25 and the density is  $2 \text{ t/m}^3$  at all depths.

### 3.2.3 Misfit

The misfit of the ellipticity is defined by

$$misfit = \frac{(f_0)_{experimental} - (f_0)_{calculated}}{(df_0)_{experimental}} \quad (3.45)$$

where  $f_0$  is the frequency of the peak, and  $(df_0)_{experimental}$  is the standard deviation of the experimental frequency peak. In case of a joint inversion of the dispersion curve and the frequency peak of the ellipticity, the two misfits are combined with the following relation

$$(misfit)_{global} = (1 - \alpha)(misfit)_{dispersion} + \alpha(misfit)_{ellipticity} \quad (3.46)$$

From the implementation point of view,  $(f_0)_{calculated}$  is not computed easily. For each sample point of the ellipticity curve, it is necessary to calculate the corresponding sample points of the

dispersion curve. Hence, for a first estimate of  $(f_0)_{\text{calculated}}$ , only the user frequency samples are used. Calculating the misfit with this first approach leads to a misfit which highly depends upon the arbitrary user frequency samples. A more robust algorithm must be able to calculate the exact frequency of the peak (down to a reasonable precision,  $10^{-3}$  Hz by default). The peak sampling is refined with a three-point scheme. Because of the local continuity of the ellipticity curve, if  $ell_i$  is the maximum of the sampled curve, the true maximum is always located between  $ell_{i-1}$  and  $ell_{i+1}$ . A new sample is added between  $ell_{i-1}$  and  $ell_i$ , or  $ell_i$  and  $ell_{i+1}$ . The largest interval is always chosen in order to balance the sampling rate around the true peak. For each supplementary sample, the dispersion curve is re-calculated. In the new subset made of the four samples, the absolute maximum is searched and the same processing is performed until bracketing the true peak with a sufficient precision.

Additionally, when various peaks are present in the user frequency range, the same processing must be conducted for each relative maximum. A set of several  $(f_0)_{\text{calculated},i}$  is thus obtained. Due to the lack of general agreement on the signification of multiple experimental H/V peaks, only the main one is kept for inversion. The misfit value is calculated with  $(f_0)_{\text{calculated},i}$  which gives the lowest misfit.

### 3.3 Spatial auto-correlation

The spatial auto-correlation method was first proposed by Aki (1957) for horizontally propagating waves. The case of pure Rayleigh waves measured on the vertical components is considered in this work.

#### 3.3.1 Computation

Assuming a unique phase velocity per frequency and the stationarity of the noise wavefield both in time and space, Aki (1957) demonstrated that the correlation of the signals recorded at two stations separated by distance  $r$  can be written :

$$\overline{\rho(r, \omega)} = J_0 \left( \frac{\omega r}{c(\omega)} \right) \quad (3.47)$$

where,  $\bar{\rho}$  is the azimuthal average of the correlation ratio  $\rho(r, \omega) = \frac{\phi(r, \omega)}{\phi(0, \omega)}$ ,  $c(\omega)$  is the phase velocity at angular frequency  $\omega$ , and  $J_n$  is the Bessel function of the order  $n$ .

$$\phi(r, \omega) = \frac{1}{T} \int_0^T v_0(t) v_r(t) dt$$

where  $v_0(t)$  and  $v_r(t)$  are the recorded signals at two stations separated by distance  $r$ .

Equation (3.47) is valid for the vertical component. Corresponding and more complex formulae exist for the horizontal components of the surface waves (Metaxian 1994, Bettig et al. 2001).

An example of a typical station layout is given in figure 3.24(a) for an array with an aperture

of about 100 m. The irregular shape is generally induced by natural obstacles or artificial structures (trees, streets, buildings, ...). The end points of the vectors joining all pairs of stations are plotted on figure 3.24(b). For such an imperfect array, it is not possible to calculate an azimuthal average for one single distance. The solution proposed by Bettig et al. (2001) is to group pairs of stations along rings of finite thicknesses, as the pairs of grey circles drawn in figure 3.24(b). Equation (3.47) can be modified to allow the calculation of average ratios over a ring between  $r_1$  and  $r_2$ .

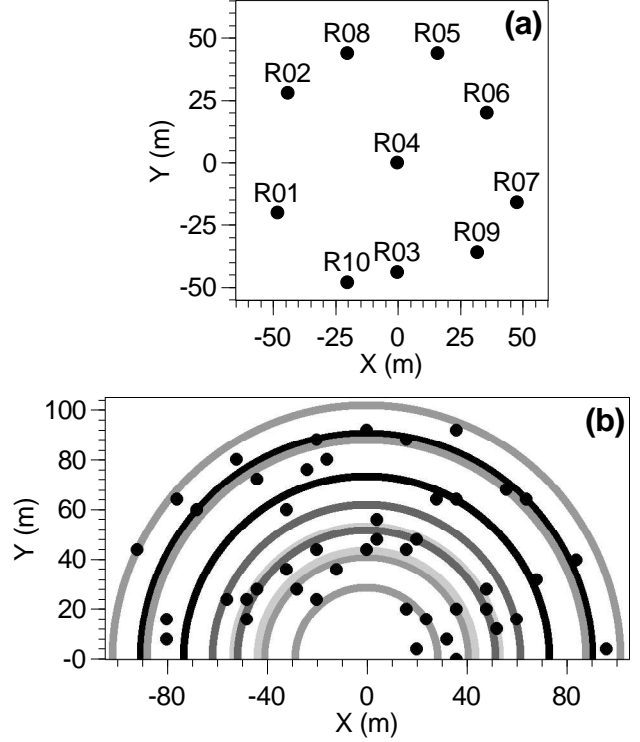


**Figure 3.24:** (a) Map of sensor locations for a typical array of 10 stations. (b) Azimuth-inter-distance plot: each dot represents one couple of stations. The pairs of grey circles show the limits that may be chosen for rings of SPAC computation.

$$\overline{\rho_{r_1, r_2}(\omega)} = \frac{2}{r_2^2 - r_1^2} \frac{c(\omega)}{\omega} \left[ r_2 J_1 \left( \frac{\omega r_2}{c(\omega)} \right) - r_1 J_1 \left( \frac{\omega r_1}{c(\omega)} \right) \right] \quad (3.48)$$

Equation (3.48) has the same general shape as equation (3.47) and is strictly equal if  $r_1$  tends to  $r_2$ . In the following, we will refer to equation (3.47) for the sake of simplicity.

### 3.3.2 Misfit

The misfit is evaluated for all data samples. It is defined in the same way as for the dispersion curve inversion (equation (3.38) and Wathelet et al. 2004), taking into account the standard deviation observed for each spatial auto-correlation sample :

$$misfit = \sqrt{\frac{1}{\sum_{k=1}^{n_R} n_{Fk}} \sum_{i=1}^{n_R} \sum_{j=1}^{n_{Fi}} \frac{(\rho_{dij} - \rho_{cij})^2}{\sigma_{ij}^2}} \quad (3.49)$$

where,  $\rho_{dij}$  is the SPAC ratio of data curves at frequency  $f_j$  and for ring  $i$  which is defined by all inter-station distances between  $r_{i1}$  and  $r_{i2}$ ,  $\rho_{cij}$  is the SPAC ratio of calculated curves at frequency  $f_j$  and for ring  $i$ ,  $\sigma_{ij}$  is the observed variance for the sample at frequency  $f_j$  and for

ring  $i$ ,  $n_R$  is the number of rings considered, and  $n_{Fi}$  is the number of frequency samples for ring  $i$ .

As for dispersion curves, the implemented algorithm can calculate a misfit for a set of modal curves by including the contributions of all modes in the sum of equation (3.49). The technique described in section 3.1.7 is also used for higher modes with a limited valid frequency band. Options exist to restrict the misfit computation to the first decreasing part of the auto-correlation curve (argument of Bessel's function less than 3.2) and to avoid the part of the curves close to 1 (argument of Bessel's function greater than 0.4). In this case, even the fundamental mode may have a restricted valid frequency interval for which the misfit is corrected in the same way as for higher modes. However, experience has proved that those options are generally useless and that the whole frequency range can be used for inversion (section 5.2).

### 3.3.3 Sensitivity

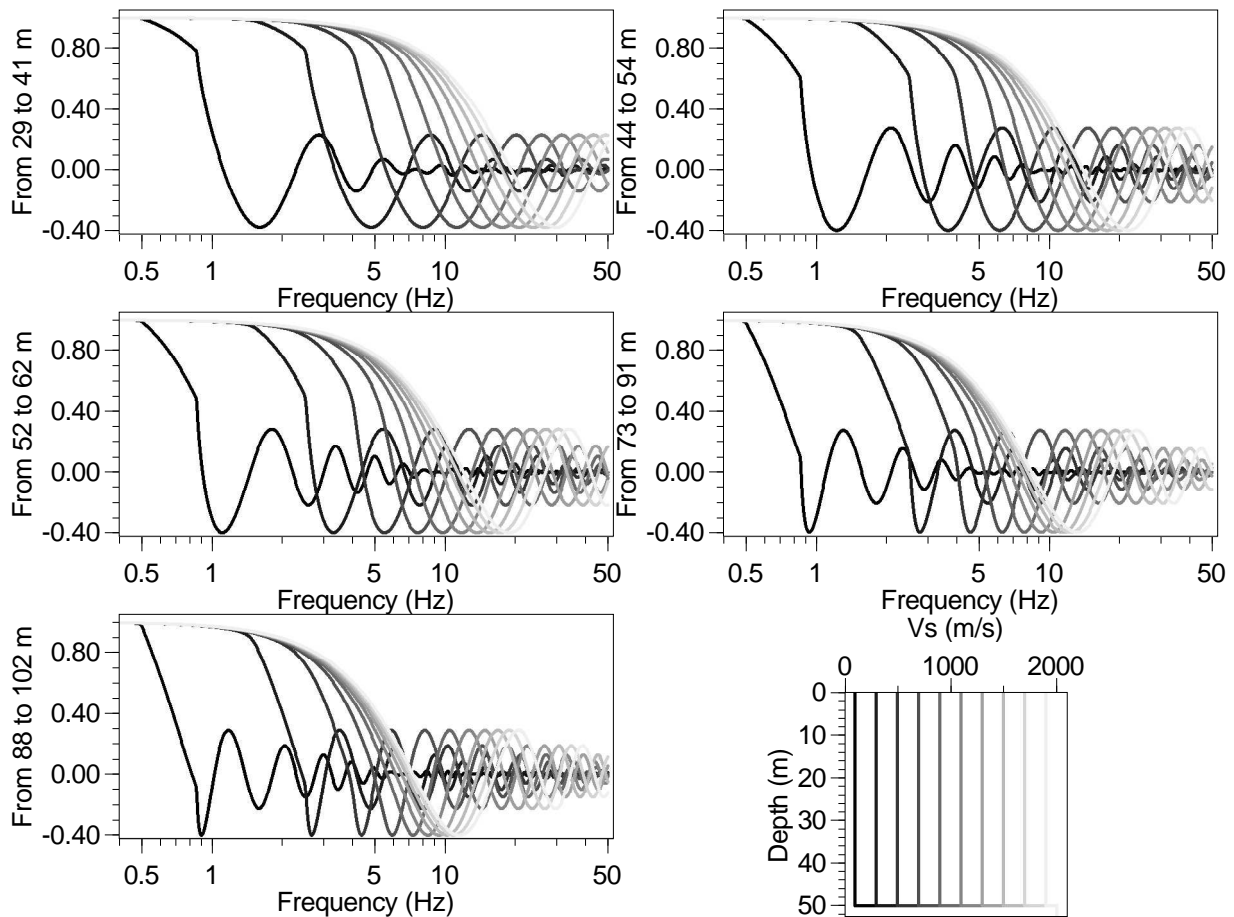


**Figure 3.25:** Influence of  $V_{s0}$  with a constant Poisson's ratio.  $V_{s0}$  varies from 100 to 1900 m/s.  $V_{s1}$  is 2000 m/s. Poisson's ratio is 0.25 and the density is  $2 \text{ t/m}^3$  at all depths.

The case of figure 3.9(b) is taken as an example. Thus, Poisson's ratio is 0.25, and  $V_{s0}$  varies from 100 to 1900 m/s. The auto-correlation curves are calculated for all rings described in figure 3.24(b) with equation 3.48. The results are plotted in figure 3.25. All curves are between -0.4 and 1, converging towards 1 for low frequencies, and oscillating around zero for

high frequencies. The shapes observed for the dispersion curves are transposed to the auto-correlation, for instance, the strong variation in the slope at 0.9 Hz for the darkest curve. A translation towards higher velocities on the dispersion curve appears as a translation of the first minimum of the auto-correlation curve towards a higher frequency.

### 3.4 Conclusion

A robust and fast dispersion curve algorithm for one-dimensional models is developed and tested in representative cases. However, the sensitivity study carried in this chapter is far from being exhaustive. The objective is limited to the determination of the significant parameters which might be inverted. Traditionally,  $V_s$  is the only one parameter included in the inversion of dispersion curves. Nevertheless, this work demonstrates that, in some cases,  $V_p$  has also a non negligible influence. The ellipticity and the auto-correlation curves can be easily computed as well. For each spectral property, a misfit function is defined. These forward algorithms can be used in a non-linear and stochastic inversion such as the neighbourhood algorithm (chapter 4).

# Chapter 4

## Parameterization of a ground model

The inversion principles are presented in chapter 2 as well as the particular method used in this work: the neighbourhood algorithm. Chapter 3 details the computation of dispersion, ellipticity and auto-correlation curves for a one-dimensional ground model, as well as the misfit calculation in each case. To perform an inversion of experimental data, it is also necessary to identify the physical unknowns of the problem. For most of the stochastic inversion methods, models are characterized by a set of uniform random deviates between 0 and 1. The objective of this chapter is to investigate the possible alternatives for transforming those random vectors into physical parameters of a one-dimensional ground model. In a first approach, it can be seen as a scaling of the interval  $[0, 1]$  to the prior uncertainty of a particular layer property. But things become more complicated when some combinations of parameter values are not physically acceptable. This problem is analysed in the first section. The efficiency of the inversion algorithm decreases with the number of parameters. When the number of layers increases, low velocity zones are likely to be present in the generated profiles. The second section reviews the problems encountered with models with a great number of layers. The third section proposes various solutions to handle velocity variations with a reduced number of parameters.

### 4.1 Theoretical model used in parameterization tests

During this work, numerous ground models and parameterizations have been tried while developing the inversion software. In the next sections, the influence of the parameterization is illustrated through inversion examples with a common reference ground model. This latter one is made of three layers including the bottom half space. The properties of each layer are specified in table 4.1. The velocity profiles, the dispersion and the ellipticity curves are shown in figure 4.1.

The fundamental Rayleigh curve of figure 4.1(b) is considered in the next section as the data curve that would have been obtained by any of the experimental methods presented in chapter 1. Various inversion schemes are tried to retrieve the original velocity profiles. The other curves are used in chapter 5 where more specialized inversions are reviewed.

Contrary to synthetic curves that can be calculated on any arbitrary frequency interval, the experimental curves are generally available on a restricted frequency band. Because there is a close relation between the depth and the signal frequency content (section 3.1.8), the quality of inversion strongly depends upon the frequency range of the measured dispersion

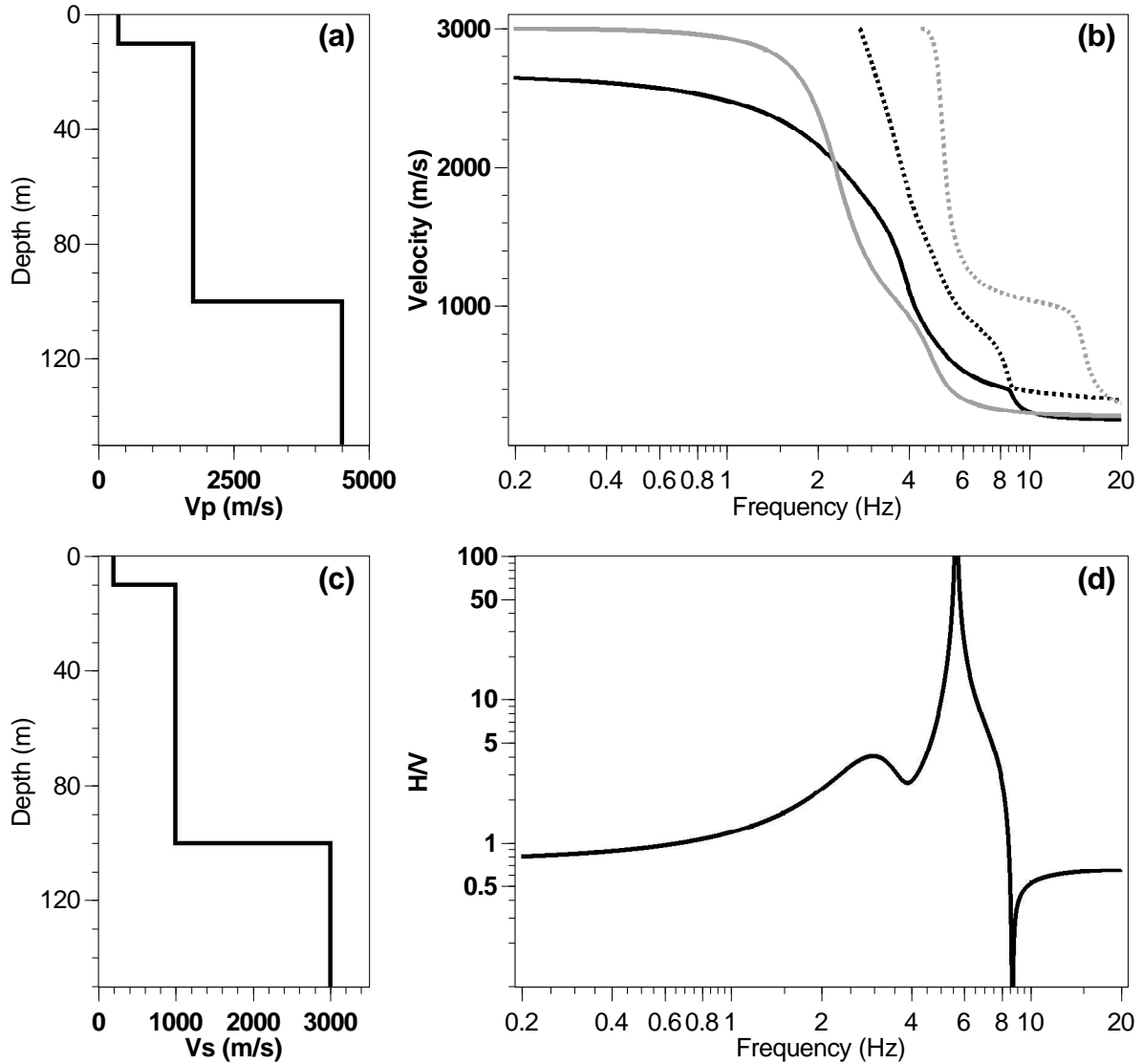


**Figure 4.1:** Theoretical case for testing parameterizations. (a)  $V_p$  profile. (b) Dispersion curve for the fundamental (solid) and the first higher mode (dots) of Love (grey) and Rayleigh (black). (c)  $V_s$  profile. (d) Rayleigh fundamental ellipticity.

Layer	Thickness	$V_s$	$V_p$	Poisson's ratio	Density
Sediments 1	10 m	200 m/s	375 m/s	0.3	2 t/m <sup>3</sup>
Sediments 2	90 m	1000 m/s	1750 m/s	0.25	2 t/m <sup>3</sup>
Basement	–	3000 m/s	4500 m/s	0.10	2 t/m <sup>3</sup>

**Table 4.1:** Properties of the reference model.

curve. Scherbaum et al. (2003) showed that the energy on the vertical component drastically decreases in the vicinity and below the fundamental frequency of the soil structure. Rayleigh dispersion curves are currently best measured on the vertical components, perpendicular to the free surface. It implies that the uncertainties on the apparent velocity determination below the

threshold frequency are usually significant and limit the range of available dispersion curves. From the shape of the ellipticity (figure 4.1(d)), this effect is assumed to occur below 5.5 Hz. Actually, the ellipticity curve has two maxima at 2.5 and 5.5 Hz. Hence, the energy on the vertical component might be still sufficient below 5.5 Hz. In the absence of ambient vibration simulations for this case, we cannot predict the value of the peak frequency of the measured H/V and thus the magnitude of the high-pass filter effect. Hereafter, two cases are considered: a broad band (0.2 to 20 Hz) and a narrow band (5.5 to 15 Hz) dispersion curve. The second one is probably closer to frequency range obtained for real experiment with Rayleigh waves.

## 4.2 Thickness, $V_p$ , and $V_s$

For each layer of the ground model, the considered parameters are: the thickness ( $h$ ), and the velocities  $V_p$  and  $V_s$ . The density is generally not inverted here as its influence on the dispersion curve is usually small compared to the other parameters' one (section 3.1.8).

In this section, we make use of the standard neighbourhood algorithm developed in Fortran by Sambridge (1999a). For each generated parameter set, a misfit value must be calculated by the forward algorithm, even if the parameters do not fulfil with physical and prior conditions. With the original inversion code, it is not possible to reject a particular model. The wrong model might be discarded by returning an arbitrary high misfit to the neighbourhood algorithm. However, we prove hereafter that it is an inefficient method, especially when the number of parameters is increasing. Assuming a parameter set  $P_1 \dots P_n$ , when there is only one physical condition of the type  $P_i < P_j$ , there is one chance over two to get a good model. From the combinatorial probabilities, if the number of conditions increases up to  $m$ , the chance of getting one good model reduces to  $\frac{1}{2^m}$ . Typically, for a three-layer model, the number of parameters is 8 and the number of physical conditions of the type  $P_i < P_j$  is also 8. Hence, the probability of generating one good model is  $1/256$ . Usual values for the tuning parameters of the neighbourhood algorithm are  $it_{max}=100$ ,  $n_s=100$ , and  $n_r=100$  to generate 10000 models. In most cases, three iterations are thus necessary to get at least one good model. At the next iteration, 100 new models are generated in the 100 best cells. Hence, one new model is added close to the good model and 99 other models are still selected in the wrong regions of the parameter space. Finally, very few good models are obtained and the good regions of the parameter space are poorly investigated. All the wrong models are stored by the neighbourhood algorithm and all of them are included in the computation of the Voronoi geometry. As the number of models is increasing, the rate of the model generation is always decreasing, slowed down by useless wrong models. At the end of our work, we developed a modified neighbourhood algorithm that takes into account the model rejection in an efficient way (sections 2.4). However, this study is based on the standard algorithm which requires an appropriate parameter transformation in order to avoid generating wrong ground models. This part is covered in this section.

The thicknesses of the layers may take whatever positive value. Thus, the transformation is just a linear scaling from  $[0, 1]$  to  $[h_{min}, h_{max}]$ . The layer thicknesses may also be set by

specifying the absolute depth of the bottom of each layer ( $z_i$ ). In this case, the user must avoid overlapping of the depth ranges which may induce negative thickness. As for thickness, it also reduces to a linear scaling from  $[0, 1]$  to  $[z_{min}, z_{max}]$ . Mixtures of both types of position parameters are not possible in the developed software.

$V_p$  and  $V_s$  are linked by Poisson's ratio. For geological materials, Poisson's ratio is always between 0 and 0.5. Hence,  $V_p$  and  $V_s$  must satisfy the following inequalities  $0 < V_s < \frac{\sqrt{2}}{2}V_p = 0.707V_p$ . There are two alternatives to parameterize  $V_p$  and  $V_s$  satisfying the conditions, which both make use of ratio  $V_{sp}(\nu) = \frac{V_s}{V_p}$ :

1. Calculating  $V_s$  from the first parameter with a scaling from  $[0, 1]$  to  $[V_{s,min}, V_{s,max}]$ . The second parameter is the ratio  $V_{sp}$  scaled to  $[V_{sp,min}, V_{sp,max}]$  where  $0 < V_{sp,min}$  and  $V_{sp,max} < \frac{\sqrt{2}}{2}$ .
2. Calculating  $V_p$  from the first parameter with a scaling from  $[0, 1]$  to  $[V_{p,min}, V_{p,max}]$ . The second parameter is the ratio  $V_{sp}$  with the same limits as in the last case.

The first option is more intuitive because  $V_s$  has the greatest influence on the dispersion curve. However, the generated  $V_p$  values range from  $\sqrt{2}V_s$  to  $\infty$  or to any value above common real observations. Secondly, the prior probabilities of  $V_s$  and  $V_{sp}$  are uniform on the user specified range. Considering parameters independently ( $V_s$  or  $V_{sp}$ ), it means that the whole parameter space is equally investigated. From the parameterization point of view, every model has an equal chance to be taken at random. However, considering  $V_p$ , it is the ratio of two uniform random variables  $V_s$  and  $V_{sp}$ , and its density of probability is far from being constant over the user specified range. Thus, some  $V_p$  values have more chances to be generated by the neighbourhood algorithm than others. Because  $V_p$  is not always well constrained by the dispersion curve, the parameterization may artificially orientate the inversion towards particular models rather than exploring the whole parameter space. From the user point of view, the  $V_p$  profile may appear better constrained than it is really.

On the other hand, taking the second option,  $V_p$  profiles are uniformly investigated. Because  $V_s$  is relatively well constrained by the dispersion curve, the influence of the parameterization is only sensitive at the beginning of the process. Once the area of solution is delineated, the bias introduced by the non-uniform probability becomes negligible. Also, the range for  $V_p$  is fixed by the user and no abnormal  $V_p$  value is generated.  $V_s$  values are always less than  $\frac{\sqrt{2}}{2}V_p$ . For models with a reasonable number of layers (up to three or four), this option is probably the best one and it has been chosen in the software implementation tested in the next sections.

For a stack of layers, a common condition is the absence of low velocity zones or a monotonous increasing profile. This aspect is studied in section 4.3 for a stack of  $N$  layers. The increasing of velocity with depth may be parameterized by setting the velocity increment at each interface as parameters ( $P$ ), and  $(V_p)_i = (V_p)_{i-1} + P$ .  $V_s$  is calculated as above with the values of  $V_{sp}$ . Low velocity zones may still appear on  $V_s$  profiles. When necessary, they may be avoided by multiplying the final misfit by a penalty factor, function of the magnitude of the low velocity zone. This technique works only for a reduced number of layers (up to three or four), for reasons

probably similar to the ones detailed in the introduction of this section. We use it in the simple parameterizations hereafter.

### 4.2.1 Two layers

The shape of the fundamental Rayleigh dispersion curve in figure 4.1(b) has a complex shape. However, we first test if it is possible to invert it with a simple model made of one layer overlying a half space. The curve is resampled with 50 points regularly distributed on a log frequency scale. The utilized parameters are detailed in table 4.2. The neighbourhood algorithm is

Layer	Thickness	$V_p$	$V_s/V_p$	Density
Sediments	1 to 200 m	200 to 2,000 m/s	0.01 to 0.707	2 t/m <sup>3</sup>
Half-space	–	+10 to 3,000 m/s	0.01 to 0.707	2 t/m <sup>3</sup>

**Table 4.2:** Parameterized model for two-layer inversions. The "+" sign stands for incremental velocity: the parameter is the velocity gap between the first and the second layer.

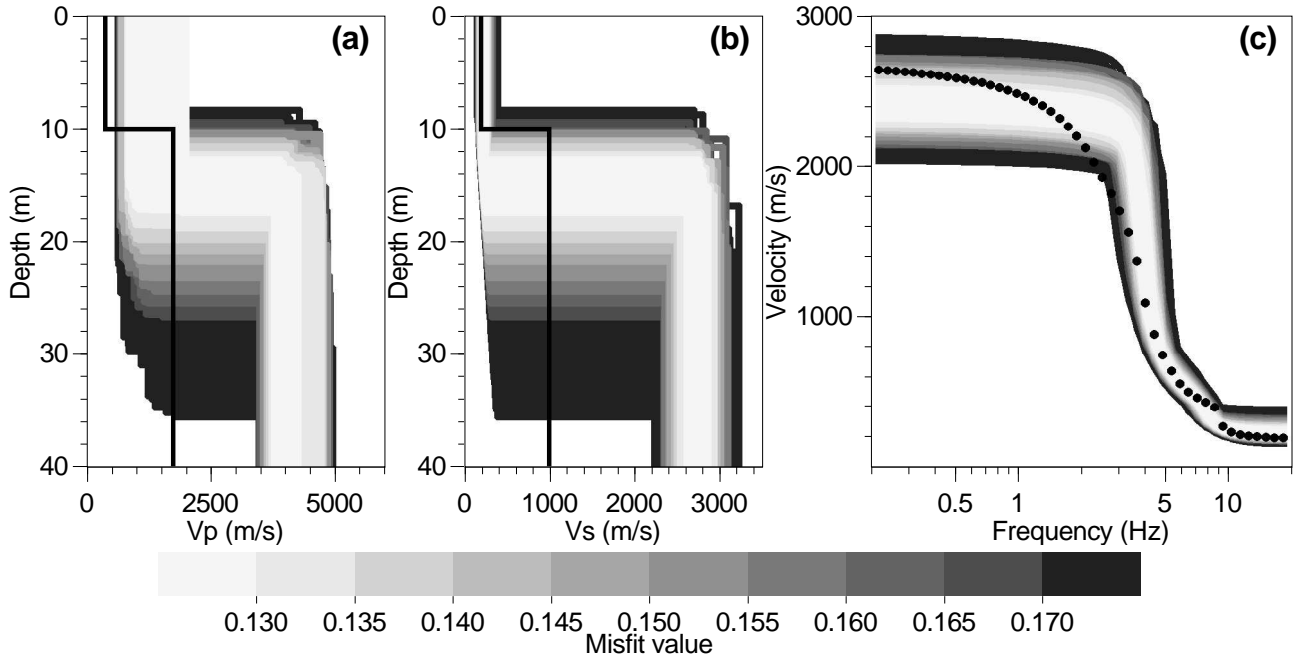


**Figure 4.2:** Inversion of the full dispersion curve with a two-layer model. (a) Resulting  $V_p$  profiles. (b) Resulting  $V_s$  profiles. The black lines are the theoretical velocity profiles. (c) Dispersion curves corresponding to models of figures (a) and (b). The black dots are the theoretical dispersion curve used as the target curve during inversion.

tuned to be as exploratory as possible, generating 100 models per iteration ( $n_s$ ) in the current 100 best cells ( $n_r$ ). Runs of 50 iterations are started with five distinct random seeds (chapter 2) to test the robustness of the results. These parameters are usually adjusted by trial and error. The dimension of the parameter space is 5. Each individual process generates an ensemble of 5100 possible solutions ranked by their misfit values. The results of the inversion are shown in figure 4.2 in terms of velocity profiles. Only the models with a misfit less than 0.1 are selected. The shape of the dispersion curve at low frequency (figure 4.1) is obviously too complex to be correctly inverted with a simple model made of two layers. A more complex structure has

to be assumed in order to invert the dispersion curve between 0.2 and 20 Hz (section 4.2.2). However, the  $V_s$  profile below 8 m is well retrieved. The shapes of the reference and the calculated dispersion curve at high frequency (above 5 Hz) are similar. The low frequency part of the curve prevents the misfit from being improved and it influences the error on the depth and on  $V_p$ . In the next paragraph, better results can be achieved by considering only the dispersion curve at high frequency.

The fundamental Rayleigh dispersion curve between 5.5 and 15 Hz, resampled with 30 points regularly distributed on a log frequency scale and described in section 4.1 (figure 4.1) is inverted in the same conditions as above. Figure 4.3 shows the minimum misfit evolution with the number of generated models. The curve is never regular as already noticed by Sambridge (1999a). But in general, the variations are progressively damped if the number of generated models is sufficient.

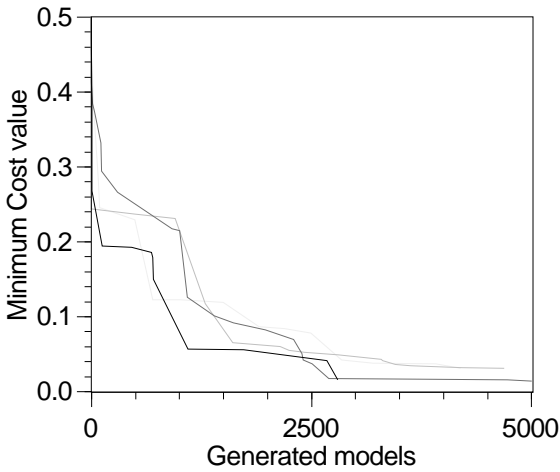


**Figure 4.3:** Inversion with a two-layer model: variation of the minimum misfit with the inversion advance. The five curves correspond to the five inversion processes initiated.

In figure 4.4, each generated model is represented by a dot with a grey scale depending on the misfit value. Figure 4.4(a) is a projection of the five dimension parameter space on the plane  $z_1 - V_{s0}$ , while the other plots (figures 4.4(b) to 4.4(f)) show the one-dimensional variation of each parameter versus the misfit value. The minimum achieved misfit is around 0.01. All generated models are plotted in figure 4.4(a). The shapes for lowest misfit values in figures 4.4(b) to 4.4(f) give valuable information about the posterior marginal uncertainties of one parameter. For instance, accepting a level of error on the experimental curve of 0.05, all values of  $V_{p0}$  between 300 and 2000 m/s ensure a good fit of the data curve.  $V_{p0}$  (theoretical value is 375 m/s) is better resolved only if misfits below 0.03 are considered. In

figures 4.4(d) to 4.4(f), it is clear that the inversion algorithm is not exploratory enough to sample the whole parameter space for poorly resolved parameters. For well constrained param-

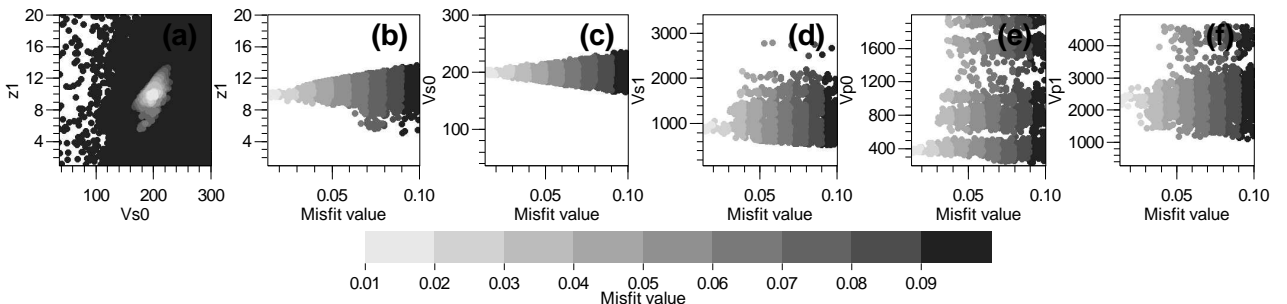


**Figure 4.4:** Inversion with a two-layer model: parameter space. (a) Projection of model points on the plane  $z_1 - V_{s0}$ . One-dimensional marginal for (b)  $z_1$ , (c)  $V_{s0}$ , (d)  $V_{s1}$ , (e)  $V_{p0}$ , and (f)  $V_{p1}$ .

eters ( $z_1$  and  $V_{s0}$ ), the results are approximately the same for all runs. For other parameters,

each additional run may brought some new solutions, improving the global sampling of the parameter space. Even with only five parameters, the complexity of the parameter space is such that an exhaustive sampling would be prohibitive.

The results of the inversion are shown in figure 4.5 in terms of velocity profiles. Only the models with a misfit less than 0.1 are selected ( $\approx 25000$  models). Retrieved  $V_p$  and  $V_s$

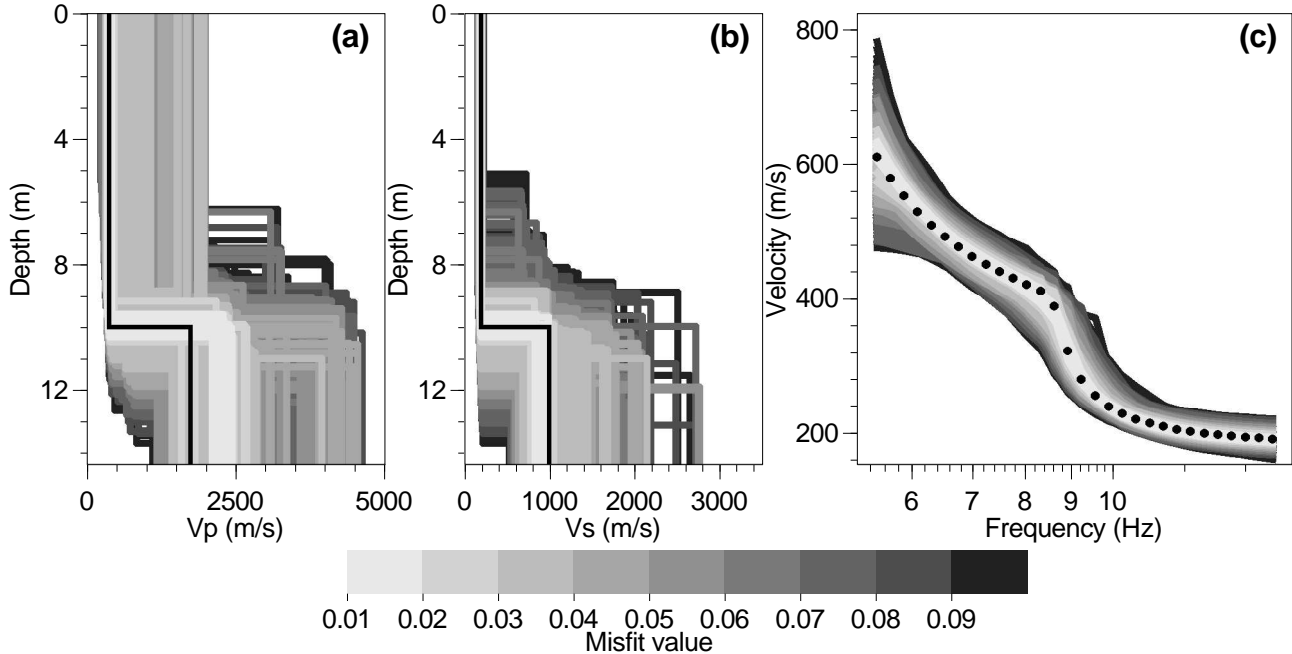


**Figure 4.5:** Inversion with a two-layer model: velocity profiles. (a) Resulting  $V_p$  profiles. (b) Resulting  $V_s$  profiles. The black lines are the theoretical velocity profiles. (c) Dispersion curves corresponding to models of figures (a) and (b). The black dots are the theoretical dispersion curve used as the target curve during inversion.

profiles are visible in figures 4.5(a) and 4.5(b). The black lines are the theoretical velocity profiles. The dispersion curve calculated for profiles of figures 4.5(a) and 4.5(b) are shown in figure 4.5(c) where the black dots are the simulated experimental curve defined on a restricted range (section 4.1). According to the level of confidence on the experimental curve, darkest models may be discarded. The lightest models (misfit  $< 0.3$ ) fit nicely with the theoretical model except for  $V_p$  within the basement.  $V_s$  is well retrieved for the first 8 m whereas a wide range of  $V_p$  values may explain the observed dispersion curve. Even for  $V_s$ , the uncertainties greatly increase from 8 m, below the depth of the velocity contrast. However, if the dispersion is known with a very good confidence and a good precision,  $V_{p0}$  can be correctly estimated because it is not possible to find any model with  $V_{p0} > 500\text{m/s}$  and a misfit below 0.03.

A common solution to improve the precision for deeper structure is to enlarge the frequency range of the dispersion curve. For a two-layer parameterization, broader frequency ranges lead to badly resolved structures with a minimum achievable misfit above 0.1 (figure 4.2). Hence, it is not possible to find an equivalent two-layer model for the more complex soil structure. In a real situation, when a two-layer parameterization gives worse results than a more complex parameterization, it is a piece of evidence that the structure is probably not simply made of homogeneous sediments overlying a hard-rock basement. In the next section, a three-layer parameterization is used and the influence of the frequency range is checked.

### 4.2.2 Three layers

The fundamental Rayleigh dispersion curve shown in figure 4.1 is inverted with a three-layer model. Various types of dispersion curve sampling are reviewed in this section. Finally, the effect of the prior information on the depths is checked.

#### Broad band dispersion curve

The dispersion curve is sampled with 50 points regularly distributed on a log frequency scale and on a wide frequency range from 0.2 to 20 Hz. The parameters are of the same type as for the preceding case with one supplementary layer. Table 4.3 gives the list of parameters and their prior intervals. The  $V_p$  profile is imposed to be monotonously increasing by setting positive velocity variations as parameters rather than the absolute value.  $V_s$  is kept monotonous by the penalization technique (introduction of section 4.2) on the low velocity zones.

Layer	Thickness	$V_p$	$V_s/V_p$	Density
Sediments 1	1 to 50 m	200 to 2,000 m/s	0.01 to 0.707	2 t/m <sup>3</sup>
Sediments 2	1 to 200 m	+10 to 2,000 m/s	0.01 to 0.707	2 t/m <sup>3</sup>
Half-space	–	+10 to 3,000 m/s	0.01 to 0.707	2 t/m <sup>3</sup>

**Table 4.3:** Parameterized model for three-layer inversions. The "+" sign stands for incremental velocity: the parameter is the velocity gap between the first and the second layer.

Five independent runs are started with  $n_s$  (number of samples per iteration) and  $n_r$  (number of cells to resample) being 100. The number of iterations is set arbitrarily to 150. The evolution of the minimum misfit with the number of generated models (not shown) finally proves that values for the tuning parameters are necessary and sufficient. The total number of generated model is hence 75500, with a minimum misfit around 0.02. The  $V_p$  and  $V_s$  profiles of models (8900) for which the misfit is less than 0.1 are plotted in figures 4.6(a) and 4.6(b), respectively. The corresponding dispersion curves are shown in figure 4.6(c).

On the first ten metres, the inverted profiles are very similar to those obtained with the two-layer parameterization. The velocities of the basement are also relatively well retrieved (below 100 m). The posterior uncertainties of the intermediate layer are higher than the one of the first layer, mainly because of the low sensitivity of the dispersion curve to the intermediate layers (section 3.1.8 on page 54). Though Poisson's ratio is left totally free, the uncertainties on  $V_p$  and  $V_s$  of the intermediate layer are of the same order. The uncertainty on the depth determinations are always high even for the first interface at ten metres (errors up to nearly 40%<sup>1</sup>). A precise inversion of the depths is possible but requires a very high precision on the dispersion curve.

This case is theoretical. During real experiments, the dispersion is not defined down to 0.2 Hz if the resonance frequency (given by the main peak of the ellipticity or of the measured H/V) is around 5.5 Hz. The effect of such limitation is tested in the next section.

<sup>1</sup>The depth of the best models is around 10 m. Considering a misfit of 0.05 as acceptable, the depth may varies between 8 and 14 m, which makes an error between 20 and 40%.

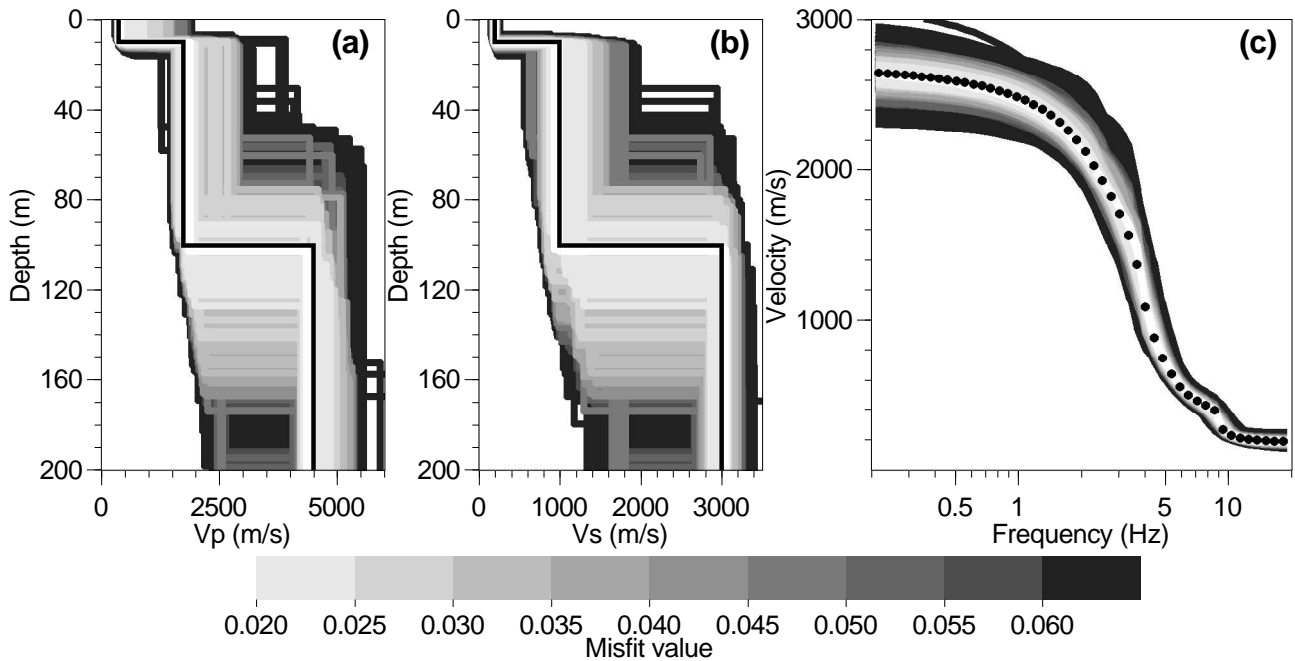


**Figure 4.6:** Inversion with a three-layer model over a broad frequency range. (a) Resulting  $V_p$  profiles. (b) Resulting  $V_s$  profiles. The black lines are the theoretical velocity profiles. (c) Dispersion curves corresponding to models of figures (a) and (b). The black dots are the theoretical dispersion curve used as the target curve during inversion.

### Narrow band dispersion curve

The dispersion curve is resampled with 30 points on a narrow frequency range from 5.5 to 15 Hz as in section 4.2.1. The parameterization is exactly the same as in the above section (table 4.3). Ten independent runs are started with the same characteristics as in the above section. The number is increased to improve the parameter-space sampling.

The models with a misfit lower than 0.1 ( $\approx 4800$  matches) are displayed in figure 4.7. The minimum misfit is around 0.02. The  $V_s$  profile is correctly retrieved down to 8 or 10 m like in the two layer case in section 4.2.1. Below, a lot of models are virtually possible. With a very high precision on the dispersion curve,  $V_s$  profile seems to be correctly retrieved down to 100 m, for instance the white one in figure 4.7(b). However, hereafter (narrow band dispersion curve with prior information on  $V_p$ , on page 77), we show that the parameter space investigation is not sufficient in this case leading to optimistic conclusions. Below 100 m, all models are possible even with a very low misfit (the white one with an interface at 170 m).

### Low frequency dispersion curve

From the above discussion, the low frequency part of the dispersion is absolutely necessary to investigate deep layers. In this paragraph, we show an example of inversion without the high frequency part, simulating an experiment with only large aperture arrays. The fundamental Rayleigh dispersion curve in figure 4.1(b) is resampled with 30 samples from 0.2 to 8 Hz.

The inversion is run with five distinct processes with the parameterization detailed in table 4.3. The retrieved velocity profiles are shown in figures 4.8(a) and 4.8(b). The corresponding dispersion curves are plotted in figure 4.8(c). Whereas the depth and the velocities ( $V_p$  and  $V_s$ )

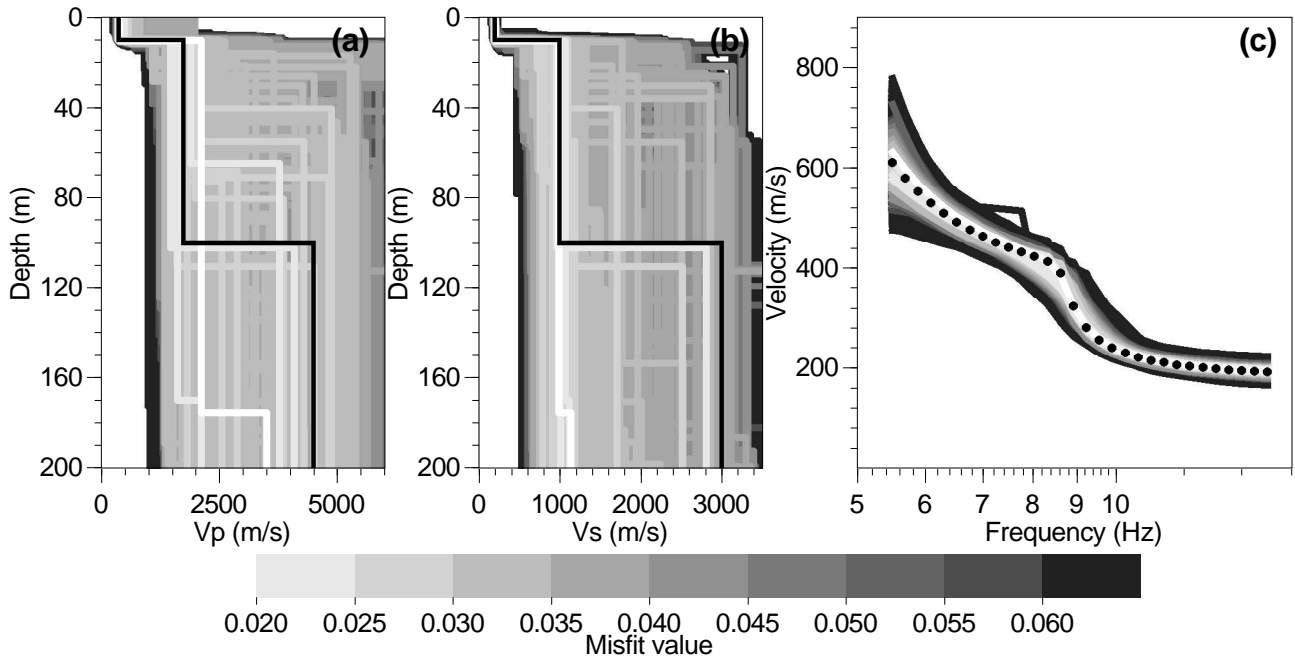


**Figure 4.7:** Inversion with a three-layer model over a restricted frequency range. (a) Resulting  $V_p$  profiles. (b) Resulting  $V_s$  profiles. The black lines are the theoretical velocity profiles. (c) Dispersion curves corresponding to models of figures (a) and (b). The black dots are the theoretical dispersion curve used as the target curve during inversion.

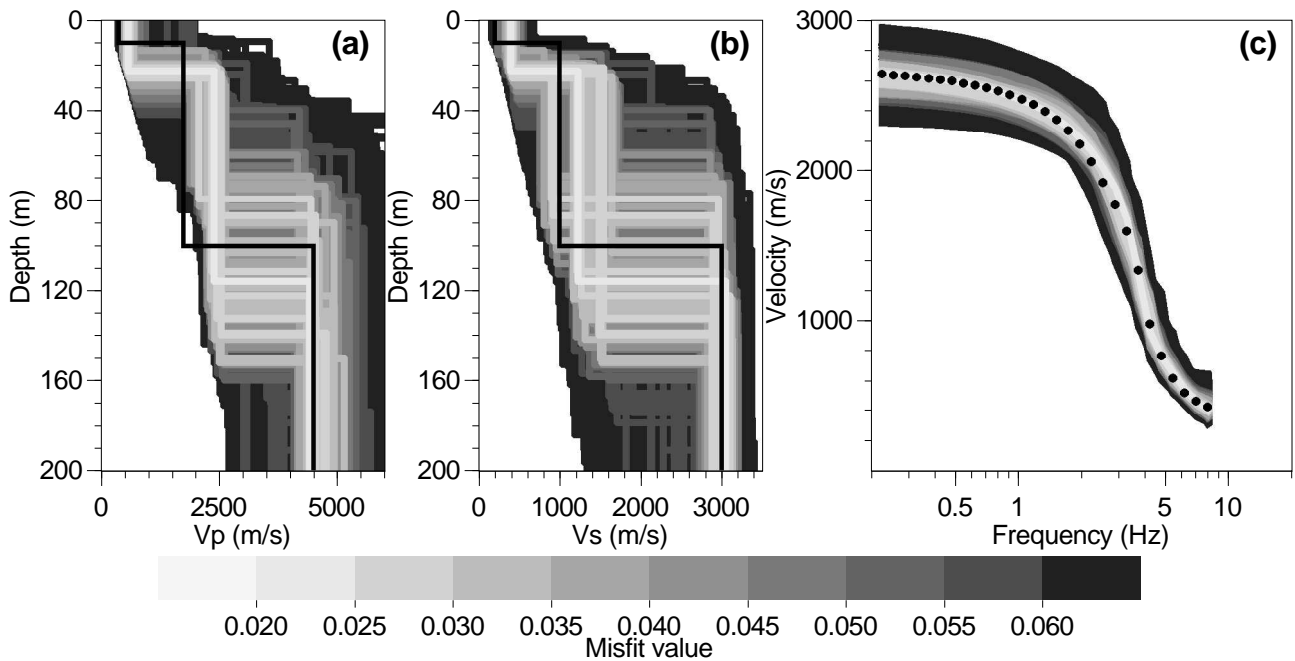


**Figure 4.8:** Inversion with a three-layer model over a low frequency range. (a) Resulting  $V_p$  profiles. (b) Resulting  $V_s$  profiles. The black lines are the theoretical velocity profiles. (c) Dispersion curves corresponding to models of figures (a) and (b). The black dots are the theoretical dispersion curve used as the target curve during inversion.

of the basement are obtained with approximately the same precision as in figure 4.6, strong bias is observed for the properties of the first layers. Contrary to all preceding inversion examples of this chapter, the average retrieved profile is false. The average  $V_{s0}$  found is 400 m/s while the correct value is 200 m/s. Even more annoying, the models with  $V_{s0} = 200$  m/s have all very bad misfits. In the absence of any constraint on  $V_{s0}$ , the neighbourhood algorithm and the chosen parameterization<sup>2</sup> orientate the search to an arbitrary and false profile.

Those results highlight the need for a good definition of the dispersion curve at high frequency (from 8 or 10 Hz in this case). In many cases, the ambient noise techniques loose reliability in the highest frequency range due to various factors (unknown sources distribution and source type, higher modes, too large aperture for arrays, . . .). Active sources methods, for which a better control on the source parameters is possible, are able to provide complementary information at such frequencies.

### Prior information on depth

If the depth of any particular velocity contrast is known from other investigations like a reference borehole or a penetration test, it can be introduced in the parameterization. Such a test is performed on the same dispersion curve as in figure 4.6 with the parameters defined in table 4.4. The depth is supposed to be known with an error of 5 m.

Layer	Depth	$V_p$	$V_s/V_p$	Density
Sediments 1	1 to 90 m	200 to 2,000 m/s	0.01 to 0.707	2 t/m <sup>3</sup>
Sediments 2	95 to 105 m	+10 to 2,000 m/s	0.01 to 0.707	2 t/m <sup>3</sup>
Half-space	–	+10 to 3,000 m/s	0.01 to 0.707	2 t/m <sup>3</sup>

**Table 4.4:** Parameterized model for three-layer inversions with prior depth. The "+" sign stands for incremental velocity: the parameter is the velocity gap between the first and the second layer.

Five runs are launched generating the models displayed in figure 4.9. The misfit values can be compared directly to the ones of figure 4.7 because the dispersion samples used to calculate them are exactly the same. Reducing the depth prior interval has obviously a positive influence in the inversion process. The main effect is to reduce the uncertainty of the velocities of the intermediate layer.

In figure 4.9, the improvement of the posterior uncertainty may be due to the strong constraint on the large band dispersion curve. The same parameterization is also tested on the dispersion curve with a narrow frequency band as in figure 4.7. The results are shown in figure 4.10. Forcing the depth of the basement indisputably allows a better retrieval of the velocity in the second layer below 10 m. However, the parameterized model made of three uniform layers imply that the velocity has a constant profile between 10 and 100 m. Stating that the velocity profiles are correctly measured down to 100 m is certainly false. The results at 100 m are influenced by the constraints on  $V_s$  between 10 and 25 m. Inversions with one

<sup>2</sup>For  $V_s$ , the prior density of probability is not uniform in this parameterization, as explained at the beginning of section 4.2

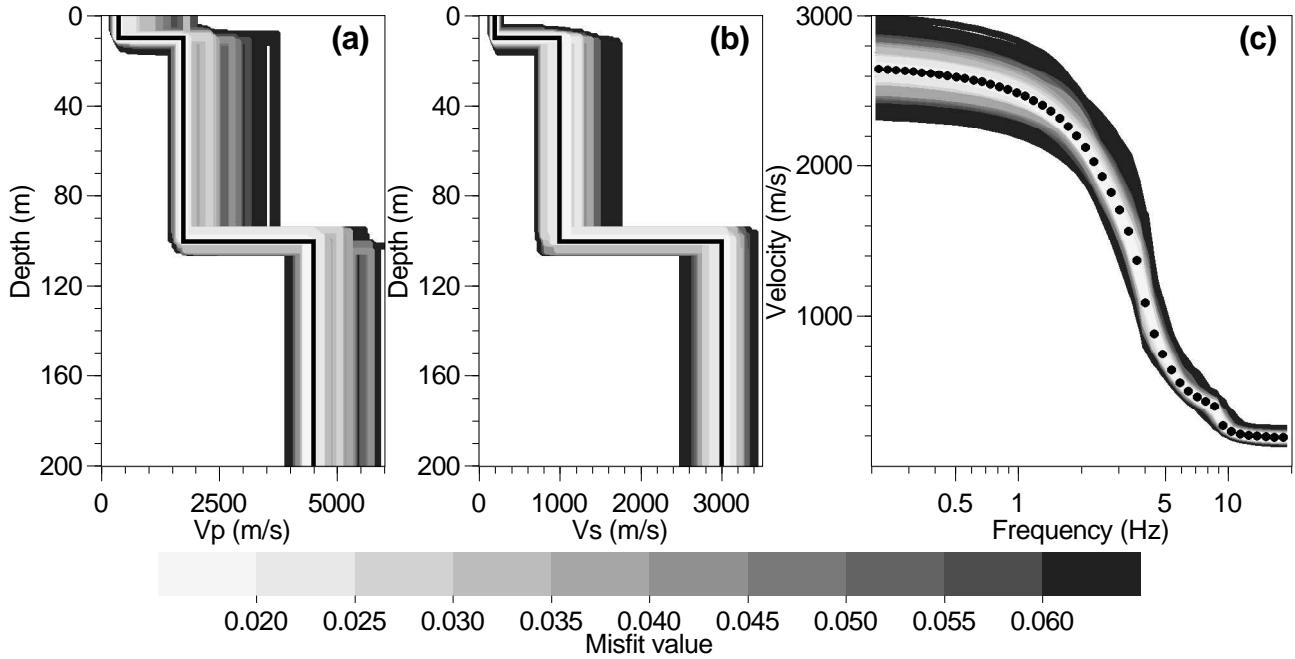


**Figure 4.9:** Inversion with a three-layer model with prior depth. (a) Resulting  $V_p$  profiles. (b) Resulting  $V_s$  profiles. The black lines are the theoretical velocity profiles. (c) Dispersion curves corresponding to models of figures (a) and (b). The black dots are the theoretical dispersion curve used as the target curve during inversion.

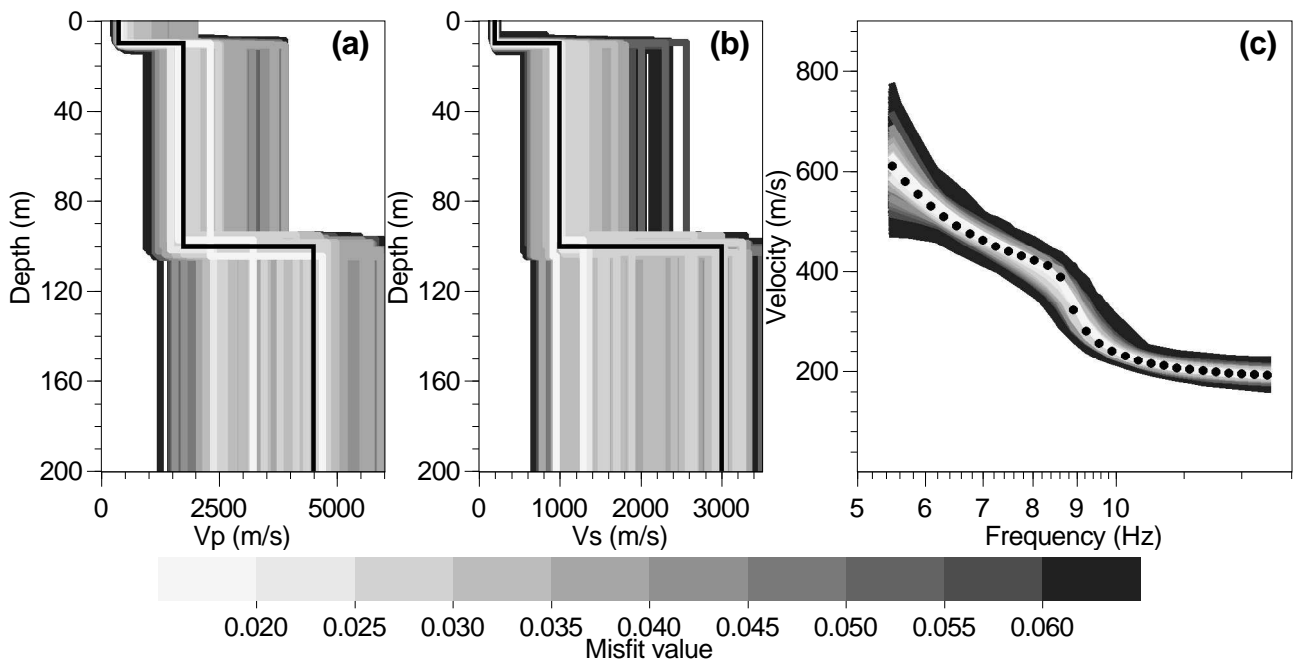


**Figure 4.10:** Inversion with a three-layer model at high frequency with prior depth. (a) Resulting  $V_p$  profiles. (b) Resulting  $V_s$  profiles. The black lines are the theoretical velocity profiles. (c) Dispersion curves corresponding to models of figures (a) and (b). The black dots are the theoretical dispersion curve used as the target curve during inversion.

or more supplementary degrees of freedom must be carried out to define the total penetration depth of the method.

In conclusion, any prior information about the depths of the known velocity contrasts help the inversion of the dispersion curves even for incomplete ones. Like any other information source, its reliability must be ensured and the length of the fixed depth interval set according to the data source confidence.

### Prior information on $V_p$

$V_p$  profiles may also be measured by other means not related to surface wave properties. Refraction tests, borehole logging, cross-hole, ... may bring valuable information about  $V_p$ . Like the depth, the prior information about  $V_p$  is introduced in the parameterization itself. In the above sections, the  $V_p$  profile is left as totally free in a very large interval. Here, we fix it in a deterministic way, removing  $V_p$  from the parameter list. Table 4.5 details the remaining parameters. The dimension of the parameter space reduces from 8 to 5.

Layer	Thickness	$V_p$	$V_s/V_p$	Density
Sediments 1	1 to 200 m	375 m/s	0.01 to 0.707	2 t/m <sup>3</sup>
Sediments 2	1 to 200 m	1750 m/s	0.01 to 0.707	2 t/m <sup>3</sup>
Half-space	–	4500 m/s	0.01 to 0.707	2 t/m <sup>3</sup>

**Table 4.5:** Parameterized model for three-layer inversions with prior  $V_p$ .

Using the standard implementation of the neighbourhood algorithm, it is not possible to disconnect the depths of the  $V_s$  and  $V_p$  profiles. Hence, a real  $V_p$  profile cannot be fixed without forcing the  $V_s$  profile to have interfaces at the same depths. For this test, the depths of the  $V_p$  profile are left as free parameters and they follow the depths of the  $V_s$  profile. The conditional neighbourhood algorithm (section 2.4) would allow totally independent profiles for  $V_s$  and  $V_p$ . Consequently, the  $V_p$  profile could be fixed without affecting directly the inversion of  $V_s$ .

The results are shown in figures 4.11 and 4.12 for a dispersion curve defined over a broad and a narrow frequency band, respectively (five distinct inversion processes in each case). The minimum misfit is around 0.002 for both cases. In figure 4.11, 31000 models have a misfit lower than 0.1 (23000 in figure 4.12), the threshold used to select model.

Comparing figures 4.6 and 4.11, the uncertainty of  $V_s$  on the intermediate layer is greatly reduced, showing a direct effect of the fixing  $V_{p0}$ . However, fixing  $V_p$  has also an effect on the depth error of the deepest contrast. Other tests with wrong prior  $V_p$  values show that the final  $V_s$  results are weakly affected by over-estimated  $V_p$  profiles. In contrast, any under-estimation of  $V_p$  completely ruins the inversion of  $V_s$  because the maximum of  $V_s$  is automatically set to  $\frac{\sqrt{2}}{2}V_p$ . This is why  $V_p$  values can be fixed only when reliable data exist. Tests with and without the prior information must be carried out. When there is no pre-existing data about  $V_p$ , the best option is to include it in the parameterization like in preceding section, with a very large prior interval.

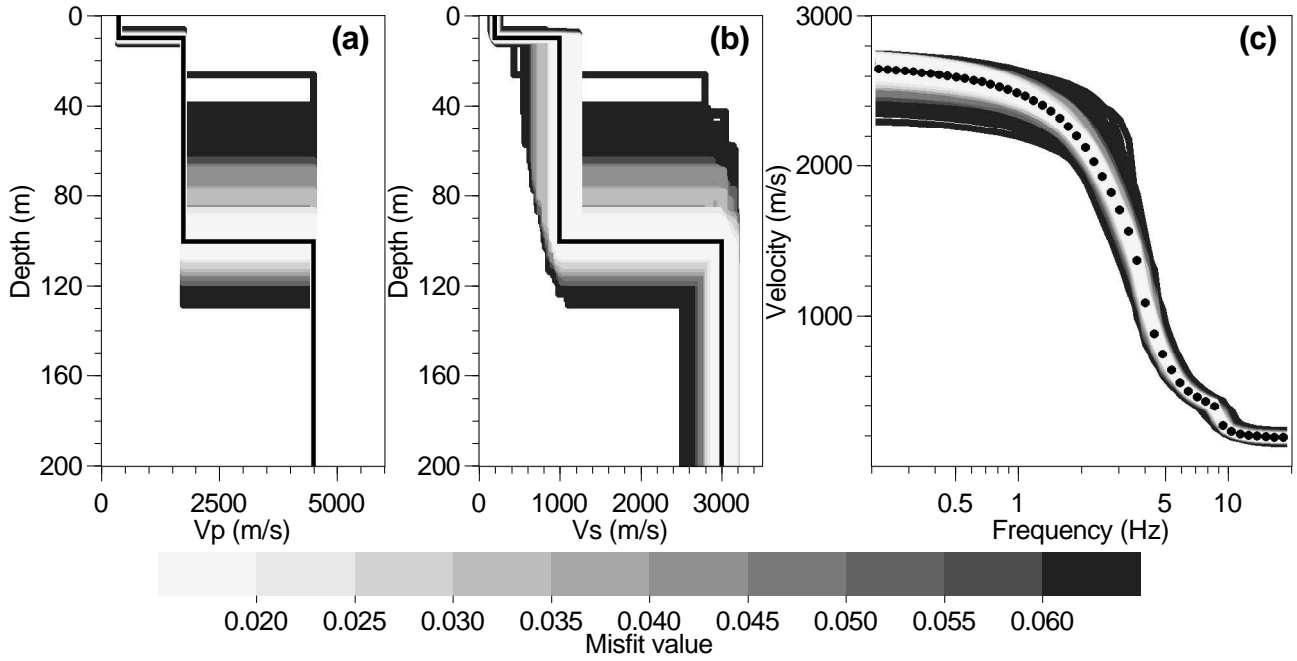


**Figure 4.11:** Inversion with a three-layer model with prior  $V_p$ . (a) Resulting  $V_p$  profiles. (b) Resulting  $V_s$  profiles. The black lines are the theoretical velocity profiles. (c) Dispersion curves corresponding to models of figures (a) and (b). The black dots are the theoretical dispersion curve used as the target curve during inversion.

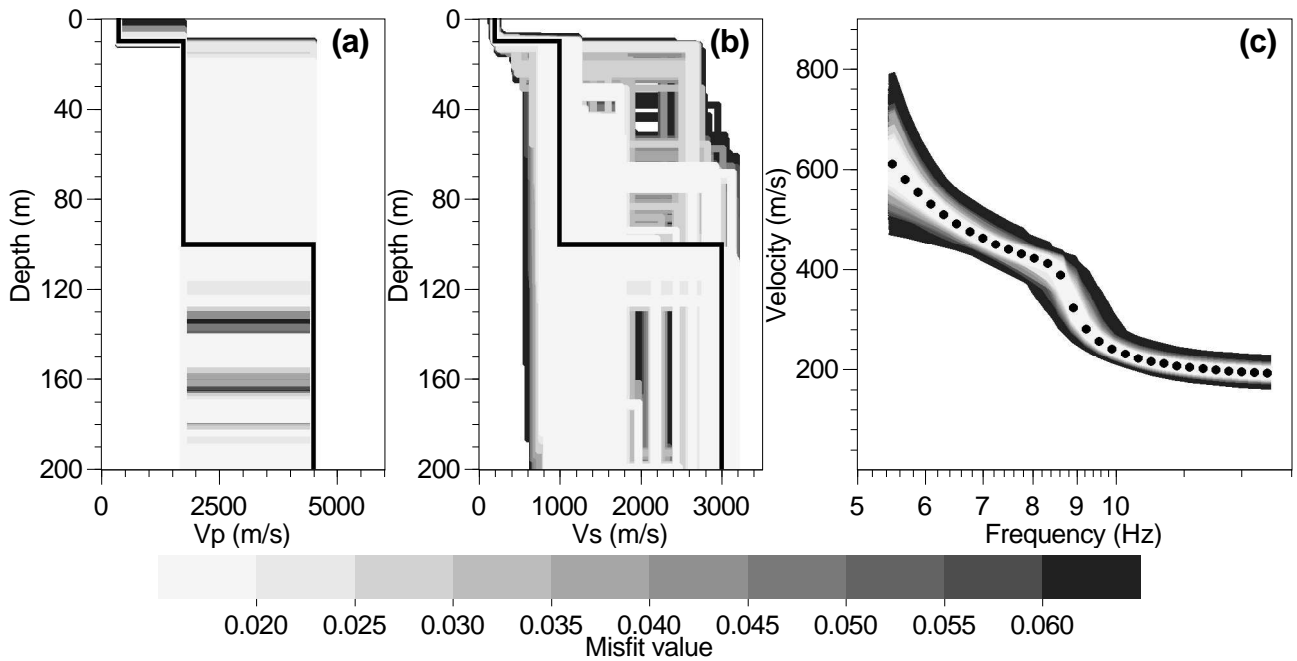


**Figure 4.12:** Inversion with a three-layer model at high frequency with prior  $V_p$ . (a) Resulting  $V_p$  profiles. (b) Resulting  $V_s$  profiles. The black lines are the theoretical velocity profiles. (c) Dispersion curves corresponding to models of figures (a) and (b). The black dots are the theoretical dispersion curve used as the target curve during inversion.

The parameterization used for generating figure 4.12 is a particular case of the more general parameterization relating to figure 4.7. Hence, if the investigation of the parameter space was perfect for figure 4.7, all models appearing in figure 4.12 would be also generated by the inversion process illustrated in figure 4.7. Clearly, the introduction of reliable prior information about  $V_p$  also makes the inversion more efficient leading to a better parameter space investigation. From figure 4.12, if the dispersion curve is known with a sufficient precision (acceptable misfit at 0.2),  $V_{s1}$  can be determined with a precision of 200 m/s ( $\approx 20\%$ ) down to 20 or 30 m. Without the  $V_p$  information this uncertainty is greater than 200 m/s (case of figure 4.7).

## 4.3 Stack of N layers

In section 4.2, the soil structure is modeled with a few layers of varying thicknesses. Alternatively, the velocity variation may be discretized by a great number of thin layers with fixed thicknesses. It is the usual technique for linearized inversion methods (Herrmann 1994). It generally implies a greater number of parameters than the approach described in section 4.2.

In this section, we invert the same dispersion curve as in section 4.2. However,  $V_p$  is supposed to be known in a deterministic way and without bias to allow the comparison of arbitrary and increasing profiles. In section 4.3.1, an additional inversion case is proposed with  $V_p$  and  $V_s$  as the variable parameters. The variation of velocity is represented by a stack of ten layers with fixed thicknesses (2, 3, 5, 8, 12, 17, 23, 30, 38, and 47 m) plus a half space. The density is fixed to 2 t/m<sup>3</sup> in all layers.

### 4.3.1 Arbitrary profile

The model is made of 11 layers with one parameter per layer ( $V_{sp}$ , the ratio of  $V_s$  over  $V_p$ ). Table 4.6 summarizes the properties of each layer.

Layer	Depth	$V_p$	$V_s/V_p$	Density
0	2 m	375 m/s	0.01 to 0.707	2 t/m <sup>3</sup>
1	5 m	375 m/s	0.01 to 0.707	2 t/m <sup>3</sup>
2	10 m	375 m/s	0.01 to 0.707	2 t/m <sup>3</sup>
3	18 m	1750 m/s	0.01 to 0.707	2 t/m <sup>3</sup>
4	30 m	1750 m/s	0.01 to 0.707	2 t/m <sup>3</sup>
5	47 m	1750 m/s	0.01 to 0.707	2 t/m <sup>3</sup>
6	70 m	1750 m/s	0.01 to 0.707	2 t/m <sup>3</sup>
7	100 m	1750 m/s	0.01 to 0.707	2 t/m <sup>3</sup>
8	138 m	4500 m/s	0.01 to 0.707	2 t/m <sup>3</sup>
9	185 m	4500 m/s	0.01 to 0.707	2 t/m <sup>3</sup>
Half-space	–	4500 m/s	0.01 to 0.707	2 t/m <sup>3</sup>

**Table 4.6:** Parameterized model for N-layer inversions.

Poisson's ratios are totally independent and  $V_s$  profiles might be generated with eventually various LVZs. The inversion is started with five distinct random seeds. The number of new

models per iteration is 100 ( $n_s$ ) and the number of cells resampled is 100 ( $n_r$ ). 150 iterations are successively performed to obtain a total of 75,500 models. The results are shown in figure 4.13. The minimum misfit is around 0.005.

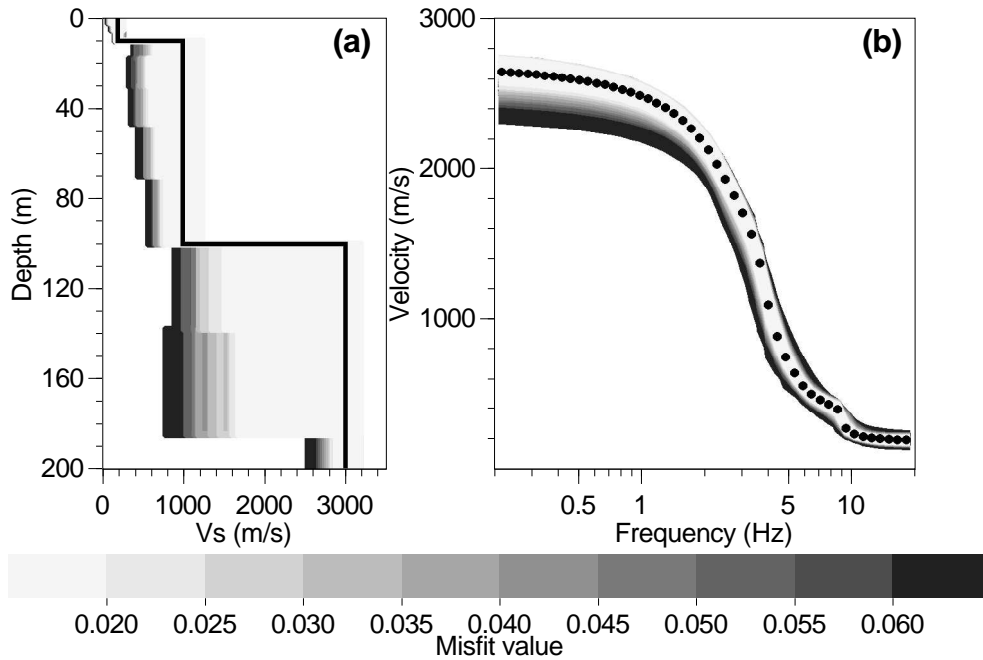


**Figure 4.13:** Inversion with a N-layer model accepting LVZ ( $V_s$  only). (a) Resulting  $V_s$  profiles. The black lines are the theoretical velocity profiles. (b) Dispersion curves corresponding to models of figure (a). The black dots are the theoretical dispersion curve used as the target curve during inversion.

The  $V_s$  profiles in figure 4.13(a) can be directly compared with figure 4.11(b) also obtained with a fixed  $V_p$  profile and on the same dispersion curve. The presence of LVZs slightly increases the non-uniqueness of the problem. The effect of a very slow layer may be thwarted when overlying a faster layer.

In figure 4.13, the fixed  $V_p$  profile prevents from generating a number of additional models. Another inversion case is then proposed with varying  $V_p$  and  $V_s$  profiles. The range of  $V_p$  values inside each layer is set to [200, 6000] m/s. The inversion is started with 20 distinct random seeds to obtain a total of 202,000 models. The results are shown in figure 4.14. The minimum misfit is around 0.012. 90,000 models have misfit less than 0.1.

The  $V_s$  profiles in figure 4.14(b) can be directly compared with figure 4.6(b) obtained on the same dispersion curve. In this case, the presence of LVZs drastically increases the non-uniqueness of the problem. From figure 4.14, no information can be retrieved between 10 m and 185 m. By contrast, figure 4.6 shows for the same dispersion curve that interesting information can be extracted by assuming that no LVZ are present. However, in figure 4.6, the velocities just below 10 m and just above the contrast around 100 m must be the same, which is probably too restrictive. In the next sections, various approaches are proposed to allow velocity variations inside layers and avoiding LVZs with the standard neighbourhood algorithm. However, a simpler solution can be implemented with the conditional neighbourhood algorithm.

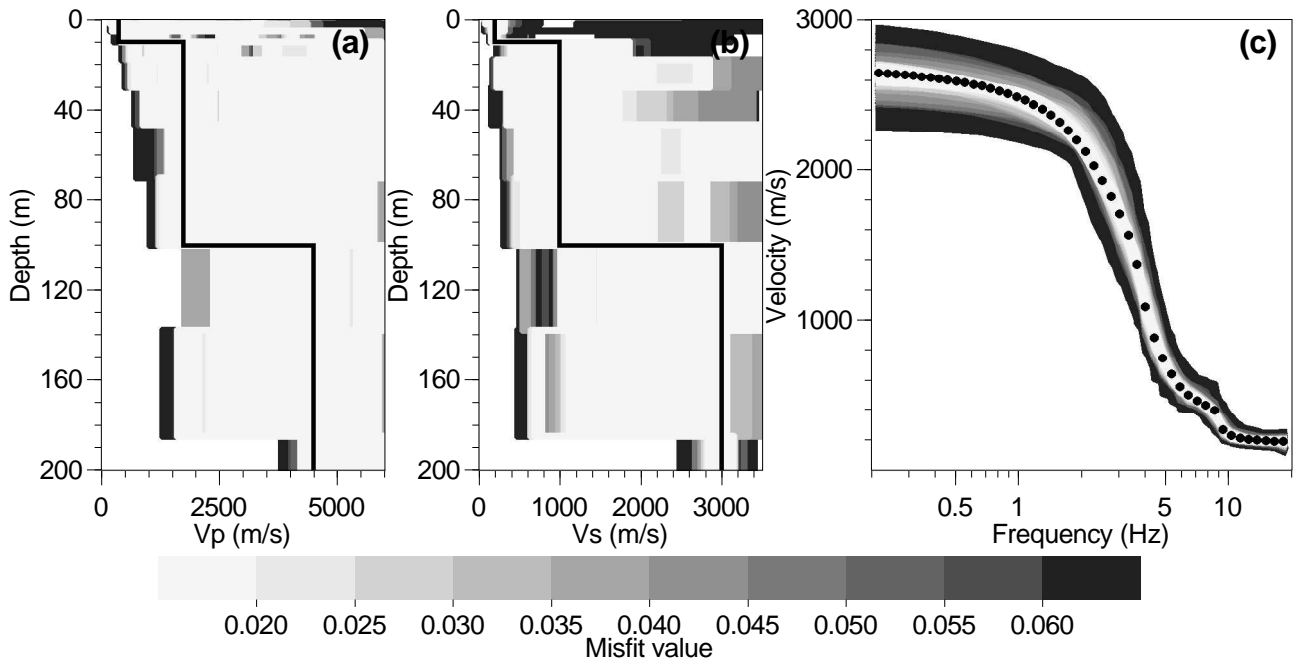


**Figure 4.14:** Inversion with a N-layer model accepting LVZ ( $V_p$  and  $V_s$ ). (a) Resulting  $V_p$  profiles. (b) Resulting  $V_s$  profiles. The black lines are the theoretical velocity profiles. (c) Dispersion curves corresponding to models of figure (a) and (b). The black dots are the theoretical dispersion curve used as the target curve during inversion.

### 4.3.2 $V_s$ inversion without LVZ

In common geological situations,  $V_s$  increases with depth: rock weathering, sediment compaction, . . . (Bachrach et al. 2000, Scherbaum et al. 2003). However, the velocity may decrease with depth in some cases: saturated layers, clays overlaid by sandy formations, hard ground above unconsolidated sediments, lava flows, . . . From the above example (section 4.3.1), if the soil structure is made of thin intercalations of soft and rigid layers, the dispersion curve inversion cannot resolve the properties of each individual layer. Consequently, a limited number of LVZs can be tolerated in the model when the geological structure of the area justifies it. Between two particular LVZs, the velocity must be constant or must increase with depth. Taking these conditions into account during inversion is capital but not straightforward. There are numerous ways of implementing such prior information, we developed some of them, described in appendix B.

Theoretically, the parameterization must ensure that any ground model included in the parameter space has an equal chance to be generated by the neighbourhood algorithm. If this is not verified, the inversion algorithm itself introduces prior information, preferring particular classes of models to others. For instance, in section 4.3.1, all  $V_p$  profiles have the same chance to be generated, but the  $V_s$  profiles are calculated by the multiplication of two random variables and have not a uniform probability (figure B.1). The prior distributions of the proposed methods are detailed in appendix B.

The inversion of the broad band dispersion curve is started with five distinct random seeds, using the scaled diagonal parameterization for  $V_s$  profiles and a fixed  $V_p$  profile (section B.8). 50 iterations are launched per inversion process generating a total of 25500 models. Among

them, 14000 have a misfit lower than 0.1. The results are shown in figure 4.15. In the same conditions, the scaled interpolate method tested in figure B.8 produces only 285 models with misfit lower than 0.1. In this case, the choice of the method for generating models has a strong influence on the global efficiency of the inversion algorithm.

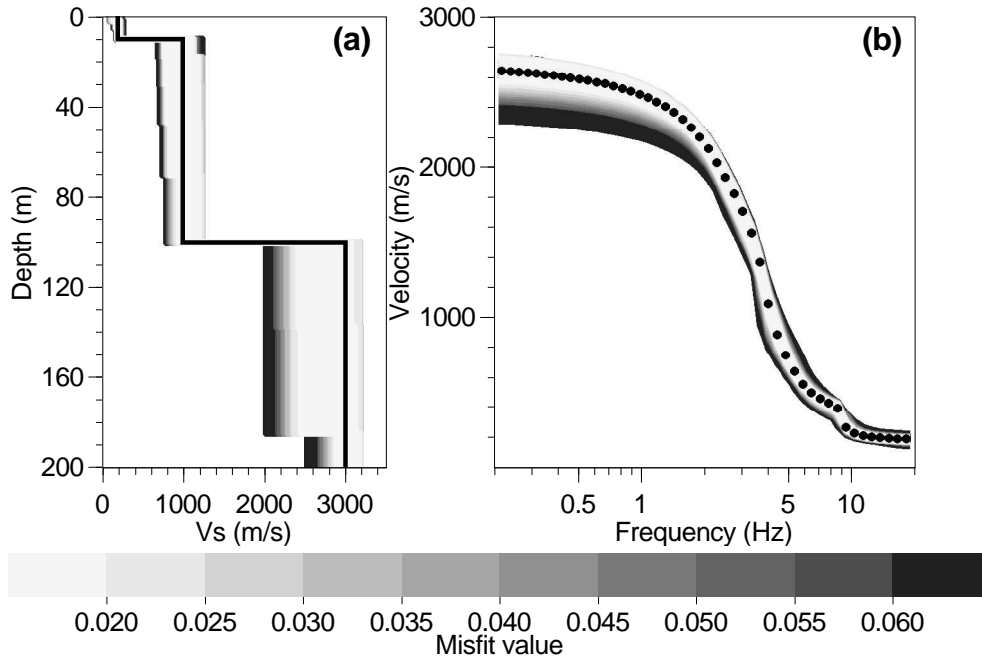


**Figure 4.15:** Inversion with a N-layer model rejecting LVZ by the diagonal method. (a) Resulting  $V_s$  profiles. The black lines are the theoretical velocity profiles. (b) Dispersion curves corresponding to models of figure (a). The black dots are the theoretical dispersion curve used as the target curve during inversion.

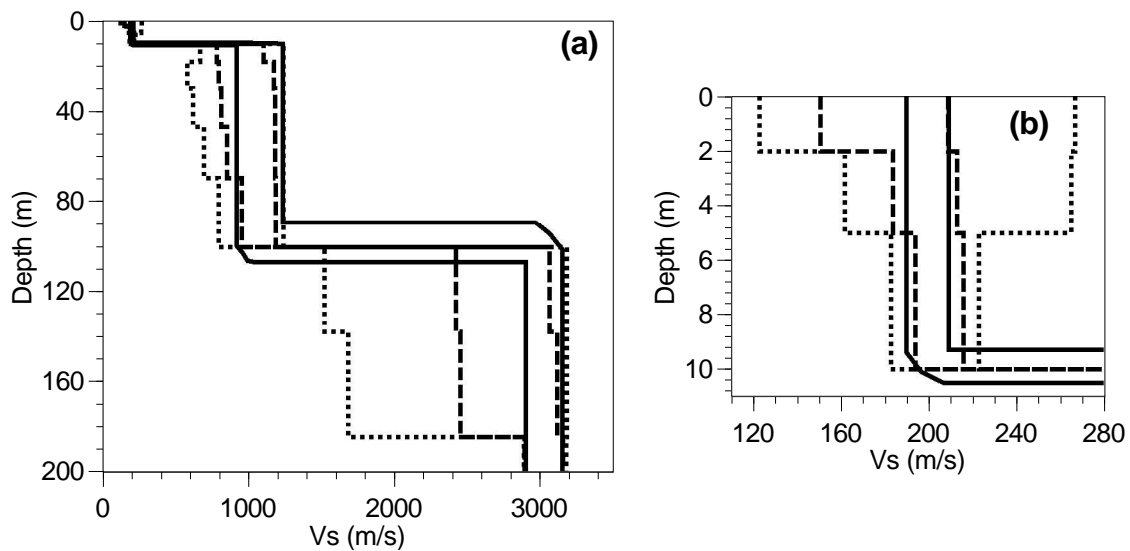


**Figure 4.16:** Comparison of a three-layer and N-layer inversions. The minimum and maximum  $V_s$  for models with a misfit lower than 0.02 are reported for each inversion case: three-layer inversion (plain lines), N-layer with LVZs (dotted lines), and N-layer without LVZs (dashed lines). Figure (b) is a zoom on the first ten metre for clarity.

In figure 4.16, the inversion with a three-layer model and with a N-Layer model accepting LVZs (figure 4.13) or rejecting LVZs (figure 4.15) are compared. The misfit are calculated on the same data curves in the three cases. Only the minimum and maximum  $V_s$  observed at each depth for each case is reported in the figures. The inversion which accepts LVZ always results

with quite large uncertainties compared to the inversions assuming an increase of the velocity with depth. The three-layer inversion gives more information about the depth uncertainty, compared to other cases, whereas it under-estimates the uncertainty on the velocity, especially below the velocity contrasts (between 10 and 70 m, and between 100 and 180 m) and near the surface (between 0 and 5 m).

In conclusion, inverting with a very simple model made of uniform layers does not provide the complete uncertainty about the ground structure. In contrast, the inversion with a great number of layers requires the introduction of relationships between the velocities of adjacent layers, to avoid generating lot of low velocity zones. Those relationships can be translated into parameterization rules for a simple structure where  $V_p$  is constant or increasing.

## 4.4 Non-uniform layers

In the preceding section, it has been shown that simple models with homogeneous layers usually under-estimate the posterior uncertainty. A solution to this issue is proposed in this section by the introduction of vertically heterogeneous layers. A linear and a power law increase of the velocity with depth are considered here. The dispersion curve computation is designed for layers with homogeneous properties. Consequently, in both cases, the variation is discretized by several sub-layers for which properties are managed by the characteristics of the main heterogeneous layer.

### 4.4.1 Linear variation

The velocity (either  $V_p$  or  $V_s$ ) at depth  $z_i$  is given by

$$V_i = V_0 + \frac{V_n - V_0}{z_n - z_0}(z_i - z_0) \quad (4.1)$$

where  $z_0$  is the top of the considered layer,  $V_0$  is the velocity at  $z_0$ ,  $z_n$  is the bottom of the considered layer, and  $V_n$  is the velocity at  $z_n$ . For dispersion curve computations, the function  $V_i(z)$  is discretized into a fixed number of homogeneous sub-layers. Their number ( $n$ ) is generally kept as low as possible (between 5 and 10) to avoid an increase of the inversion computation time. The thicknesses of the sub-layers are all equal. This kind of profile is not implemented in the inversion algorithm based on the standard neighbourhood algorithm. For historical reasons, it is only available for the conditional neighbourhood algorithm.

### 4.4.2 Power law variation

The velocity (either  $V_p$  or  $V_s$ ) at depth  $z_i$  is given by

$$V_i = V_0((z_i + 1)^\alpha - (z_0 + 1)^\alpha + 1) \quad (4.2)$$

where  $z_0$  is the top of the layer considered,  $V_0$  is the velocity at  $z_0$ ,  $\alpha$  is the power-law exponent, generally varying between 0 and 1. The subtraction in equation 4.2 is necessary if the power law variation is used for deep layers ( $z_0 > 0$ ). Like the linear profiles, the function  $V_i(z)$  is divided into a fixed number of homogeneous sub-layers. Setting the exponent  $\alpha$  as a parameter is not a good choice, because it generates models with an uncontrolled maximum velocity. The situation is even worse if several heterogeneous layers are used in the same structure. A better solution is to set the top ( $V_0$ ) and the bottom ( $V_n$ ) velocity as two distinct parameters. For the conditional neighbourhood algorithm, the simple condition  $V_0 < V_n$  is introduced. For the standard neighbourhood algorithm,  $V_0$  and  $dV$  are the parameters,  $V_n$  being equal to  $V_0 + dV$ .  $\alpha$  is calculated by solving the following equation:

$$f(\alpha) = (z_n + 1)^\alpha - (z_0 + 1)^\alpha - \frac{V_n - V_0}{V_0} = 0 \quad (4.3)$$

A few iterations with the bisection method are generally necessary. There is always only one solution between 0 and 1 because  $f(\alpha)$  is monotonously increasing. Other iterative methods are not appropriate.

If the thicknesses of the sub-layers are constant, the power law variation is badly sampled. Very high velocity jumps are observed for the first sub-layers. Thus, it is better to impose a constant velocity jump from one sub-layer to the next one, equal to  $\frac{dV}{n}$ . The depth of the top and of the bottom of each sub-layer is then easily calculated from

$$z_0, \dots, \left( i \frac{dV}{V_0} + (z_0 + 1)^\alpha \right)^{1/\alpha} - 1, \dots, z_n \quad (4.4)$$

Inside each sub-layer, for the sake of simplicity, we set the velocity of the sub-layer to the value of the analytical power law function at the middle of the sub-layer. Hence,

$$V_i = V_0 \left[ \left( \frac{z_{i-1} + z_i}{2} + 1 \right)^\alpha - (z_0 + 1)^\alpha + 1 \right], i = 1, \dots, n \quad (4.5)$$

To summarize, from the thickness of the layer and  $dV$  (or  $V_n$ ), it is possible to define in a unique way the individual thicknesses of each sub-layer and their velocities. An intermediate computation is necessary to obtain the value of the exponent. The exponent  $\alpha$  can be recalculated from the thicknesses and the velocities of the two first sub-layers by solving the equation

$$g(\alpha) = (z_2 + 1)^\alpha - \frac{V_2}{V_1} (z_1 + 1)^\alpha + \left( \frac{V_2}{V_1} - 1 \right) (z_0 + 1)^\alpha = \frac{V_2}{V_1} - 1 \quad (4.6)$$

$g(\alpha) - \left( \frac{V_2}{V_1} - 1 \right)$  is also monotonously increasing and have only one root between 0 and 1. It is solved by bisection.

The parameters for a layer with power law gradient are  $V$  (either  $V_p$  or  $V_s$ ),  $dV$  (or  $V_n$ ), and the thickness  $H$  (or  $z_0$  and  $z_n$ , the depth of the top and of the bottom of the layer). The number of sub-layers is only a tuning parameter.

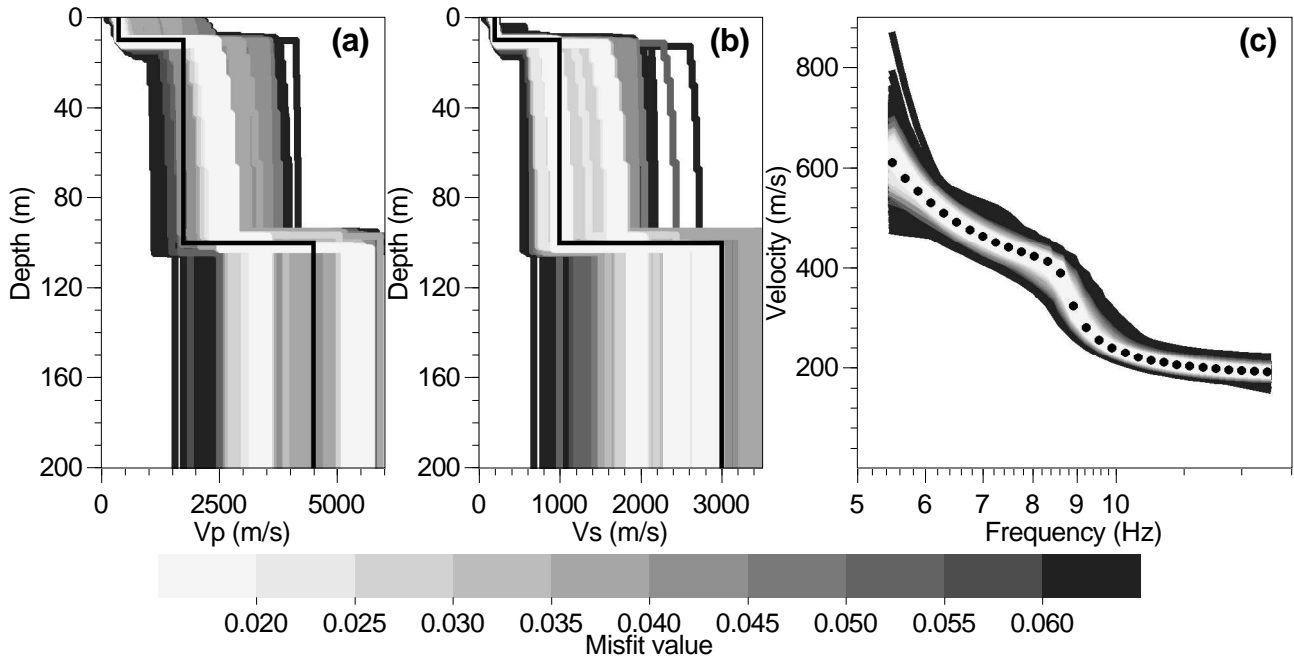


**Figure 4.17:** Inversion with a three-layer model with heterogeneous layers, with prior information about the depth of basement. (a) Resulting  $V_p$  profiles. (b) Resulting  $V_s$  profiles. The black lines are the theoretical velocity profiles. (c) Dispersion curves corresponding to models of figures (a) and (b). The black dots are the theoretical dispersion curve used as the target curve during inversion.

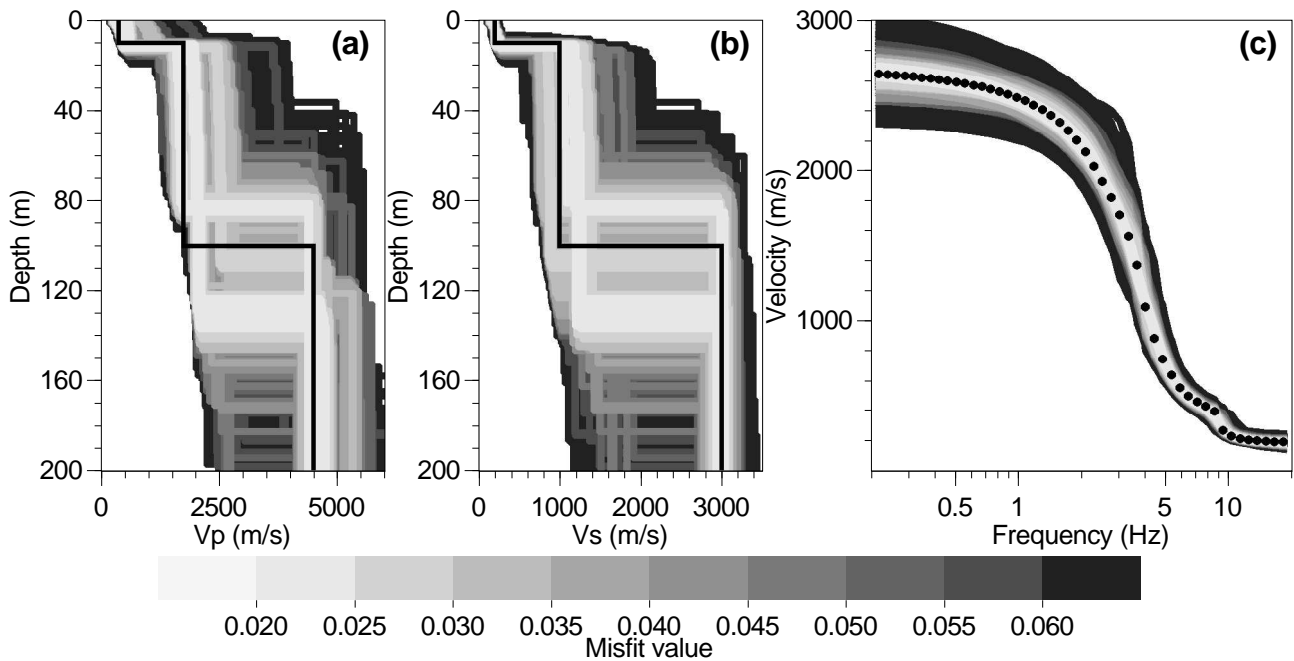


**Figure 4.18:** Inversion with a three-layer model with heterogeneous layers. (a) Resulting  $V_p$  profiles. (b) Resulting  $V_s$  profiles. The black lines are the theoretical velocity profiles. (c) Dispersion curves corresponding to models of figures (a) and (b). The black dots are the theoretical dispersion curve used as the target curve during inversion.

An example of the use of layers with a power law variation in the inversion is shown in figure 4.17. This is the same case as in figure 4.10 where the two first homogeneous layers are replaced by layers with power law variations. The number of fixed layers is five in each case. Two parameters are added to the parameter space (making a total of 10 parameters) of the inversion plotted in figure 4.10. The  $V_p$  variation across the layers can vary between 0 and 2000 m/s. The minimum achieved misfit is similar to the homogeneous case, but the posterior uncertainty on the second layer is larger in these later inversions.

This kind of layer is also tested with a large band dispersion curve (from 0.2 to 20 Hz) in figure 4.18. Compared to figure 4.6, the uncertainty are slightly increased.

## 4.5 Conclusions

To conclude, figure 4.19 summarizes the  $V_s$  profiles obtained for a three-layer inversion with uniform velocity layers (from figure 4.6) and with gradient velocity layers (from figure 4.18), and for a N-layer model accepting low velocity zones (from figure 4.14). The calculated uncertainties are different in each case. The parameterization has a drastic influence over the inversion of dispersion curves, the solution of which is poorly constrained if the correct prior information is not introduced.

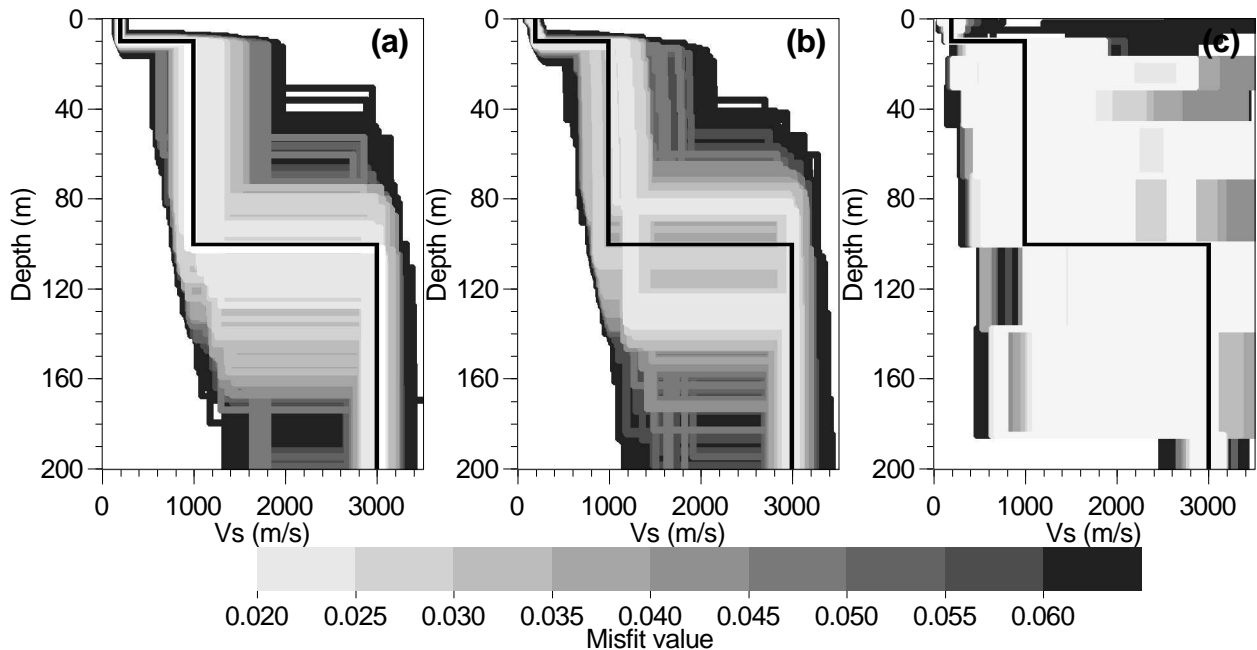


**Figure 4.19:** Comparison of three type of parameterizations ( $V_s$  profiles): (a) inversion with a three-layer model with homogeneous layers, (b) inversion with a three-layer model with gradient layers, and (c) ten layers of fixed thicknesses, accepting low velocity zones.

This chapter shows that even for a simple model with only two contrasts, the inversion of the dispersion curve does not provide one unique solution. This work highlights the need for large band dispersion curves in order to reach deep soil structures. For real cases, the dispersion curves do not have a perfect shape as it is the case in this chapter. Three-dimensional effects, lateral heterogeneities, . . . are some of the effects that may alter the shape of the measured curve.

In this context, the prior information is of prime importance.



# Chapter 5

## Enhanced inversions

In this chapter, the inversion of fundamental Rayleigh dispersion curves (chapter 2) is extended to several types of special inversions. The first part is dedicated to the exploitation of the various modes, including higher Rayleigh and Love modes. The second part deals with the direct inversion of spatial auto-correlation curves. Finally, inversion algorithms are also developed for Rayleigh ellipticity.

### 5.1 Multimodal curves

For ambient vibration and active source experiments, higher Rayleigh modes are sometimes observed. The presence of higher modes depends upon the depth and the type of acting sources and upon the stratigraphy (Aki and Richards 2002, Xia et al. 2003, Socco and Strobbia 2004). For the interpretation of ambient vibrations, there is absolutely no control over the source distribution (space, time and energy content). The apparent velocity measured on vertical components is not always due to body waves and Rayleigh fundamental mode but higher modes may be recorded as well. The inversion of dispersion curves described in the preceding chapters requires that the target curve used to calculate the misfit is effectively the fundamental Rayleigh mode. In a similar way, when processing the horizontal components of ambient noise measurements, the frequency-wavenumber method provides the apparent velocity of the most energetic waves which may be of Love or Rayleigh type. Again, a correct identification of each mode is necessary to proceed with a dispersion curve inversion.

Inverting the higher modes or Love modes may be promising issues to improve the obtained velocity profiles. Xia et al. (2003) suggested that for the same wavelength, the inversion of higher modes can "see" deeper than the fundamental mode. Beaty et al. (2002) observed an improvement of the inversion results when higher modes are included. The horizontal components are high-pass filtered at a frequency lower than the resonance frequency unlike the vertical components high-pass filtered around the resonance frequency (Scherbaum et al. 2003). The horizontal components still carry a sufficient signal to noise ratio to provide reliable information on the wave propagation. Horizontal components contain a mixture of Love and Rayleigh modes but some synthetic tests show that the Love wave may predominate (Bonneyfoy-

Claudet et al. 2004). The measurement of the Love curve at a frequency for which the Rayleigh curve cannot be estimated extends the frequency range of the dispersion curve. Consequently, with the same array deployment, the method can give reliable velocity profiles down to deeper soil structures. Those two assertions are tested in detail with the developed inversion tool.

In a last section, attention is paid to the identification of higher modes. In most cases, confusing two modes have a dramatic influence over the final results and usually ruins the quality of the obtained velocity profiles. A technique has been developed to identify mode in an automatic way.

Like in chapter 2, the reference model used in this section is described in figure 4.1.

### 5.1.1 Rayleigh higher modes

The fundamental mode and the first higher mode are considered here. The first higher mode is inverted alone before being mixed with the fundamental mode. The fundamental mode alone is studied in chapter 4 but it is inverted again to measure the correctness of the first higher mode when only the fundamental mode is used as a constraint. The effect of including the first higher mode with a narrow frequency band is finally estimated.

#### First higher mode alone

The first higher mode curve in figure 4.1(b) is resampled with 30 points and a constant frequency step on a log scale between 2.75 and 20 Hz. This curve is inverted with the parameterization described in table 4.3. The results are shown in figure 5.1. The fundamental mode is required

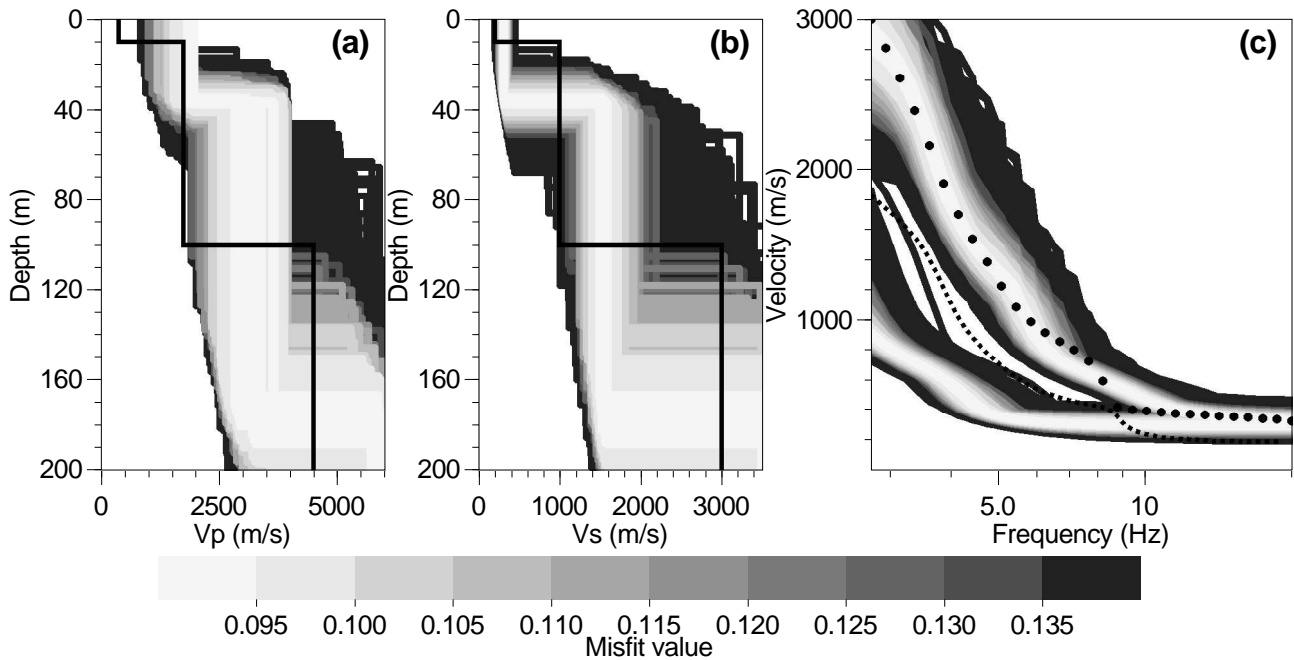


**Figure 5.1:** Inversion of first higher mode alone: no prior information. (a) Resulting  $V_p$  profiles. (b) Resulting  $V_s$  profiles. The black lines are the theoretical velocity profiles. (c) Dispersion curves corresponding to models of figures (a) and (b). The grey curves are the calculated fundamental mode (lowest curves) and the first higher mode (highest curves). The black dots are the theoretical dispersion curve used as the target curve during inversion. The dotted line is the fundamental curve, not used for the misfit computation

to calculate the first higher mode (section 3.1.5). This is why both modes are plotted in figure 5.1(c), clearly visible with two families of curves, the highest velocity values being the first higher mode. The high misfit obtained (compared to less than 0.02 in figure 4.6) is due to the bad fit of the first higher mode between 6 and 12 Hz. When comparing the theoretical fundamental curve (dotted black line) with the calculated fundamental mode (second family of curves, the lowest), a clear gap is observed. In figure 5.1(b), almost no model is generated with a depth of the first interface above 20 m. Contrary to fundamental mode, with this parameterization, the inversion seems to be trapped in a secondary minimum of the parameter space with a misfit around 0.1.

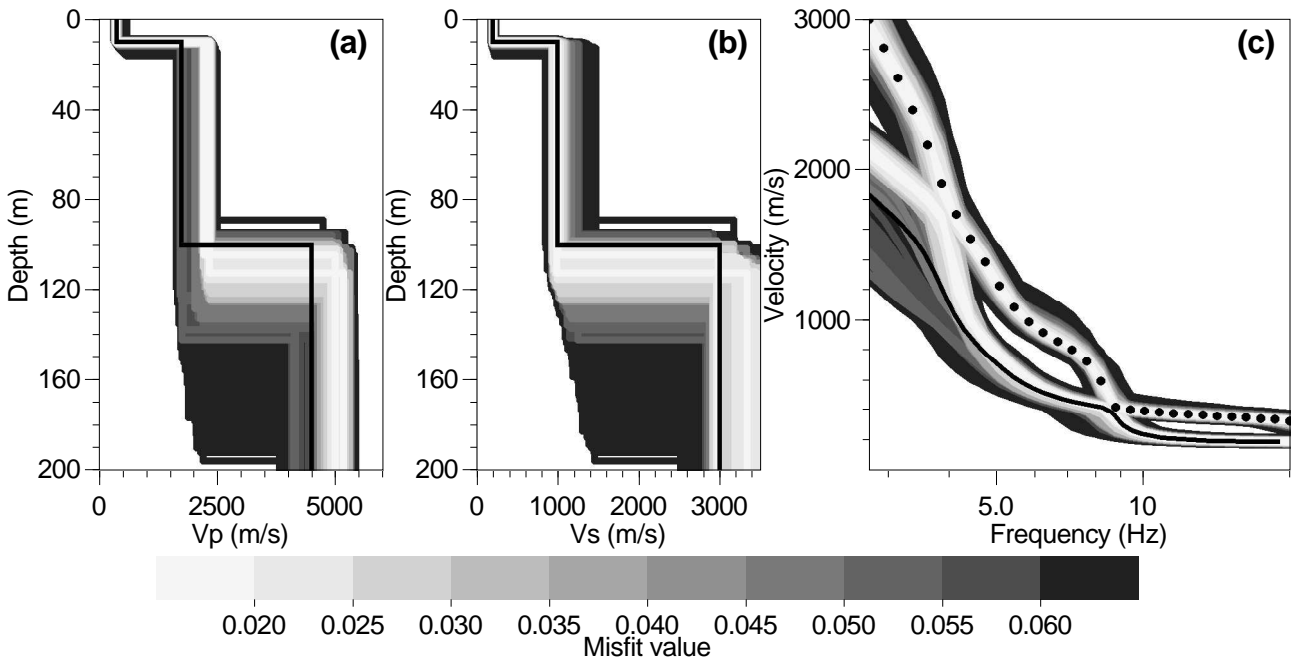


**Figure 5.2:** Inversion of first higher mode alone: depth between 1 and 20 m/s. (a) Resulting  $V_p$  profiles. (b) Resulting  $V_s$  profiles. The black lines are the theoretical velocity profiles. (c) Dispersion curves corresponding to models of figures (a) and (b). The grey curves are the calculated fundamental mode (lowest curves) and the first higher mode (highest curves). The black dots are the theoretical dispersion curve used as the target curve during inversion. The dotted line is the fundamental curve, not used for the misfit computation.

To force the algorithm to explore other regions of the parameter space, the inversion is done again with the interval for the first thickness reduced to  $[1, 20]$  m. The results are displayed in figure 5.2 in the same way as in figure 5.1. A minimum misfit less than 0.01 is found with a depth and a fundamental model that better fit the theoretical model. From 4 Hz and below, the calculated fundamental curve does not follow the theoretical curve. This indicates that the solution is not completely investigated by the neighbourhood algorithm and that the first higher mode does not carry exactly the same information as the fundamental mode. Intensive inversion runs would generate good fitting models with a fundamental mode around the theoretical curve (not done here). In this case, we know that a better solution exists for depths lower than 20 m. But even for real cases, this kind of operation is advised to check the validity of the obtained profiles.

### Fundamental mode alone

To estimate the quality of the information carried by each mode, it is necessary to visit again the fundamental mode inversion. The inversion plotted in figure 4.6 is relaunched with the simultaneous computation of the first higher mode. The results are shown in figure 5.3. Comparing figures 5.2(c) and 5.3(c), where all models with a misfit less than 0.1 are selected, the

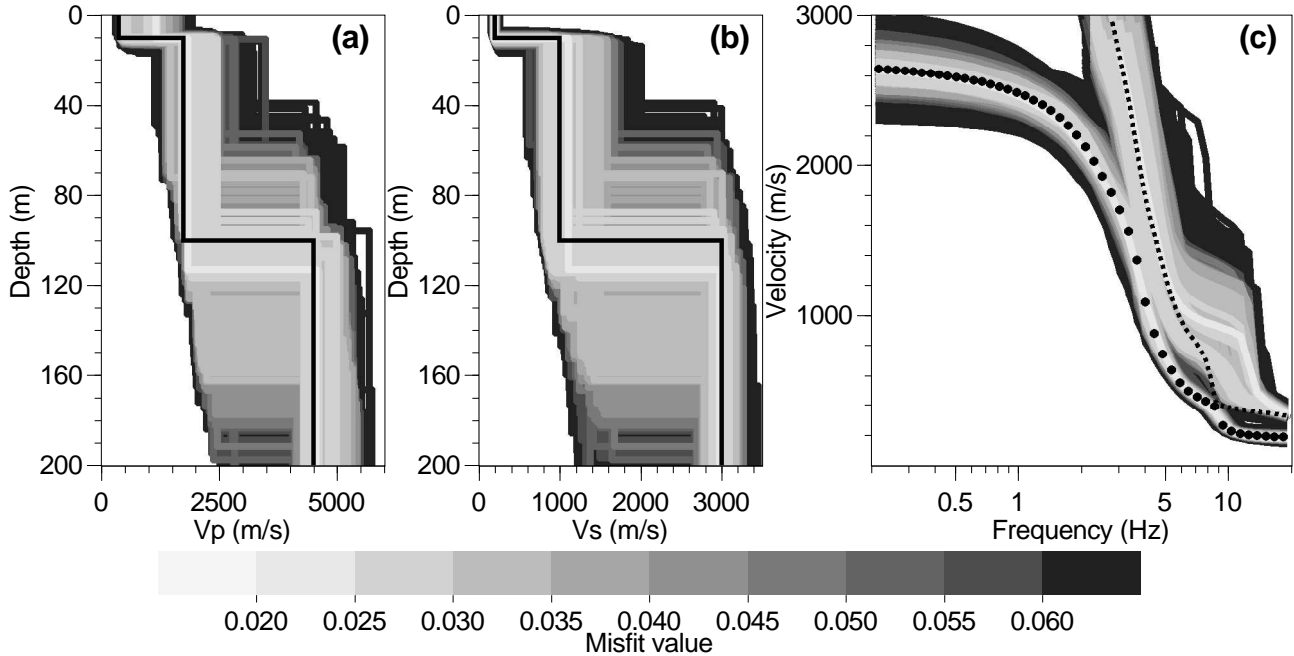


**Figure 5.3:** Inversion of the fundamental mode alone. (a) Resulting  $V_p$  profiles. (b) Resulting  $V_s$  profiles. The black lines are the theoretical velocity profiles. (c) Dispersion curves corresponding to models of figures (a) and (b). The grey curves are the calculated fundamental mode (lowest curves) and the first higher mode (highest curves). The black dots are the theoretical dispersion curve used as the target curve during inversion. The dotted line is the first higher mode, not used for the misfit computation.

deviations around the target curves (black dots) are similar. Obviously, the fundamental curve offers a weaker constraint over the depth of the second layer than the inversion of the first higher mode (figures 5.2(b) and 5.3(b)). However, the fundamental curve inversion does not tolerate  $V_s$  greater than 3400 m/s just below 100 m, whereas for the first higher mode, many models with  $V_s$  greater than 3200 m/s are found with a low misfit. In figure 5.3, the average curve calculated for the first higher mode fits perfectly the theoretical curve for all frequencies below 5 Hz. Between 5 and 15 Hz, the fundamental mode does not constrain the first higher mode, in a similar way that the first higher mode cannot constrain the fundamental mode below 5 Hz (figure 5.2). From these observations, the fundamental curve seems to be necessary below 5 Hz and the first higher mode is mandatory above 5 Hz, other parts are carrying redundant information. These threshold frequencies are valid only for this case and do not have a general meaning.

### Fundamental and first higher modes

To check these conclusions, the fundamental mode below 5 Hz and the first higher mode above 5 Hz are jointly inverted in figure 5.4. The black dots in figure 5.4(c) are the sample points

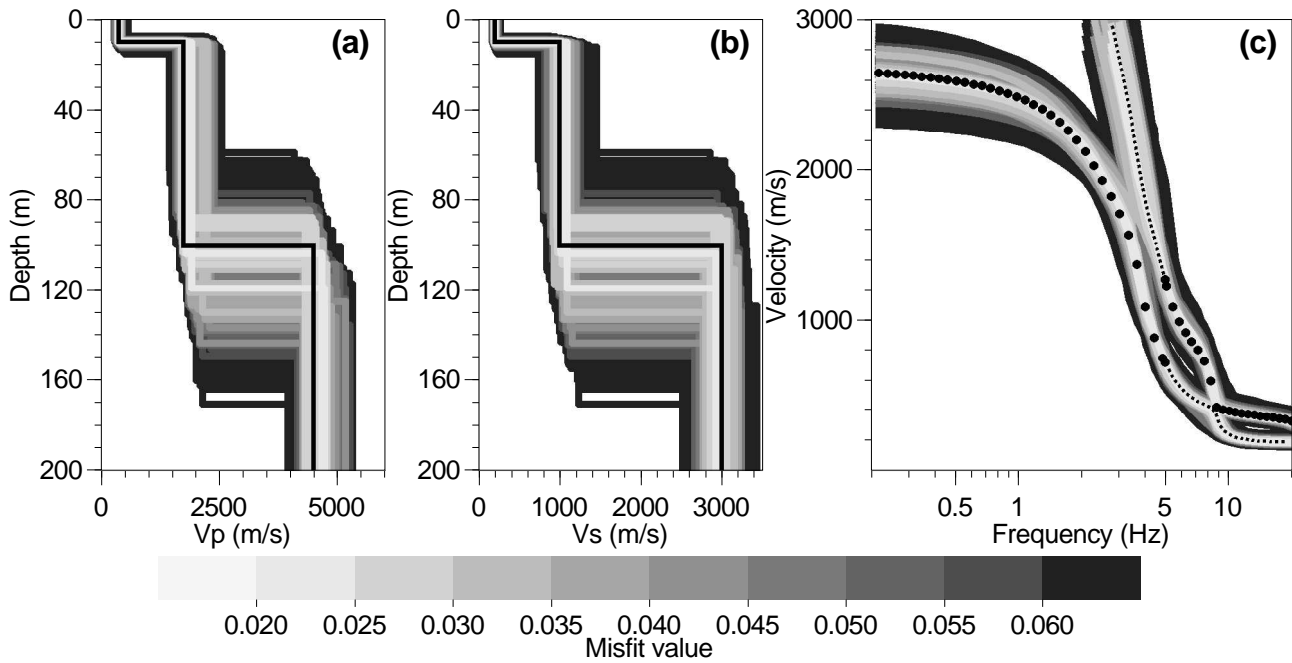


**Figure 5.4:** Inversion of the fundamental and the first higher mode. (a) Resulting  $V_p$  profiles. (b) Resulting  $V_s$  profiles. The black lines are the theoretical velocity profiles. (c) Dispersion curves corresponding to models of figures (a) and (b). The grey curves are the calculated fundamental mode (lowest curves) and the first higher mode (highest curves). The black dots are the theoretical dispersion curves used as the target curve during inversion. The dotted lines are the fundamental and first higher mode not used for the misfit computation.

of the inverted dispersion curve. The thin dotted lines are the theoretical dispersion curves of the unconstrained parts of the dispersion curves. These later ones do not show any special spreading of the calculated dispersion curves, proving that they contain redundant information.

Layer	Depth	$V_p$	$V_s/V_p$	Density
Sediments 1	1 to 20 m	200 to 2,000 m/s	0.01 to 0.707	2 t/m <sup>3</sup>
Sediments 2	30 to 120 m	+10 to 2,000 m/s	0.01 to 0.707	2 t/m <sup>3</sup>
Half-space	–	4000 to 5,000 m/s	0.65 to 0.68	2 t/m <sup>3</sup>

**Table 5.1:** Parameterized model with a basement between 30 and 120 m. The "+" sign stands for incremental velocity: the parameter is the velocity gap between the first and the second layer.

Layer	Depth	$V_p$	$V_s/V_p$	Density
Sediments 1	1 to 15 m	200 to 2,000 m/s	0.01 to 0.707	2 t/m <sup>3</sup>
Sediments 2	15 to 30 m	+10 to 2,000 m/s	0.01 to 0.707	2 t/m <sup>3</sup>
Half-space	–	4000 to 5,000 m/s	0.65 to 0.68	2 t/m <sup>3</sup>

**Table 5.2:** Parameterized model with a basement between 15 and 30 m. The "+" sign stands for incremental velocity: the parameter is the velocity gap between the first and the second layer.

In a real case, the fundamental dispersion curve is rarely available down to 0.2 Hz when the first peak of the ellipticity is at 5 Hz. Usually, one can expect to get a reliable dispersion curve only below 5 Hz, which is redundant with the high frequency part of the first higher mode. As a last example, the inversion of the narrow band dispersion curve shown in figure 4.7 is re-started adding the first higher mode as a supplementary constraint. Like the fundamental mode, the higher mode is rarely well defined at low frequencies. In this case, the first higher mode is

supposed to be observed down to 9 Hz. Five runs are launched with the same parameterization as the inversion of figure 4.7. This parameterization contains very little prior information as reported by table 4.3. The majority of the models generated by the neighbourhood algorithm inside this parameter space have a  $V_s$  below 1500 m/s down to 120 m which can give the illusion that the inversion with the first high mode really offers a better constraint. But three other inversions (two with the parameters of table 5.1 and one with table 5.2) are also run to force the generation of models with a high  $V_s$  at shallow depths. The results displayed in figure 5.5 gather all the models of the eight runs. Comparing with figure 4.7, it clearly shows that the first higher mode does not provide any special information about deeper layers, because it is possible to find models with a very good misfit having almost any  $V_s$  values below 10 or 15 m.

The same composite dispersion curve is also inverted with a prior depth information like in the inversion shown in figure 4.10 (not shown here). There is no significant improvement of the solution induced by the use of the first higher mode.

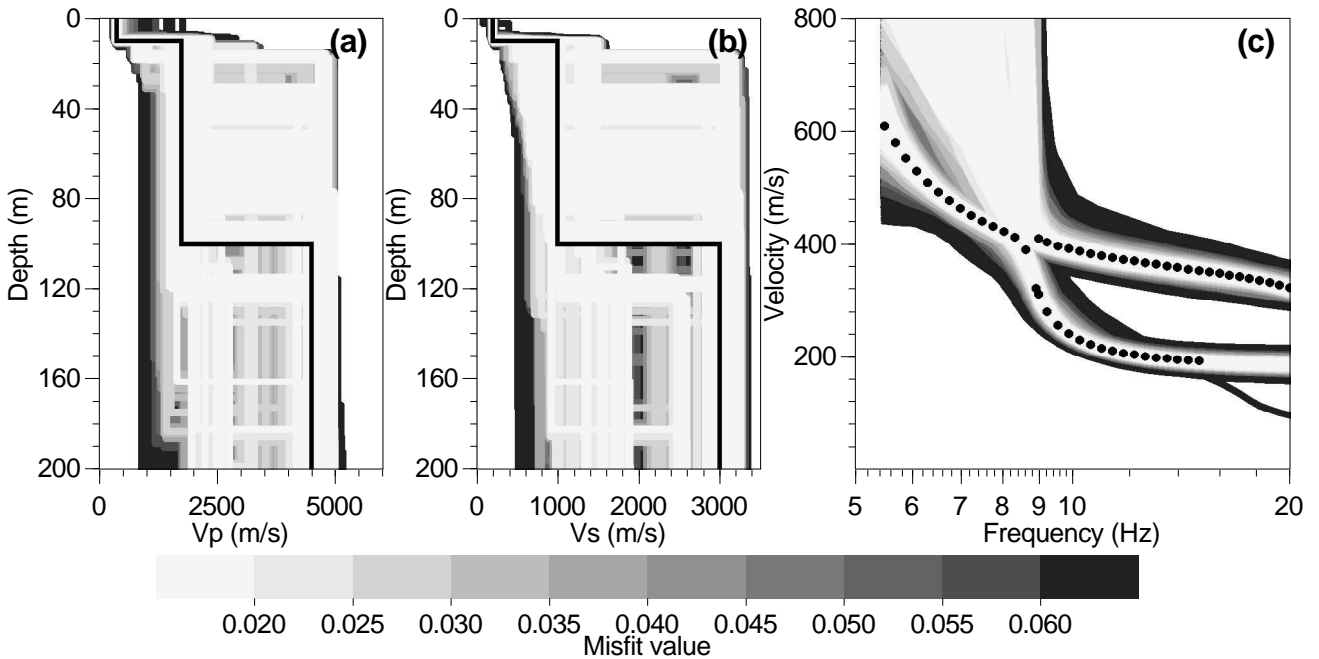


**Figure 5.5:** Inversion of the fundamental and the first higher mode: narrow band. (a) Resulting  $V_p$  profiles. (b) Resulting  $V_s$  profiles. The black lines are the theoretical velocity profiles. (c) Dispersion curves corresponding to models of figures (a) and (b). The grey curves are the calculated fundamental mode (lowest curves) and the first higher mode (highest curves). The black dots are the theoretical dispersion curves used as the target curve during inversion

## Conclusions

In theory, combining the fundamental mode with the first higher mode results in  $V_s$  and  $V_p$  profiles better defined over the whole soil column. The influence of the first higher mode in the inversion is probably more complex than the conclusions of Xia et al. (2003). In our tests, the first higher mode alone better constrains the velocity of the intermediate layer and the depth of the basement than the fundamental mode even defined on a very wide frequency range. However, the velocity of the half space basement is better retrieved with the fundamental mode.

In a real case, the limited range of the available dispersion curves ruins all positive aspects of the inclusion of the first higher mode. Redundancy of both curves (above 5 Hz in this case) just allows a cross-check of the results found with the fundamental curve alone.

### 5.1.2 Love and Rayleigh

From the above results, it can be seen that the measurement of the dispersion curve down to low frequencies is the only way of improving the penetration depth of the method. This issue is documented in chapter 2 for the the Rayleigh dispersion curve. An example of a joint dispersion curve inversion with the low frequency being of Love type is shown. The Rayleigh fundamental dispersion curve is supposed to be available from 5.5 to 15 Hz. The Love fundamental curve is assumed to be observed between 1 and 5 Hz.

Run index	$it_{max}$	$n_s$	$n_r$	parameterization	number of models
1 to 5	150	100	100	table 4.3	5*15100
5 to 10	100	100	50	table 4.3	5*10100
11	100	100	50	table 4.3 with $V_{p1} \in [1600, 2000]$ $V_{s1} \in [1040, 1414]$	10100
12	100	100	50	table 4.3 with $z_2 \in [120, 160]$	10100

**Table 5.3:** Inversion runs for Love-Rayleigh dispersion curves.

Twelve joint inversion processes are launched with distinct seeds and their results are gathered in figure 5.6. The parameters of the neighbourhood algorithm and the parameterization are described in table 5.3. The last two runs (11 and 12) are designed to force the search in particular zones of the parameter space and to make sure that no model with a low misfit can be found there. Comparing with figure 4.6, inverting without the low frequency part of the Rayleigh dispersion does not alter the final result. Even more, the Love dispersion curve allows the retrieval of  $V_p$  and  $V_s$  profiles with a lower uncertainty. Though the Love dispersion curve has no direct relationship with the  $V_p$  profile, its inversion with the high frequency Rayleigh dispersion curves improves the definition of  $V_p$  even for deep layers compared to Rayleigh alone inversions (figure 4.7). This issue is out of the scope of this work.

In conclusion to this brief example, inversion of low frequency Love dispersion curve together with higher frequency Rayleigh dispersion curve is a promising solution to deepen the penetration limits of an ambient vibration experiment. However, these interesting results assume that the Love dispersion curve can be determined with a sufficient degree of confidence.

### 5.1.3 Higher mode identification

In sections 5.1.1 and 5.1.2, the modes are supposed to be correctly identified before proceeding with the inversion. In many real cases when dealing with the vertical component, the apparent dispersion curve with the lowest velocity is usually interpreted as the fundamental mode of Rayleigh waves. For active source experiments measured at high frequencies (above 10 Hz), higher modes may predominate (Gabriels et al. 1987, Forbriger 2003b, Xia et al. 2003, Socco

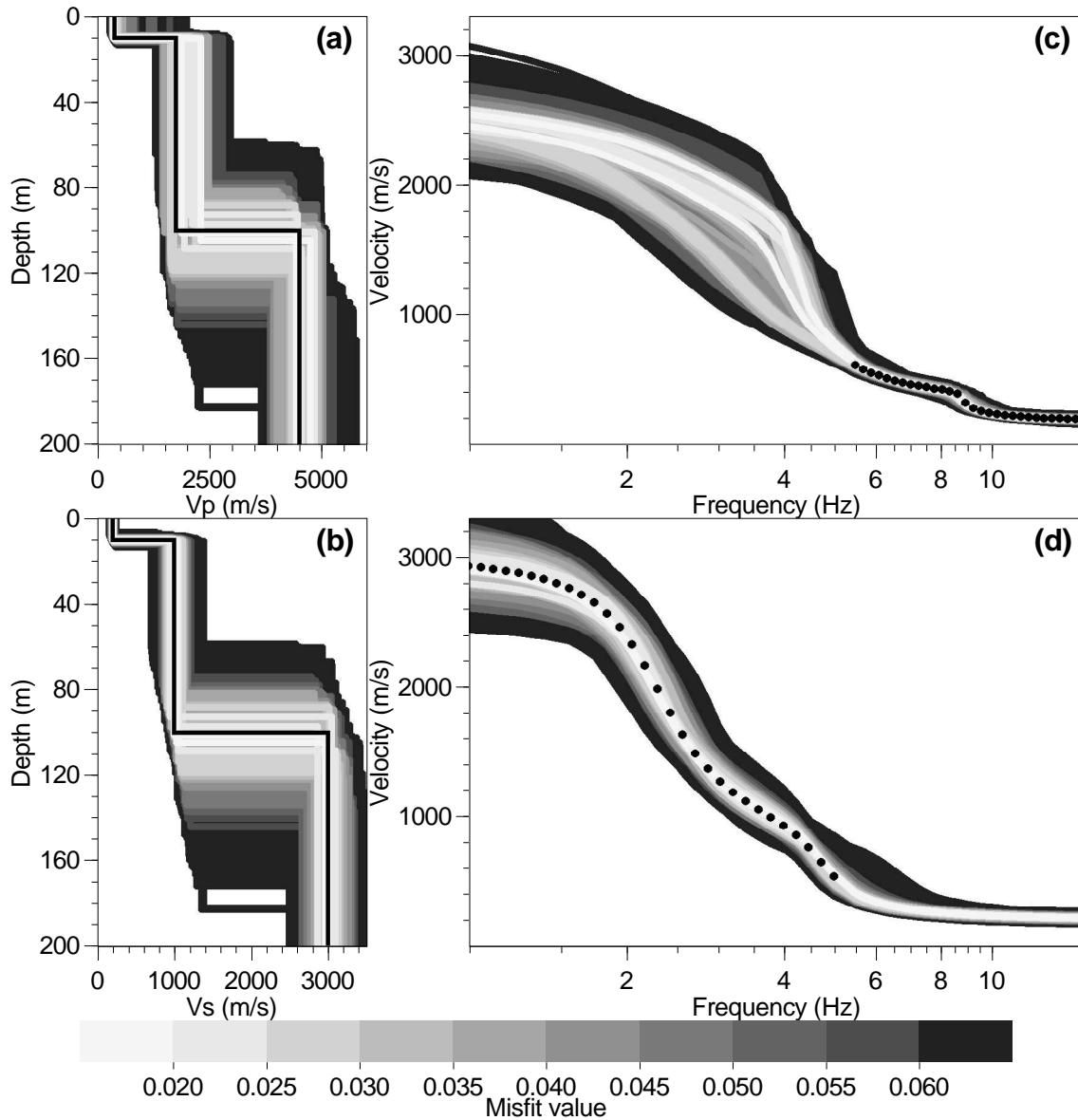


**Figure 5.6:** Joint inversion of the Love and Rayleigh fundamental modes. (a) Resulting  $V_p$  profiles. (b) Resulting  $V_s$  profiles. The black lines are the theoretical velocity profiles. (c) Rayleigh and (d) Love dispersion curves corresponding to models of figures (a) and (b). The black dots are the theoretical dispersion curves used as the target curve during inversion.

and Strobbia 2004). For ambient vibrations, which commonly yield dispersion curve at low frequencies, higher modes are less studied but their presence is sometimes suspected. According to the array resolution power, it is not always possible to separate modes and an intermediate velocity may be observed. In this last case, no post-processing can be considered on the observed apparent velocity values because there are too much parameters to play with (array geometry, source distance, energy partition between co-existing modes, ...). A prior knowledge of the ground structure or other geophysical acquisitions are necessary to detect anomalies on the supposed fundamental dispersion curve. This case is not analysed in this section.

For other cases, a bad identification of modes may ruin all inversion results as demonstrated by Zhang and Chan (2003) and by the following example. The same soil structure as in section 4.2 is used here. In figure 4.1(b), the fundamental and the first higher modes for Rayleigh waves are very close to each other around 9 Hz (osculation point). Depending on experimental

conditions, it may be possible to select a branch below 9 Hz corresponding to fundamental mode and another branch above 9 Hz following the first higher mode. This situation is depicted in figure 5.7 where the observed apparent velocity is marked by black dots. At first glance, the obtained curve may be interpreted as a single fundamental mode. This curve is inverted as

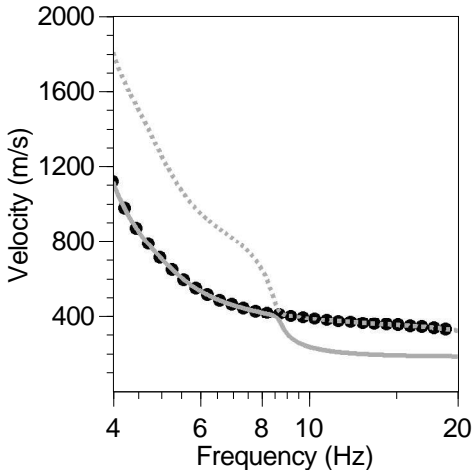


**Figure 5.7:** Composite dispersion curve. The black dots represent the dispersion as it can be observed. The grey line are the theoretical dispersion curves of the fundamental (plain line) and the first higher (dotted line) modes.

the fundamental Rayleigh mode with a prior information that the depth of the basement is situated between 95 and 105 m like in the inversion plotted in figure 4.10. The results of five runs are summarized in figure 5.8. The black lines in figures 5.8(a) and 5.8(b) are the theoretical ground model. The difference is especially strong on the first 20 metres where the velocity profiles are usually well retrieved. There are more than 50% of bias in the obtained results. For real sites, this phenomenon can be detected only if external data or a prior knowledge are also available. Indeed, there is no argument to reject the interpretation of figure 5.8 from the dispersion curve itself.

If the results of the inversion with the fundamental Rayleigh mode are far from the expected profiles, the inversion with other Rayleigh modes can be tested with an inversion algorithm we developed to automatically identify higher modes. The inversion with this option requires only one data curve and the assumption of the number modes ( $n_m$ ) that are encountered by the data curve. For each generated model and for each frequency sample of the data curve,  $n_m$  modes are simultaneously calculated. Compared to usual inversions, the misfit is computed in a completely different way. The velocity difference ( $\delta v_i = v_{di} - v_{ci}$ ) at each frequency between the data velocity and the theoretical Rayleigh velocities of each mode (up to  $n_m$ ) is calculated. Only the minimum value is kept in the summation of equation 3.38. Virtually, the best fitting mode may be different for each frequency sample. However, these kinds of oscillations are rarely observed due to the curve smoothness which naturally restricts the number of mode changes to one or two on the available frequency range. This method effectively adds one or two pseudo degrees of freedom to the inversion problem and it is sometimes necessary to use more restricted parameterized model.

The inversion method is tested on the dispersion curve displayed in figure 5.7 with the assumption that two modes may be present in the experimental curve. Tests with more than two modes have not been carried out so far. The frequency range of the dispersion curve is similar to the range used in figure 4.7<sup>1</sup> where it is clear that no information below 10 m is recovered. The parameterization used in figure 4.10 (table 4.4) offers a slightly better constraint and is chosen for the inversion with automatic mode identification. The results of the five inversion runs (5\*15100 models) are gathered in figure 5.9. In figure 5.9(c), two modes are plotted for

<sup>1</sup>The range is extended to 4 Hz in this case to get larger frequency range for the fundamental mode. Tests with a limit at 5.5 Hz do not work because the velocity rise is not sufficiently marked.

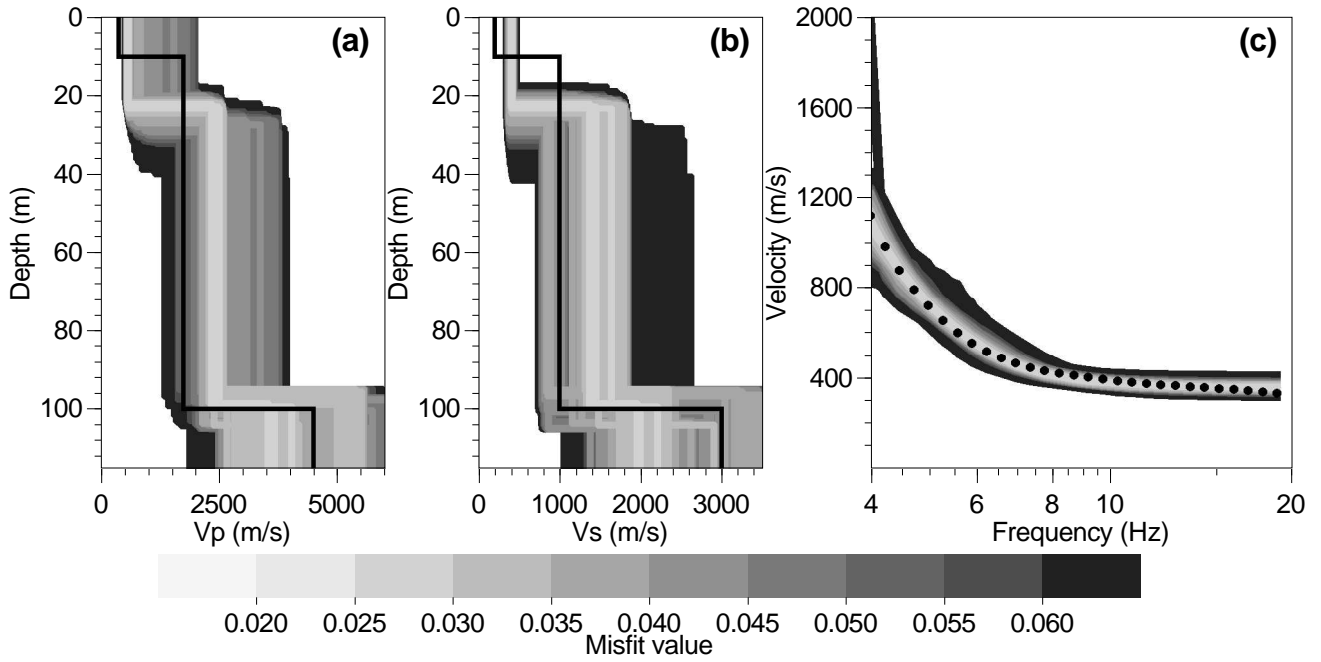


**Figure 5.8:** Inversion of the composite curve assuming fundamental mode. (a) Resulting  $V_p$  profiles. (b) Resulting  $V_s$  profiles. The black lines are the theoretical velocity profiles. (c) Fundamental mode dispersion curves corresponding to models of figures (a) and (b). The black dots are the composite dispersion curves used as the target curve during inversion.

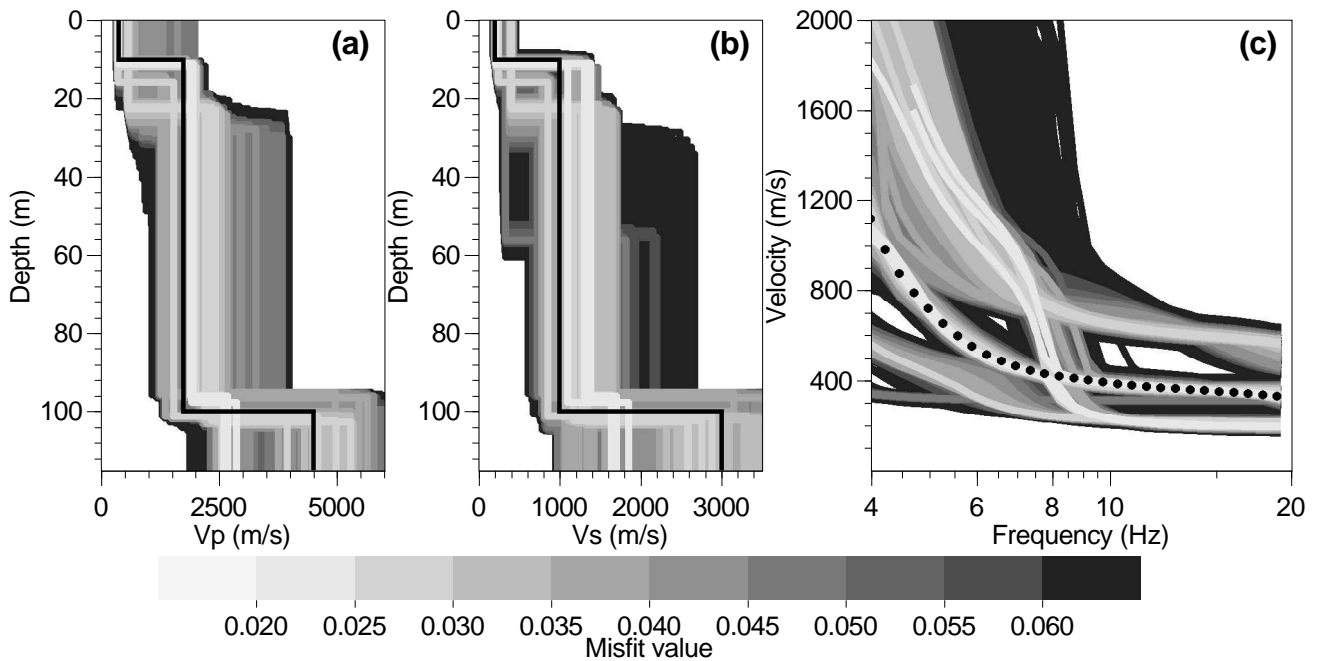


**Figure 5.9:** Inversion of the composite curve with mode identification. (a) Resulting  $V_p$  profiles. (b) Resulting  $V_s$  profiles. The black lines are the theoretical velocity profiles. (c) Fundamental and first higher mode dispersion curves corresponding to models of figures (a) and (b). The black dots are the composite dispersion curves used as the target curve during inversion.

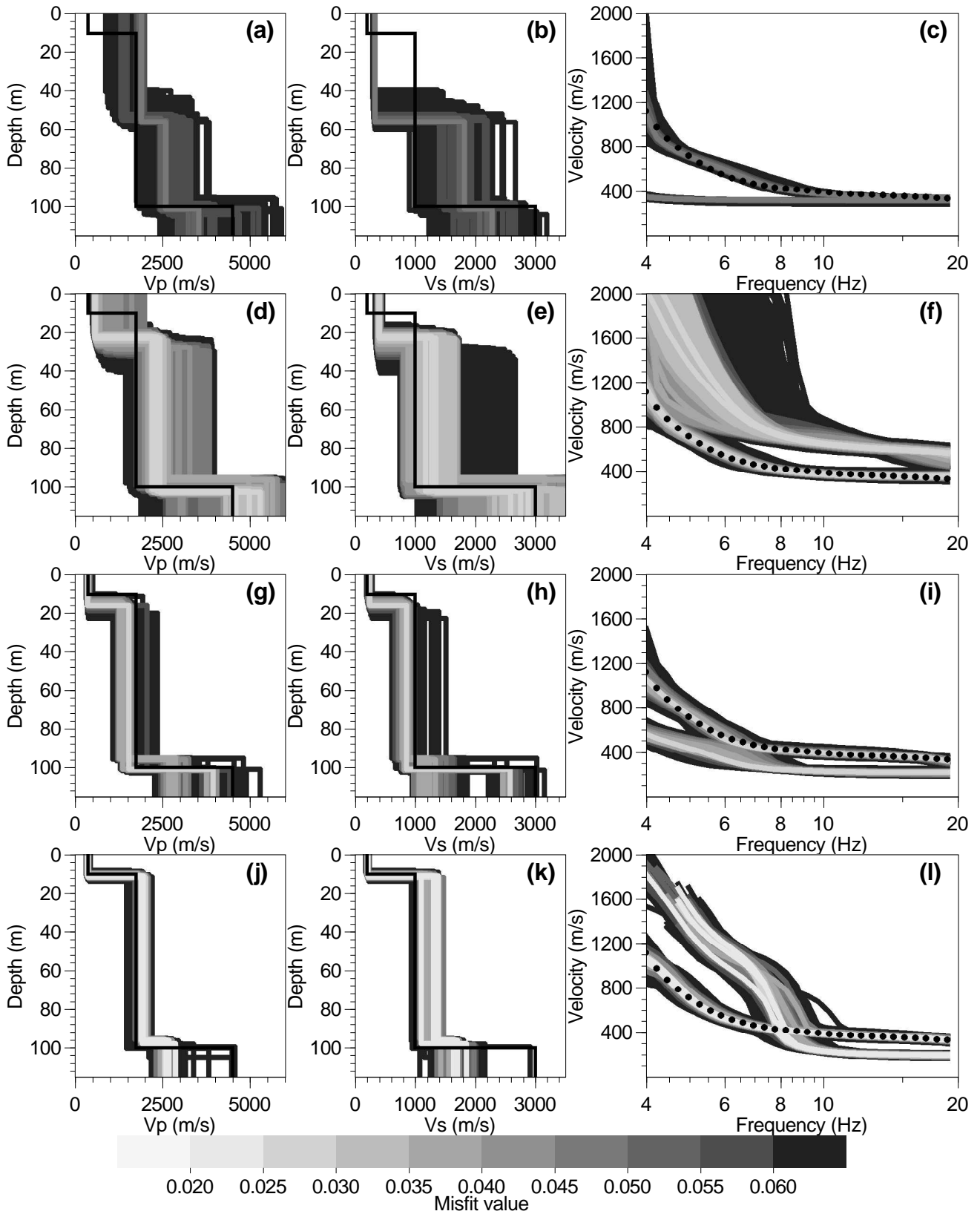


**Figure 5.10:** Inversion of the composite curve with mode identification, splitting model families. (a), (d), (g), and (j) Resulting  $V_p$  profiles. (b), (e), (h), and (k) Resulting  $V_s$  profiles. The black lines are the theoretical velocity profiles. (c), (f), (i), and (l) Fundamental (below) and first higher (above) mode dispersion curves corresponding to models of the other figures. The black dots are the composite dispersion curves used as the target curve during inversion (see text for details).

each model in figures 5.9(a) and 5.9(b).

Four families of curves with low misfit values can be distinguished. For clarity, these four categories are shown individually in figure 5.10. In the first category (figures 5.10(a) to 5.10(c)), the data curve is considered as being entirely the first higher mode. The minimum achieved misfit is higher (0.055) than for other groups, but it does not automatically mean that models are to be discarded. Valid arguments to reject them would be that superficial measurements revealed a lower  $V_s$  or that a strong contrast between 40 and 60 m is not geologically admissible. The second category is the same as our first hypothesis (all data considered as fundamental mode). Lower misfit values are obtained (0.025). Here again, complementary acquisitions about the superficial  $V_s$  or depth criteria help to discard those models. In the third family of models, the data curves is also likened to first higher mode but in a different way than the first category. Here the difference with the theoretical model in terms of  $V_s$  and depth is more subtle. The measurement of the dispersion curve on a larger frequency band, for instance if Love modes can be observed, may help the interpretation. And finally in the last category, a mode jump is noticed around 9 Hz and the velocity profiles correspond to the theoretical ground model. The parameter space sampling is certainly not exhaustive for depth below 100 m. Further model generation can be conducted with a shallow depth restricted around 10 m to get a more complete and confirmed model uncertainty (not done here). Tests were conducted with the parameterization of table 4.3 but nothing could be retrieved due to the insufficient level of constraint.

This algorithm allows a great flexibility to scan the various modes possibly contained in the observed dispersion curve. However, it adds at least one more degree of freedom, increasing then the non-uniqueness of the problem. The prior information is here, probably more than elsewhere, of prime importance to select the right model family.

Exactly the same technique has also been tested on synthetics to identify Love and Rayleigh modes (not shown here).

## 5.2 Spatial auto-correlation

In section 3.3, it is shown that auto-correlation curves are theoretically calculated from the dispersion curves. Classically, obtaining the  $V_s$  profile at one site is a two-stage processing: derivation of the dispersion curve from the auto-correlation curves with a least-square scheme (e.g. Betti et al. 2001) and inversion of the dispersion curve to determine the  $V_s$  profile. Recently, Asten et al. (2004) proposed to merge them into a single inversion based on least-square optimisation (Herrmann 1994), allowing the determination of  $V_s(z)$  directly from the auto-correlation curves. The approach proposed here is conceptually the same except that we make use of the neighbourhood algorithm (section 2.3) for the inversion. It allows an exploration of nearly all equivalent minima in terms of the misfit function and thus enables additionally an improved uncertainty analysis when compared to classical linearized inversion schemes (least-squares). Shapiro (1996) showed, that the solutions obtained from classical

surface wave inversion schemes are too restrictive and uncertainties are not correctly estimated.

The text and the figures of this section are extracted from a paper we submitted to the Bulletin of Seismological Society of America in October 2004. This is why the reference model utilized here below differs from the one used in other sections.

### 5.2.1 Uniqueness of auto-correlation curves

The auto-correlation inversion has basically the same limits as the dispersion curve inversion, as auto-correlation curves are calculated from dispersion curves: non-uniqueness, loss of resolution with depth and equivalence for profiles with low velocity zones. As we plan to invert auto-correlation curves to obtain  $V_s$  profiles, we first address the question of the relationship between auto-correlation and dispersion curves. Obviously, equation (3.47) does not insure a one-to-one relation between the two types of curves, as the arguments for  $J_0(x)$  that satisfy equation (3.47) can be numerous for small values of  $\overline{\rho(r, \omega)}$ . However, equation (3.47) does not imply any coupling of  $c(\omega)$  with the auto-correlation at other frequencies than  $\omega$ , meaning that the inversion can be made independently frequency by frequency. Consequently, transforming auto-correlation curves at frequency  $\omega$  into their equivalent common dispersion curve is just a matter of solving a system of equations of the same form as (3.47) (one equation by considered ring) and solutions  $c(\omega)$  are discrete numbers. If all the auto-correlation curves for the different rings are consistent with each other, there is a minimum of one solution that satisfies all apertures. From the discrete nature of the solutions and the number of rings likely to be considered, there is little chance of having two distinct solutions for  $c(\omega)$  that perfectly match all equations.

### 5.2.2 Synthetic model

The inversion method is first applied on a perfect synthetic model defined by a sedimentary layer overlying a rocky basement.  $V_s$  and  $V_p$  values inside the two layers are plotted on figure 5.11(a) and 5.11(b) (black lines). We set up a 100 m aperture array with a quasi-circular shape characteristics of which are given in figure 3.24(a). From the azimuth-distance plot of figure 3.24(b), we selected five distinct rings including 7 to 12 station pairs each, with an average of ten. The limits of rings are arbitrary chosen. Parametric tests show that the final results are very little dependent on the ring selection. We introduce uncertainties into the original model assuming a normal distribution around the average model (black plain lines, figures 5.11(a) and 5.11(b)) with the standard deviation shown by dotted lines in the same figure. Theoretical auto-correlation ratios were computed for 5000 randomly generated models, keeping Poisson's ratio constant. Auto-correlation curves for the five rings are regularly distributed around the ones computed for the average model (black dots of figures 5.11(d) to 5.11(h)).

### 5.2.3 Validation of auto-correlations

The measured auto-correlation curves do not always fit the shape of Bessel's function and the system of auto-correlation equations (of type (3.47) or (3.48)) may have no common solution for

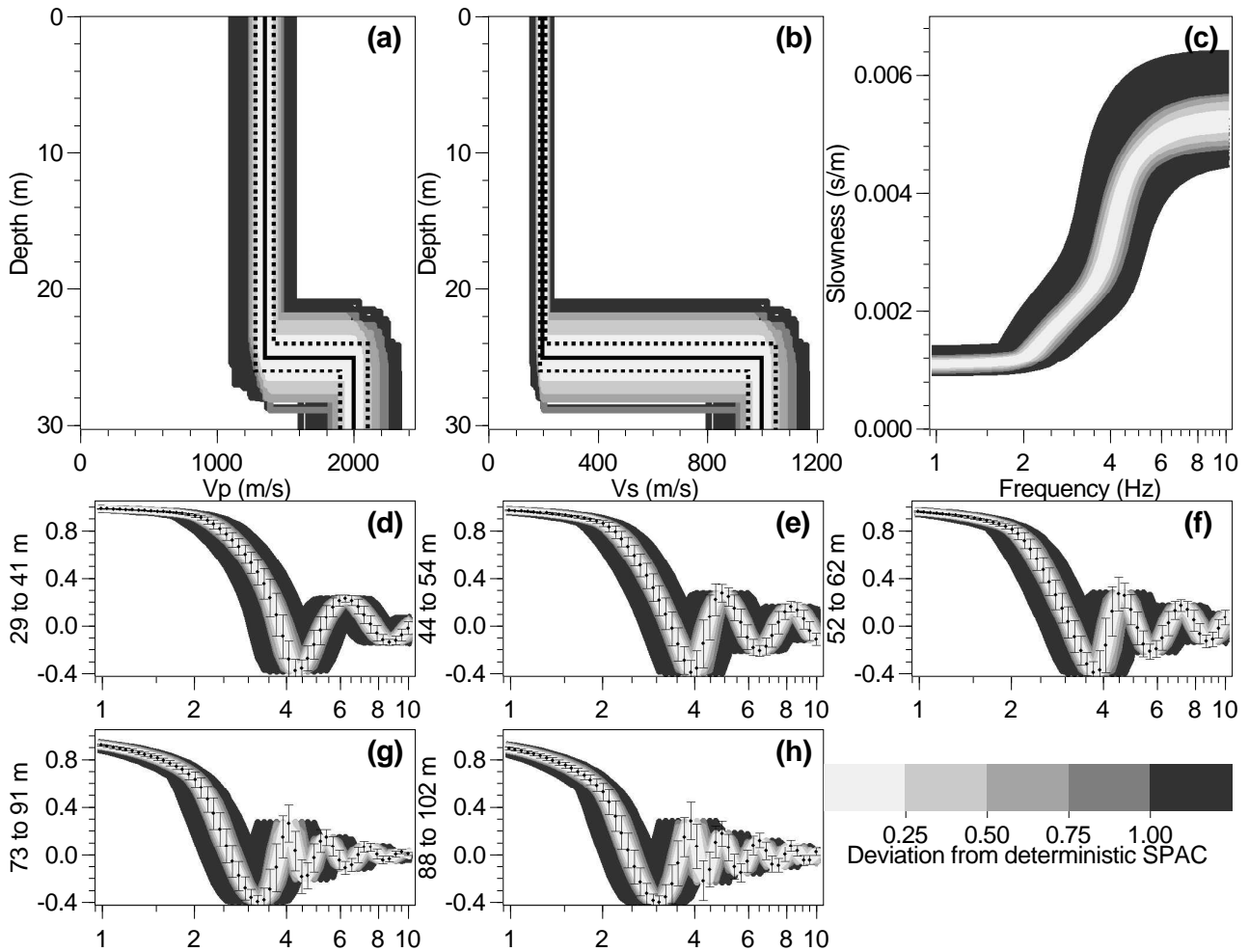


**Figure 5.11:** Reference model for auto-correlation inversion. (a)  $V_p$  profiles: input average model (plain line), input standard deviations (dotted lines) and generated random models ranked by their auto-correlation misfit (common grey scale). (b)  $V_s$  Profiles: same legend as for  $V_p$ . (c) Dispersion curves of random models for the fundamental mode of Rayleigh. (d) to (h) Auto-correlation ratios for chosen rings plotted against frequency, average and standard deviation for all samples (dots).

all array apertures. Feeding the inversion process with contradictory auto-correlation curves is likely to give an uncontrolled average solution. If the contradiction comes from a defect in the array response (e.g. too wide aperture for the considered wavelength) or in the noise content (e.g. uncorrelated noise due to long distance between sensors for the considered frequency, or insufficient energy level at low frequency), the probability of obtaining an unrealistic solution is high. A selection of the relevant parts of the auto-correlation curves is thus necessary. The problem is complex and there are no objective and commonly applicable rules. Without a prior knowledge of the soil structure, the only reliable features are the array geometry and the auto-correlation curves themselves. From the array geometry, some rough limits can be deduced for a correct response in terms of wavenumber (Woods and Lintz 1973, Asten and Henstridge 1984), theoretically for the frequency-wavenumber processing only (section 1.1.1 on page 7). On the other hand, from the auto-correlation curves for the different rings, we can test the consistency of the system of equations, and discard the samples that are obviously out of the general trend.

Practically, from a very large a priori in terms of apparent velocity (e.g. from 100 to 3000

m/s), all possible solutions  $c(\omega)$  of equation (3.47) or (3.48) are calculated independently for each ring. For doing so, we define the function:

$$g(c, \omega) = \overline{\rho_{calc}(r, \omega, c)} - \overline{\rho_{obs}(r, \omega)} \quad (5.1)$$

where,  $\omega$  is the considered frequency band,  $\rho_{calc}$  is calculated by equation (3.47) or (3.48), and  $\rho_{obs}$  is the auto-correlation ratio calculated on the recorded signals. The roots of function  $g(c, \omega)$  are successively bracketed by a coarse grid search starting from the lowest velocity, and then refined by an iterative scheme based on the Lagrange polynomial constructed by the Neville's method (Press et al. 1992). The same algorithm as for the internal computation of dispersion curves is used (section 3.1.5). In a second stage, we construct a grid for each ring in the frequency-slowness domain. The grid cells are filled with 1 if at least one solution exists within the cell, with 0 in the contrary case. All the grids are stacked and the values in each cell give the number of consistent rings for a particular couple frequency-slowness.

If the auto-correlation curves are consistent, the cells where the density of solutions is maximum should delineate the corresponding dispersion curve. From this plot, we determine the minimum and the maximum slowness for each frequency, as well as the minimum and the maximum wavenumber for which we observe a focused dispersion curve. To reduce the subjectivity of the selection, zones where no clear consistency between auto-correlation curves is observed are systematically rejected. Once the dispersion curve limits are set, it is straightforward to reject the contradictory data on the auto-correlation curves. This procedure is tested on the pure synthetic case (figure 5.11) where no contradictory samples are present in the auto-correlation curves. Figure 5.12 shows the resulting frequency-slowness grid obtained after seeking for all possible solutions. The dispersion curve can be entirely retrieved from the auto-correlation curves between 1 and 10 Hz. When the auto-correlation value is less than 0.025 (arbitrary threshold to avoid an infinite number of solutions), no solution is calculated. This is why, for high frequency, the large apertures provide no points and hence the density vanishes to one or two occurrences only.

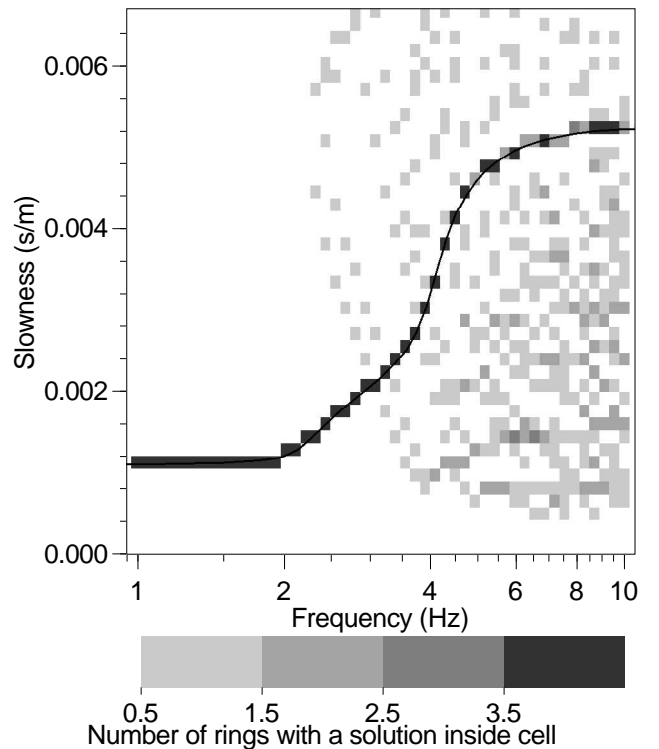


**Figure 5.12:** Grids in frequency-slowness domain representing the density of dispersion curve solutions. (a) Solutions of equation (3.48) for the perfect auto-correlation curves of figure 5.11. The theoretical dispersion curve is represented by a plain line.

When the auto-correlation value is less than 0.025 (arbitrary threshold to avoid an infinite number of solutions), no solution is calculated. This is why, for high frequency, the large apertures provide no points and hence the density vanishes to one or two occurrences only.

### 5.2.4 Inversion

A two-layer model is considered with the parameter ranges specified in table 5.4. In the shallow layer, the velocity can increase with a power law relation, and the parameters are four ( $V_p$ ,  $V_s/V_p$ , the thickness and the  $V_p$  increase between the top and the bottom). The constant velocity layer corresponding to the true model is a particular realization of the parameterization. The bedrock parameters are two ( $V_p$  increase, and  $V_s/V_p$ ). The neighbourhood algorithm has been started using 3 independent runs with distinct random seeds, generating a total of 30,000 models. Among them about 13,500 have a misfit less than 1 and are plotted in figure 5.13. The lowest misfit is 0.03.

Layer	Thickness	$V_p$	$V_s/V_p$	Density	$V_p$ variation
Sediments	10 to 50 m	200 to 2,000 m/s	0.01 to 0.707	2 t/m <sup>3</sup>	10 to 1,000 m/s
Half-space	–	+10 to 3,000 m/s	0.01 to 0.707	2 t/m <sup>3</sup>	–

**Table 5.4:** Parameters for auto-correlation inversion. The “+” sign stands for incremental velocity: the parameter is the velocity gap between the first and the second layer. The power law gradient across the first layer is represented by a stack of 5 sub-layers. The value of the parameter is the total velocity variation across the layer.

The  $V_s$  and  $V_p$  models resulting from the auto-correlation inversion are plotted in figures 5.13(a) and 5.13(b) with their misfit value. On these figures, is drawn the theoretical model of figure 5.11. Most of the solutions with a misfit lower than 0.4 are able to explain in a consistent way the auto-correlation data given their standard deviations (figures 5.13(a) and 5.13(b)). In figure 5.13(c) are plotted the corresponding dispersion curves. The  $V_s$  profile (figure 5.13(b)) is very well constrained from 6 to 20 metres deep. The very superficial layers (less than 6 m) are at a depth lower than one third of the minimum wave length (20 m) and  $V_s$  values are less constrained, resulting from the limited bandwidth at high frequency. Below 35 metre,  $V_s$  values are well retrieved due to the wide low frequency range of the auto-correlation curves. In real data, this well constrained velocity in the bedrock is usually missing due to the site high-pass filter of the Rayleigh waves below the fundamental frequency (Scherbaum et al. 2003, chapter 6). The dispersion curves computed for the best fitting models compare very well with the theoretical one (figures 5.11(c) and 5.13(c)). The resolution is relatively poor between 22 m and 35 m: a velocity jump at 22 metres gives a misfit value equivalent to the one for a contrast at 35 metres. Other inversion tests (not presented here) have shown that this lack of resolution results from the uncertainties considered on the auto-correlation data. However, the lowest misfit model correctly finds an interface around 25 m depth.

Usually,  $V_p$  has a low influence on the dispersion curve, and hence on the auto-correlation curves. Boore and Toksöz (1969) proved for a five-layer model that the influence of  $V_p$  on the dispersion curve is about one tenth the influence of  $V_s$ . However, for low Poisson’s ratios,  $V_p$  has more influence. In this latter situation, the final  $V_s$  profile depends upon the correctness of the  $V_p$  profile. In classical iterative inversions (least-square scheme),  $V_s/V_p$  or Poisson’s ratio is kept constant because the small influence of  $V_p$  on the auto-correlation curves generally leads to unrealistic velocities. For the neighbourhood algorithm inversions, the parameterization is

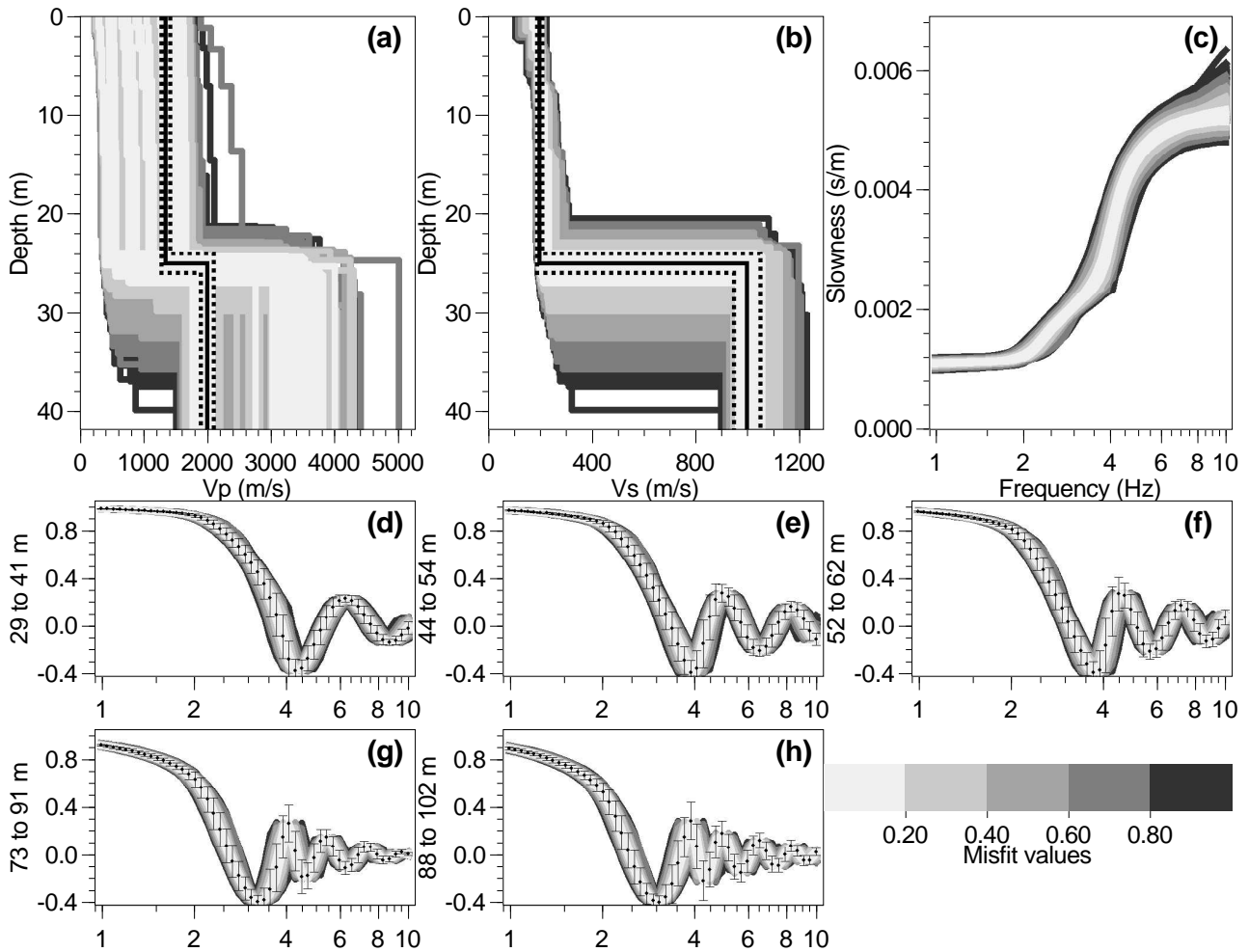


**Figure 5.13:** Inversion of the auto-correlation curves. (a)  $V_p$  profiles: true average model (plain line), true standard deviations (dotted lines) and inverted models ranked by their auto-correlation misfit (common grey scale). (b)  $V_s$  Profiles: same legend as for  $V_p$ . (c) Dispersion curves of generated models. (d) to (h) Auto-correlation ratios for chosen rings plotted against frequency, average and standard deviation of data points to be fitted (dots).

easily adjusted to fit the physical limits of  $V_p$  and the prior information, for instance, about the superficial values of  $V_p$ . When no information is available about  $V_p$ , it is still used as a parameter with large prior intervals to prevent from altering the final result with unreliable assumptions. For this inversion test, we assumed that no prior information exists on  $V_p$ . As the Poisson's ratio for the theoretical model is 0.49, the compressional-wave velocity ( $V_p$ ) profile is badly recovered. Equivalent models are found for the whole prior  $V_p$  range (from 200 to 2000 m/s in the upper layer).

### 5.3 Ellipticity inversion

The principles and the solutions developed for the inversion of the Rayleigh ellipticity are discussed in section 3.2. The ellipticity shown in figure 4.1(d) is first inverted alone with a simple model made of one layer overlaying an infinite half-space. The shape of the ellipticity curves is not inverted but only the frequency of peak, which is exactly found at 5.63 Hz. The secondary peak at 3 Hz is not considered here. It is not possible to retrieve a complete ground structure only from the frequency of the ellipticity peak. Hence, a model with only two parameters (thickness and  $V_{s0}$ ) is used in the inversion, detailed in table 5.5. The  $V_s/V_p$  value in the half space is fixed to ensure a constant  $V_s$  of 1000 m/s. Five runs are launched with ten iterations each generating a total of 5500 models. The minimum misfit achieved is 0, because only one single frequency is fit with a precision of  $10^{-3}$  Hz. The results are shown in figure 5.14. A clear relationship between the thickness and  $V_{s0}$  is found corroborating the conclusions of Scherbaum et al. (2003) about the inversion of the frequency of the ellipticity peak for a two-layer model. The theoretical model has a  $z_1$  of 10 m and  $V_{s0}$  is 200 m/s.

Layer	Thickness	$V_p$	$V_s/V_p$	Density
Sediments	1 to 50 m	375 m/s	0.01 to 0.707	2 t/m <sup>3</sup>
Half-space	–	1750 m/s	0.57143	2 t/m <sup>3</sup>

**Table 5.5:** Parameters for ellipticity alone inversion.

The last example confirmed that the frequency of the ellipticity peak contains pertinent information about the thickness and the shear velocity of the first layer. The ellipticity target is then added to a usual dispersion curve inversion to test its ability to improve the final solution. The case of a narrow frequency band and a two-layer parameterization inverted in figure 4.5 is utilized again. As detailed in section 3.2, the misfit is calculated by a weighted sum of the dispersion and the ellipticity misfits. 10 and 90 % weights were chosen for the dispersion and the ellipticity misfits, respectively. This ensures that nearly all generated model are complying with an ellipticity peak at 5.63 Hz. Consequently, to achieve a comparable good fit of the dispersion curve as in figure 4.5, the misfit scale is divided by 10. Five runs are launched with the parameters described in table 4.2. To make sure that the parameter space is sufficiently sampled in terms of  $z_1$  (depth of the top of the half space), two more inversion processes are started with the depth restricted to [8, 10] m and [11, 14] m, respectively. The ensemble of all models with a misfit less than 0.01 is plotted in figure 5.15.

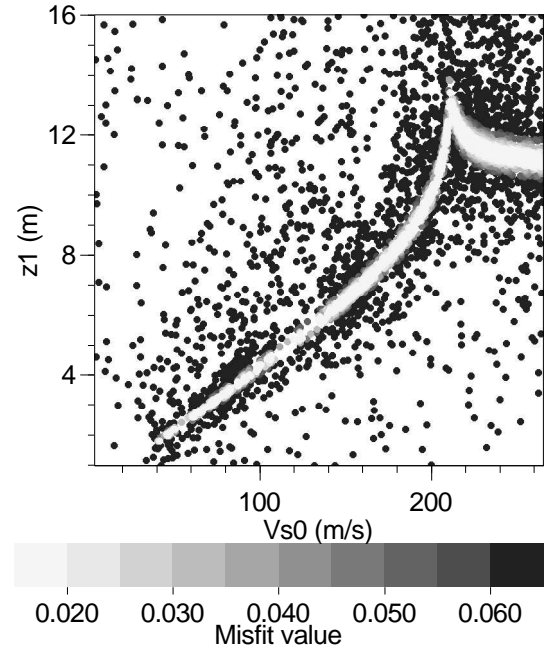


**Figure 5.14:** Inversion of the ellipticity alone showing the trade-off between the depth of the velocity contrast and  $V_s$ .

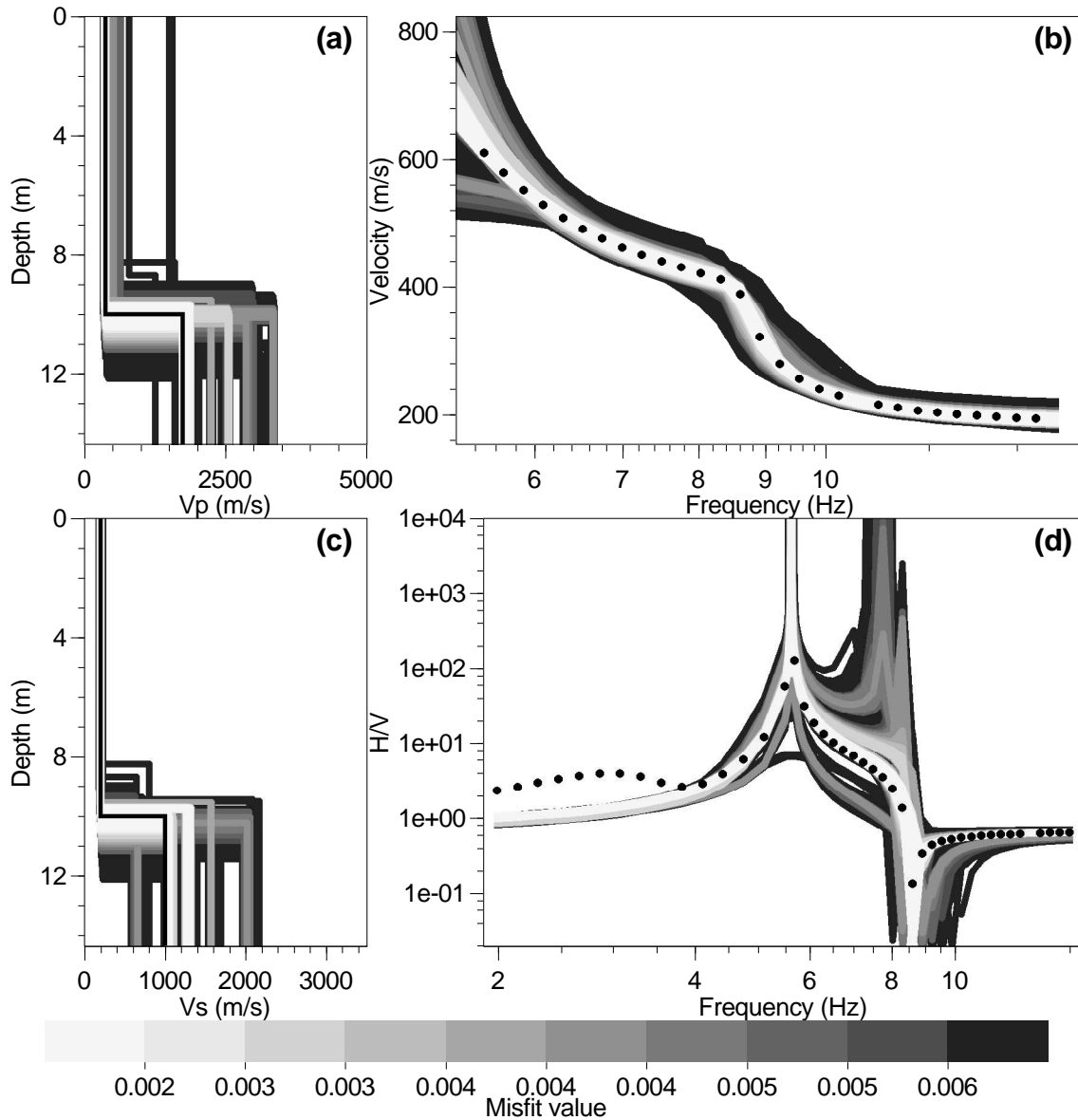


**Figure 5.15:** Joint inversion of the dispersion curve and the ellipticity peak. (a) Resulting  $V_p$  profiles. (b) Resulting  $V_s$  profiles. The black lines are the theoretical velocity profiles. (c) Dispersion curves  $V_p$  corresponding to models of figures (a) and (b). The black dots are the theoretical dispersion curves used as the target curve during inversion. (d) Ellipticity curves calculated for models of figures (a) and (b). The black dots are the theoretical ellipticity curve but only the frequency of the main peak is used as the inversion target.

Compared to figure 4.5, the posterior error obtained for the depth of the basement interface is greatly reduced. According to the level of confidence put into the dispersion curve, the depth is known with a one-metre precision whereas the uncertainty in figure 4.5 is much greater. However the velocity in deeper layer is not retrieved as in the first inversion. Tests were also conducted with a three-layer parameterization but no significant improvement has been observed. Other inversions could have been started with the low frequency secondary peak appearing in figure 4.1(d) at 3 Hz, but there are few chances for this peak to be detected with a real experiment.



# Chapter 6

## Test cases

In the preceding chapters, a flexible and powerful algorithm is developed for the inversion of dispersion curves. Its capabilities have been proved in the case of noiseless data curves. In this chapter, the dispersion curves (or the auto-correlation curves) are retrieved from a synthetic and a real wavefield with the techniques described in chapter 1 and they are inverted. Even for noisy observables, the inversion tool reveals itself as an efficient way to infer the soil structure together with its global uncertainty.

A special attention is paid to the interpretation of multiple array geometries. The advantages and the drawbacks of each method and each configuration are exploited to develop robust guidelines for the interpretation of real measurements.

### 6.1 Synthetic ambient vibrations

In this section, the recorded signals are simulated with the method developed by Hisada (1994). The theoretical model is described hereafter. Then, the signals are processed with the methods detailed in chapter 1.

#### 6.1.1 Model description

The synthetic ground model is composed of a soil layer with a thickness of 25 m overlying an infinite bedrock. The properties of each layer are specified in table 6.1. The theoretical

Thickness	$V_p$	$V_s$	Density	$Q_p$	$Q_s$
25 m	1350 m/s	200 m/s	1.9 t/m <sup>3</sup>	50	25
–	2000 m/s	1000 m/s	2.5 t/m <sup>3</sup>	100	50

**Table 6.1:** Properties of the reference model.

Rayleigh dispersion curves (the fundamental and the first four higher modes in the case of an elastic media) for this model are shown in figure 6.1(a) between 1 and 15 Hz. For frequencies below 15 Hz, only the first five modes are present and appear to be well separated in terms of velocity. Figure 6.1(b) shows the fundamental ellipticity and the  $S_H$  transfer function. The

fundamental resonance frequency is 2 Hz while the peak of the fundamental ellipticity is at 1.9 Hz. This frequency difference, recently studied by Malischewsky and Scherbaum (2004), is mainly influenced by the magnitude of the velocity contrast between the sediments and the bedrock.

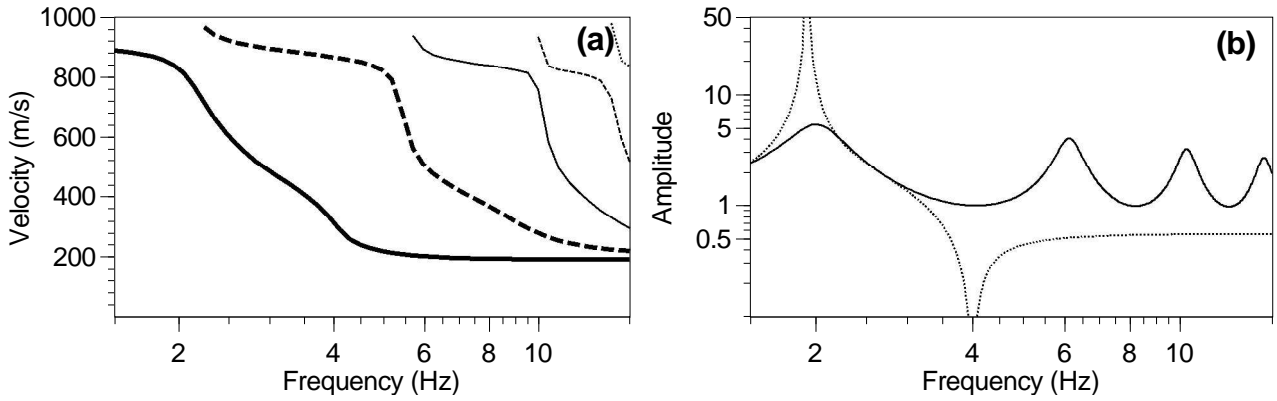


**Figure 6.1:** Theoretical model for synthetic ambient vibrations. (a) Dispersion curves for Rayleigh modes calculated with the synthetic model: fundamental model (thick plain line), first (thick dashed line), second (thin plain line), third (thin dashed line), and fourth higher mode (thin dotted line). Other modes do not exist in the plotted range. (b) Theoretical  $S_H$  transfer function for the synthetic model (plain line) and fundamental Rayleigh ellipticity curve (dotted line).

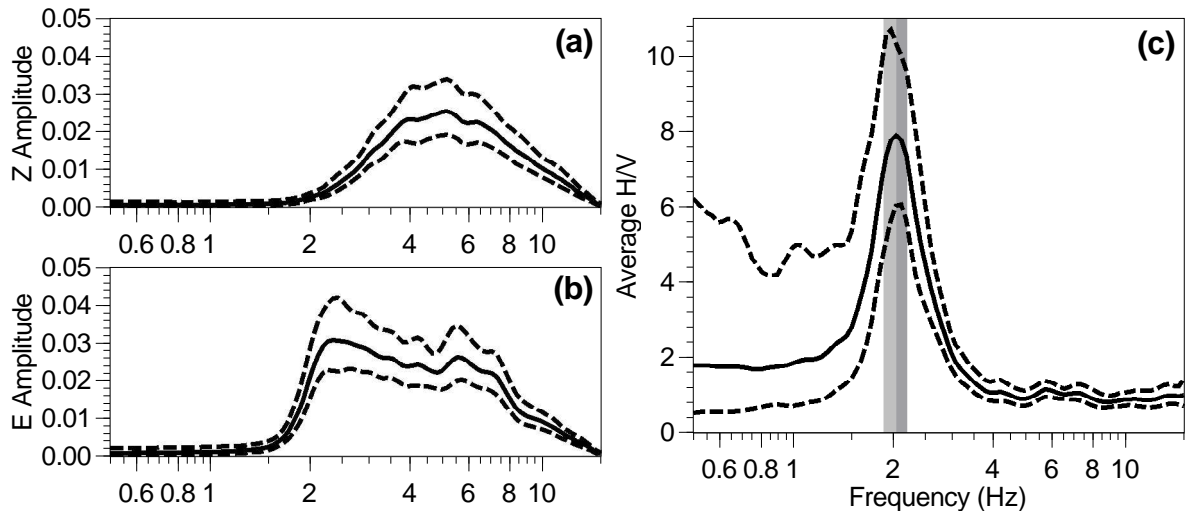


**Figure 6.2:** Spectral curves of the central station of array A to C. The plain line is the average and the dashed lines are located at one standard deviation. (a) Amplitude spectrum of the vertical component. (b) Amplitude spectrum of one horizontal component. (c) Spectral ratio Horizontal to Vertical (H/V). Grey bands indicate the average and standard deviation of the frequency peak values observed for each individual time window.

Synthetic ambient vibrations have been computed during 6 minutes using the method proposed by Hisada (1994 and 1995), and Bonnefoy-Claudet et al. (2004) which is valid for a one-dimensional model with sources and receivers placed at any depth. This dataset includes 333 source points randomly distributed from 140 to 750 m from the central receiver. Sources are punctual forces with delta-like functions of random amplitudes and directions. All types of waves existing in such media are modelled generating a wave field containing body, Love and Rayleigh waves. The frequency spectrum of generated waves is limited to 15 Hz in order to reduce CPU time. The spectra of the vertical (V) and one horizontal (H) component of the

central station is shown in figure 6.2(a) and 6.2(b), as well as the H over V ratio (figure 6.2(c)). The frequency of the H/V peak (2 Hz) matches the resonance frequency of the soft layer (figure 6.1(b)). The Fourier spectra show that the energy of the vertical component vanishes in the vicinity of and below the fundamental frequency as reported by Scherbaum et al. (2003), while the energy on the horizontal component decreases below 1.5 Hz.

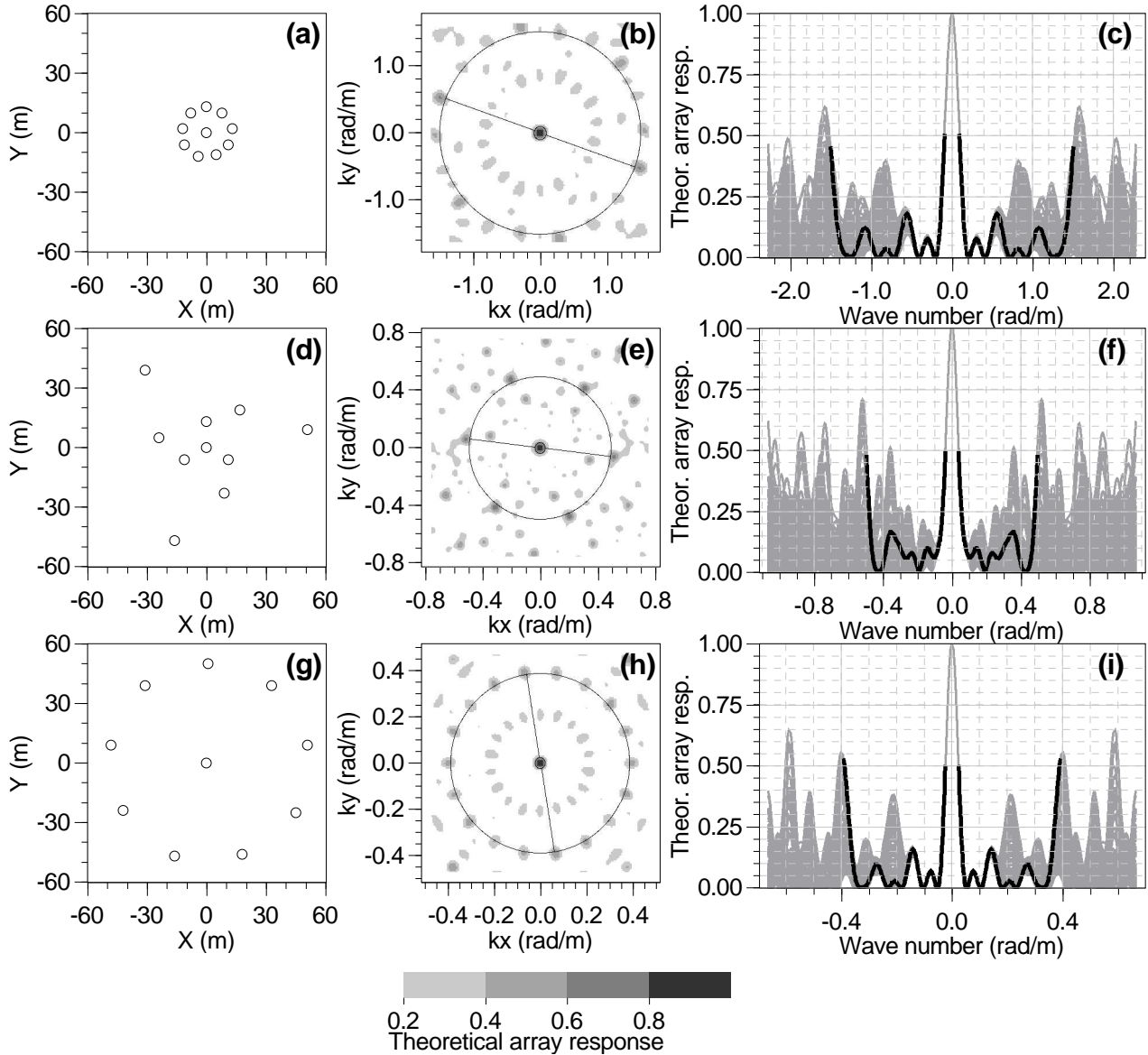


**Figure 6.3:** Array geometries and their f-k responses. (a), (d) and (g) Geometries of arrays for arrays A, B, and C, respectively. (b), (e) and (h) Their corresponding theoretical frequency-wavenumber responses. The circles correspond to the chosen wavenumber limits detailed in table 6.2. (c), (f) and (i) Sections across several azimuths for the theoretical frequency-wavenumber grids of arrays A, B, and C, respectively. The black curve is oriented along the line drawn in figures (b), (e) and (h).

On this model we set up three arrays (labelled A, B and C) the geometries of which are plotted in figures 6.3(a), 6.3(c) and 6.3(e), respectively. Array A is composed of nine sensors roughly distributed around a central sensor, with an approximate aperture of 25 metres. Array B is made of three triangles approximately rotated by  $40^\circ$  and with increasing aperture up to 90 metres. Finally, array C is made of nine sensors roughly distributed around a central sensor, with an approximate aperture of 100 metres. Theoretical f-k responses (section 1.1.1 on

Array name	Min. dist.	Max. dist.	$k_{min}$	$k_{max}$	$f_{min}$	$f_{max}$
A	8 m	25 m	0.095	1.50	4.4	$\geq 15.0$
B	13 m	87 m	0.037	0.495	3.25	7.6
C	34 m	99 m	0.024	0.39	3.0	7.2

**Table 6.2:** Properties of the array geometries. For each array the minimum and maximum distance between sensors. The minimum and maximum wavenumbers deduced from the theoretical frequency-wavenumber responses in figures 6.3(b), 6.3(e) and 6.3(h). Also the minimum and maximum frequencies corresponding to those wavenumbers (Hz).

page 7) for arrays A, B, and C are shown in figures 6.3(b), 6.3(d) and 6.3(f), respectively. The resolution and aliasing limits deduced from Woods and Lintz (1973) and Asten and Henstridge (1984) criteria are marked by circles and are summarized in table 6.2. Sections are made across each of them along several azimuths (628) and they are plotted by grey curves in figures 6.3(c), 6.3(e) and 6.3(g). The bold black curves correspond to the minimum aliasing azimuths which are marked by black lines in figures 6.3(b), (d) and (f). From equation (1.2), a wave travelling at  $k_{max}$  appears in the semblance map with the main peak right on the aliasing limit and the lateral aliasing peaks greater than 0.5 are located on a circle crossing the origin. In the case of a complex wavefield with waves travelling in several directions, there are lot of chances to confuse the true peak with sums of secondary aliasing peaks that do not correspond to the correct apparent velocity. Hence, a safe approach would be to limit the valid range to  $k_{max}/2$ , which is illustrated by the results of the next sections.

### 6.1.2 Single source wavefield

The f-k method is first applied to a wavefield produced by a single source of the aforementioned dataset, situated at about 650 m ( $310^\circ$  counted clockwise from the North or Y axis) from the centre of arrays A, B and C. The source is punctual with a force vector oriented along direction  $293^\circ$  and inclined at  $50^\circ$  from the vertical axis. From its orientation and its position far from the arrays, Rayleigh waves are supposed to be mainly recorded. The signals computed at the ten receivers of array B are shown in figure 6.4. Their energy is spread over a 6 second period for a total calculated duration of 360 seconds.

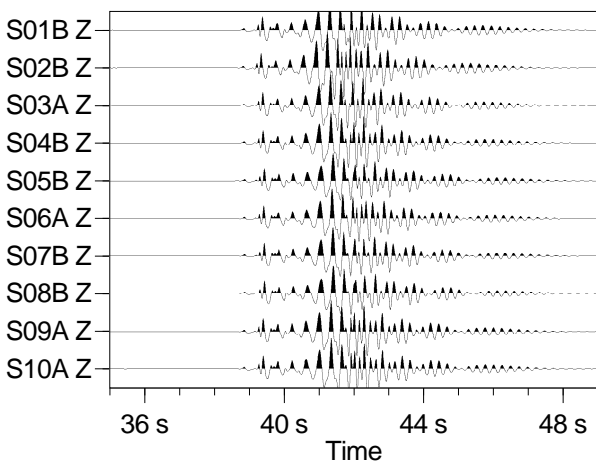


**Figure 6.4:** Single source wavefield measured by the vertical sensors of array B.

The array response is calculated for single windows of varying durations: 20 s, 6 s, and 3 s, all centred around the most energetic part of the signal. The velocity at the semblance maximum is plot for all frequency bands in figures 6.5(a) to 6.5(c), for the duration 20 s, 6 s and 3 s, respectively. The theoretical dispersion curves (the fundamental and the first three higher

is plot for all frequency bands in figures 6.5(a) to 6.5(c), for the duration 20 s, 6 s and 3 s, respectively. The theoretical dispersion curves (the fundamental and the first three higher

modes) are plotted on the same graphs for comparison. The validity curves are drawn at constant  $k_{min}$  (plain lines),  $k_{max}/2$  (dotted lines) and  $k_{max}$  (dashed lines). For the long time window, the velocity determination is nearly perfect for the whole frequency range except below 2 Hz, which corresponds to 40 cycles (20 s times 2 Hz). When decreasing the time length of the processed signal, the dispersion curve quality is degrading at low frequency. We define a minimum threshold frequency in each case indicating where the calculated dispersion curve leaves the theoretical curve. For the six-second window this threshold frequency is around 2.5 Hz (15 cycles) and around 5 Hz (15 cycles) for the three-second case. Comparing to the response of the arrays A and C, figures 6.6(a) and 6.6(b), respectively (six-second time window), it can be observed that the limit of 2.5 Hz is independent of the array aperture or array geometry. Array A provides a correct velocity estimation, though being far outside the valid wavenumber range. This frequency limit is linked to the energy content of the vertical spectrum shown in figure 6.2(a) as reported by Scherbaum et al. (2003).

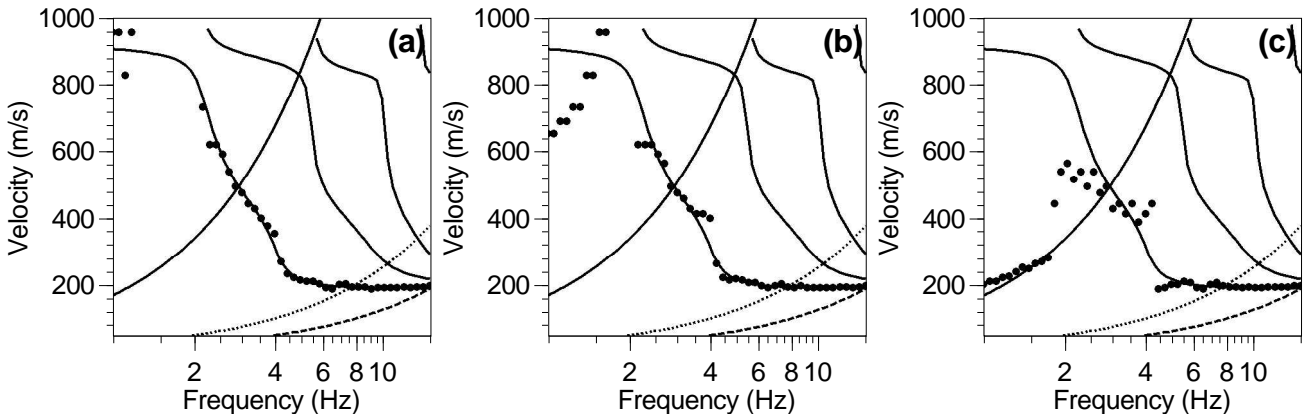


**Figure 6.5:** Frequency-wavenumber analysis for array B with various time windows: (a) 20 s., (b) 6 s., and (c) 3 s. For each plot, the thin lines are the theoretical dispersion curves for the original ground model (first modal curves of figure 6.1). The three exponential curves represent constant wavenumber curves values of which are deduced from theoretical frequency-wavenumber response (figure 6.3): minimum (continuous line), half the maximum (dots) and maximum wavenumber (dashed).

The calculated curves in figures 6.5(b), 6.5(c), 6.6(a) and 6.6(b) show at least two major defects: one located at 4 Hz where the velocity increase is not retrieved and the other between 6 and 9 Hz, especially obvious for array A. The first one is not present on the 20 s. results (figure 6.5(a)), proving that the choice of a long enough window is crucial to correctly process the signals. The second defect may be investigated by examining the responses of arrays A and B in the plane  $(k_x, k_y)$  (figures 6.7(a) and 6.7(b)). Below 6 Hz (not shown here) the shape of the array response is quite similar to the theoretical response, supporting the assumption of a single dominant surface wave. Above 6 Hz, the general shape is changing with the apparition of a secondary main peak at higher velocity, as shown by figure 6.7 (calculated at 6.5 Hz). Because of its relative low resolution limit ( $[k_{min}]_B < [k_{min}]_A$ ), array A cannot distinguish the two peaks and the exact position of the fundamental peak is shifted erroneously towards a higher velocity. This explains the velocity bump on the dispersion curve of figure 6.6(a).

The signal processing shows that the simulated vibrations are mostly composed of surface wave which dispersion curve is perfectly retrieved in figure 6.5(a) above 2.5 Hz. Waves travel-

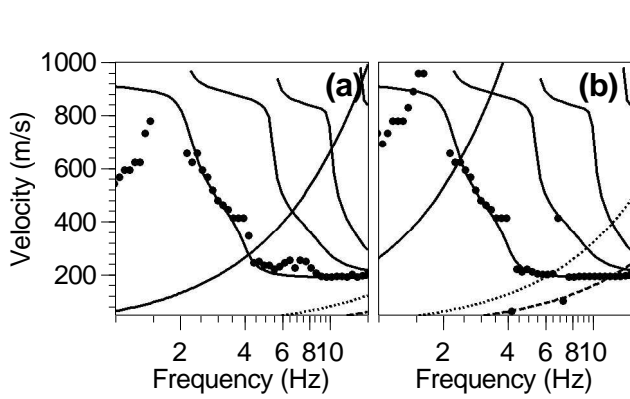


**Figure 6.6:** Frequency-wavenumber analysis for arrays A and C in figures (a) and (b), respectively. The window length is 6 seconds.

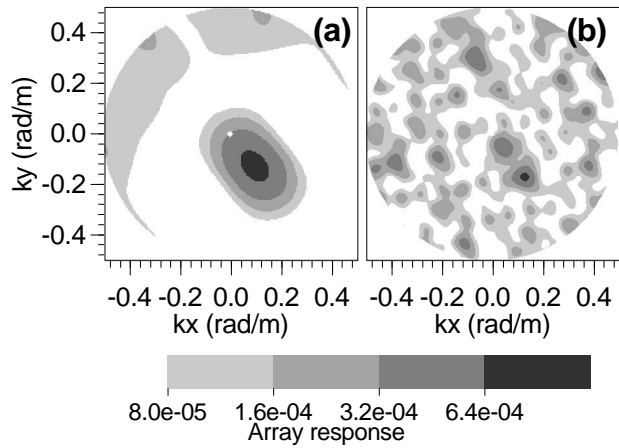


**Figure 6.7:** Array responses for arrays A and B in figures (a) and (b), respectively, calculated at 6.5 Hz.

ling at a higher velocity are detected between 6 and 9 Hz (figures 6.6(a) and 6.7(b)), probably corresponding to the first higher mode. Comparison of arrays with different resolving power allows the rejection of non trusted samples. The parameters of the signal processing, particularly the choice of a too short time window, may introduce undesirable effect on the dispersion curve construction. The results obtained with a single source suggest the use of windows of at least 15 to 40 periods. In the following, a complex wavefield is analysed by the means of three processing techniques (frequency-wavenumber, high resolution and auto-correlation methods).

### 6.1.3 Frequency-wavenumber method

The contributions of 333 sources similar to the one analysed in the last section are summed together to simulate ambient vibrations. To estimate the uncertainty on the apparent velocity determination, the whole signals are split in several smaller time windows for which the array responses are computed. For each time window, the velocity of the semblance peak is searched for wavenumbers below 1.5 rad/m and for velocities between 150 and 2000 m/s. From a coarse gridding in the wavenumber plane, the vector  $(k_x, k_y)$  of the highest peak is iteratively refined to an arbitrary small precision. Thus, for each frequency band, an histogram of the velocities at the observed maxima is constructed (e.g. figure 6.8(a) for array C and 10 cycles). The areas below the histograms are normalized to one in the slowness domain, explaining the high values for the probability density functions. The curves in figure 6.8(c) are sections across the histograms of figures 6.8(a) and 6.8(b) at 3 Hz.

The influence of the window length is first checked by calculating the histograms for time windows containing 10 and 50 cycles (figures 6.8(a) and 6.8(b), respectively) for array C. The theoretical dispersion curves are represented by the three thin plain lines. The three exponential curves (validity curves) represent constant wavenumber curves values of which correspond to the deduced  $k_{min}$  (continuous line) and  $k_{max}$  (dashed line). The dotted line is situated at  $k_{max}/2$ . In figure 6.8(a), the average deviates from the theoretical dispersion curve with a constant bias of 50 or 100 m/s towards lower velocity, whereas all the velocity estimates are closer to the

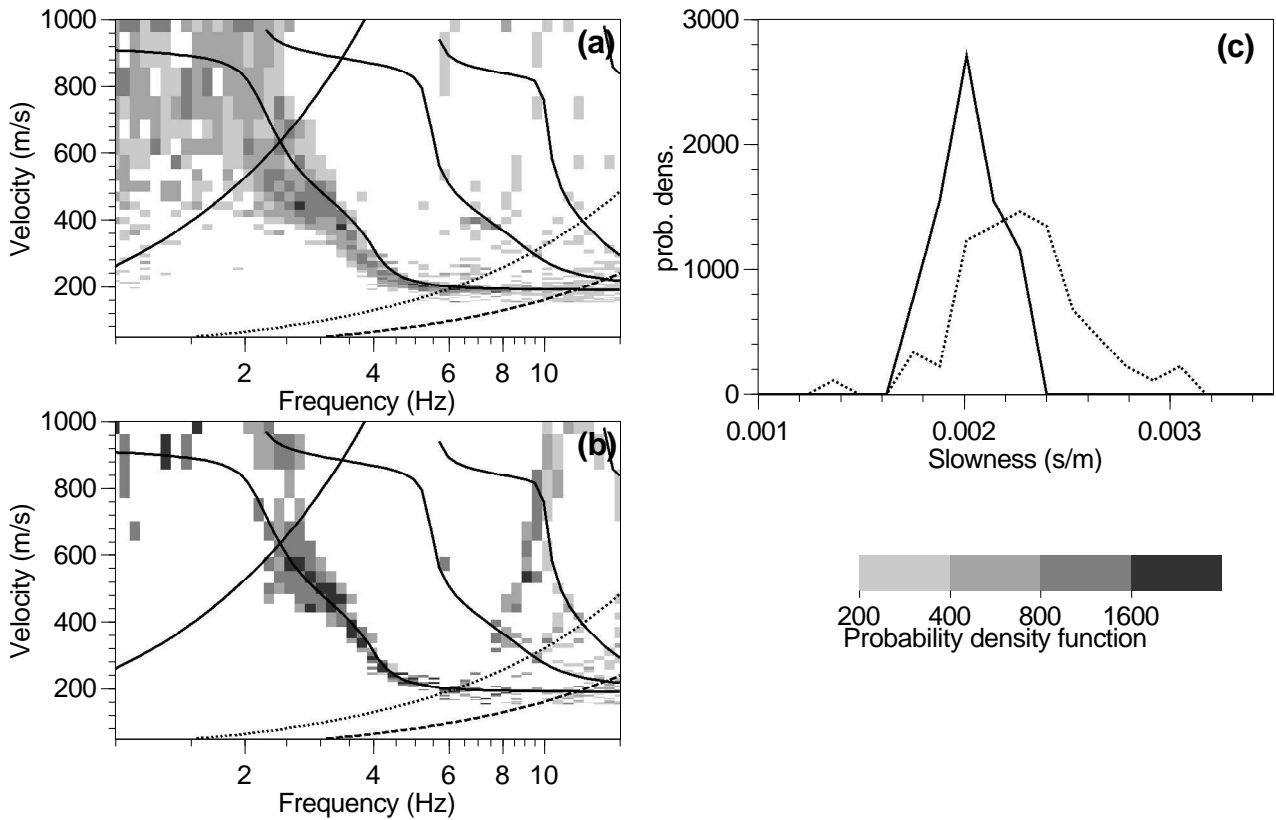


**Figure 6.8:** Comparison of frequency-wavenumber analysis for array C, influence of the time window length. (a) Histograms of velocities with a maximum  $f$  semblance obtained with time windows of 10 cycles. (b) Same processing with time windows of 50 cycles. (c) Cross section at 3 Hz, of the histograms of figures (a) and (b), shown by dotted and plain lines, respectively. The curves are of the same types as in figure 6.5.

theoretical curve and the standard deviations are much smaller for the 50-cycle case (figure 6.8(b)). Both cases are calculated with the same duration of signals (six minutes), resulting in five times more windows in the 10-cycle case. To test the robustness of the statistics, one minute and 12 seconds of signals are also processed with time windows of 10 cycles, containing the same number of time windows as in the 50-cycle case calculated with the six minutes of signals. The obtained histograms are the same as in figure 6.8(a). Hence, with short time windows, increasing the number of samples neither reduces the gap to the theoretical curve nor the size of resulting error bars.

A similar processing is applied to the signals of arrays A and B (six minutes of signals and time windows of 50 cycles). The velocity histograms of arrays A, B and C can be compared in figures 6.9(a), 6.9(b) and 6.8(b), respectively. The validity curves of constant wavenumber are drawn in the same way as in figure 6.8. For all arrays,  $k_{min}$  is clearly linked to the point where the velocity estimates strongly deviate from the theoretical dispersion curve shown with the thin black lines. In figure 6.8(b), bad estimations of velocity due to aliasing take place effectively between  $k_{max}/2$  and  $k_{max}$ . A similar conclusion could be drawn for array B, where errors towards low velocity slightly increase above  $k_{max}/2$ . Due to the limited available frequency range, the aliasing effect cannot be observed for array A. Between the limits  $k_{min}$  and  $k_{max}/2$ , arrays B and C exhibit correct velocity estimates. For array A, the measured velocity is slightly above the theoretical Rayleigh velocity with a velocity bump between 6 and 9 Hz similar to the

one of figure 6.6(a). For each array, an average and a standard deviation is calculated between  $k_{min}$  and  $k_{max}/2$  based on the histograms of figures 6.8(b) and 6.9. The three curves are averaged taking into account the respective weights (number of time windows) to construct the final dispersion curve plotted in figure 6.10. The measured dispersion is reliable for frequencies above 3 Hz. This limit is linked to the array sizes but also to the dramatic decrease of the noise vertical component amplitude close to the fundamental resonance frequency (2 Hz).

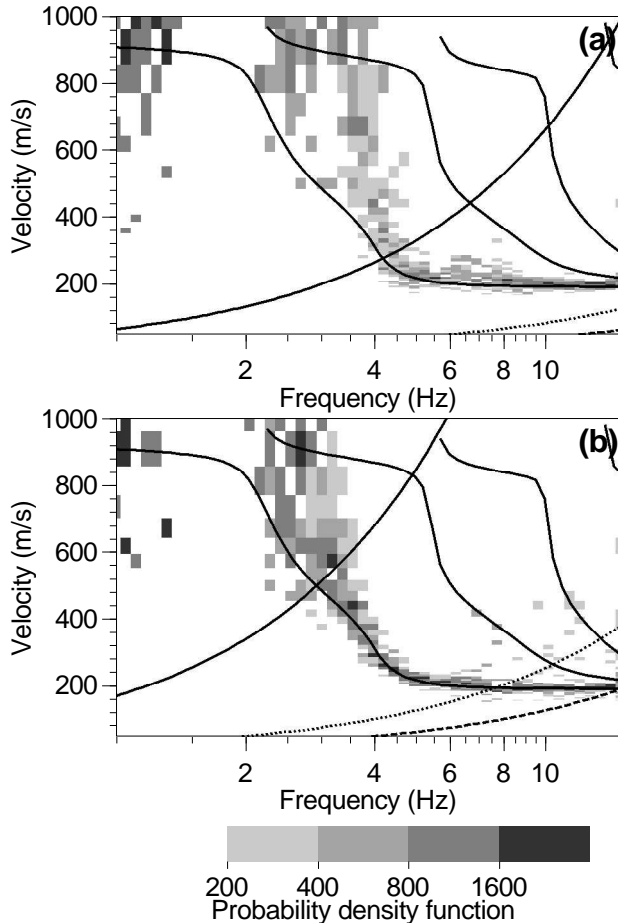


**Figure 6.9:** Results of the frequency-wavenumber method applied to arrays A (a) and B (b) with time windows including 50 cycles as in figure 6.8(b). The histograms are of the same type as at figure 6.5, the curves as well. Wavenumber limits correspond to each array geometry.

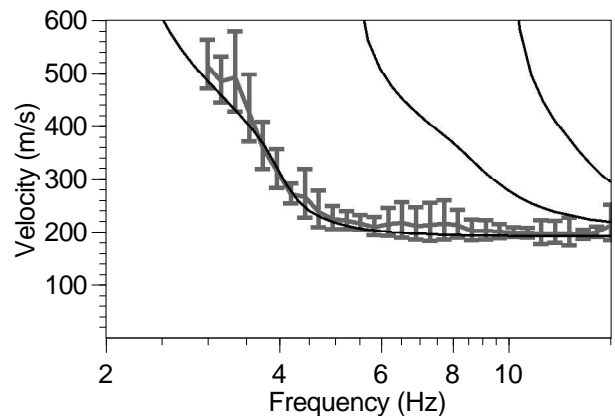


**Figure 6.10:** Average and standard deviations (vertical bars) of apparent dispersion curve from arrays A, B and C. The thin lines are the theoretical dispersion curves for the original ground model.

The obtained dispersion curve is inverted with five distinct runs of the neighbourhood algorithm, generating a total of 50,000 models. The parameterized model consists of a sediment layer the wave velocity of which increases with depth according to a power law, and a half-space at the base. The parameters are six:  $V_p$  and  $V_s/V_p$  in the two layers, the layer thickness and the  $V_p$  increase between the top and the bottom of the sediment layer. Figure 6.11(a) and 6.11(b) show the velocity profiles obtained for  $V_p$  and  $V_s$ , respectively, for all models fitting the dispersion curve with a misfit lower than one. The misfit function is defined by equation (3.38). The dispersion curves corresponding to the misfit threshold of one are plotted in figure 6.11(c). Dispersion curve inversion leads to a good definition of the  $V_s$  profile for the first 25 m. Below this depth, a large range of velocity values may explain the measured dispersion curve, due to

the lack of information at low frequency.  $V_p$  profile is very poorly constrained by the inversion, as  $V_p$  values in the layers have very little influence on the dispersion curve for high Poisson's ratio values (section 3.1.8).

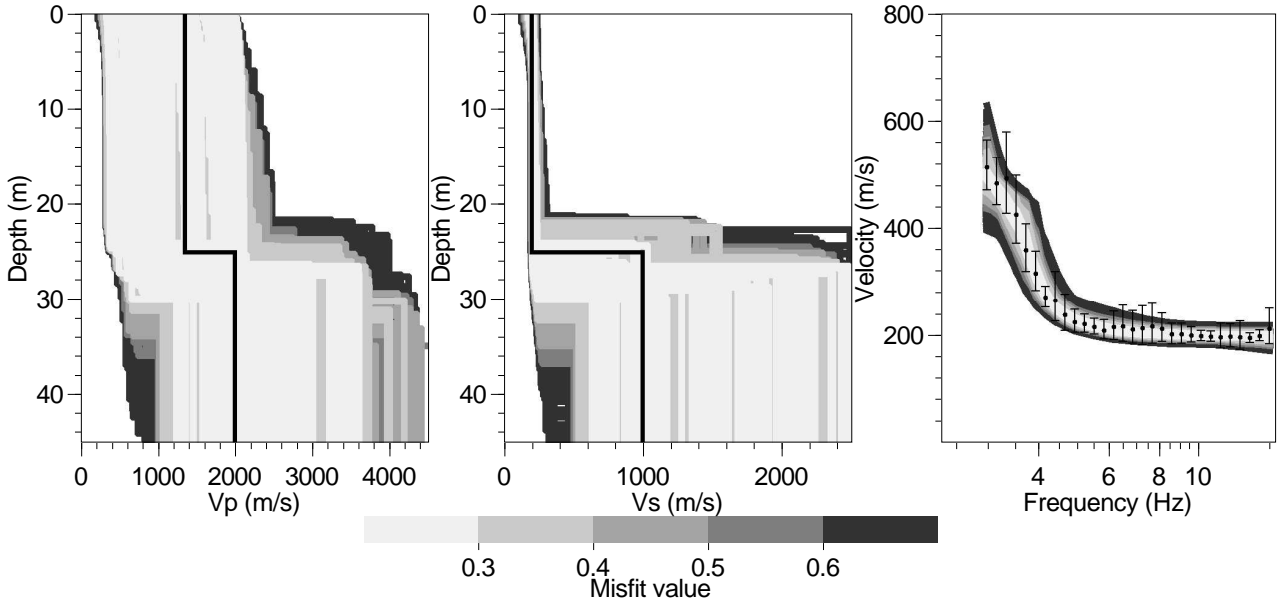


**Figure 6.11:** Results from inversion of the dispersion curve obtained with the frequency-wavenumber method. (a)  $V_p$ , (b)  $V_s$  of generated models and (c) corresponding dispersion curves. The dots and error bars represent the experimental dispersion curves to which the calculated dispersion curves are compared. The black lines of figures (a) and (b) are the velocity profiles of the true model.

### 6.1.4 High resolution method

For the three arrays A, B, and C, the dispersion curves have been calculated by searching the maximum of the high-resolution frequency wavenumber estimator defined by Capon (1969) and Ohrnberger et al. (2004a). The estimator depends upon the cross spectral matrix averaged over the 6 minutes of available signals. The results are shown in figures 6.12(a) to 6.12(c), for arrays

Array name	$k_{min}$	$k_{max}$	$f_{min}$	$f_{max}$
A	0.069	–	3.9	$\geq 15.0$
B	0.023	0.46	2.4	14.2
C	0.023	0.22	2.4	6.9

**Table 6.3:** For each array, the minimum and maximum wavenumbers deduced from the comparison of the high resolution results to the theoretical dispersion curve (rad/m). Also are given the minimum and maximum frequencies corresponding to those wavenumbers (Hz).

A, B, and C, respectively. The limits  $k_{min}$  and  $k_{max}/2$  validated for the f-k method are shown in grey. Theoretically, the resolving power of the high-resolution method should be better than the f-k method, and estimates of velocity may be reliable even outside those restrictive limits. From the observation of the stability of the high-resolution results and the comparison with the theoretical dispersion curve, we define apparent limits of the high-resolution valid for this particular case (table 6.3). This task is not possible for a real experiment. From a careful examination of

figures 6.9 and 6.12, the high resolution method provides correct answers below  $k_{min}$ , extending the frequency range by approximately 0.5 Hz. The poor resolution of array A between 6 and

9 Hz is not significantly improved by the high resolution approach. At high frequency, array B gives nearly perfect results up to its  $k_{max}$ , in contrast with array C which shows a lot of instabilities above  $k_{max}/2$ . After selecting the points between the validity curves, an average dispersion curve is calculated to feed the inversion algorithm.

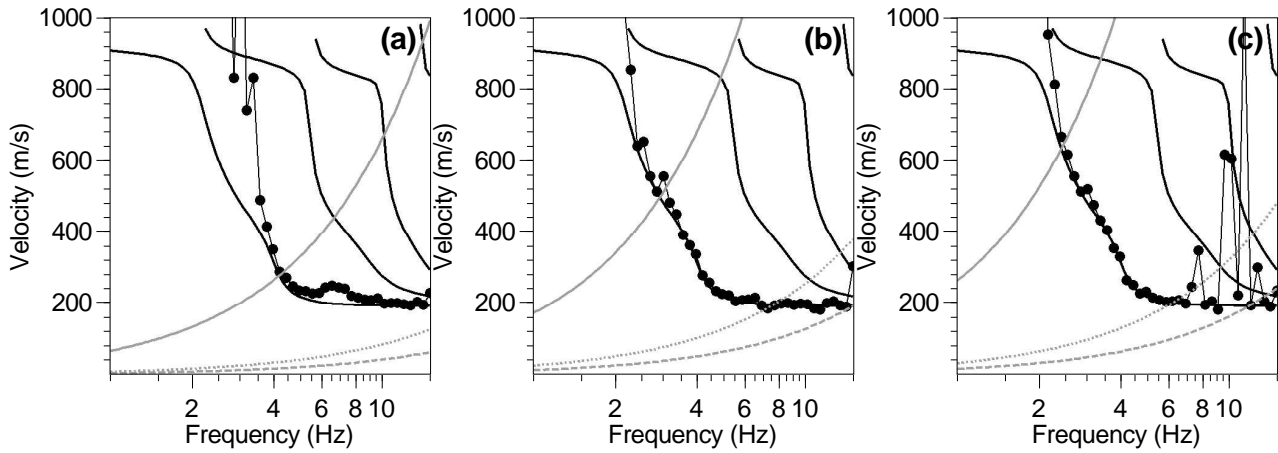


**Figure 6.12:** Results of the high resolution frequency-wavenumber method applied to arrays A (a), B (b) and C (c). The grey exponential curves are the minimum and half maximum wavenumber limits deduced from theoretical array response. The black lines with dots obtained from computations are compared to the theoretical dispersion curves (thin plain lines).

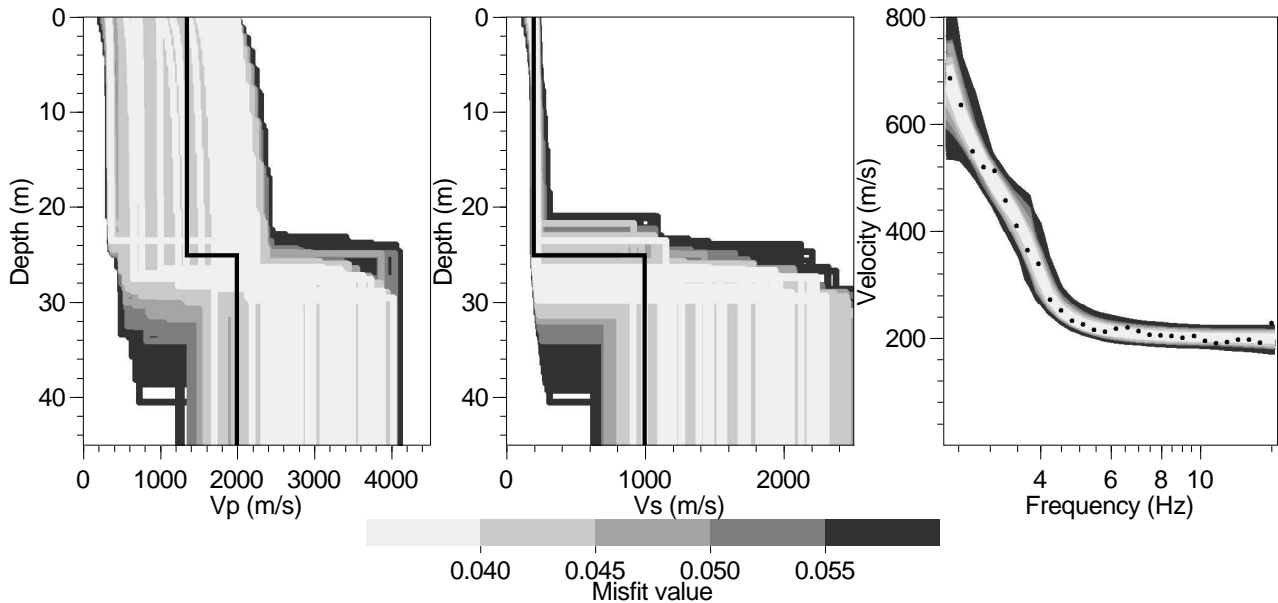


**Figure 6.13:** Results from inversion of the dispersion curve obtained with the high-resolution frequency wavenumber method. (a)  $V_p$ , (b)  $V_s$  of generated models and (c) corresponding dispersion curves. The dots represent the experimental dispersion curves to which the calculated dispersion curves are compared. The black lines of figures (a) and (b) are the velocity profiles of the true model.

We performed exactly the same inversion processes as for the f-k results (figure 6.13). As we do not have error estimation on the dispersion curve, the model selection is based on the misfit threshold (0.075) for which the dispersion curve uncertainty includes the data scattering. As for f-k method, the  $V_s$  profile up to the major impedance contrast can be determined.  $V_p$  over the whole column and  $V_s$  below 25 m are not defined by analysing the vertical component of

the ambient vibrations. The slightly extended frequency range compared to f-k method does not induce a significant difference in the inverted  $V_s$  profiles.

### 6.1.5 Spatial auto-correlation method

The signals simulated for the three arrays A, B and C are analysed using the spatial auto-correlation method described in section 5.2. The azimuths and the distances between all couples of stations are shown in figure 6.15. The pairs of grey circles are the selected rings for the spatial auto-correlation computation. Distances are summarized in table 6.4.

Array name	Min. radius	Max. radius	Number of pairs
A	7.8	9.4	9
A	12.1	13.2	9
A	15.3	17.0	9
A	21.2	22.5	9
A	24.4	25.3	9
B	12.5	18.0	6
B	22.0	26.3	9
B	34.7	43.3	12
B	49.1	63.8	12
B	73.8	87.3	6
C	33.5	35.0	9
C	48.4	54	9
C	63.9	65.1	9
C	85.6	87.3	9
C	97.5	99.4	9

**Table 6.4:** Distance limits for the selected rings for arrays A, B and C. The last column is the number of station couples included in each ring. Distances are expressed in metres.

As in the f-k method (section 6.1.3), the choice of the window length for calculating the auto-correlations is crucial. An example of its influence is presented hereafter. The average auto-correlation ratios are calculated with equation 1.11 for pairs of stations separated by distances between 30 and 40 m. In figure 6.14, the auto-correlation curves are plotted for various window lengths, counted in number of cycles of the central considered frequency ( $\omega_0$ ): 10, 25 and 50 (from light to dark grey, respectively). For the three curves, the average values are close to the true auto-correlation curve (black thick line) in the range 3.5 to 5.5 Hz. Below 3.5 Hz, the 10 cycle auto-correlation curve deviates from the correct function, while the two other curves (25 and 50 cycles) are close to it for frequency as low as 2.5 Hz. This discrepancy for short windows is probably due to a lack of source azimuth coverage (Asten et al. 2004), as the number of acting random sources is inversely proportional to the considered duration. Another explanation might be that the spectral estimates are more influenced by unavoidable side effects generated by cutting signals into time windows. Also, long time window curves are smoother than short ones and exhibit smaller standard deviations (figure 6.14). During this thesis, the 25 cycle time windows are kept for the computation of auto-correlation curves.

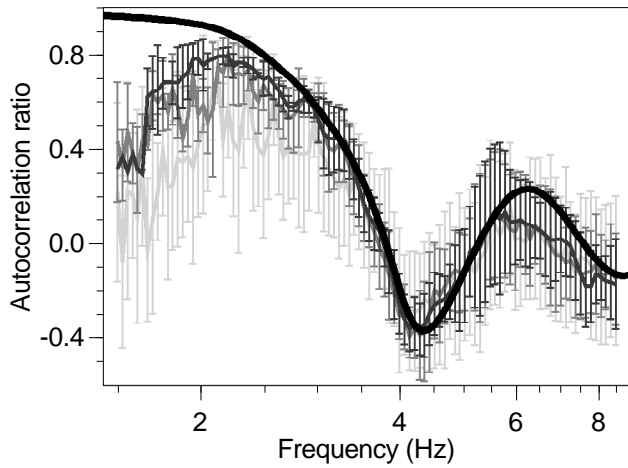


**Figure 6.14:** Influence of time window lengths on auto-correlation curves (average and standard deviations): 10 cycles (light grey), 25 cycles (medium grey) and 50 cycles (dark grey). The thick black line represent the theoretical auto-correlation curve.

Array name	$k_{min}$	$k_{max}$	$f_{min}$	$f_{max}$
A	0.015	–	1.9	$\geq 15.0$
B	0.012	0.4	1.7	13.4
C	0.011	–	1.5	$\geq 15.0$

**Table 6.5:** For each array the minimum and maximum wavenumbers deduced from the solution density grid (figure 6.17). Also the minimum and maximum frequencies corresponding to the selected samples (Hz).

A total of 15 auto-correlation ratio curves (five by array) are calculated for time windows of 25 cycles. Only one curve per array is shown in figure 6.16 with grey dots and grey error bars. The consistency of all 15 auto-correlation curves is checked on dispersion curves in figure 6.17(a) to 6.17(c), for arrays A to C, respectively.

The fifteen auto-correlation curves with the selected samples are inverted with five independent runs keeping the same parameterization as for the two preceding methods. The results are shown in figure 6.18. Only three auto-correlation curves among the fifteen are shown in figure 6.18(d) to 6.18(f). A good agreement is found between the calculated curves and the observed auto-correlations (black dots and their error bars) even below 2 Hz. The theoretical dispersion curve is drawn for comparison in figure 6.18(c). The auto-correlation method correctly retrieves the dispersion curve for all frequencies above 2.5 Hz. For lower frequency, a systematic bias is observed in figure 6.18(c). Comparing figures 6.11(b) and 6.13(b), the inversion of auto-correlation offers a little more constraint on  $V_s$  at the base of the sediment layer.  $V_p$  over the whole column and  $V_s$  below the major impedance contrast is not resolved as for the other methods.

### 6.1.6 Discussion and Conclusions

Three processing methods have been tested to retrieve the dispersion properties (dispersion curves or auto-correlation curves) on a two-layer model from simulated noise array measurements: the f-k method, the high-resolution f-k method and the spectral auto-correlation technique. Only the vertical components are processed and the dispersion (or auto-correlation) curves are inverted to obtain the  $V_s$  profile. The first conclusion is that several array apertures have to be used to construct the dispersion (auto-correlation) curves in the appropriate frequency range. From the inverted velocity profile point of view, all three methods have almost the same efficiency for this synthetic case. The  $V_s$  profile is correctly retrieved down to about

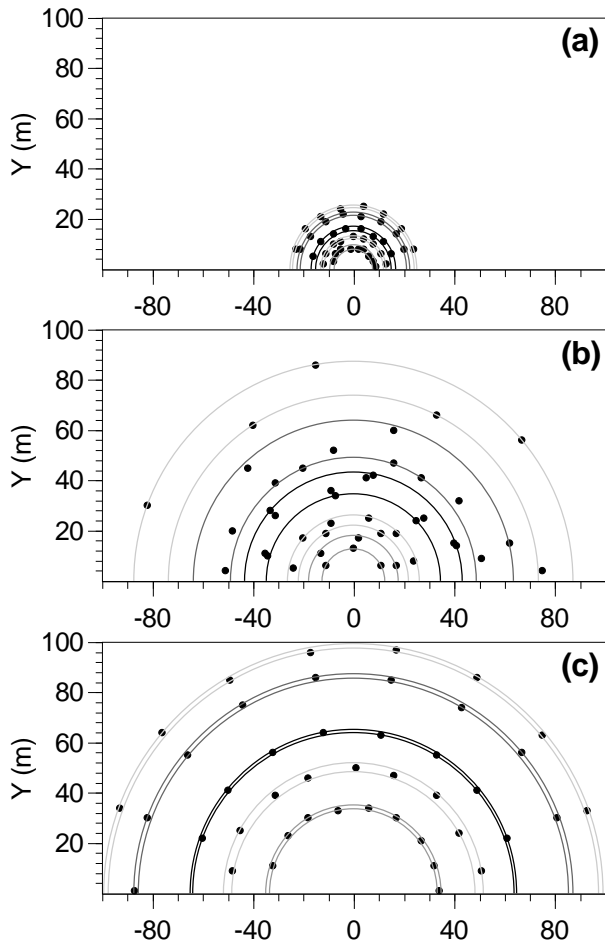


**Figure 6.15:** Azimuth-inter-distance plot: each dot represent one couple of stations. The pairs of grey circles show the limits of the chosen rings. (a) Array A, (b) array B, and (c) array C.

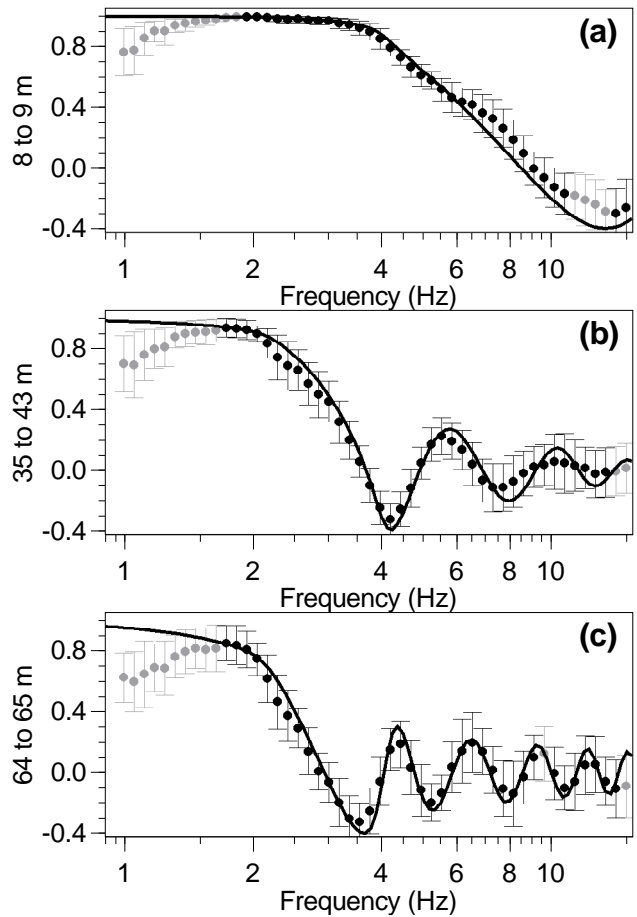


**Figure 6.16:** Examples of auto-correlation curves obtained for (a) array A, (b) array B, and (c) array C. The black dots and error bars are the samples selected according to criteria of figure 6.17.

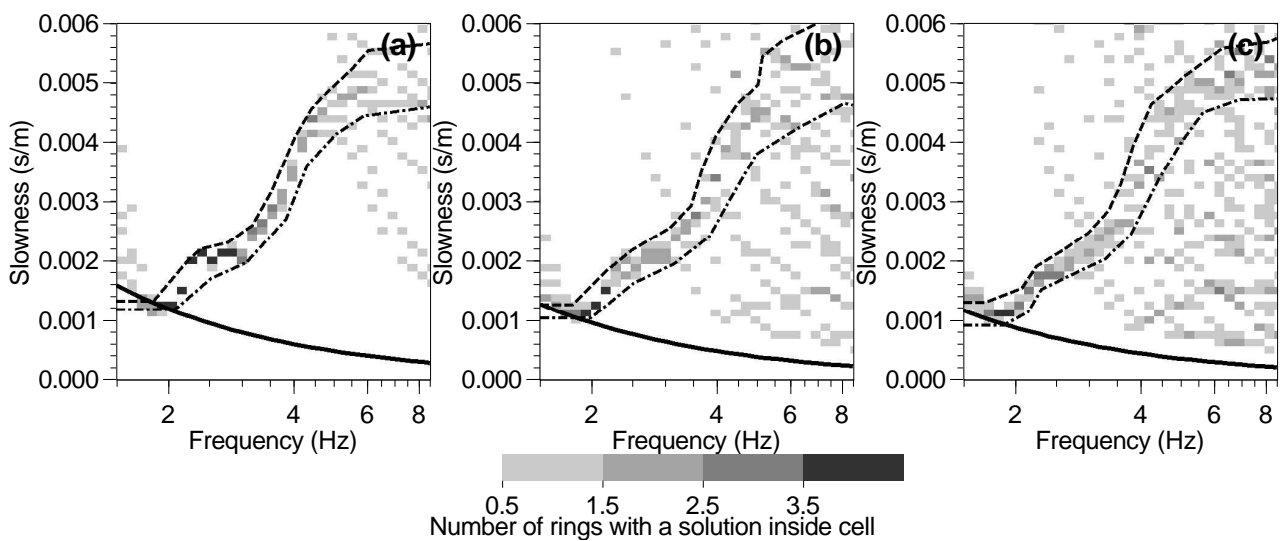


**Figure 6.17:** (a) to (c) grids in frequency-slowness domain representing the density of dispersion curve solutions for arrays A to C, respectively. The plain and the dotted lines are the wavenumber limits deduced from the solution density grids (if any). The dashed and the dot-dashed curves are the wavenumber limits of the apparent dispersion curve or the limits of the area with a high density of solutions.

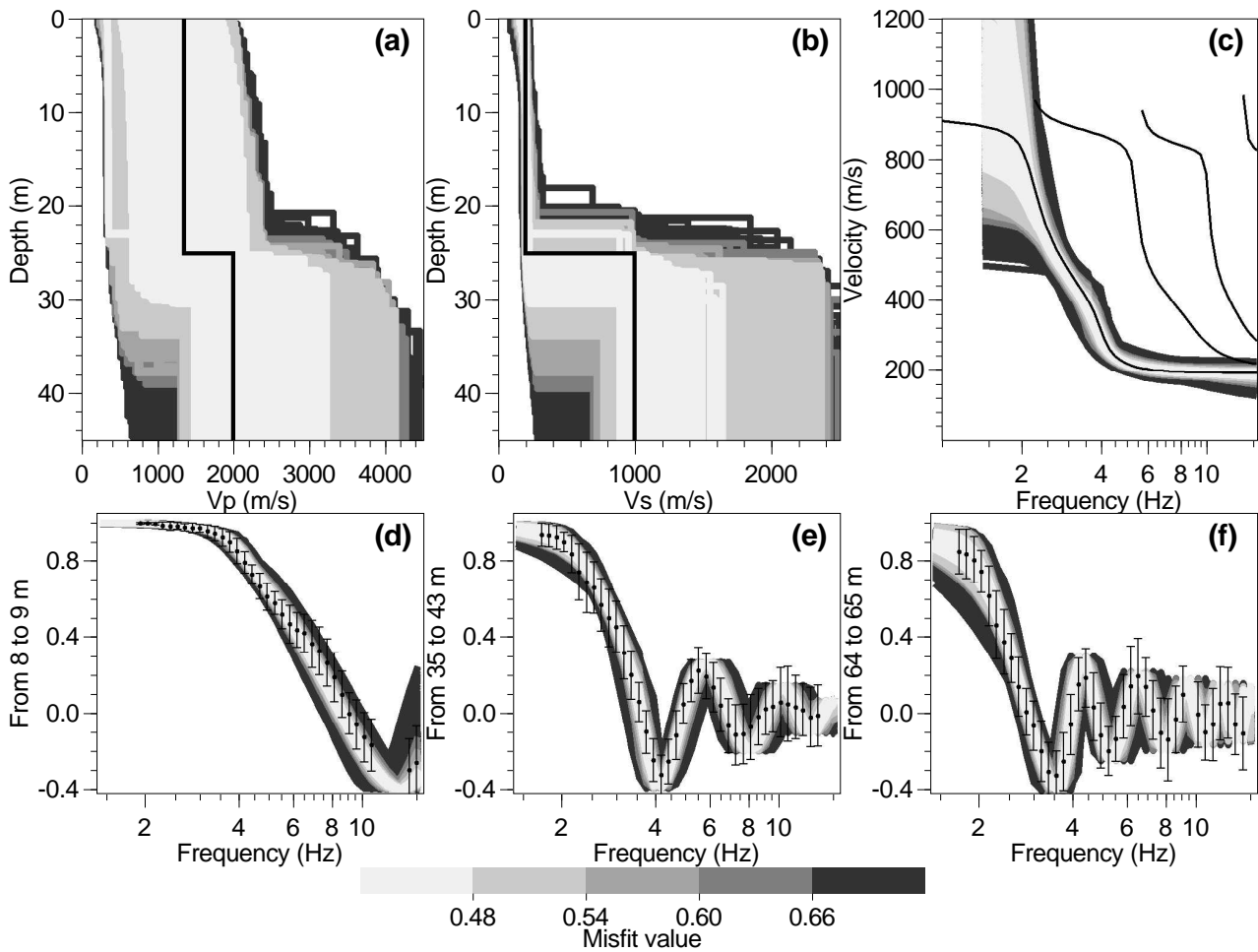


**Figure 6.18:** Inversion of the selected 15 auto-correlation curves. Only three of them are presented here. (a)  $V_p$ , (b)  $V_s$  profiles of generated models. The black lines of figures are the velocity profiles of the true model. (c) The dispersion curves corresponding to model of figures (a) and (b). The thin lines are the theoretical dispersion curves, not used during inversion. (d) to (e) One auto-correlation curve per array, A, B and C respectively. The black dots and their errors bars are the auto-correlation data points to be fit during inversion.

25 m which is the depth of the interface.

A special attention is paid to the limited reliability specific to each array. Based on the knowledge of the true dispersion curve, we conclude that the wave number limits deduced from the theoretical array response are consistent with the capabilities of the f-k method. Outside those limits, the calculated curves may exhibit strong bias. The high-resolution f-k method is sometimes more efficient than the f-k approach in defining the dispersion curve but no definitive and systematic improvement may be found. Like the auto-correlation method, the high-resolution method can be seen as complementary technique confirming the results of the f-k method.

No method is able to retrieve the velocity below the interface at 25 m. This limited penetration depth is a direct consequence of the high-pass filtering effect of the ground structure on the vertical component. This characteristic is a strong limitation of the method for assessing the local amplification factor in earthquake engineering, which depends upon the value of the velocity contrast.

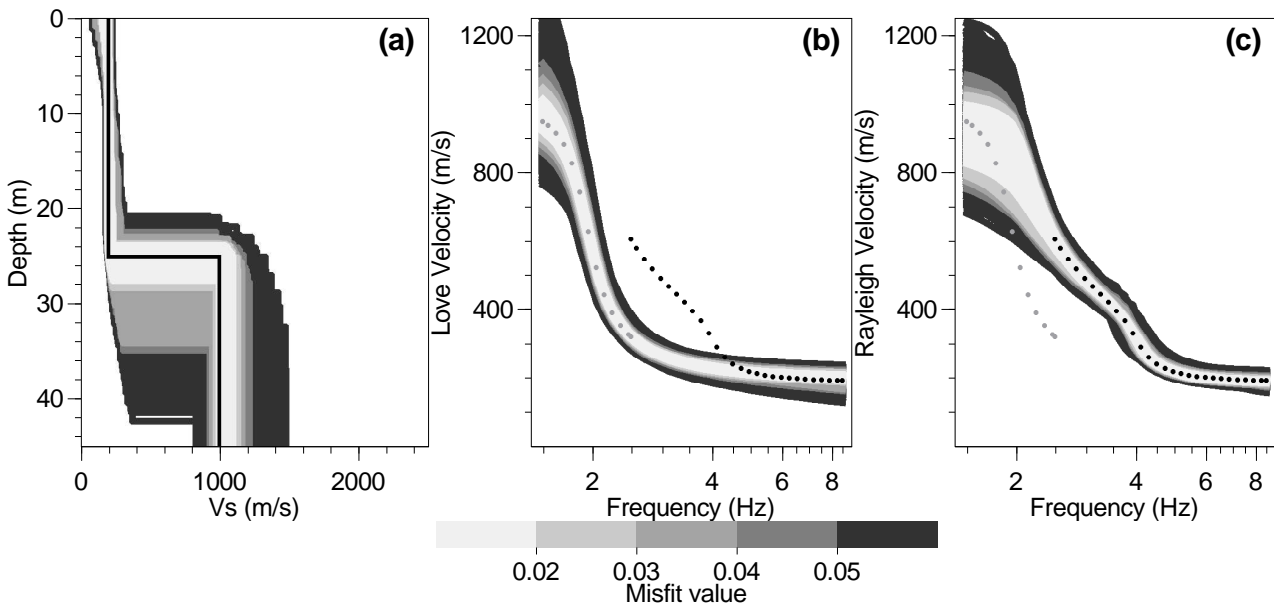


**Figure 6.19:** Inversion of Love and Rayleigh fundamental modes for perfect dispersion curves. (a)  $V_s$  models. (b) Calculated Love dispersion curves. (c) Calculated Rayleigh dispersion curves. The black dots are the target Rayleigh dispersion curves. The grey dots are the target Love dispersion curve.

Further improvement of the technique should consider horizontal components which are richer in low frequency waves than the vertical ones (figure 6.2). This alternative is tested in section 5.1.2 where the Love dispersion curve measured at low frequency combined with the Rayleigh dispersion curve allows an extension of the reliability of the inversion towards deeper layers. We compute the theoretical Love and Rayleigh dispersion curves for the ground model used in simulations. The Rayleigh dispersion curve is cut between 2.5 and 8.5 Hz as observed in figure 6.2 while the Love dispersion curve is supposed to be known only between 1.5 and 2.5 Hz, in the vicinity of the fundamental resonance frequency. The theoretical Love samples used for the inversion are represented with grey dots, and the Rayleigh samples with black dots in figures 6.19(b) and 6.19(c). These two curves are jointly inverted with five independent

runs and the results are shown in figure 6.19. Only the  $V_s$  profiles of the generated models are shown in figure 6.19(a). The corresponding calculated dispersion curve for Love and Rayleigh are shown in figure 6.19(b) and 6.19(c), respectively. Compared to the Rayleigh wave inversions, the combined Love and Rayleigh wave inversion correctly retrieves the  $V_s$  value below the main velocity contrast at 25 m. This result stresses out the interest of developing techniques of Love wave extraction from noise array measurements.

## 6.2 Liège site

For a simulated wavefield, the theoretical model is perfectly known and the inversion reliability is easily checked by comparing the results to the known velocity structure. On real sites, the results have to be validated by external geological or geotechnical information like existing borehole descriptions, cone penetration test (CPT) or conventional geophysical prospecting data. Actually, those data are also affected by uncertainties which must be considered in the validation process. This section compares the results of the three processing techniques applied to array vibration measurements in the city of Liège, Belgium. The reliability of the techniques is evaluated using newly acquired seismic refraction data and existing borehole data. Signals generated by hammer shots were recorded on vertical sensors for measuring the first P-wave arrivals and the apparent velocity of the triggered surface waves. A special care is paid to the uncertainties of the interpretation of usual refraction data. Within an urban context, the signal to noise ratio is relatively low, and the picking of the P-wave first arrivals can be ambiguous. For each picked time, an error value is estimated. The traveltime-distance curves are then inverted using the neighbourhood algorithm (Sambridge 1999a) to obtain one-dimensional  $V_p$  profiles. This method offers the advantage over other common approaches to take into account the picking uncertainties. The artificially triggered surface waves were processed to give the high frequency part of the dispersion curve (Stokoe et al. 1989, Malagnini et al. 1995), which might be uncertainly deduced from the processing of microtremor arrays (see below). The overlapping frequency ranges of ambient vibrations and triggered waves offer the opportunity to validate the array results. Though only the vertical components of the sensors are used for the array processing, we measured the three components of the particle motion. The horizontal to vertical spectral ratios (H/V method, Bard 1998) were computed for all the sensors. The frequency of the peak of the H/V curve is known to be close to the resonance frequency of the site (Bonneyoy 2004), giving an additional constraint to the  $V_s$  profile.

### 6.2.1 The test site

The experimental site is situated in the alluvial plain of Meuse river, near the centre of Liège city, Belgium (figure 6.20). At this location, the valley is about one kilometre wide and the river divides into two branches (the main stream and its derivation), delineating a lenticular island of 1.5 km long and 500 m large. The test site, which is a flat and unbuilt zone with a triangular shape of 200 m side, is located at the North-East end of the island (figure 6.20).

It is surrounded by several streets and one main road on its South-East side along the Meuse derivation (figure 6.20).

The geology structure below the city centre is made of alluvial layers overlying a shaly Paleozoic basement. The layer geometry and properties are well documented on geotechnical maps (Fagnoul 1975) gathering the existing information (mainly Cone Penetration Tests and borehole data).

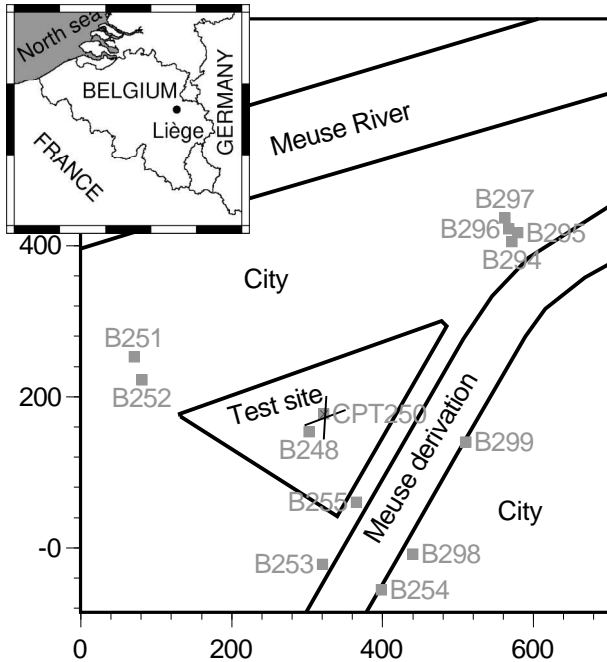


**Figure 6.20:** Local map of the test site. The grey squares represent the locations of boreholes. The Cone Penetration Test is marked by a black cross inside a grey square. The North-South and East-West  $P-S_V$  profiles are shown with thin black lines.

prospecting along two profiles oriented North-South and East-West (see figure 6.27 for location). Along each line were deployed twenty-four 4.5 Hz vertical sensors with a spacing of 2.5 m and the waves were generated with a hammer and an explosive source. An example of signals generated by an explosive source is given in figure 6.21. P-wave arrival times and Rayleigh waves are clearly visible and were inverted to obtain  $V_p$  and  $V_s$  profiles, respectively.

## Refraction

A method based on the neighbourhood algorithm described in section 1.2.1 is used to invert real data. For our particular real case, the geological structure evinced from the boreholes is roughly one-dimensional and the data uncertainties are relatively high due to the bad signal to noise ratio. Thus, we limit our inversion to velocity structures without dipping interfaces.

The two refraction lines are analysed separately using the method described in section 1.2.1. The time-distance curves are shown in figures 6.22 and 6.23 (plots labelled (e) to (h)). From their shapes, it is obvious that a model with at least three layers has to be used for the

borehole data). Twelve boreholes were drilled to the bedrock in the neighbourhood of the test site. They are reported in figure 6.20 and their logs are summarized in table 6.6. Three types of soft sediments are encountered from top to bottom: backfills of varying thickness (from 2 to 8 m), fluvial silts or clays of irregular distribution (down to 6 m depth, sometimes completely replaced by backfills), and finally a few metres of sand and/or gravel overlying the bedrock. The top of the bedrock was found at a depth ranging from 10.5 to 13 m. It is made of Wesphalian shales and sandstones with numerous coal veins, intensively exploited during the XX<sup>th</sup> century.

The bedrock depth reported by the borehole descriptions may not correspond to a sharp increase of the seismic velocity, due to the presence of a few metre thick weathered rock layer Jongmans and Campillo (1990). In the absence of specific information about the seismic properties at the test site, we conducted active seismic

Borehole	Backfills	Silts or Clay	Sand and gravel	Bed-rock	Water level
B248	0.0 to 2.7	2.7 to 6.0	6.0 to 10.0	-	-
B251	-	0.0 to 3.0	3.0 to 12.0	12.0	-
B252	-	0.0 to 2.5	2.5 to 10.6	10.6	-
B253	0.0 to 7.5	-	7.5 to 11.3	11.3	-
B254	0.0 to 5.5	-	5.5 to 10.3	10.3	-
B255	0.0 to 4.5	-	4.5 to 10.3	11.3	-
B294	0.0 to 3.6	3.6 to 6.2	6.2 to 13.0	13.0	-
B295	0.0 to 3.9	3.9 to 4.6	4.6 to 12.6	12.6	3.9
B296	0.0 to 2.0	2.0 to 4.4	4.6 to 12.7	12.7	3.5
B297	-	0.0 to 2.8	2.8 to 11.0	11.0	2.8
B298	0.0 to 2.7	2.7 to 4.9	4.9 to 11.3	11.3	-
B299	0.0 to 8.5	-	8.5 to 13.0	13.0	-

**Table 6.6:** Borehole descriptions around the site (from geotechnical database). From B294 to B297, the silty layer is replaced by soft blue clays. Only B248 is included in the area investigated by arrays and geophysical experiments. Depths measured from surface are in metres.

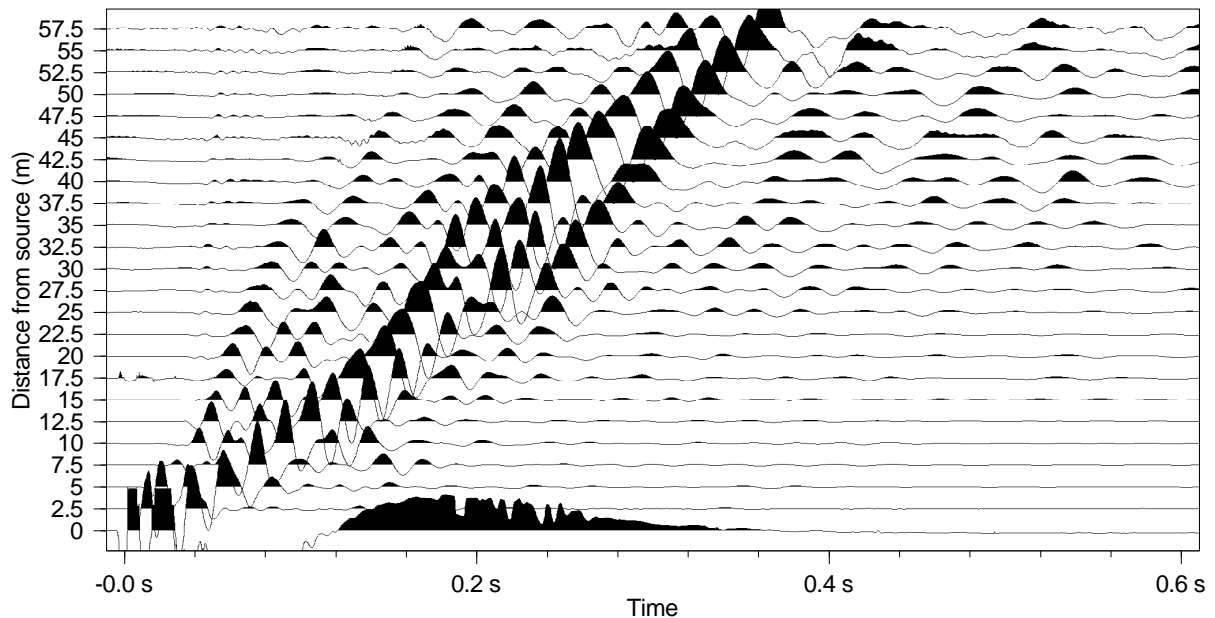


**Figure 6.21:** Recorded signals for East-West  $P - S_V$  refraction line, West source. First P-wave are visible on the left with small amplitudes. Surface waves develop between 0.1 and 0.4 seconds and constitute the most energetic part of the signal.

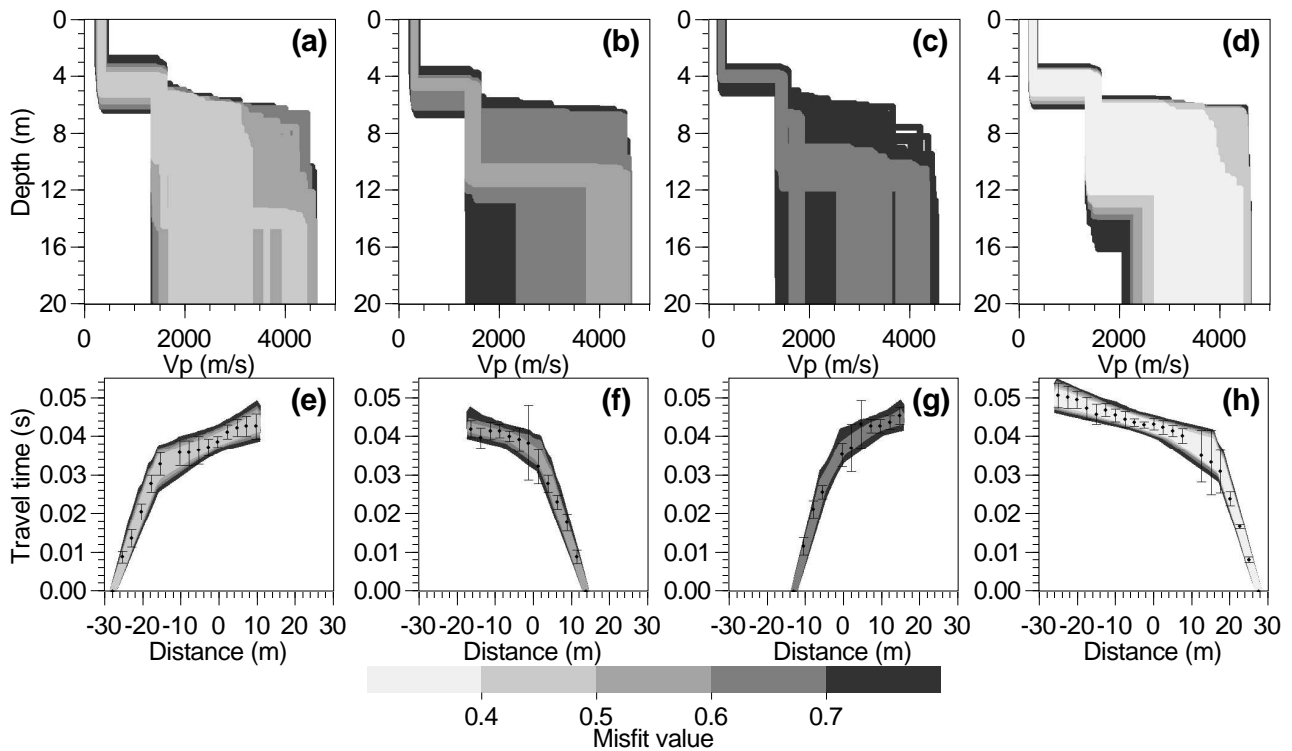


**Figure 6.22:** Refraction results obtained with travel time NA inversion for profile East-West. (a) to (d)  $V_p$  profiles obtained by inversion for South, Central towards South, Central towards North, and North shots, respectively. (e) and (h) corresponding calculated traveltime-distance curves (in the same order). The black dots and the error bars are the experimental times picked on recorded signals.

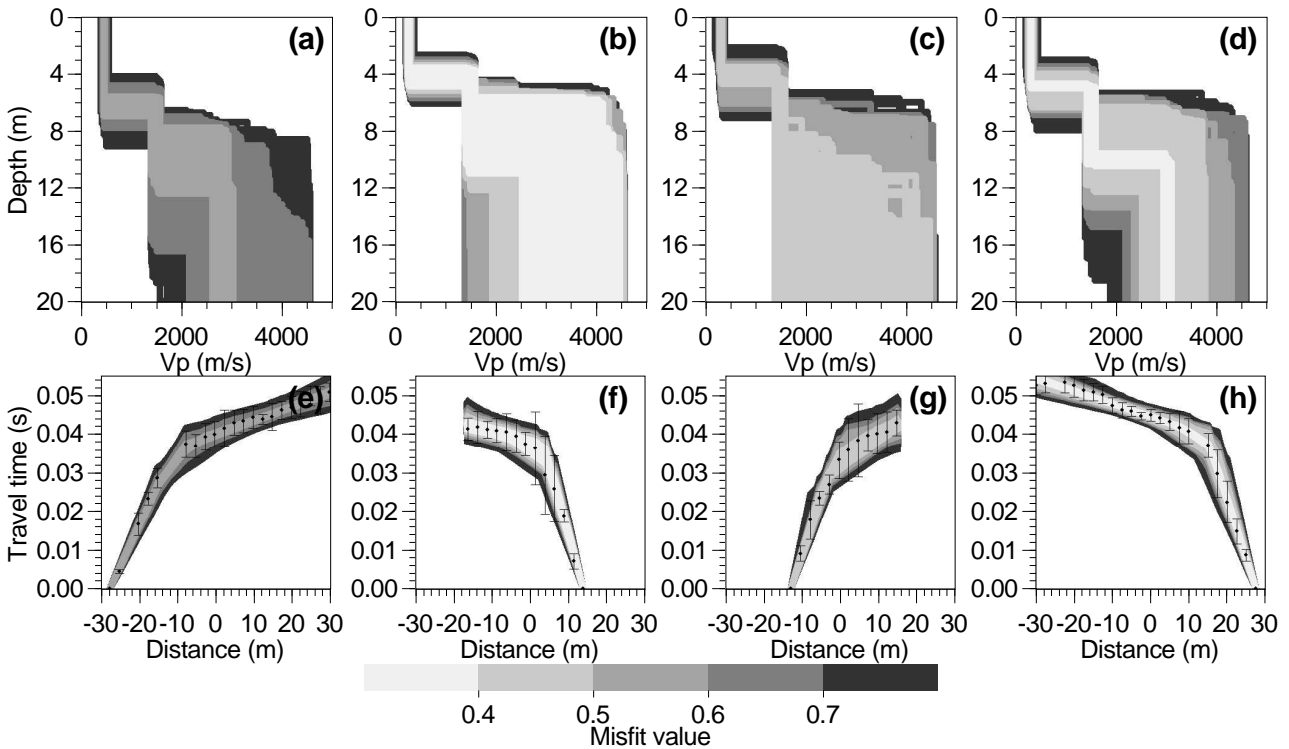


**Figure 6.23:** Refraction results obtained with travel time NA inversion for profile North-South. (a) to (d)  $V_p$  profiles obtained by inversion for West, Central towards West, Central towards East, and East shots, respectively. (e) and (h) corresponding calculated traveltime-distance curves (in the same order). The black dots and the error bars are the experimental times picked on recorded signals.

data inversion. The water table is a few metre deep (between 2.5 and 3.9 m from the closest boreholes) in the alluvial layers and the velocity in the intermediate layer was constrained between 1400 and 1600 m/s. Five parameters (three  $V_p$  and two thickness values) are inverted. The results are shown in figures 6.22 and 6.23 for lines East-West and North-South, respectively. The generated ground models are presented in figures (a) to (d) and the comparison of the calculated traveltimes with the experimental curves is shown in figures (e) to (h). The lowest misfit found is around 0.2 and a common grey scale for the misfit is adjusted to all cases. A threshold of one is chosen for the misfit to select all models with traveltime-distance curve inside the experimental uncertainties.

The feature common to all profiles is the  $V_p$  increase to around 1500 m/s at about four metres deep. It is consistent with the observed level of the river around the site (bank walls) and with the water table in the holes. Some slight variations may be observed between the different shots for the superficial layer velocity: for the best model of each shot,  $V_p$  ranges from 275 to 350 m/s, and from 200 to 430 m/s considering the complete uncertainty interval. The velocity in the basement is poorly constrained, with a range between 2000 and 4000 m/s. However, from the extremity shots (figures 6.22(d), 6.23(a) and 6.23(d)), the velocity below 15 m is probably around 3000 m/s. There is no evidence of a well defined contrast for the basement, but a transition zone located between 7 and 15 m is observed for all shots. This intermediate zone corresponds to the bottom of the alluvial deposits and to the weathered rock layer which can reach a thickness of five metres (Jongmans and Campillo 1990).

### Rayleigh wave processing

During the same campaign, the geophone layout was used to record artificially generated Rayleigh waves. Sources were placed with an offset of 20 m in order to avoid near-field effects on the closest receivers. Two kinds of sources were used: hammer shots like in the preceding section and explosive loads (100 gr of black powder) buried at about 0.8 m deep. Eight shots were recorded, corresponding to the two profiles, the two source types, and the two extremities of profiles. The averages and the standard deviations of the frequency spectra observed for the two sources are compared to the ambient noise level in figure 6.24. The amplitude for the explosive shots is about 25 times greater than the amplitude for the hammer shots. The energy level of the ambient vibrations is so high that the results from hammer shots might be valid

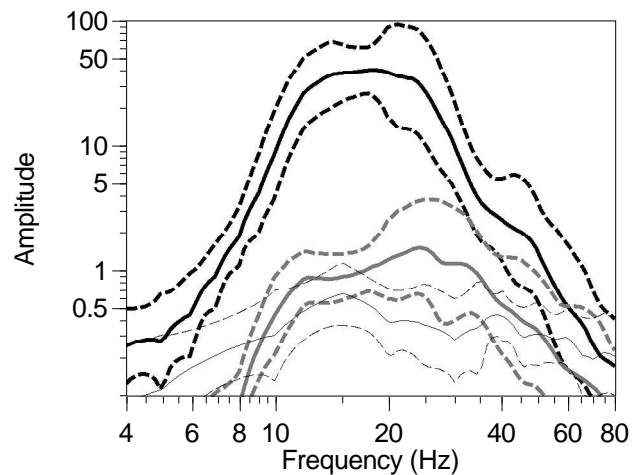


**Figure 6.24:** Triggered surface waves along  $P - S_V$  profiles North-South and East-West. Average spectra (plain lines) and standard deviations (dashed lines) for 24 receivers recording a black powder shot situated at 20 m from the first sensor (thick black lines) and a hammer shot (grey lines) and the ambient vibrations recorded with the same sensors (thin black lines).

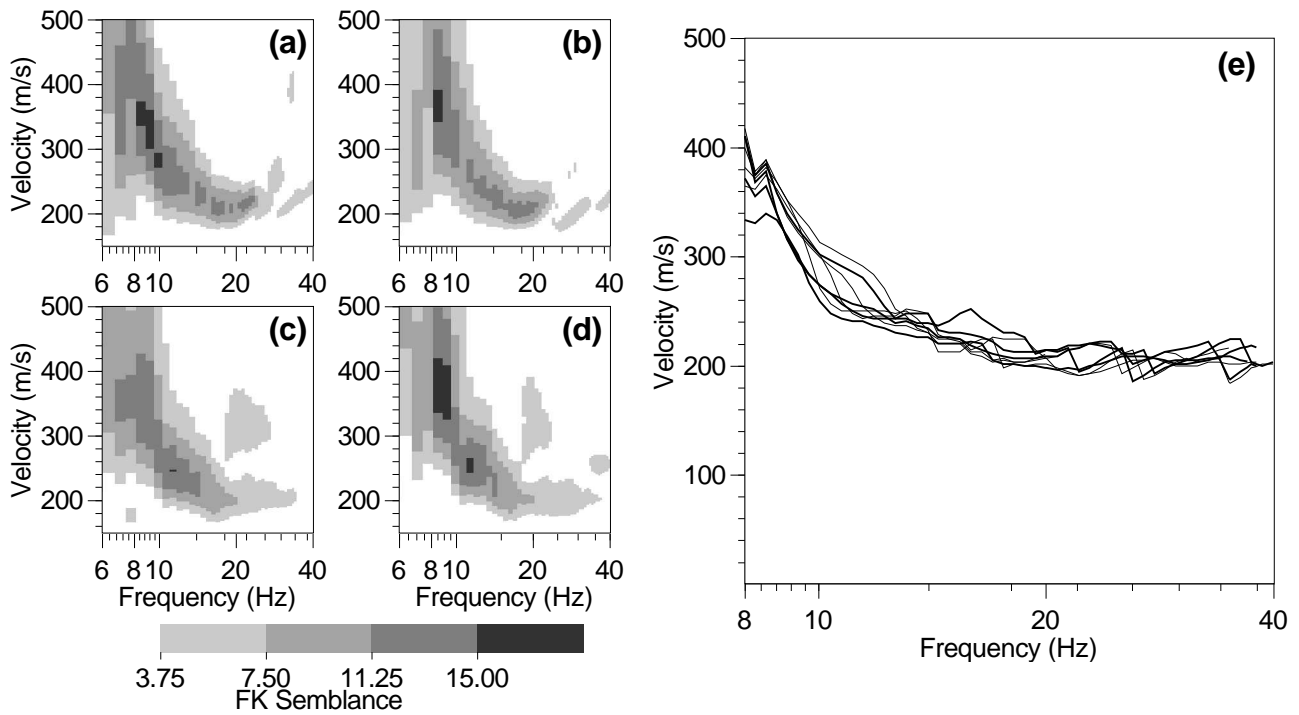


**Figure 6.25:** Triggered surface waves along  $P-S_V$  profiles North-South and East-West. (a) to (d) Frequency-wavenumber semblance maps for the different shots: (a) East explosive shot and (b) East hammer shot on EW profile, (c) South explosive shot and (d) South hammer shot on NS profile. (e) Picking of the maximum apparent velocity for all source locations and types (8 curves, thin lines for hammers and thick lines for explosives).

only inside a narrow frequency band between 15 and 25 Hz. On the other hand, explosive shots are far above the ambient noise for all frequencies between 6 and 50 Hz.

For each shot and for all frequency bands, a frequency-wavenumber semblance is calculated for the linear arrays of sensors. The technique is exactly the same as for the processing of microtremor arrays (section 1.2.3), except that only one time window is processed. The apparent velocity is deduced for each frequency band. The calculated semblance plots are shown for two shot positions in figures 6.25(a) to 6.25(d). Figures (a) and (c) are for explosive shots and figures (b) and (d) for hammer shots. The consistency of the measured dispersion curve (maximum of semblance) checked for all eight sources in figure 6.25(e) is remarkable. All plots are cut between 8 and 40 Hz which is inside the valid interval for explosive shots but, amazingly, outside the hammer shot validity range. One reason could be that the ambient noise is predominantly made of surface waves, leading to a global coherency of the semblance function. Below 10 Hz, for both explosive and hammer shots, the uncertainties over the velocity estimates drastically increase (figures 6.25(a) to 6.25(d)).

The Rayleigh dispersion curve is not directly inverted here to obtain the  $V_s$  or  $V_p$  profile. It is used in the next sections, comparing to array results.

### $S_H$ refraction

One  $S_H$  refraction profile has been achieved in the centre of the site with two shot points at each extremity. The S-wave arrivals are picked with an estimation of the error, considering all directions for each shot. The observed traveltime-distance curve are shown in figures 6.26(c)

and 6.26(d) by black dots and their associated error bars. From their shapes, it is obvious

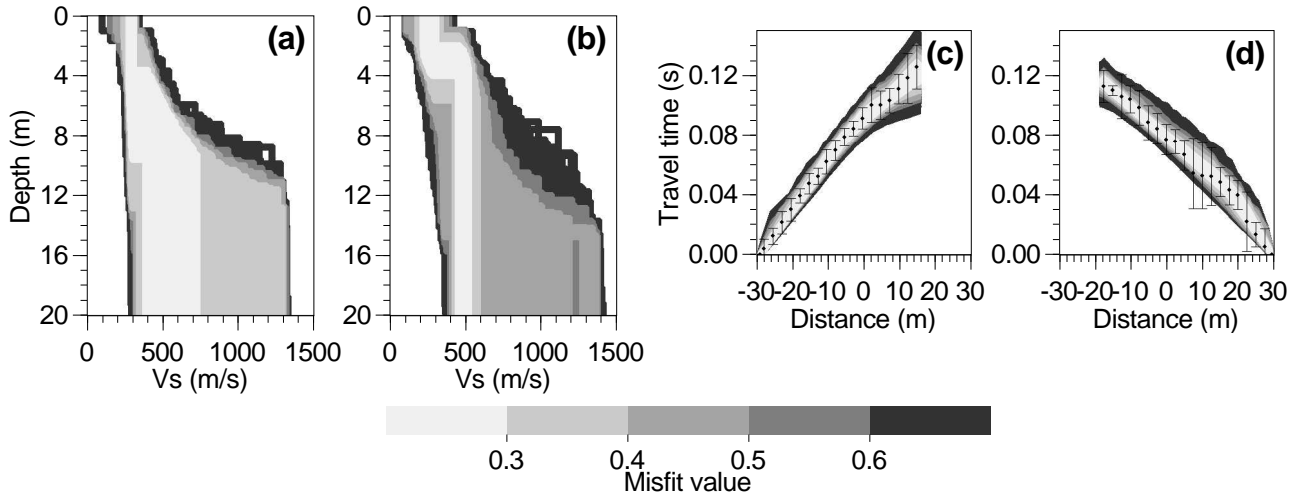


**Figure 6.26:** Refraction results obtained with travel time NA inversion for  $S_H$  profile. (a) and (b)  $V_s$  profiles obtained by inversion for the West and East shots, respectively. (c) and (d) corresponding calculated traveltime-distance curves (in the same order). The black dots and the error bars are the experimental times picked on recorded signals.

that a two-layer model is sufficient. The neighbourhood algorithm is then launched with three parameters ( $V_s$  of each layer and thickness of first layer). The results are shown in figures 6.26(a) to 6.26(d). The generated ground models are presented in figures (a) and (b) and the comparison of the calculated traveltime-distance curves with the experimental curves is shown in figures (c) to (d). The lowest misfit found is around 0.2, similar for both shots.  $V_s$  at the surface is between 100 and 400 m/s considering all models. For the best models, the velocity is between 260 and 290 m/s. Between 0 and 10 m,  $V_s$  increases up to 500 m/s. The maximum possible velocity at 10 m is around 1000 m/s.

### 6.2.2 Ambient vibrations recording

Ambient vibrations were measured with two sets of sensors: 10 three-component Lennartz sensors (resonance frequency of 0.2 Hz) and 22 vertical 4.5 Hz geophones used for the  $P - S_V$  experiments. For the first array (A), 22 4.5 Hz vertical sensors were set up 5 m apart on a 17.5 m radius circle (figure 6.27(a)). The hole in the circle of figure 6.27(a) comes from a defective receiver, resulting in 21 available signals. The ten Lennartz sensors were set up with three distinct geometries (Arrays B to D, shown on figures 6.27(b) to 6.27(d), respectively). The geometry of arrays B and D was made of one central sensor and three triangles rotated by  $40^\circ$ , with maximum apertures of 40 and 50 m, respectively. Array C has a central sensor and nine sensors distributed on a circle with a radius of 40 m. All the sensor positions were measured with a theodolite, expecting a centimetric accuracy.

The horizontal to vertical spectra are calculated for all individual three-component signals. Typical spectra are shown for the central station in figures 6.28(a) to 6.28(c). The plain line is the average of all time windows while the dashed lines are drawn at one standard deviation (geometrical average). The total recording length is 6 hours. Statistics are calculated over

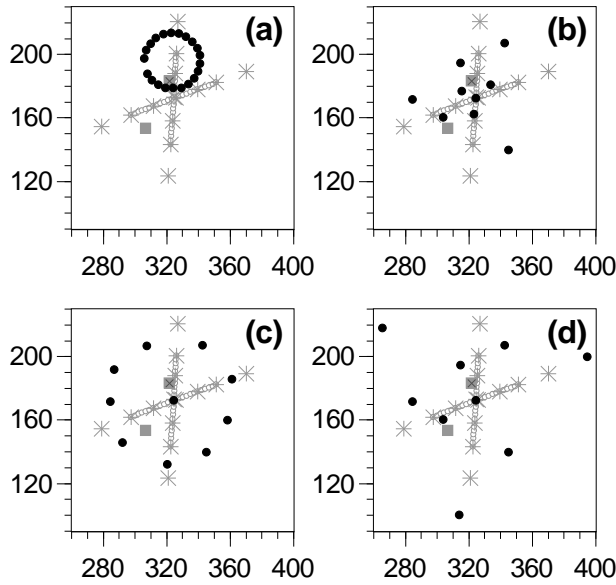


**Figure 6.27:** Local maps showing the array geometries (black dots), the refraction lines (shots with grey stars and receivers with grey circles), borehole and cone penetration test locations (grey square and grey squares with cross, respectively). Y axis is oriented towards the magnetic North (site of the old Bavière Hospital, Liège, Belgium, 50.64°N, 5.57°E, 19th March 2002). Each ambient noise array geometry is represented on a separate plot: (a) Array A, (b) Array B, (c) Array C and (d) Array D.

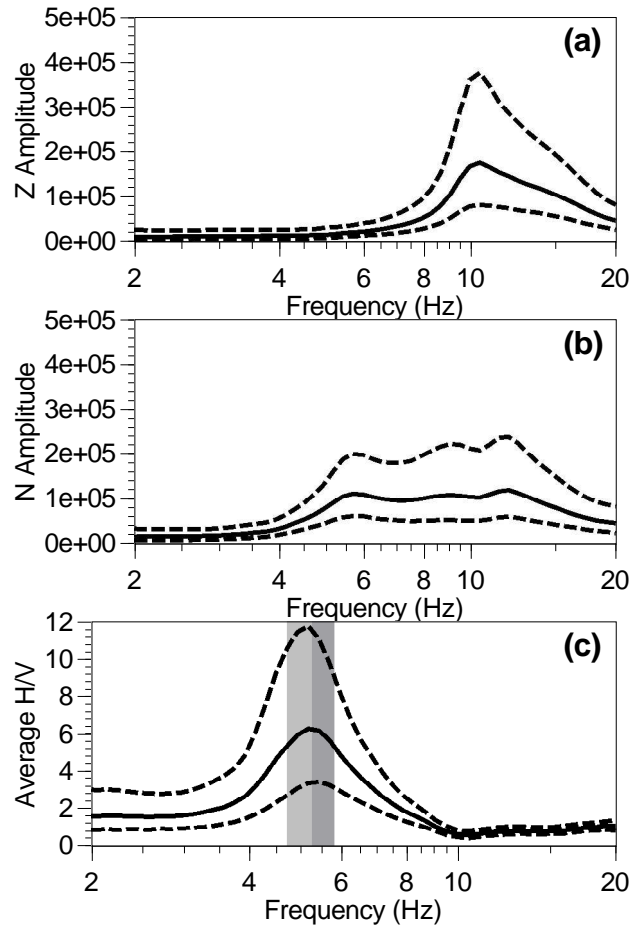


**Figure 6.28:** Spectral curves of the central station of array A, B and C. The plain line is the average and the dashed lines are located at one standard deviation. (a) Amplitude spectrum of the vertical component. (b) Amplitude spectrum of one horizontal component. (c) Spectral ratio Horizontal to Vertical (H/V). Grey bands indicate the average and standard deviation of the frequency peak values observed for each individual time window.

3690 time windows of five seconds each. The vertical and an horizontal component spectra are presented in figures 6.28(a) and 6.28(b), respectively. A clear high pass filter effect is observed for the vertical component as demonstrated by Scherbaum et al. (2003) for a synthetic case. The ratio of the vertical to the horizontal average component is shown in figure 6.28(c) and it exhibits a well developed peak at 5.3 Hz. The results are quite similar for the other stations, with a mean frequency varying from 4.8 to 5.3 Hz with a standard deviation of about 0.5 Hz. The average value of the peak frequency is  $5.17 \pm 0.57$  Hz (29015 time windows of five seconds) over the whole area. The small spatial variation of the resonance frequency is supporting the assumption of a one-dimensional structure.

### 6.2.3 Frequency-wavenumber method

As shown in section 6.1, the computation of the theoretical frequency-wavenumber array response is a mandatory tool for assessing the reliable range of the dispersion curve. These

theoretical responses are calculated for arrays A to D in figures 6.29(a) to 6.29(d). The resolution and aliasing limits (section 1.1.1) defined from plots (a) to (d) are reported in table 6.7.

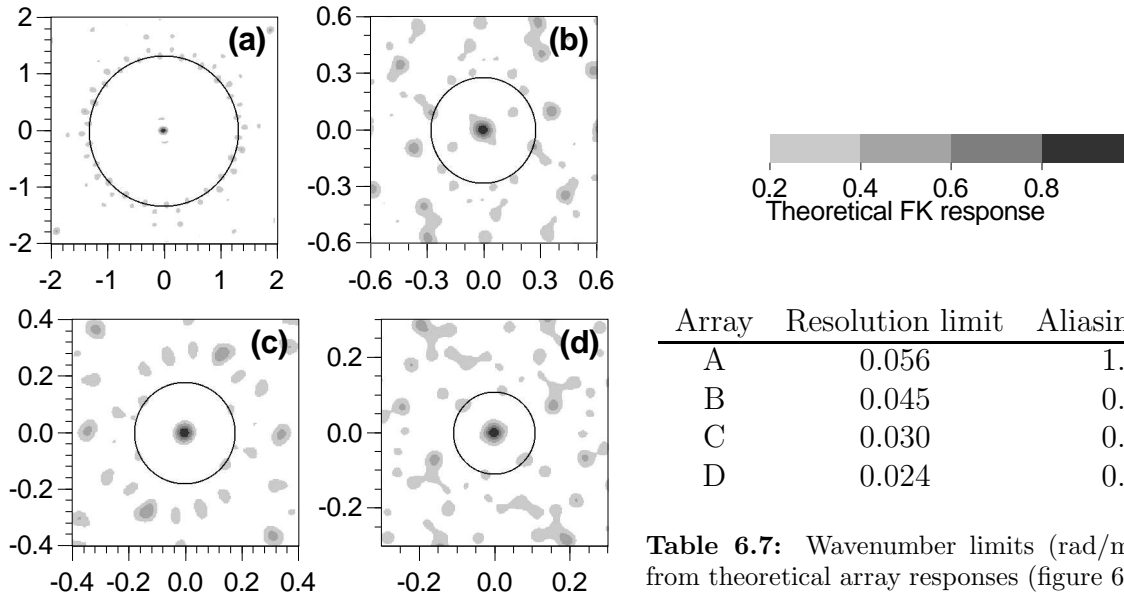


**Figure 6.29:** Theoretical frequency-wavenumber response calculated for Arrays A to D (figures (a) to (d), respectively).

For array A, the signals were recorded with 16 short windows of four minutes. For arrays B to D, continuous signals are available during 1 hour, 46 minutes, and 1 hour 20 minutes, respectively. For each array, vertical components are processed from 2 to 20 Hz using the method described in section 6.1. The apparent velocity is estimated from time windows with a length of 50 cycles, with an overlap of 50% with their neighbours. The statistical results (velocities of the semblance peaks) in the velocity-frequency plane are presented with one histogram per frequency band in figures 6.30(a) to 6.30(d) for arrays A to D, respectively. The three curves indicate the wavenumber limits ( $k$  equal to a constant) deduced from the theoretical array response: resolution (plain lines), half of the aliasing (dotted lines), and aliasing wavenumber (dashed lines). For arrays A and B, the velocity estimate is remarkably stable against time within the wavenumber limits. According to the resolution criterion (table 6.7) the velocity values may be biased below 6 Hz for those two arrays. Indeed, the average velocity values observed at 5 Hz for arrays B and A ( $\gtrsim 1600$  m/s) are higher than the velocity measured by array C ( $\approx 1200$  m/s) which has a correct response at this frequency. Moreover, the uncertainties below 6 Hz increase for all arrays, even within the valid wavenumber range of array C. This is probably due to the energy drop on the vertical component at the vicinity of and below the resonance frequency (around 5.2 Hz from H/V results).

Figure 6.31 shows the average dispersion curve (black curve and error bars) calculated from arrays A to D, keeping the data between the resolution and half the aliasing limits. On the same graph is plotted in grey the average dispersion curve calculated from the triggered surface waves. An indisputable agreement is found between 12 and 20 Hz. In this range, the curve differences all fall inside the respective standard deviations. Between 8 and 12 Hz,

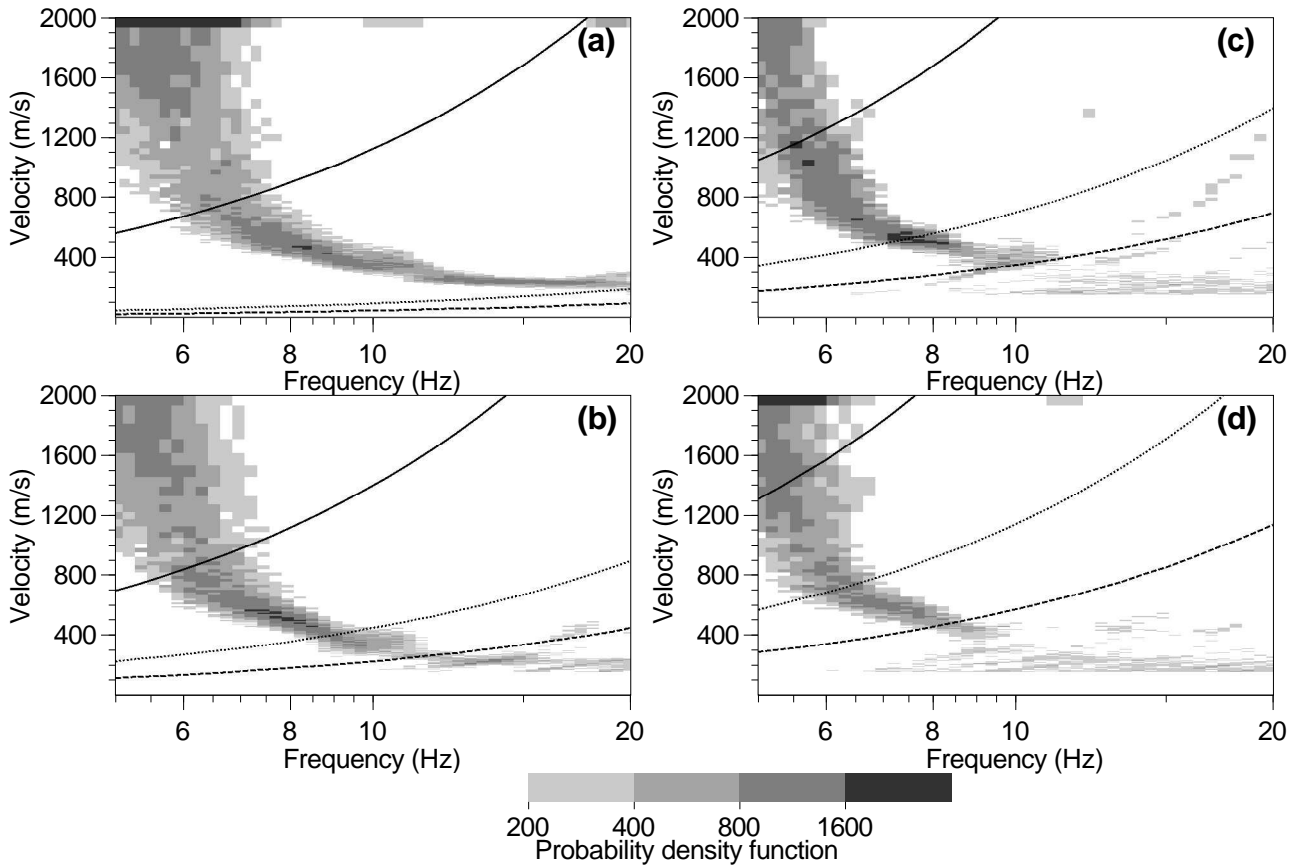


**Figure 6.30:** Results of the frequency-wavenumber method applied to arrays A to D ((a) to (d), respectively). The three exponential curves represent constant wavenumber curves values of which are deduced from theoretical frequency-wavenumber response (figures 6.29): minimum (continuous line), half the maximum (dots) and maximum wavenumber (dashed).

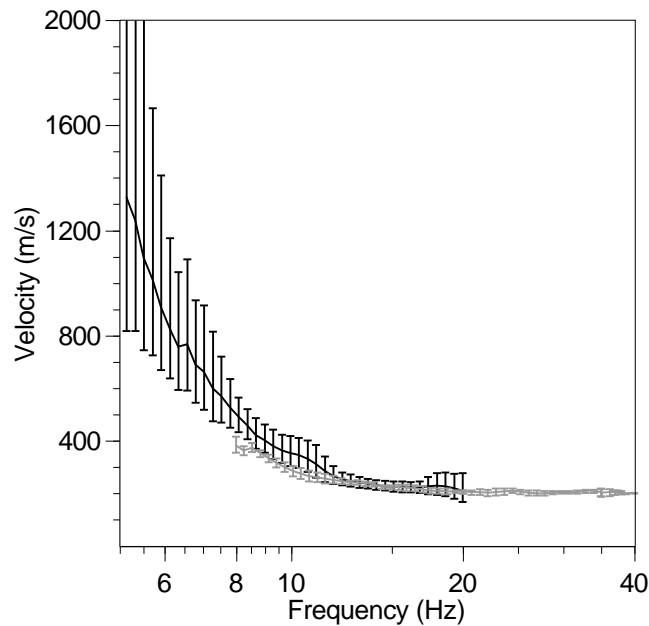


**Figure 6.31:** Average and standard deviations (vertical bars) of apparent dispersion curve from arrays A to D (black dots). The grey dots represent the average dispersion curve calculated from figure 6.25(e) for triggered surface waves.

the array velocity is slightly higher than the active experiment results which are affected by a relatively high uncertainty (figure 6.25). The array dispersion curve is then considered in the low frequency range and extended from 20 to 40 Hz using the active experiment results. The global dispersion curve is shown with black dots in figure 6.32(c).

Before inversion, the ranges of the seven parameters ( $V_p$  and  $V_s$  in the three layers and the thicknesses of the two uppermost layers) are defined in table 6.8 according to the geometry and characteristics discussed in section 6.2.1 on page 125. This parameterisation was used to generate 50,000 models by five independent runs with the neighbourhood algorithm. Of these, the 17,500 models found with a misfit less than 1 are plotted in figures 6.32(a) and (b) with a misfit grey scale. The lowest misfit obtained is 0.44. The corresponding dispersion curves are shown in figure 6.32(c) with the same grey scale.

Layer	Bottom depth	$V_p$	$V_s/V_p$	Density	$V_p$ variation
Sediments	2 to 7 m	200 to 430	0.01 to 0.707	2 t/m <sup>3</sup>	–
Sediments	7 to 15 m	1400 to 1600	0.01 to 0.707	2 t/m <sup>3</sup>	–
Half-space	–	2000 to 5000 m/s	0.01 to 0.707	2 t/m <sup>3</sup>	–

**Table 6.8:** Parameters and their prior interval for spectral curve inversions (dispersion curves and auto-correlation curves).

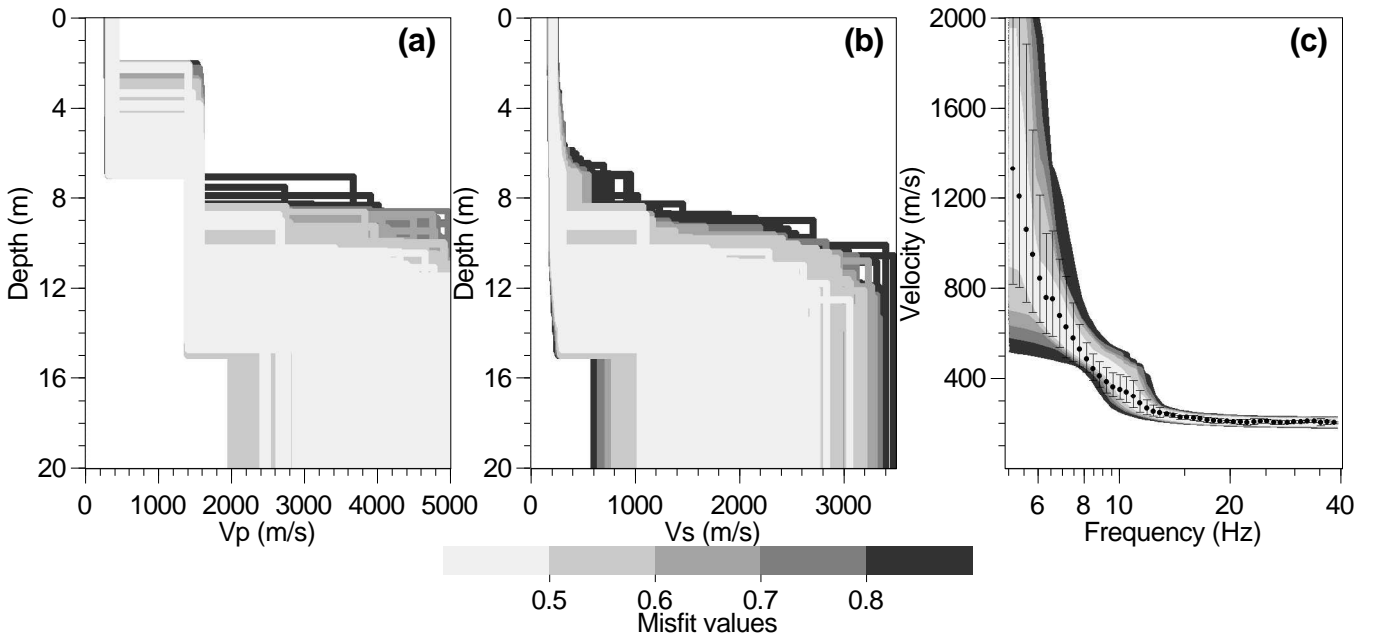


**Figure 6.32:** Inversion of the average dispersion curve of figure 6.31. (a)  $V_p$  profiles and (b)  $V_s$  profiles of the generated models. (c) The corresponding dispersion curves (grey scale). The observed curve of figure 6.31 is shown by black dots and error bars.

From figure 6.32(b), the  $V_s$  profile is well constrained and almost constant on the first six metres, with a slight increase from 220 m/s at the surface to 250 m/s at 6 m. Below this depth, the uncertainties increase dramatically. The depth of the major velocity contrast is between 10 and 15 m with a basal shear wave velocity between 1000 and 3000 m/s. The relatively high frequency content of the Rayleigh waves and the uncertainty on the dispersion curve do not allow a more precise definition of the depth and of the shear wave velocity below 8 m. The

$V_p$  profile is little constrained by the dispersion curve inversion (figure 6.32(a)) and does not provide additional information above 8 m, when comparing to the refraction results (figures 6.22 and 6.23).

The ellipticity and the  $S_H$  transfer function have been calculated for the best model. They exhibit a single peak around 5.2 Hz which corresponds to the H/V measurements. However, for the ensemble of models shown in figure 6.32, the peak of the theoretical ellipticity is widely distributed. Consequently, according to the H/V criterion, some models may be discarded. A joined inversion described in section 5.3 is hence performed with the same parameterization as in figure 6.32 (table (6.8)). The weights for the dispersion curve and the ellipticity frequency are 0.5. The results are presented in figure 6.33. The lowest misfit obtained is 0.23 which is approximately half of the misfit in figure 6.32, meaning that the frequency of the H/V peak is nearly perfectly fit, because the minimum misfit that can be achieved with the parameterization of table 6.8 is around 0.44.

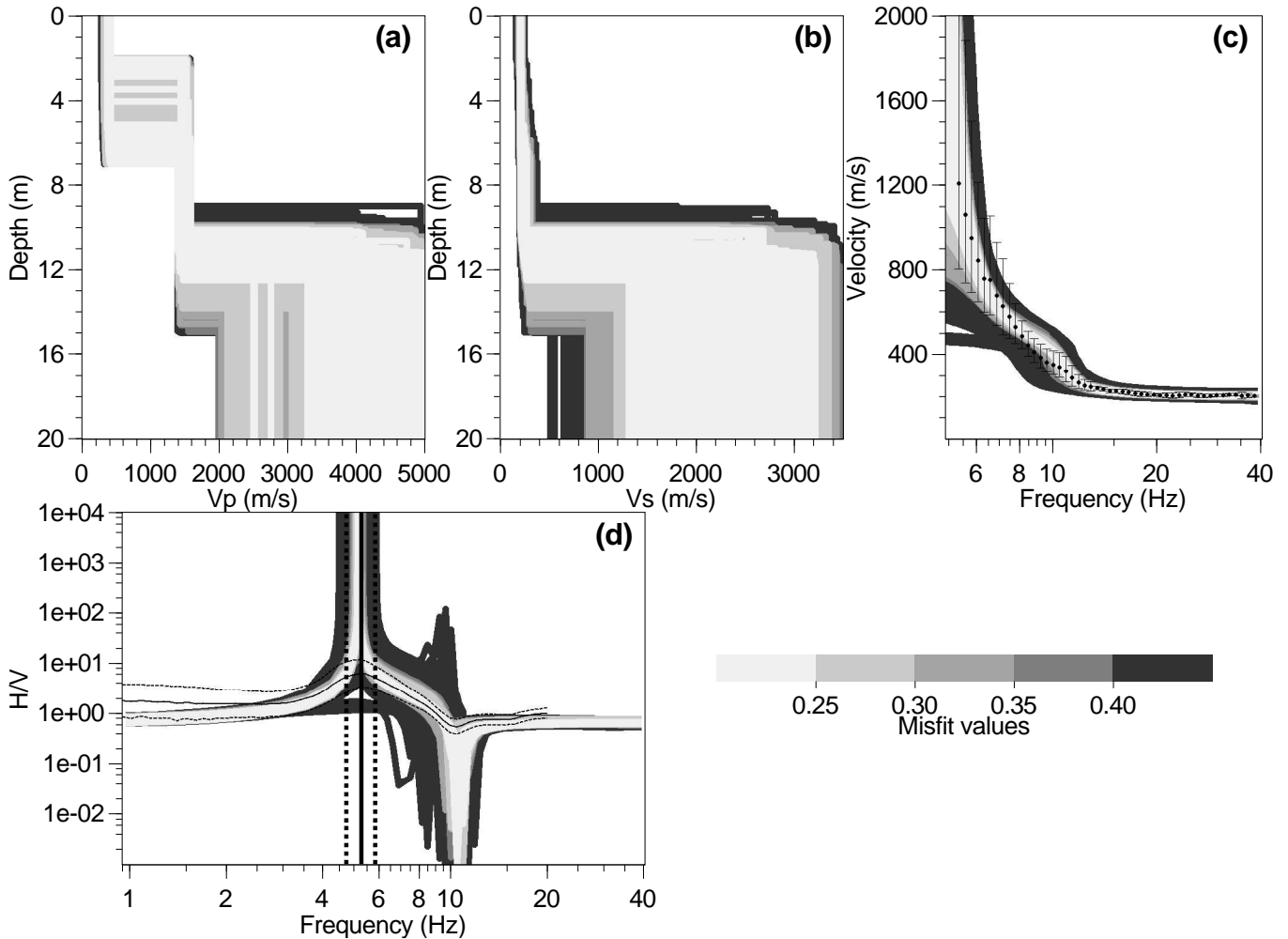


**Figure 6.33:** Inversion of the average dispersion curve of figure 6.31 and ellipticity peak. (a)  $V_p$  profiles and (b)  $V_s$  profiles of the generated models. (c) The corresponding dispersion curves (grey scale). The observed curve of figure 6.31 is shown by black dots and error bars. (d) Calculated ellipticities (grey scale). The vertical black lines delineate the target frequency of the peak ( $5.17 \text{ Hz} \pm 0.57 \text{ Hz}$ ). The thin black curve is the average H/V ratio observed for the central station (figure 6.28(c)).

Comparing figures 6.32(b) and 6.33(b), the joined inversion with the ellipticity clearly results in a better defined depth of the basement. It is impossible to find a model that fits the frequency

of the H/V peak with a depth above 9 m. The highest limit of the depth interval is also slightly reduced, probably around 14 m.

### 6.2.4 High resolution method

The high resolution frequency-wavenumber method is used on the same signals as the f-k method. The results are shown in figures 6.34(a) to 6.34(d) for array A to D, respectively. For array A, 16 signal windows were processed separately providing 16 velocity estimates by frequency band (figure 6.34(a)) while only one velocity estimate is available for arrays B and C. For array D, two windows are available and two velocity estimates are determined by frequency band (figure 6.34(d)). The average dispersion curve obtained with the f-k method is plotted for comparison, as well as the wavenumber limits deduced from the theoretical array responses.

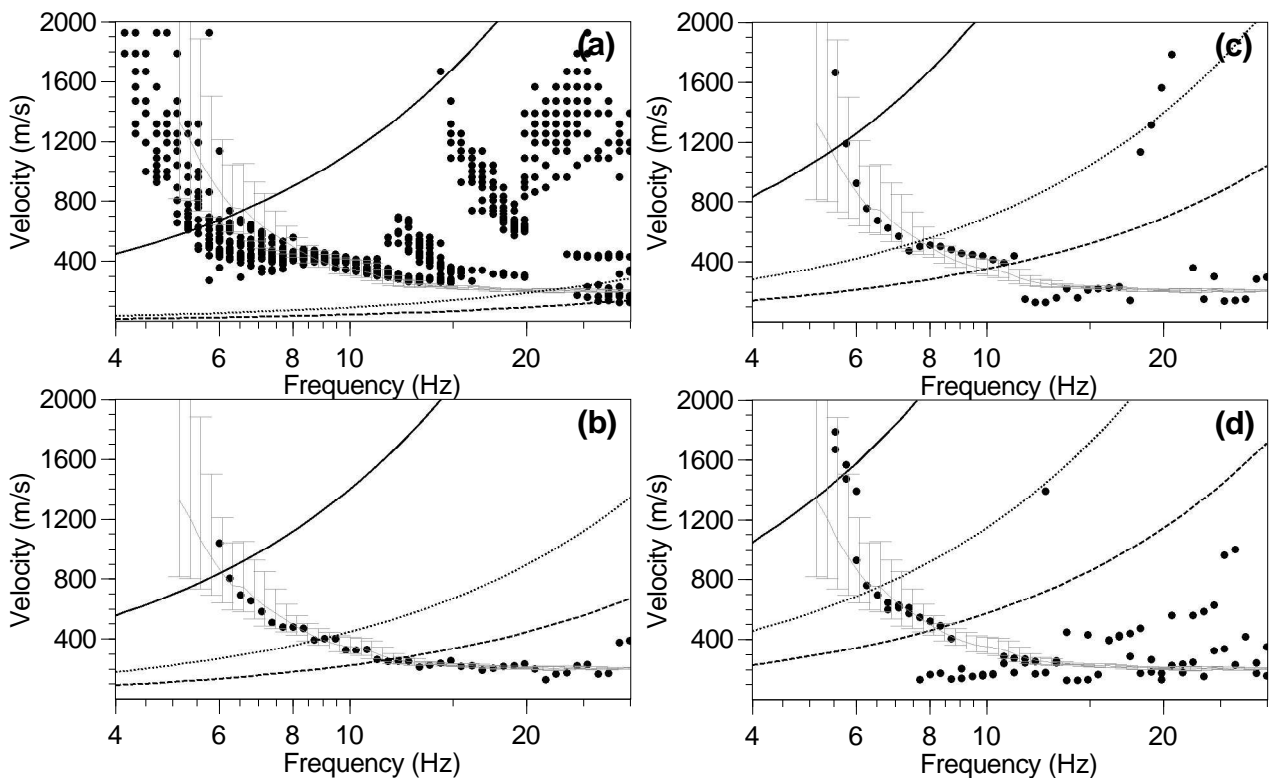


**Figure 6.34:** Results of the high resolution frequency-wavenumber method applied to arrays A to D (figures (a) to (d), respectively), represented with black dots. The dispersion curve observed for frequency-wavenumber method is plotted for comparison in grey. Wavenumber limits deduced for the f-k method are also shown with the same legend as in figure 6.30.

For synthetic signals (section 6.1), the high resolution method results were consistent between each other and agreed with the ones obtained with the f-k method and even gave a better estimate of the true dispersion curve for some frequencies. For this real case, strong discrepancies are observed between the different curves for the high resolution method and between the two methods for some frequencies, even in the theoretical validity range. For instance, the velocity value measured by array A at 6.5 Hz (around 500 m/s) with the high resolution method is lower than the one measured with the same method by the other arrays (about 700 m/s). This last value is consistent with the results of the f-k method. Also an abnormal jump on the high

resolution curve is observed (figure 6.34(d), array D) around 6 Hz, while the curve obtained by f-k method exhibits a regular decrease with frequency. The high resolution results for array A at high frequency seem to indicate the existence of higher modes. The uncertainty on these results is obviously too high to use this information for inversion purposes. As a conclusion, the high resolution method appears to be unable to obtain a reliable velocity estimate below 6 Hz in this case. Over 6 Hz, a good agreement is reached between the high resolution and the f-k methods in the valid frequency range of the arrays. The f-k method then appears to be more robust in the whole frequency range, with an increase of the uncertainty in the low frequency range.

### 6.2.5 Spatial auto-correlation method

This method is applied to the four arrays but only array A is shown here. Arrays B, C, and D are not shown here because the obtained auto-correlation curves are not consistent according to the test described in section 5.2.3. The array geometries are probably not well adapted for the auto-correlation method. For non circular arrays, the spatial auto-correlation method requires the definition of rings (Bettig et al. 2001) and the ten rings chosen for array A are shown in figure 6.36. The auto-correlation curves are calculated using the method described in section 6.1. Three of the ten auto-correlation curves are presented in figure 6.35 (black and grey dots). The consistency of all 10 auto-correlation curves is checked in figure 6.37 with the grid method described in section 5.2.3. From 5 to 12 Hz, all rings are consistent with each other and a common dispersion curve is delineated by the dashed lines and the wavenumber limits (plain and dotted lines). The data outside of those limits are considered as incoherent and are discarded. They are marked with grey dots on the auto-correlation curves of figure 6.35. The data selected from the ten auto-correlation curves are inverted together with the neighbourhood algorithm as in section 6.1. Five runs are used with the same parameterization as for the frequency wavenumber method (table 6.8). The  $V_s$  profiles are shown in figure 6.38. The three of the ten calculated auto-correlation curves are shown in figures 6.38(d) to 6.38(f) with the experimental black dots and the error bars shown in figure 6.35. The minimum misfit found is 0.65. This relatively high value is due to the residual inconsistencies between the ten auto-correlation curves. Above 8 Hz, both frequency wavenumber and auto-correlation methods give the same dispersion curve. If we assume that a misfit of one is a good threshold to select all models within the experimental uncertainties, this example shows that the final  $V_s$  uncertainty range for all depth above 8 m is larger for the auto-correlation method than for the wavenumber method. For frequencies below 8 Hz, a huge gap is observed between the two methods, with much lower velocity estimates for the auto-correlation results. Moreover, the experimental auto-correlation curves are not correctly fit below 6 Hz. In figure 6.38(f), the experimental points below 8 Hz are located on the left side of the calculated curves, which correspond to an increase of the velocity and to a better agreement with f-k methods. On the contrary, in figure 6.38(e), fitting the experimental points below 6 Hz would imply an even lower velocity. The same type of deviation is observed for the high resolution method (figure 6.34(a)). This

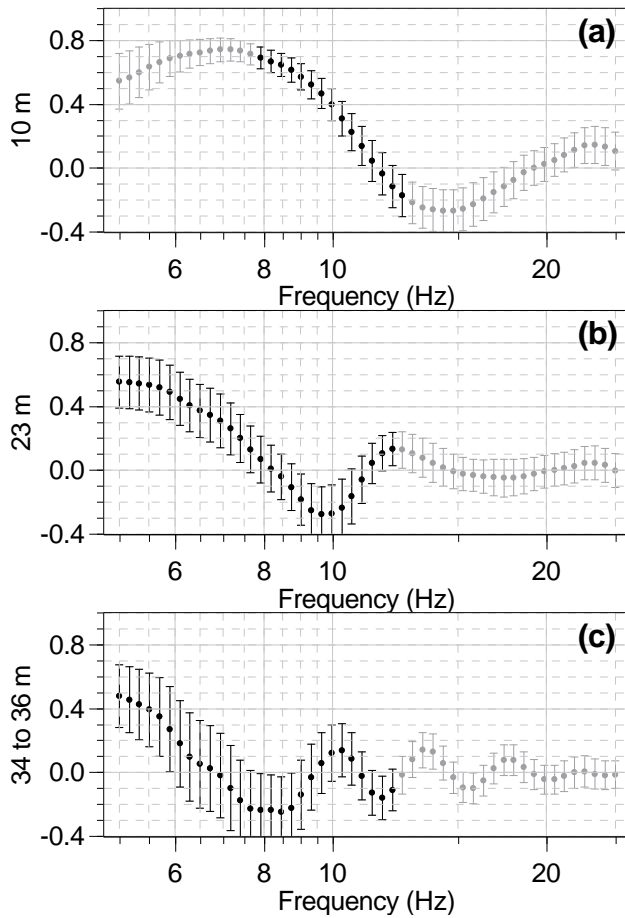


**Figure 6.35:** Examples of auto-correlation curves obtained for array A. The black dots and error bars are the samples selected according to criteria of figure 6.37.

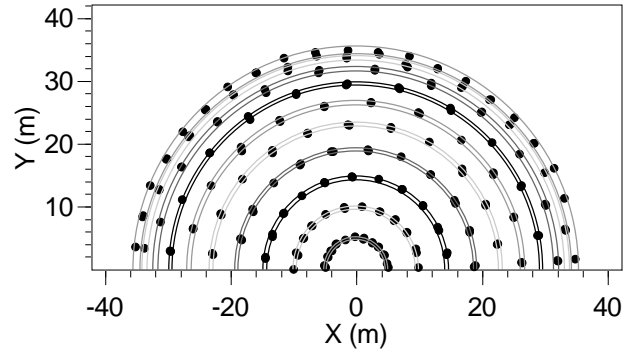


**Figure 6.36:** Azimuth-inter-distance plot for array A: each dot represent one couple of stations. The pairs of grey circles show the limits of the chosen rings.

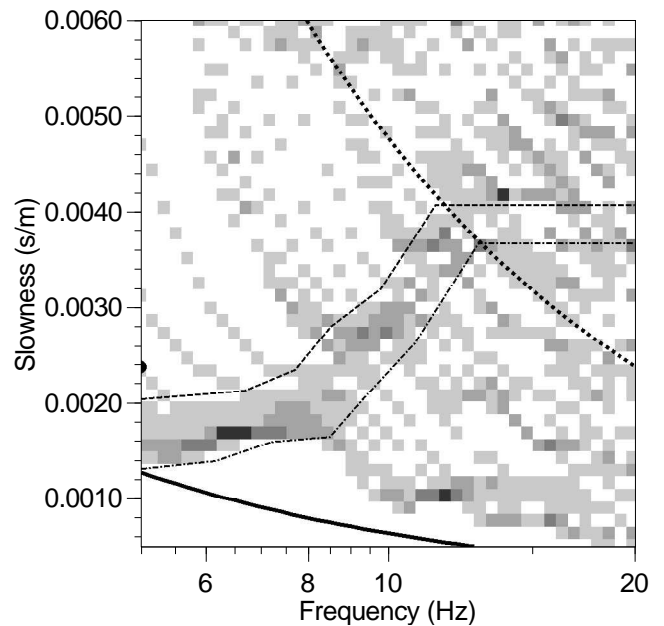


**Figure 6.37:** Grid in frequency-slowness domain representing the density of dispersion curve solutions for array A. The plain and the dotted lines are the wavenumber limits deduced from the solution density grid. The dashed and the dot-dashed curves are the wavenumber limits of the apparent dispersion curve.

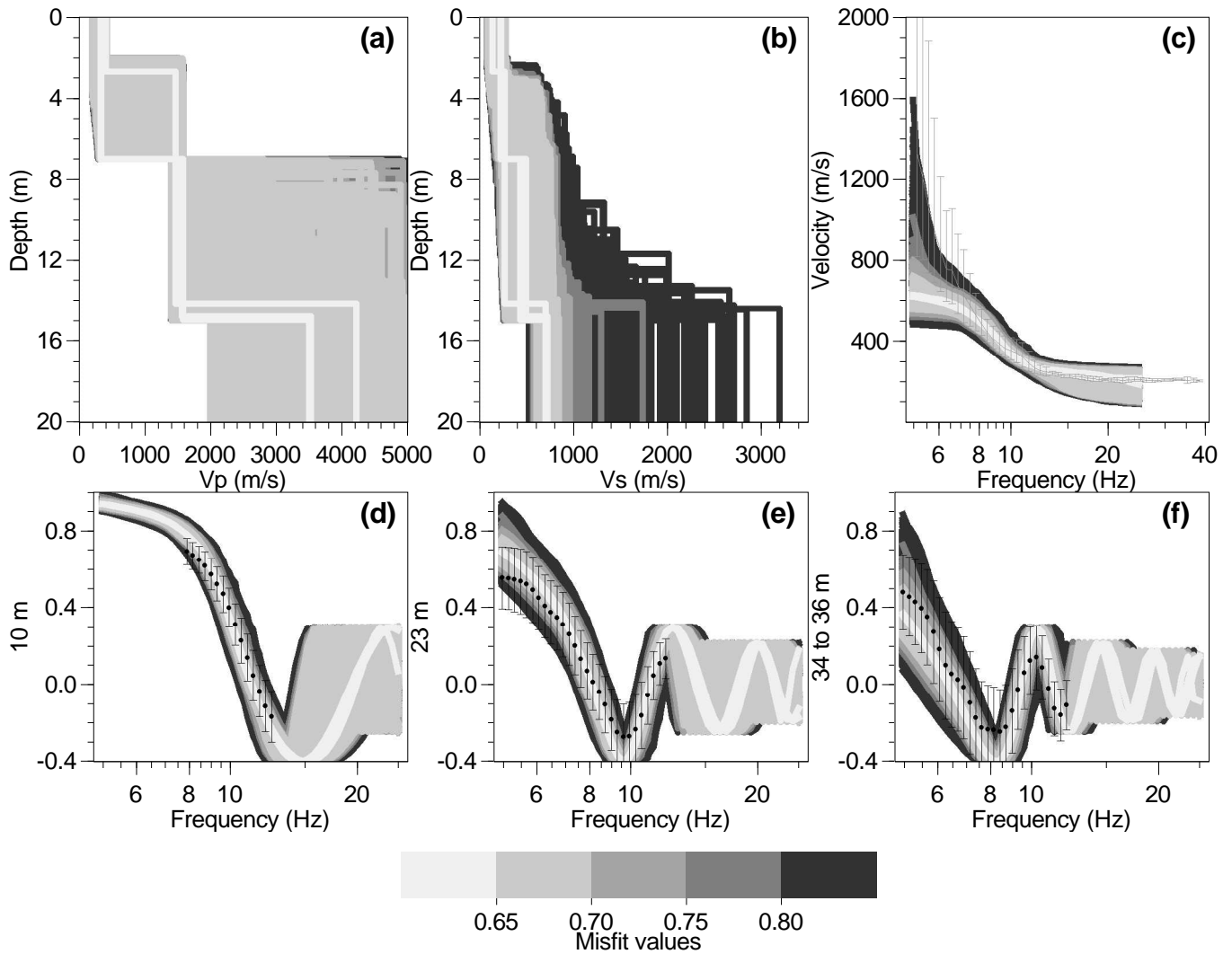


**Figure 6.38:** Inversion of the selected samples of 10 auto-correlation curves for array A. Only three of them are presented here. (a)  $V_p$ , (b)  $V_s$  of generated models and (c) corresponding dispersion curves. The dispersion curve observed for frequency wavenumber method is plotted for comparison in grey. (d) to (e) Auto-correlation curves for three rings with the observed ones (black dots and error bars).

difference has a strong influence over the inversion as shown by figure 6.38(b).

### 6.2.6 Conclusions

A shallow sedimentary structure (10 to 15 m) of alluvial sediments over a shaly bedrock is investigated with ambient vibration arrays to derive the shear-wave velocity profile. Four arrays with distinct geometries are deployed on the site. Three array processing methods are used to derive either the dispersion curve or the auto-correlation curves. These curves are then inverted with the neighbourhood algorithm, which is well-suited to problems affected by strong non-uniqueness. Additionally, information from boreholes, classical refraction and active surface wave experiments are analysed to check the validity of the array results.

Of the three processing techniques, only the f-k method provided coherent dispersion curves for the three arrays and proved to be the more robust. The results provided by the high resolution technique globally agree with the first method but exhibit unexpected sharp variations of the dispersion curve at some frequencies. Finally, the auto-correlation technique was only usable for one array and appeared to be very sensitive to uncorrelated noise.

The refraction results provide a  $V_p$  profile with its uncertainties. For the inversion of ambient vibrations,  $V_p$  profiles are uniformly chosen within this uncertainty interval. With only the vertical component, a good definition of  $V_s$  down to 8 or 10 m is achieved. Below, the experimental uncertainties are too great to obtain a correct estimation of the velocity. The introduction of the H/V peak frequency as a supplementary constraint improves the final results by reducing the posterior uncertainty about the depth of the basement.

This example clearly demonstrates that any single method and any single array aperture is not valid for a reliable determination of the  $V_s$  profile. On the contrary, we used all available methods to find out the robust features and to discard the contradictory results. The use of the horizontal components would probably improve the determination of the deeper structure.

# Conclusions

In the framework of array measurements of ambient vibrations, the objective of this thesis was to improve the inversion of dispersion curves in order to retrieve the  $V_s$  profile of a ground structure. The uncertainties in the determination of the dispersion curve generally lead to a problem highly affected by non-uniqueness. Direct search methods, like the neighbourhood algorithm considered in this work, offer at least two advantages over classical linearization approaches: the whole parameter space is investigated and prior information is easily introduced by restricting the search to particular regions of the parameter space. However, these methods require a great number of forward computations. Moreover, the calculation of theoretical dispersion curves is done numerically and classical codes need to be tuned on a case-by-base basis to give the right answer. Consequently, we developed a new optimized and reliable algorithm to calculate the theoretical dispersion curve of any one-dimensional model, including fundamental and higher modes of Rayleigh and Love waves. We also extended the capabilities of the tool to the inversion of the auto-correlation curves.

The Rayleigh dispersion curves observed on the vertical components are generally not available at low frequency due to the high-pass filter effect of the ground structure, which drastically reduces the penetration depth of the method. A variety of strategies were tested to overcome this limitation. The contribution of prior information about  $V_p$ , about the depth of the major contrasts, and about the frequency of the H/V peak were considered. No significant improvement was found with only one of these types of additional constraints, but their combined effects always help in a better definition of the  $V_s$  profile.

Configurations with a great number of layers, ten in our case, showed that the non-uniqueness of the problem dramatically increases when low velocity zones are allowed in the ground model. However, forbidding such model feature is not straightforward with the original neighbourhood code. Several strategies were developed which prove that this kind of prior information is of prime importance. The lack of flexibility with these approaches led us to revise the neighbourhood algorithm itself. It was re-written in C++ with the possibility of fixing prior conditions between parameters, like the one induced by Poisson's ratio or by the absence of negative velocity contrast. This alternative offers good perspectives, eventually for other purposes, but intensive testing is still necessary.

The horizontal components are usually high-pass filtered at a lower frequency than the vertical ones. If the dispersion curve of Love waves can be estimated, the joint inversion of high frequency Rayleigh and low frequency Love dispersion curves is a good alternative to

investigate the deep part of the ground model. This is an interesting property that opens perspectives towards a better prediction of the site amplification from array measurements.

The observed dispersion curves might follow the fundamental (usual assumption) or any of the higher modes. If the harmonic branches can be correctly identified, including all modes into the inversion slightly improves the final results. It also provides a good way of confirming the inversion results obtained with the fundamental mode. However, for our test case, the frequency range where the first higher mode is likely to be observed contains redundant information with the fundamental mode. On the contrary, we show that a misidentification of the observed modes introduces bias in the results. An experimental code is developed to search all possible solutions not requiring a preliminary and subjective identification of the modes. Assuming the number of potential modes, we show that only a few model classes really fit the data curve. Prior information is still necessary to select the appropriate family of models.

We tested the inversion tool for non-perfect dispersion curves estimated from microtremor recordings, either synthetic or real. Signal processing of array measurements includes the frequency-wavenumber, the high resolution frequency-wavenumber, and the auto-correlation methods. These methods provide a reliable dispersion curve over a limited wavenumber range which mainly depends upon the array geometry. Including biased part of the curves into the inversion might lead to incorrect results. Hence, strict rules for pre-processing input curves are developed. We tested the relevance of the limits deduced from the theoretical array response which is entirely calculated with the array geometry. A good agreement is found between them and the range of the correct determination of the dispersion curve.

Among the methods for processing the raw recordings of ambient vibrations, the auto-correlation method does not provide the dispersion curve in a direct way like the frequency-wavenumber methods. Classical approaches involve two inversion processes which are known to be highly non-linear. We developed a one step inversion with the neighbourhood algorithm. Besides the simplicity, the advantage of this method is that the auto-correlation data uncertainties are fully considered during the inversion. An original contribution of this work is also the definition of a methodology for assessing the valuable parts of the auto-correlation curves to invert.

The alluvial plain of Meuse river (Liège, Belgium) has been chosen for the deployment of the array method due to its one-dimensional structure (shallow alluvial deposits overlying a shaly bed-rock) and due to the available geotechnical data. Information from boreholes, classical refraction, active surface wave experiments, and from the H/V peak frequency were analysed to check the validity of the array results. Only the frequency-wavenumber method provided consistent dispersion curves for all arrays and proved to be the most robust. The results of the high resolution technique globally agreed with the first method but exhibit unexpected sharp variations of the dispersion curve at some frequencies. Finally, the auto-correlation technique was only usable for one array. These last two methods appeared to be very sensitive to uncorrelated noise. A reliable  $V_s$  profile was obtained down to 10 m. The depth of the main velocity contrast is estimated with a relatively good precision (the depths found vary from 9 to

14 m) but no information can be retrieved below. This reinforces the interest of investigating the three-components techniques to retrieve the Love dispersion curve.

— — —

During this thesis, we developed a collection of interpretation techniques devoted to ambient vibration measurements. Prior information is necessary to overcome the non-uniqueness of the dispersion curve inversion. We provided the tool for integrating them in a rational way.

Several promising improvements have still to be studied and tested. The extraction of Love dispersion curve from ambient vibrations is not as direct as the determination of Rayleigh dispersion curve from the vertical component. Signal processing methods have to be tested on synthetic and real experiments to assess the real potentialities. The spatial auto-correlation method applied on the three components of the recordings also offers a solution to characterize the relative portions of Love and Rayleigh waves in microtremors, which is a necessary step for understanding the noise wavefield structure.

The conditional neighbourhood algorithm developed in this thesis takes into account the physical conditions between parameters, which is necessary to avoid the low velocity zones during inversion. This work proved that this kind of prior information is of prime importance. However, this code still needs intensive testing.

The use of a resampling of the ensemble of models (Sambridge 1999b) may provide objective statistics that are not possible with the current misfit based approach.

The joint inversion with refraction measurements and a better recognition of the higher modes by means of external information are also topics to study in order to improve the velocity accuracy.

All the preceding discussion focalized on one-dimensional models. Extension to three-dimensional cases might be considered in the future with the current development of finite difference codes to simulate the ambient vibrations. If the direct inversion is still not considered with these codes, currently available three-dimensional synthetic wavefields will give the opportunity of a better understanding of the noise properties in such cases.



# Appendix A

## Sub-determinants of $R^{(i)}$

The solution of the equation of motion for Rayleigh modes implies the computation of sub-determinants of matrix  $R(z_0)$  (section 3.1.4, equation (3.34)). In this appendix, we present the complete analytical expressions of these terms. For doing so, we define the following adimensional real quantities:

$$h_n = \hat{h}_n/k \quad (\text{A.1})$$

$$k_n = \hat{k}_n/k \quad (\text{A.2})$$

$$\left. \begin{aligned} SH &= 0.5 \frac{1 - e^{-2d_n \hat{h}_n}}{h_n} \\ CH &= 0.5(1 + e^{-2d_n \hat{h}_n}) \end{aligned} \right\} \text{if } h_n \text{ is real.} \quad (\text{A.3})$$

$$\left. \begin{aligned} SH &= \frac{\sin(-id_n \hat{h}_n)}{h_n} \\ CH &= \cos(-id_n \hat{h}_n) \end{aligned} \right\} \text{if } h_n \text{ is imaginary.} \quad (\text{A.4})$$

$$\left. \begin{aligned} SK &= 0.5 \frac{1 - e^{-2d_n \hat{k}_n}}{k_n} \\ CK &= 0.5(1 + e^{-2d_n \hat{k}_n}) \end{aligned} \right\} \text{if } k_n \text{ is real.} \quad (\text{A.5})$$

$$\left. \begin{aligned} SK &= \frac{\sin(-id_n \hat{k}_n)}{k_n} \\ CK &= \cos(-id_n \hat{k}_n) \end{aligned} \right\} \text{if } k_n \text{ is imaginary.} \quad (\text{A.6})$$

where  $d_n = z_n - z_{n-1}$  is the thickness of layer  $n$ .

$$\gamma_n = 2k^2 / (\omega / V_{pn})^2 \quad (\text{A.7})$$

$$\begin{aligned} a_1 &= \gamma_n^2 - 2\gamma_n + 1 \\ a_2 &= h_n^2 k_n^2 \\ a_3 &= \gamma_n^2 + a_1 \\ a_4 &= 1 - \gamma_n \\ a_5 &= \gamma_n^2 a_2 \end{aligned} \quad (\text{A.8})$$

$$\text{expCorr} = e^{-\hat{h}_n d_n - \hat{k}_n d_n} \quad (\text{A.9})$$

And we also define the following two dimensional quantities:

$$\begin{aligned} c_1 &= \rho_n \omega^2 / k \\ c_2 &= 1/c_1 \end{aligned} \tag{A.10}$$

The sub-determinants of  $G_n$  are detailed here below ( $G_{ijkl} = g_n \begin{vmatrix} i & j \\ k & l \end{vmatrix}$ ,  $G$  is real,  $i$  before  $G$  means that this component is imaginary) :

$$\begin{aligned} G_{1212} &= a_3 CHCK - (a_1 + a_5) SHSK - (a_3 - 1) expCorr \\ G_{1213} &= c_2 (CHSK - h_n^2 SHCK) \\ iG_{1214} &= ic_2 ((a_1 - \gamma_n^2) (expCorr - CHCK) + (a_4 - \gamma_n a_2) SHSK) \\ iG_{1223} &= iG_{1414} \\ G_{1224} &= c_2 (k_n^2 CHSK - SHCK) \\ G_{1234} &= c_2^2 (2CHCK + (1 + a_2) SHSK) \\ G_{1312} &= c_1 (\gamma_n^2 k_n^2 CHSK - a_1 SHCK) \\ G_{1313} &= CHCK \\ iG_{1314} &= i(a_4 SHCK + \gamma_n k_n^2 CHSK) \\ iG_{1323} &= iG_{1314} \\ G_{1324} &= k_n^2 SHSK \\ G_{1334} &= G_{1224} \\ iG_{1412} &= ic_1 ((a_1 - a_4)(a_4 - \gamma_n) (expCorr - CHCK) + (a_4 a_1 - \gamma_n a_5) SHSK) \\ iG_{1413} &= i(\gamma_n h_n^2 SHCH + a_4 CHSK) \\ G_{1414} &= expCorr + G_{1423} \\ G_{1423} &= CHCK - G_{1212} \\ iG_{1424} &= iG_{1314} \\ iG_{1434} &= iG_{1214} \\ iG_{2312} &= iG_{1412} \\ iG_{2313} &= iG_{1413} \\ G_{2314} &= G_{1423} \\ G_{2323} &= G_{1414} \\ iG_{2324} &= iG_{1314} \\ iG_{2334} &= iG_{1214} \\ G_{2412} &= c_1 (a_1 CHSK - \gamma_n^2 h_n^2 SHCK) \\ G_{2413} &= h_n^2 SHSK \\ iG_{2414} &= iG_{1314} \end{aligned} \tag{A.11}$$

$$\begin{aligned}
iG_{2423} &= iG_{1413} \\
G_{2424} &= G_{1313} \\
G_{2434} &= G_{1213} \\
G_{3412} &= c_1^2(2\gamma_n^2 a_1 CHCK + (a_1^2 + \gamma_n^2 a_5) SHSK) \\
G_{3413} &= G_{2412} \\
iG_{3414} &= iG_{1412} \\
iG_{3423} &= iG_{1412} \\
G_{3424} &= G_{1312} \\
G_{3434} &= G_{1212}
\end{aligned}$$

$T_{ijkl} = t_n^{-1} \begin{vmatrix} i & j \\ k & l \end{vmatrix}$  and from equation (3.31),  $T_{1214}$  and  $T_{1223}$  are equal and imaginary. Using equation (3.34) and definition of  $G$  (equations (A.11)), it follows:

$$\begin{aligned}
R_{1212}(z_{n-1}) &= T_{1212}G_{1212} + (T_{1213}G_{1312} - 2T_{1214}iG_{1412} + T_{1224}G_{2412} - T_{1234}G_{3412})/\omega^2 & (A.12) \\
R_{1213}(z_{n-1}) &= \omega^2 T_{1212}G_{1213} + T_{1213}CHCK - 2T_{1214}iG_{1413} - T_{1224}G_{2413} + T_{1234}G_{2412} \\
R_{1214}(z_{n-1}) &= \omega^2 T_{1212}iG_{1214} + T_{1213}iG_{1314} + T_{1214}(2G_{1423} + expCorr) - T_{1224}iG_{1413} + T_{1234}iG_{1412} \\
R_{1223}(z_{n-1}) &= \omega^2 T_{1212}iG_{1214} + T_{1213}iG_{1314} + T_{1214}(2G_{1423} + expCorr) - T_{1224}iG_{1413} + T_{1234}iG_{1412} \\
R_{1224}(z_{n-1}) &= \omega^2 T_{1212}G_{1224} + T_{1213}G_{1324} - 2T_{1214}iG_{1314} + T_{1224}CHCK + T_{1234}G_{1312} \\
R_{1234}(z_{n-1}) &= -\omega^2 T_{1212}G_{1234} + T_{1213}G_{1224} - 2T_{1214}iG_{1214} + T_{1224}G_{1213} + T_{1234}G_{1212}
\end{aligned}$$



# Appendix B

## Generating increasing velocity profiles

As reported in section 4.3.1, ensuring an increasing velocity across a ground structure is necessary to retrieve information from the inversion of dispersion curves. Methods of parameterizations to achieve this requirement are proposed in this appendix. The parameterization may introduce prior information into the inversion by preferring some classes of models to others. The best method is the one that provides an equal chance to all models to be generated at random.

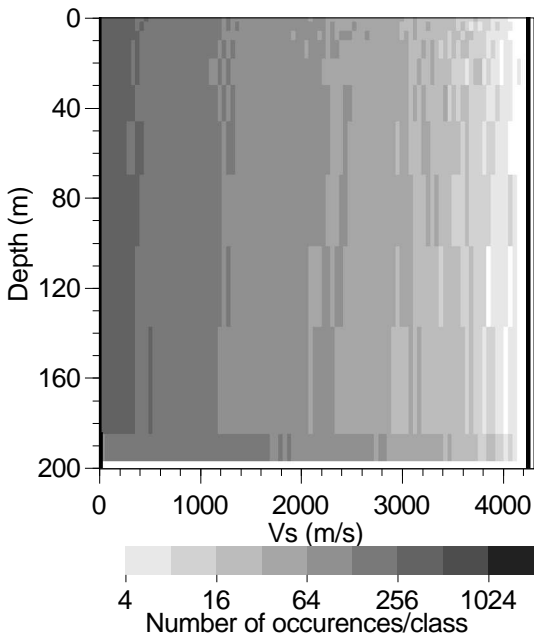


**Figure B.1:** Prior information carried by parameterization: LVZ ( $V_s$  profile). The black lines are the minimum and maximum velocity profiles admissible.

The various methods are tested in terms of prior information brought by the parameterization itself. For doing so, 10000 models are randomly generated with each type of parameterization. At each depth, an histogram is constructed counting the number of occurrences in each velocity class (100 classes from 0 to the maximum velocity allowed by the parameterization). All histograms are summarized in a velocity-depth plot with the number of occurrence indicated by grey scales. A first example is shown in figure B.1 for the  $V_s$  profile of the inversion of section 4.3.1. The distribution at each depth is not perfectly uniform which is prone to introduce some uncontrolled prior information if  $V_s$  is not well constrained by the dispersion curve. On the contrary, for the same case, the  $V_p$  profile has a perfect uniform distribution (not shown here). This fact is unavoidable when making a variable transformation to obtain the physical parameters of the ground model (section 4.2).

## B.1 Selection method

Among the random models generated as in section 4.3.1, the parameterization algorithm selects only the one fulfilling the physical condition and having an increasing profile. With a great number of layers, this method needs quite a lot of time as the probability of having no LVZ is very small. Practically, it does not work. Like the parameterization in figure B.1, the prior information provided by the parameterization is optimum (uniform distribution).

## B.2 Sorting method

A possibility to obtain an increasing velocity profile would be to generate  $N$  random velocities and to sort them. This method presents the major drawback that each random deviate is not linked to the velocity at a particular depth. The parameter space may be very complex. Moreover, there are little chances to generate a model with a deep and sharp contrast, because it requires that nearly all random values are small.

## B.3 Velocity-jump method

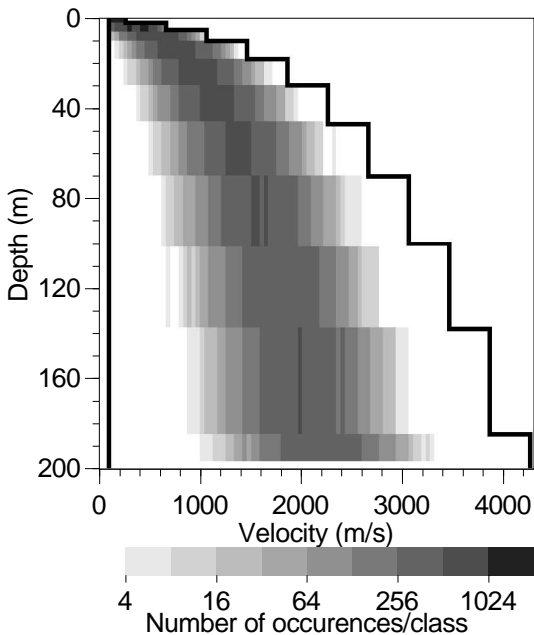


**Figure B.2:** Prior information carried by parameterization: velocity jump. The black lines are the minimum and maximum velocity profiles admissible.

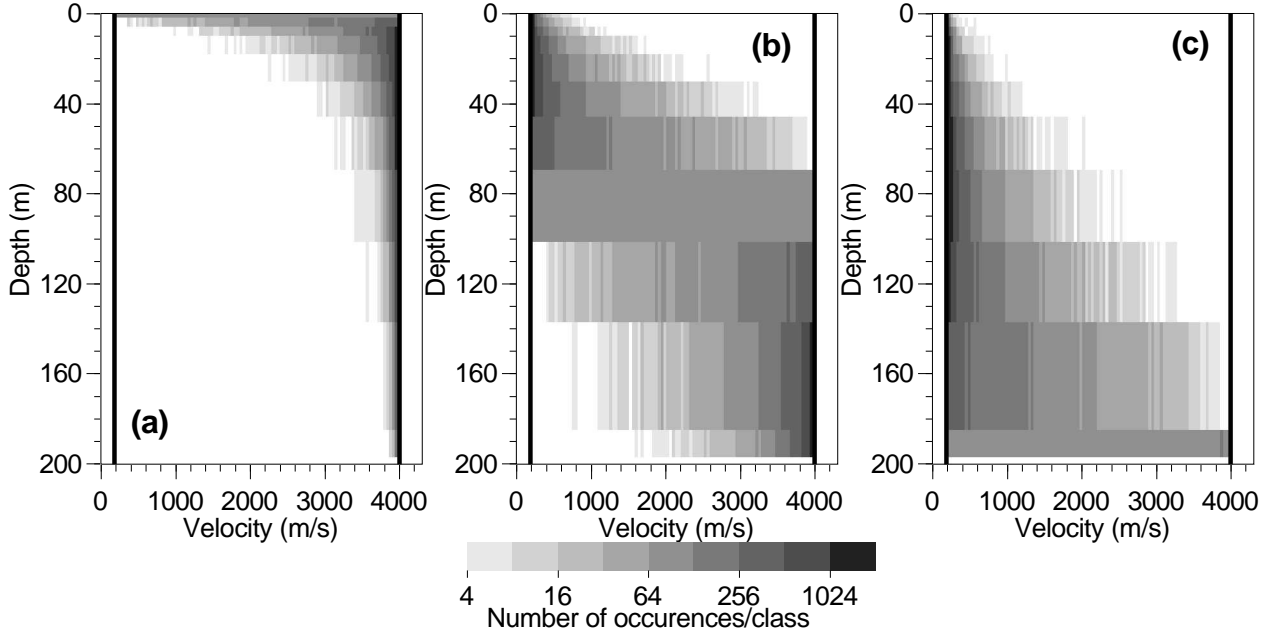
The velocity of the first layer is the first parameter. The other parameters are the velocity jumps from one layer to the next one. This is the basic approach that has been implemented when the number of layers is small (section 4.2). The velocity for any layer  $i$  is defined by  $V_0 + \sum_{j=1}^i dV_j$  where  $V_0$  is the random velocity of the first layer and  $dV_j$  the velocity jump at each interface.  $V_0$  and  $dV_j$  are random variables with a uniform distribution in the best case. Then  $V_i$  is the sum of uniform random variables and its distribution tends to a Gaussian distribution when the number of layers increases (central limit theorem).

Figure B.2 shows the histograms for a parameterization where the velocity varies between 100 and 265 m/s ( $\approx \frac{\sqrt{2}}{2}V_{p0}$ ) at the surface and where all  $dV_j$  are randomly chosen between 0 and 400 m/s. This kind of parameterization may be acceptable for  $V_p$  because there are usually no special conditions on  $V_p$  values. On the contrary,  $V_s$  values are linked to  $V_p$

values ( $0 \leq \nu \leq 0.5$ ) and this condition is impossible to impose with this method. As shown by figure B.2, this kind of parameterization naturally orientates the inversion towards a regular increase of the velocity with depth.

## B.4 Interpolation method

In the preceding method, it is impossible to allow strong velocity contrast (the maximum in the example is 400 m/s) and to limit the maximum velocity ( $> 4000$  m/s in the example) of the model. To improve the method, a minimum ( $V_{min}$ ) and a maximum ( $V_{max}$ ) velocity are first defined. The velocity of any layer ( $V_i$ ) is defined as the first parameter ( $V_{min} < V_i < V_{max}$ ). The velocities of the other layers are successively calculated to the top and to the bottom by



**Figure B.3:** Prior information carried by parameterization: interpolation. The black lines are the minimum and maximum velocity profiles admissible. Starting layer is the (a) first one, (b) the 7<sup>th</sup>, and (c) the last one.

$V_{i-1} = V_{min} + p(V_i - V_{min})$  and  $V_{i+1} = V_i + p(V_{max} - V_i)$ , respectively ( $p$  is a random parameter between 0 and 1).

Figure B.3 shows the histograms for the several starting layers with  $V_{min} = 200$  m/s and  $V_{max} = 4000$  m/s. The starting layer has a strong influence on the prior information provided by the parameterization. To give all models an equal chance of being a solution, various inversions with complementary starting layers must be run.

## B.5 Interpolation method with random start

This method tries to improve the parameter space exploration by changing the index of the first layer. A random integer, between 0 and  $n - 1$  (if  $n$  is the number of layers), specifies the index of the starting calculation. The computation of the velocity profile is done in the same way. A new degree of freedom must be added and the parameter space has a more complex shape. In the preceding method, there is a one-to-one relationship between the velocity profile and the set of generated random deviates. With this new parameter, one velocity profile corresponds to an infinity of possible sets of random deviates. In figure B.4, this method clearly provides a more uniform prior distribution than the preceding approaches but at the cost of a supplementary

parameter.

## B.6 Bisection method

Without adding a new parameter, the bisection method may bring a better prior distribution than the basic interpolation method. The velocities are defined by a minimum value (first parameter,  $V$ ). The other parameters are between 0 and 1. A total velocity variation is calculated from the second parameter  $p_1$ ,  $\delta V = p_1 * (V_{max} - V)$ . The velocity of the first layer and last layer are set to  $V$  and  $V + \delta V$ , respectively. The calculation of velocities starts from the layer at the middle of the stack,  $V_i = V + p_i \delta V$ . The stack is then cut in two sub-stacks limited by velocities  $V$ ,  $V_i$  and  $V_i$ ,  $V + \delta V$ . The calculation is the same in each sub-stack until every layer has been affected a velocity. The resulting prior distribution is shown in figure B.5. Comparing it with figures B.2 and B.3, a more uniform distribution is achieved without adding a new parameter. Contrary to the preceding method, each basic random parameter is directly linked to the velocity at a fixed depth, which tends to simplify the parameter space. Profiles with a low velocity at depth are rarely generated. If the velocity of the last and first layer are set to  $V$ , and  $V - \delta V$ , respectively, a symmetric image is obtained.

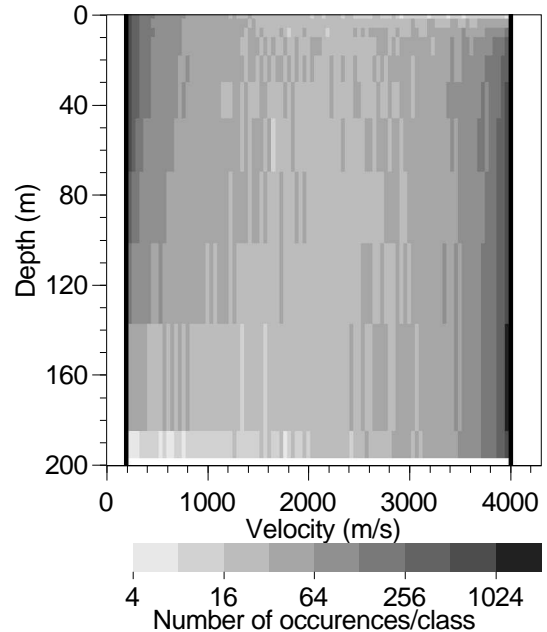


**Figure B.4:** Prior information carried by parameterization: random interpolation. The black lines are the minimum and maximum velocity profiles admissible.

## B.7 Diagonal method

The spirit of this method is to give the same chance to models with a regular velocity increase and to models with sharp contrasts. The velocities are defined by a minimum value (first parameter,  $V$ ). The other parameters are between 0 and 1. A total velocity variation is calculated from the second parameter  $p_1$ ,  $\delta V = p_1 * (V_{max} - V)$  where  $V_{max}$  is the fixed maximum velocity (4000 m/s in this case). The third parameter is the intersection of the profile with the ascending diagonal of the rectangle defined by the  $V$  and  $V + \delta V$  of the top and the bottom layer, respectively. 0 means minimum velocity to be affected to the deepest layer. 1 means maximum velocity to be affected to the highest layer. The already defined layer separates the stack into two sub-stacks that can be processed in the same way. The prior distribution for this method is given in figure B.6. The results are quite similar to the results of the preceding method, except for profiles with low velocity at depth where this method appears to be slightly more efficient. A symmetric distribution can also be generated by inverting the velocity of the

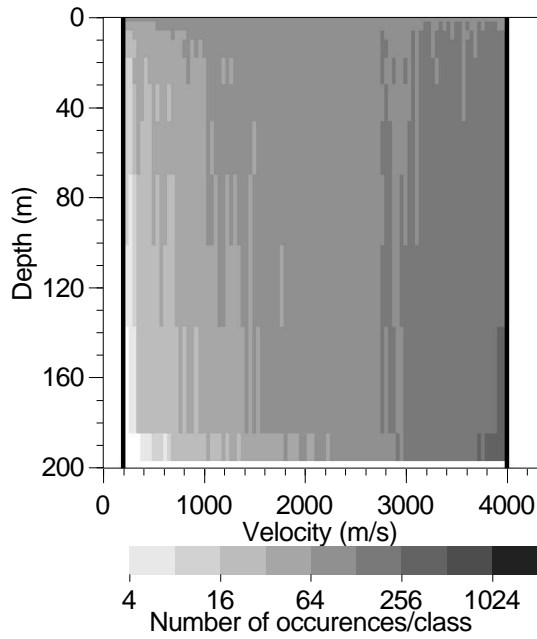


**Figure B.5:** Prior information carried by parameterization: bisection. The black lines are the minimum and maximum velocity profiles admissible.

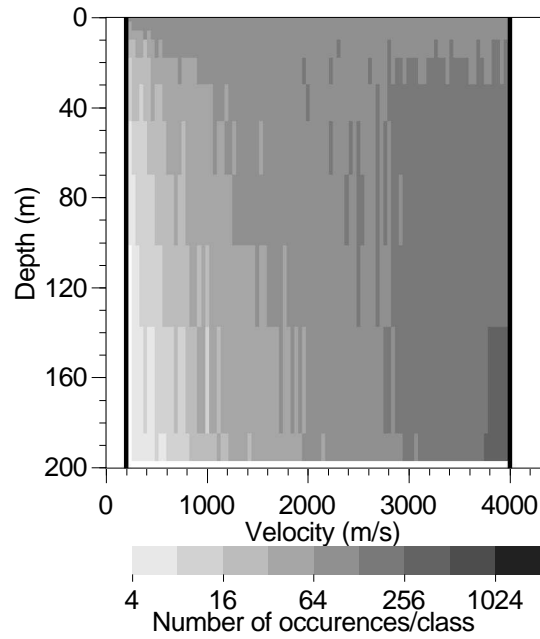


**Figure B.6:** Prior information carried by parameterization: diagonal. The black lines are the minimum and maximum velocity profiles admissible.

first and last layer like in the above method.

## B.8 Including Poisson's ratio

None of the described methods offers a really uniform prior distribution like the one obtained for the arbitrary profiles (section 4.3.1 and figure B.1). And the physical limits, like the limits on the Poisson's ratio, are not handled. However, with a fixed  $V_p$  profile (not random), it is possible to generate pseudo  $V_s$  profiles between 0 and 1 m/s with one of the available methods. In a second step,  $V_s$  in each layer is scaled to  $[V_{min}, V_{i,max}]$ , the maximum values being calculated from the increasing and fixed  $V_p$  profile. The minimum value must be the same for all layers to avoid any LVZ when scaling the pseudo profile. The effect of the scaling transformation applied to the diagonal method (section B.7) is shown in figure B.7 for a fixed  $V_p$  profile equal to the one of the theoretical model (figure 4.1(a)). By comparison the scaling transformation is also applied to the interpolate method, starting from last layer (section B.4). If  $V_p$  is also variable, the  $V_s$  prior density of probability is less uniform than in figure B.7. With the interpolate method, the maximum  $V_s$  profile represented by the black line has almost no chance to be generated by the inversion algorithm. The diagonal offers a more uniform prior distribution with an similar probability for all model.

## B.9 Conclusions

For the parameterization described in section 4.2, the model can be constructed from the parameters in a direct way. For the methods proposed in this appendix, integrating the relationships

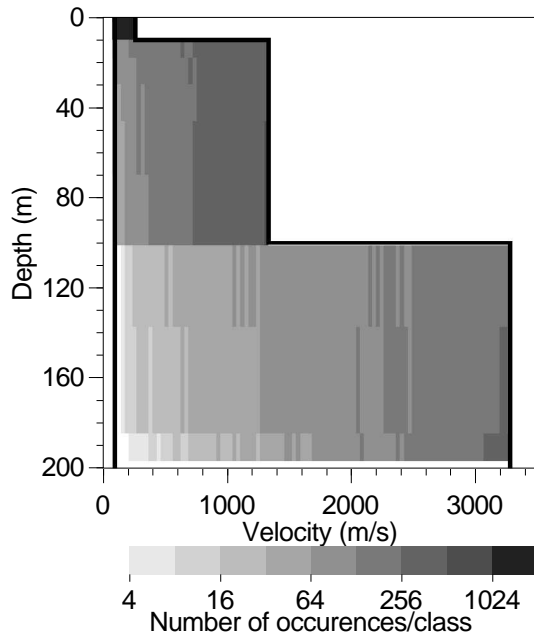


**Figure B.7:** Prior information carried by parameterization: scaled diagonal. The black lines are the minimum and maximum velocity profiles admissible.

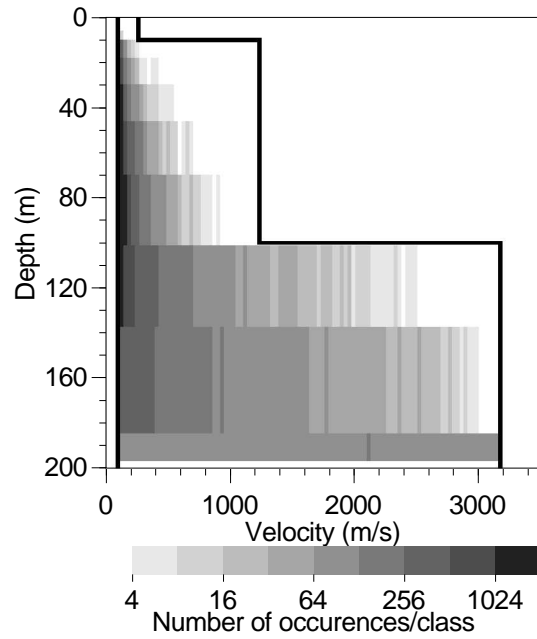


**Figure B.8:** Prior information carried by parameterization: scaled interpolate. The black lines are the minimum and maximum velocity profiles admissible.

between layers into a generic structure would require the definition at the user level of blocks and sub-blocks of layers where  $V_p$  and  $V_s$  are managed for the whole block and not for each particular layer. The description of such models would be less flexible than the basic description layer by layer detailed in section 4.2. The examples of this section have been calculated by hard coding<sup>1</sup> the layer structure for each case. No generic construction tool has been developed until now. Actually, the new conditional neighbourhood algorithm offers the possibility to set whatever condition between any parameters in a very flexible way. This why no special effort has been put on developing ready to use codes for the methods detailed in this section.

<sup>1</sup>parameter values explicitly written in the code, compilation is necessary to change it

# References

- Aki, K. (1957). Space and time spectra of stationary stochastic waves, with special reference to microtremors, *Bull. Earthq. Res. Inst.* **35**, 415–456.
- Aki, K and P. G. Richards (2002). Quantitative seismology, Second Edition, University Science Books.
- Asten, M. W. and J. D. Henstridge (1984). Array estimators and use of microseisms for reconnaissance of sedimentary basins, *Geophysics* **49**, 1828–1837.
- Asten, M. W., T. DHU and N. Lam (2004). Optimized array design for microtremor array studies applied to site classification; comparison of results with SCPT logs, In *Proc. of 13th World Conf. on Earthquake Engineering, Vancouver*.
- Bachrach, R., J. Dvorkin and M. A Nur (2000). Seismic velocities and Poisson’s ratio of shallow unconsolidated sands, *Geophysics* **65**, 559–564.
- Bailey, D. H. (2004). High-Precision Floating-Point Arithmetic in Scientific Computation, <http://crd.lbl.gov/~dhbailey/dhbpapers/index.html>.
- Bard, P.-Y. (1994). Effects of surface geology on ground motion: recent results and remaining issues, In *Proc. of the 10th European Conf. on Earthquake Engineering, Vienna*, 305–323.
- Bard, P.-Y. (1998). Microtremor measurements: A tool for site effect estimation?, In *Proc. 2nd Intl. Symp. on The Effects of Surface Geology on Seismic Motion*, Irikura, Kudo, Okada & Sasatani (eds), Balkema, 1251–1279.
- Beatty, K. S., D. R. Schmitt and M. Sacchi (2002). Simulated annealing inversion of multimode Rayleigh wave dispersion curves for geological structure, *Geophys. J. Int.* **151**, 622–631.
- Bettig, B., P.-Y. Bard, F. Scherbaum, J. Riepl, F. Cotton, C. Cornou and D. Hatzfeld (2001). Analysis of dense array noise measurements using the modified spatial auto-correlation method (SPAC). Application to the Grenoble area., *Bolletino di Geofisica Teorica ed Applicata* **42**, 281–304.
- Bonnefoy-Claudet, S., C. Cornou, J. Kristek, M. Ohrnberger, M. Wathelet, P.-Y. Bard, P. Moczo, D. Fäh and F. Cotton (2004). Simulation of seismic ambient noise: I. Results of H/V and array techniques on canonical models, In *Proc. of 13th World Conf. on Earthquake Engineering, Vancouver*.

- Bonnefoy, S. (2004). Nature du bruit de fond sismique: implication pour les études des effets de site, Phd thesis Université Joseph Fourier (LGIT), Grenoble, France.
- Boore, D. M. and M. N. Toksöz (1969). Rayleigh Wave Particle Motion and Crustal Structure, *Bull. Seism. Soc. Am.* **59**, 331–346.
- Boschetti, F., M. C. Dentith and R. D. List (1996). Inversion of seismic refraction data using genetic algorithms, *Geophysics* **61**, 1715–1727.
- Boschetti, F. and L. Moresi (2001). Interactive inversion in geosciences, *Geophysics* **66**, 1226–1234.
- Calderón-Macías, C., M. Sen and P. Stoffa (2000). Artificial neural networks for parameter estimation in geophysics, *Geophysical Prospecting* **48**, 21–48.
- Capon, J. (1969). High-resolution frequency-wavenumber spectrum analysis, *Proc. IEEE* **57**, 1408–1418.
- Chouet, B., G. De Luca, G. Milana, P. Dawson, M. Martini and R. Scarpa (1997). Source and path effects in the wave fields of tremor and explosions at Stromboli Volcano, Italy, *Journal of Geophys. Res.* **102**, 15129–15150.
- Chouet, B., G. De Luca, G. Milana, P. Dawson, M. Martini and R. Scarpa (1998). Shallow velocity structure of Stromboli Volcano, Italy, derived from small-aperture array measurements of strombolian tremor, *Bull. Seism. Soc. Am.* **88**, 653–666.
- Chunduru, R. K., M. K. Sen and P. L. Stoffa (1996). 2-D resistivity inversion using spline parameterization and simulated annealing, *Geophysics* **61**, 151–161.
- Cornou, C., P.-Y. Bard and M. Dietrich (2003). Contribution of Dense Array Analysis to the Identification and Quantification of Basin-Edge-Induced Waves, Part I: Methodology, *Bull. Seism. Soc. Am.* **93**, 2604–2623.
- Devilee, R. J. R. (1999). An efficient, probabilistic neural network approach to solving inverse problems: Inverting surface wave velocities for Eurasian crustal thickness, *Journal of Geophys. Res.* **104**, 28841–28857.
- Dunkin, J. W. (1965). Computation of modal solutions in layered, elastic media at high frequencies, *Bull. Seism. Soc. Am.* **55**, 335–358.
- Edwards, A. W. F. (1992). Likelihood, expanded edition, John Hopkins.
- Fagnoul, A. (1975). Carte géotechnique 42.6.1 Liège, Centre de Cartographie Géotechnique de l'Université de Liège.
- Fäh, D., F. Kind and D. Giardini (2001). A theoretical investigation of average H/V ratios, *Geophys. J. Int.* **145**, 535–549.

- Fäh, D., F. Kind and D. Giardini (2003). Inversion of local S-wave velocity structures from average H/V ratios, and their use for the estimation of site-effects, *Journal of Seismology* **7**, 449–467.
- Forbriger, T. (2003a). Inversion of shallow-seismic wavefields. Part 1: Wavefield transformation, *Geophys. J. Int.* **153**, 719–734.
- Forbriger, T. (2003b). Inversion of shallow-seismic wavefields. Part 2: Inferring subsurface properties from wavefield transforms, *Geophys. J. Int.* **153**, 735–752.
- Foti, S. (2000). Multistation Methods for Geotechnical Characterization using Surface Waves, Phd thesis Politecnico di Torino, Italy.
- Foti, S., L. Sambuelli, L. V. Socco and C Strobbia (2003). Experiments of joint acquisition of seismic refraction and surface wave data, *Near Surface Geophysics* **1**, 119–129.
- Friego, M. and S. G. Steven (2005). The Design and Implementation of FFTW3, *Proceedings of the IEEE* **93**, 216–231.
- Gabriels, P., R. Snieder and G. Nolet (1987). In situ measurements of shear-wave velocity in sediments with higher-mode Rayleigh waves, *Geophysical Prospecting* **35**, 187–196.
- Gaffet, S. (1998). A dense array experiment for the observation of waveform perturbations, *Soil Dynamics and Earthquake Engineering* **17**, 475–484.
- Gilbert, F. and G. Backus (1966). Propagator matrices in elastic wave and vibration problems, *Geophysics* **31**, 326–332.
- Goldstein, P. and R. J. Archuleta (1987). Array analysis of seismic signals, *Geophysical Research Letter* **14**, 13–16.
- Haskell, N. A. (1953). The dispersion of surface waves on multilayered media, *Bull. Seism. Soc. Am.* **43**, 17–34.
- Herrmann, R. B. (1994). Computer programs in seismology, vol IV, St Louis University.
- Hisada, Y. (1994). An efficient method for computing Green's functions for a layered half-space with sources and receivers at close depths, *Bull. Seism. Soc. Am.* **84**, 1456–1472.
- Horike, M. (1985). Inversion of phase velocity of long-period microtremors to the S-wave-velocity structure down to the basement in urbanized areas, *Journal of Physics of the Earth* **33**, 59–96.
- Jongmans, D. and M. Campillo (1990). The 1983 Liège earthquake: damage distribution and site effects, *Earthquake Spectra* **6**, 713–737.
- Jongmans, D. (1992). The application of seismic methods for dynamic characterization of soils in earthquake engineering, *Bull. of the Int. Ass. of Engineering Geology* **46**, 63–69.

- Jongmans, D. and D. Demanet (1993). The importance of surface waves in vibration study and the use of Rayleigh waves for determining the dynamic characteristics of soils, *Engineering Geology* **34**, 105–113.
- Kind, F. (2002). Development of Microzonation Methods: Application to Basle, Switzerland, Phd thesis Swiss Federal Institute of Technology, Zürich.
- Knopoff, L. (1964). A matrix method for elastic wave problems, *Bull. Seism. Soc. Am.* **54**, 431–438.
- Kvaerna, T. and F. Ringdahl (1986). Stability of various fk-estimation techniques, in Semianual Technical Summary, 1 October 1985 - 31 March 1986, In *NORSAR Scientific Report, 1-86/87, Kjeller, Norway*, 29–40.
- Lacoss, R. T., E. J. Kelly and M. N. Toksöz (1969). Estimation of seismic noise structure using arrays, *Geophysics* **34**, 21–38.
- Lomax, A. J. and R. Snieder (1995). The contrast in upper mantle shear-wave velocity between the East European Platform and tectonic Europe obtained with genetic algorithm inversion of Rayleigh-wave group dispersion, *Geophysical Journal International* **123**, 169–182.
- Malagnini, L., R. B. Herrmann, G. Biella and R. de Franco (1995). Rayleigh waves in Quaternary alluvium from explosive sources: determination of shear-wave velocity and Q structure, *Bull. Seism. Soc. Am.* **85**, 900–922.
- Malischewsky, P. G. and F. Scherbaum (2004). Love's formula and H/V-ratio (ellipticity) of Rayleigh waves, *Wave Motion* **40**, 57–67.
- McMechan, G. A. and M. J. Yedlin (1981). Analysis of dispersive waves by wave field transformation, *Geophysics* **6**, 869–874.
- Metaxian, J.-P. (1994). Etude sismologique et gravimétrique d'un volcan actif: Dynamisme interne et structure de la Caldeira Masaya, Nicaragua, Phd thesis Université de Savoie, France.
- Michaels, P. and R. B. Smith (1997). Surface Wave Inversion by Neural Networks (Radial Basis Functions) for Engineering Applications, *The Journal of Environmental and Engineering Geophysics* **2**, 65–76.
- Milana, G., S. Barba, E. Del Pezzo and Zambonelli E (1996). Site response from ambient noise measurements: new perspectives from an array study in Central Italy, *Bull. Seism. Soc. Am.* **86**, 320–328.
- Mosegaard, K. and A. Tarantola (1995). Monte Carlo Sampling of Solutions to Inverse Problems, *Journal of Geophys. Res.* **10**, 12431–12447.

- Mota, L. (1954). Determination of dips and depths of geological layers by the seismic refraction method, *Geophysics* **19**, 242–254.
- Murphy, J. R. and H. K. Shah (1988). An analysis of the effects of site geology on the characteristics of near-field Rayleigh waves, *Bull. Seism. Soc. Am.* **78**, 64–82.
- Nakamura, Y. (1989). A method for dynamic characteristics estimation of subsurface using microtremors on the ground surface, *Quarterly Report of the Railway Technical Research Institute* **30**, 25–33.
- Nguyen, F., G. Van Rompaey, H. Teerlynck, M. Van Camp, D. Jongmans and T. Camelbeeck (2004). Use of microtremor measurement for assessing site effects in Northern Belgium – interpretation of the observed intensity during the  $M_S=5.0$  June 11 1938 earthquake, *Journal of Seismology* **8**, 41–56.
- Nogoshi, M. and T. Igarashi (1970). On the propagation characteristics of microtremors, *Journal of the Seismological Society of Japan* **23**, 264–280.
- Nolet, G. (1981). Linearized inversion of (teleseismic) data, In *The solution of the inverse problem in geophysical interpretation*, R. Cassinis (ed.), Plenum Press, 9–37.
- Ohrnberger, M. (2001). Continuous automatic classification of seismic signals of volcanic origin at Mt Merapi, Java, Indonesia, Phd thesis University of Potsdam, Germany.
- Ohrnberger, M., E. Schissele, C. Cornou, M. Wathelet, A. Savvaidis, F. Scherbaum, D. Jongmans and F. Kind (2004a). Microtremor array measurements for site effect investigations: comparison of analysis methods for field data crosschecked by simulated wavefields, In *Proc. of 13th World Conf. on Earthquake Engineering, Vancouver*.
- Ohrnberger, M. (2004b). User manual for software package CAP - a continuous array processing toolkit for ambient vibration array analysis. SESAME report D18.06, <http://sesame-fp5.obs.ujf-grenoble.fr>.
- Press, W. H., S. A. Teukolsky, W. T. Vetterling and B. P. Flannery (1992). Numerical Recipes in Fortran, second edition, Cambridge University Press.
- Reynolds, J. M. (1997). An Introduction to Applied and Environmental Geophysics, John Wiley and Sons Ltd, Chichester.
- Roberts, J. C. and M. W. Asten (2004). Resolving a velocity inversion at the geotechnical scale using the microtremor (passive seismic) survey method, *Exploration Geophysics* **35**, 14–18.
- Rothman, D. H. (1985). Nonlinear inversion, statistical mechanics, and residual statics estimation, *Geophysics* **50**, 2784–2796.

- Saccorotti, G., B. Chouet and P. Dawson (2003). Shallow-velocity models at the Kilauea Volcano, Hawaii, determined from array analyses of tremor wavefields, *Geophys. J. Int.* **152**, 633–648.
- Sambridge, M. (1999a). Geophysical inversion with a neighbourhood algorithm: I. Searching a parameter space, *Geophys. J. Int.* **138**, 479–494.
- Sambridge, M. (1999b). Geophysical inversion with a neighbourhood algorithm: II. Appraising the ensemble, *Geophys. J. Int.* **138**, 727–746.
- Sambridge, M. (2001). Finding acceptable models in nonlinear inverse problems using a neighbourhood algorithm, *Inverse Problems (Institute of Physics Publishing)* **17**, 387–403.
- Satoh, T., H. Kawase and S. I. Matsushima (2001). Estimation of S-Wave Velocity Structures in and around the Sendai Basin, Japan, Using Array Records of Microtremors, *Bull. Seism. Soc. Am.* **91**, 206–218.
- Scales, J. A. and L. Tenorio (2001). Prior information and uncertainty in inverse problems, *Geophysics* **66**, 389–397.
- Scherbaum, F., K.-G. Hinzen and M. Ohrnberger (2003). Determination of shallow shear wave velocity profiles in the Cologne/Germany area using ambient vibrations, *Geophys. J. Int.* **152**, 597–612.
- Schmidt, R. O. (1981). A Signal Subspace Approach to Multiple Emitter Location and Spectral Estimation, Phd thesis Stanford University, Stanford, CA.
- Sen, M. K. and P. L. Stoffa (1991). Nonlinear one-dimensional seismic waveform inversion using simulated annealing, *Geophysics* **56**, 1624–1638.
- Shapiro, N. (1996). Etude de l'interaction des ondes sismiques guidées régionales avec les hétérogénéités de la croûte, Phd thesis Université Joseph Fourier, Grenoble, France.
- Socco, L. V. and C Strobbia (2004). Surface-wave method for near-surface characterization: a tutorial, *Near Surface Geophysics* **2**, 165–185.
- Stoffa, P. L. and M. K. Sen (1991). Nonlinear multiparameter optimization using genetic algorithms: Inversion of plane-wave seismograms, *Geophysics* **56**, 1794–1810.
- Stokoe, K. H. II, G. J. Rix and S. Nazarian (1989). In Situ Seismic Testing with Surface Waves, In *Proc. XII Intl. Conf. on Soil Mechanics and Foundation Engineering*, 331–334.
- Tarantola, A. (1987). *Inverse Problem Theory*, Elsevier, Amsterdam.
- Thomson, W. T. (1950). Transmission of elastic waves through a stratified solid medium, *Journal of Applied Physics* **21**, 89–93.

- Tokimatsu, K. (1995). Geotechnical site characterization using surface waves, In *Proc. 1st Intl. Conf. Earthquake Geotechnical Engineering*, Ishihara (ed), Balkema, 1333–1368.
- Wathelet, M., D. Jongmans and M. Ohrnberger (2004). Surface wave inversion using a direct search algorithm and its application to ambient vibration measurements, *Near Surface Geophysics* **2**, 211–221.
- Woods, J. W. and P. L. Lintz (1973). Plane waves at small arrays, *Geophysics* **38**, 1023–1041.
- Xia, J., R. D. Miller, C. B. Park and G. Tian (2003). Inversion of high frequency surface waves with fundamental and higher modes, *Journal of Applied Geophysics* **52**, 45–57.
- Yamanaka, H. and H. Ishida (1996). Application of genetic algorithms to an inversion of surface wave dispersion data, *Bull. Seism. Soc. Am.* **86**, 436–444.
- Yoshizawa, K. and B. L. N. Kennett (2002). Non-linear waveform inversion for surface waves with a neighbourhood algorithm-application to multimode dispersion measurements, *Geophys. J. Int.* **149**, 118–133.
- Zhang, S. X. and L. S. Chan (2003). Possible effects of misidentified mode number on Rayleigh wave inversion, *Journal of Applied Geophysics* **53**, 17–29.